Doctoral Thesis

A nonsmooth local frame approach to frictional beam-to-beam contact

Thesis submitted in partial fulfillment of the requirements for the degree of Doctor of Philosophy (PhD) in Engineering Science

Author:
Armin Alex Etienne BOSTEN

Supervisor:
Prof. Olivier Brüls

Co-Supervisor:
Dr. Ing. Joachim Linn

July 2025

Contact details

Armin BOSTEN

Multibody and Mechatronic Systems Laboratory
Aerospace and Mechanical Engineering Department
University of Liège
Allée de la Découverte 9, 4000 Liège, Belgium

Mathematics for the Vehicle Industry
Fraunhofer Institute for Industrial Mathematics
Fraunhoferplatz 1, 67663 Kaiserslautern, Germany

Email: armin.bosten@gmail.com
Phone: +352 661 889 851

Members of the Examination Committee

Prof. Maarten ARNST (President of the Committee)
University of Liège (Liège, Belgium)

Prof. Olivier BRÜLS (Advisor)
University of Liège (Liège, Belgium)

Dr. Joachim LINN (Advisor)
Fraunhofer ITWM (Kaiserslautern, Germany)

Prof. Vincent DENOËL
University of Liège (Liège, Belgium)

Prof. Christoph MEIER
TU München (Munich, Germany)

Dr. Damien DURVILLE
Université Paris-Saclay (Paris, France)

ABSTRACT

Highly slender structures undergoing large displacements, such as cables and hoses are integral parts of most modern high performance engineering systems and interest from the industry in the virtual simulation of such systems has strongly increased in recent years. We focus on distributed line-to-line contact interactions, which are most appropriate for modeling closely packed slender structures that remain in contact over extended regions of their length. The modeling of frictional contact interactions, one of the key aspects for accurate prediction of mechanical behaviour, is particularly challenging and still a matter of scientific research.

In this thesis we adopt a geometric framework for flexible multibody systems which is characterized by a rigorous mathematical handling of frame transformations. The geometrically exact beam finite element framework on the special Euclidean group is selected for modeling slender structures. The equations of motion are interpreted as being expressed in the local frame attached to the body resulting in interesting frame invariance properties.

An essential ingredient of the selected contact model is the formulation of non-penetration conditions as a unilateral restriction of relative motions between material particles and the treatment of these conditions in a discrete setting. This work establishes the contact kinematics, including the normal gap and tangential slip, between geometrically exact beams building on the special Euclidean group formalism. The resulting formulation expresses the contact forces in the local frame and inherits the frame invariance properties from the chosen geometric framework.

These unilateral constraints may cause nonsmooth effects such as discontinuous spatial distribution of contact reaction forces, dynamic impacts and frictional stick-slip transi-

tions which require advanced numerical techniques. First, a quasi-static methodology is developed using an Augmented Lagrangian technique combined with a nonsmooth Newton solver. The elaboration of an alternative Gauß-Seidel dual solver is also explored. Then, the dynamic problem is tackled using the nonsmooth generalized-α time integration scheme. For quasi-static and dynamic cases we implemented two beam-to-beam contact elements. The first one is a simple collocation technique. The second one is the mortar method, where the non-penetration constraints are enforced in a weak sense. All the developments have been implemented into the open source software Odin connecting our work to a wide library of finite elements.

Various numerical experiments were performed for the quasi-static and the dynamic case. These include the static frictionless contact of a cantilever with a rigid wall for which a novel analytic solution was derived. The examples show the potential of combining all the previously mentioned concepts to form an appropriate framework for handling geometric non-linearities, discontinuities, and complex frictionless and frictional contact configurations exhibited by cable assemblies.

ACKNOWLEDGEMENTS

The process of writing a thesis manuscript is a rather dry experience. Everything has to be written in such serious "scientific" prose, no (not too many) jokes are allowed and English is nobody's mother tongue. If there is one place where the author has the freedom to let some of their personality shine through it is here in the acknowledgements section. It is also the only place where I will put a quote. Let's start with that:

"Gratitude is not only the greatest of virtues but the parent of all others."-Cicero

Although my name is written on the frontpage, this work is the result of a team effort and I will try to communicate my gratitude to everyone involved... in their respective mother tongue to hopefully allow for more personalized messages.

Firstly, I would like to thank my two advisors Olivier Brüls and Joachim Linn. Both were always open for discussion and happy to share their seemingly infinite wisdom, not only on thesis-related subjects, but also about life. I learned some valuable lessons from the two of you and for that I'm grateful.

Olivier, tu as tout simplement la classe.

Joachim, ich wünsche dir aus ganzem Herzen, dass der FCK in die 1.Bundesliga aufsteigt und dort bleibt.

Many thanks also go to Maarten Arnst, Vincent Denoël, Damien Durville and Christoph Meier who accepted to participate in the jury of this doctoral thesis and also gave their valuable advice at different stages of my doctoral and pre-doctoral journey.

This work received financial support from the Fraunhofer ITWM which is gratefully acknowledged, so is the involvement of the European Union via the THREAD network.

Most PhD students have what young Japanese anime affine people nowadays call a "senpai", a slightly more experienced coworker (which is not the advisor) that helps them on a daily basis. I was so lucky to have two! One for each of the two offices where I split my time.

Alejandro, I'm so done with coding in C++. It's not your fault, so please don't feel guilty. Los mejores deseos para tu linda familia.

Ben, ich hoffe ich war nicht zu lästig. Vernachlässige niemals dein Lauftraining und alles Gute in Japan. Ich hoffe du findest, wonach du suchst.

Liebe ITWM Truppe, Davide, Quirin, Ben, Muhannad, Urs, Tim, Tian, Vicky und alle anderen, die ich vergessen hätte. Eure Freundschaft hat meine Zeit hier in der Fremde so viel freudiger gemacht. Ohne euch hätte ich mich wahrscheinlich sehr einsam gefühlt.

Je suppose que si j'ai mis les gens du Fraunhofer je dois aussi te mettre Oli... Même si une thèse ce n'est pas toujours marrant, avoue qu'on a quand même eu bon quand on était ensemble. J'espère juste que le boss n'a pas trop écouté nos conversations à travers le mur de notre bureau ahah.

My deepest gratitude goes to my family and friends for their encouragements during some of the more difficult periods. Particularment o meo pequenino passero, obrigado para tua paciênca.

Dear Wout, Dear Remco, if you ever read this, please know that watching you race always filled my Belgian heart with joy, even when nothing else did.

Comme pour le travail de fin d'études mes derniers mots de remerciement sont dédiés à la Faculté des Sciences Appliquées. J'ai peut-être changé, mais la conclusion reste la même. J'aime la FSA. Cela vient du fond du coeur.

CONTENTS

INTRODUCTION

The ever-growing need of industries to improve the quality of their products while reducing costs pushes innovation. Systems become more complex and their manufacturing more tricky. A key step during the design phase is the construction and testing of prototypes. This step is iterative. Indeed, if the prototype does not meet some given requirements, the engineering team goes back to the drawing board, a new design is conjured up, and a new prototype is made. The number of cycles in this process can be drastically reduced with the help of virtual prototyping tools, which in turn saves costs. A digital model on a computer that simulates the real-world system is used to test out several design variants, and unsatisfying ones can immediately be eliminated without the need to actually produce a physical prototype. Examples of popular computer simulation software packages are *Abaqus* [1], *LS-Dyna* [2], or *Ansys* [3], to cite a few. These software packages often come with a range of features that allow one to optimize the digital prototype on the spot, yielding further time savings. Moreover, a digital model provides a perfectly controlled environment that allows one to see the in-use behavior of a design or verify its limits. Especially in industries producing large and complex systems, such as aerospace, automotive, and construction, these cost savings add up and become substantial [4].

This thesis is concerned with the mathematical modeling and numerical algorithms for mechanical systems, which constitute the backbone of the simulation software packages mentioned above. In particular, we focus on highly flexible slender objects undergoing large amplitude motion and experiencing frictional contact interactions. There are numerous examples of engineering applications whose behavior is determined by such effects and where simulation plays a crucial role. We will discuss some use cases in the next part of this introduction.

From Wire Harnesses to Textile Braiding

Figure 1 shows examples of electric cables and hydraulic hoses that may be found in abundance in cars. These cables are generally highly flexible, made of a large number of thin metallic fibers compressed inside a polymer coating and assembled into wire harnesses. Software tools used in the industry for computer-aided design and virtual assembly need data about the mechanical properties of such cables. These are, for example, the effective bending stiffness EI, the effective torsion stiffness GJ, and the effective tension stiffness EA. For simple cables made of a single heterogeneous material, these material parameters can be computed knowing the cross-section geometry.

However, in practice, cables and hoses are composite structures, and mechanical properties have to be determined by measurements. To that end, the Fraunhofer Institute for Industrial Mathematics developed the *MeSOMICS* [5] machine, which performs two tests. The first one is a standard torsion test where both ends of the cable are clamped and the specimen is twisted. During the test, the torsion angle and the resulting moment are recorded, from which the torsion stiffness can immediately be identified. The second one is a bending test that is also valid for finite displacements. For this one, the two ends are attached to moment-free bearings. By moving one mounting point towards the other, the specimen forms an arc. The bending stiffness can then be deduced from the displacement of the moving mounting point, the bending line, and the recorded resulting horizontal force. Finally, the tension stiffness can then be calculated knowing the bending and torsion stiffnesses.

One drawback of the methodology described above is the following. The measurements have to be repeated for every different type of cable. Moreover, these experiments only provide limited insight into the physical effects inside the assembly. Ideally, a fully calibrated digital model could replace experiments to a certain extent. This would have several advantages. Next to being cheaper and less time-consuming than a physical experiment, a virtual model gives access to detailed information about contact interactions or geometric rearrangements of the individual components [6–12].

In Fig. 2 on the left, a textile braiding machine can be seen, which is used to produce textile fabrics or composite materials. Composite materials made of small yarns give them very special properties, which is why they are widely used in high-performance engineering systems [13–15]. Yarn carriers move on a circular trajectory, clockwise and anticlockwise in an intertwining motion to create a certain braid pattern. The

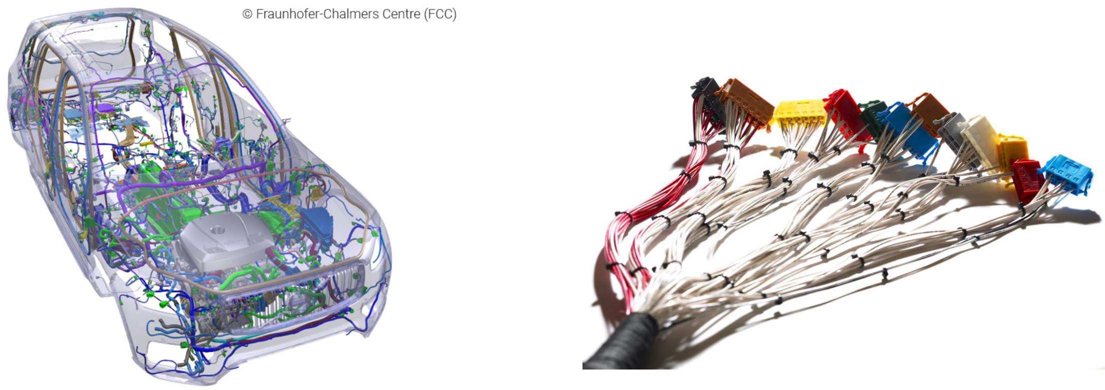

Figure 1: Application examples of contact between a large number of slender fibers: Harnesses of electric cables found in cars. Images taken from the THREAD website.

development of (digital) models that can accurately predict the behavior of the braiding machine is still a matter of ongoing research [16–23].

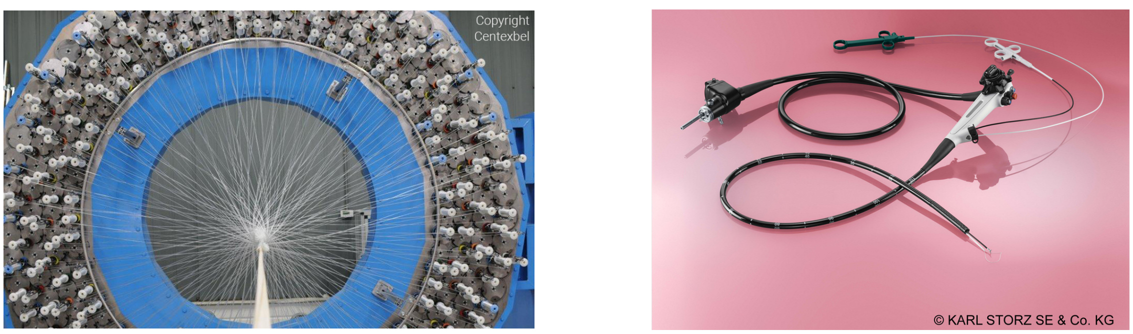

Figure 2: Application examples of contact between a large number of slender fibers: Textile manufacturing and endoscopes. Images taken from the THREAD website.

Further application areas can be discussed. Simulation tools are also employed to verify that civil engineering structures will be able to withstand the loads they will be subjected to during their lifetime. The weight of cable-stayed bridges is supported by wire ropes [24–27].

In the computer graphics community, there is a demand for the realistic animation of hair [28]. Going several orders of magnitude smaller, similar models can be exploited in the range of micro- or even nanometers. They have successfully been applied to polymers, molecular dynamics, as well as DNA strands [29, 30].

We could also mention endoscopes with their complex layered internal composite structure and their exterior contact interactions with human tissue [31–33]. From a modeling point of view, the mechanical behavior of endoscopes winding their way through the human body bears resemblance to drilling problems encountered in the oil drilling industry [34–37].

Clearly, there is no shortage of application examples. In recent years, general interest in the simulation of highly flexible systems has increased significantly, as illustrated by the emergence of THREAD[1] [38], a European project that provided funding for several young researchers active in topics directly or indirectly related to the subject of this thesis.

The common point between the above examples is that these are systems made of entangled slender structures undergoing frictional contact interactions, which largely impact their overall behavior. A common approach is to ignore these *internal* effects by employing macroscopic models. Macroscopic models are useful in practice but can be limited in their ability to represent all the complexity of the system of interest. In any case, involved modeling parameters need to be tuned with the help of additional information about the system, for example, coming from a detailed mesoscopic numerical model that includes said contact interactions. This thesis aims at making progress in the latter category of approaches.

Slender Structures as Beam Models

As mentioned in the previous section, we are interested in systems composed of flexible slender structures or rods. By that, we mean any components that have one geometric feature that is much longer than the other two. From a mathematical point of view, it is then possible to reduce a 3-dimensional problem into a 1-dimensional one. Such a 1-dimensional model is referred to as a "beam." The reason is, of course, to decrease the number of degrees of freedom in a subsequent numerical model and hence the computational cost. This is a necessary operation if computer calculations need to be done in a reasonable amount of time. But, as my advisor likes to say: "There is no free lunch." We are trading computational cost for increased mathematical complexity, both in the formulation of the mechanical component and the modeling of contact. An in-depth understanding of the mathematical consequences of the underlying hypotheses our models are based on is paramount to guide our choice of tools and methods. Even though beams are the main focus of this thesis, they are not the only constituents of our applications of interest. Indeed, systems composed exclusively of beams are rare. In general, the motion is imposed by connecting the beams to rigid bodies through different joints. Such systems are naturally modeled as so-called flexible multibody

[1] The European project THREAD investigates novel approaches to model and simulate slender, highly flexible beam-like structures for a broad variety of industrial applications.

systems. Therefore, the developments in this thesis are embedded into a much more general multibody framework, which allows making use of powerful tools from previous works. We will explain them in the next sections.

A Geometric Finite Element Framework

Many formulations of multibody systems, or beams in particular, have been proposed in the literature. We will follow the generalized *finite element method* (FEM), as developed by Géradin and Cardona [39], for its generality and flexibility. In that approach, the configuration of each body in the system is described by a set of redundant absolute variables expressed with respect to the inertial frame of reference. Kinematic connections, or joints, are represented by adding algebraic equality constraints, which are resolved using Lagrange multipliers. This way, the equations may be generated in a systematic manner. In the age of computers, this is desirable because "*systematic*" rhymes with "*automatic*." The involved system matrices are usually sparse.

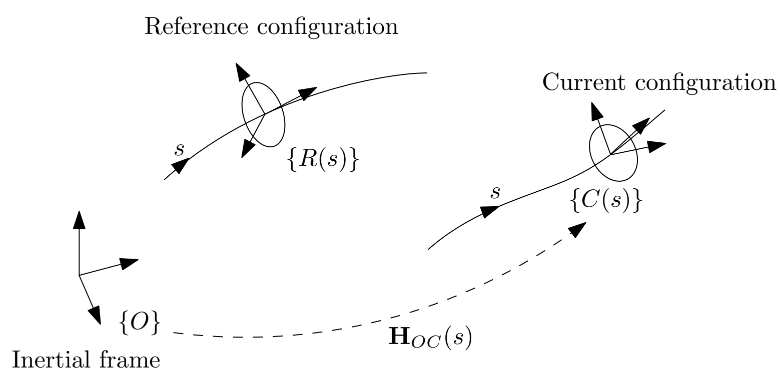

Figure 3: Kinematic description of multibody components: frame transformations from the fixed inertial frame to any frame attached to the body.

One of the main difficulties is the handling of large amplitude 3-dimensional motions including finite rotations and the nonlinearity of the deformation measures. To overcome these difficulties, Sonneville developed a fully geometric FEM framework [40], in the spirit of Géradin and Cardona, but connecting the rigorous mathematical ideas to the description of kinematics in flexible components. A key ingredient of the approach is the concept of a frame defined by a point and a triad of orthonormal vectors. On top of the inertial frame of reference, we attach a frame to each point of interest or node of our mechanical system. One frame suffices for a free rigid body, but it could be more. Additional frames may be introduced to represent the location of joints or may result from the FE discretization of flexible bodies. They could also be placed at locations where contact interactions between different bodies are expected. The configuration of each frame, i.e., its position and orientation, is represented as the (relative) transformation from the inertial frame to itself and resolved in the inertial frame, as illustrated in Fig. 3.

Mathematically, the (relative) position of a frame is a vector of $\mathbb{R}^3$ and the rotation is seen as an element of the special orthogonal group $SO(3)$. In the approach by Sonneville, which we will also follow, frame transformations are considered as elements of the special Euclidean Lie group $SE(3) = \mathbb{R}^3 \ltimes SO(3)$. Lie group theory is a nice and well-established mathematical toolbox that may be used in a straightforward manner for the continuous formulation, space discretization, and time integration of multibody systems with flexible components (beams, shells, etc.) [41]. It provides the insight that naturally leads to the so-called local frame approach by selecting the left invariant representation of the frame derivatives. The resulting equations and numerical methods have many desirable properties, which justify the increased level of abstraction when compared to other more established methods in the field of engineering. These will be discussed in chapter 1 dedicated to a literature review. In $SE(3)$, rotation and translation variables are intrinsically coupled. One consequence for the resulting beam formulation is the absence of the shear locking problems, which are present in many formulations of flexible components. Motion increments, internal and external forces, and deformations are expressed in the local frame attached to the body, and the equilibrium equations are invariant under a superimposed rigid body motion. Finally, the equations are simpler and less nonlinear as opposed to other formulations, which opens the door for efficient and easy-to-implement solution algorithms. The reader is referred to chapter 2 for more information.

The systematic use of frame transformations for the kinematics of mechanical components is not new to Sonneville's work. For example, it has actually been used for a long time in robotics [42]. However, their application to the formulation of flexible components and superelements constituted a major step towards a more systematic use of these notions in the field of structural mechanics.

A Nonsmooth Approach

One important aspect of modeling for engineering systems that shall be discussed now is contact mechanics, which brings its own set of new difficulties. Similar to joints, contact conditions characteristically restrict relative motion between two bodies. But they only do so if the two bodies touch, which they do not necessarily do. Therefore, contact is translated into unilateral constraints. These should be understood as shown in Fig. 4. If the gap function g that measures the proximity of material points on the surface of two bodies is strictly positive, no interaction occurs, and the normal reaction force F_N induced by one on the other is zero. If the gap function is zero, a non-vanishing normal reaction force can develop. At least one of the two quantities always vanishes, and thus their product is always zero. This last constraint is known as the complementarity condition. Mathematically, the normal contact conditions are expressed as

$$g \geq 0, \quad F_N \geq 0, \quad gF_N = 0. \tag{1}$$

Models of this type are called "nonsmooth" as opposed to regularized techniques. We will further discuss both approaches in the state of the art in section 1.2.

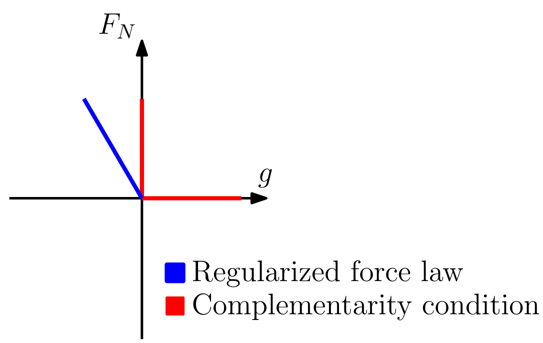

Figure 4: Contact models: Complementarity condition versus regularization.

There are additional subtleties in contact mechanics that require some more explanation. For a general deformable body, described by the theory of continuum mechanics, displacements, velocities, and stresses inside the body are continuous with respect to space [43]. Here we suppose that the surfaces of the bodies are smooth. For contact mechanics, that means that the contact stresses induced by one body touching the other should also be smooth. These smoothness properties are ensured due to the absence of restrictions on the kinematics of the bodies. They are allowed to locally deform such that the stress field may remain smooth. This no longer holds true in general for the multibody components we are working with. Indeed, these are based on reduced kinematics that prevent the deformation modes required for a smooth stress field and thereby potentially introduce *jumps in the stress field* as artifacts in the model. In particular, beam models that suppose rigid cross-sections lead to space discontinuous contact interactions [44–47], as can be seen in Fig. 5 on the right. The normal contact force $q_c(s)$ represented by the black curve is discontinuous. A deformable cross-section would exhibit behavior as represented by the red curve.

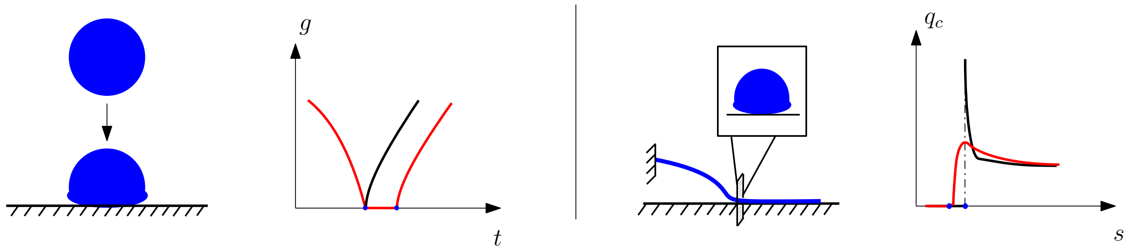

Figure 5: Smooth contact interactions (time & space) are ensured via local deformability. Left: impact of a ball on a rigid surface. Black: rigid body. Red: deformable body. Right: contact between a cantilever beam and a rigid surface, s is the material coordinate along the centerline. Black: rigid cross-section. Red: Deformable cross-section.

When extending the discussion to dynamics, we enter the realm of mechanical impacts. As shown in Fig. 5 on the left, the impact of rigid bodies is instantaneous. The gap $g(t)$ represented by the black curve is only closed exactly at the time of impact. Deformable bodies are able to store elastic energy such that they separate after a finite duration, which is represented by the red curve. Mathematically, this means that for the former we are dealing with percussions and measure differential equations, and for the latter with traditional partial differential equations. Notice that the smoothness of the behavior of a flexible body only holds under the two following conditions:

- The deformable body is not discretized.
- No kinematic hypotheses are made.

When considering the simulation of beam-to-beam contact, due to the presence of the rigidity assumption of the cross-section and numerical impacts from the finite element discretization, nonsmooth phenomena appear [48, 49], which means that the behavior shares similarities with the rigid case.

In this thesis, we make the distinction between nonsmooth behavior in time and in space. Both issues influence numerical models differently due to the fact that during numerical procedures, time and space discretizations are not performed in the same manner. This is discussed in more detail in chapters 3 and 4.

On top of the nonsmoothness introduced by the rigidity of beam models in the radial direction and the discretization procedure, we are also interested in frictional stick-slip effects modeled by Coulomb's law of dry friction. It states that when the two bodies are sliding on each other, the friction force is proportional to the normal force and always acts in the opposite direction of the relative velocity between two contacting material points. When the relative velocity is zero, the contact is in a sticking state, and the friction force is unknown but always below the sliding limit.

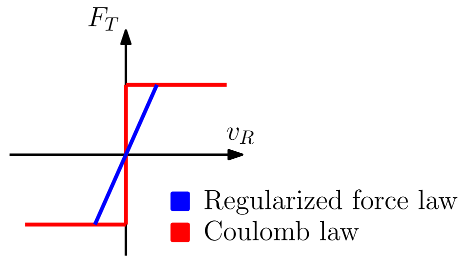

Figure 6: Coulomb law and an example of regularization.

As can be seen in Fig. 6, the friction force is a set-valued function of the relative velocity. It is non-differentiable at the origin in the classical sense. Again, regularized approaches exist that transform the friction law into a simple function. However, the ability to capture sticking is lost. This question will be further developed in chapter 1. For an extensive overview of contact mechanics for multibody systems, a comparison of nonsmooth and regularized approaches, different friction laws, and a list of open challenges, one can refer to Flores [50].

Objectives of the Thesis

The objective of this thesis is to combine the geometric finite element framework for flexible multibody systems and, in particular, the beam finite element formulation with nonsmooth algorithms for the simulation of distributed contact interactions between highly flexible slender structures. One important aspect is friction phenomena.

Outline and Contributions

The manuscript is structured as follows:

- Chapter 1: We start with a chapter about the state of the art for beam models and beam-to-beam contact. The focus is put on the most common formulations and numerical techniques applied in the engineering community. The chapter reviews the advantages and disadvantages of each approach. On this basis, several modeling choices will be introduced for the purpose of this thesis.
- Chapter 2: We follow with a chapter about the beam finite element formulated on $SE(3)$, that will be employed in this thesis. It serves as an introduction to the local frame approach and sets the notation for the remainder of the manuscript. We

explain all the building blocks of the methodology. These include a brief introduction to the Lie group $SE(3)$, the interpretation of its elements as frame transformations, the representation of derivatives, the consequences on the formulation of equilibrium equations of the beam, and finally the principles of discretizing equations written on a Lie group. After a presentation of a Simo-Reissner beam, we also present new Kirchhoff-Love and inextensible Kirchhoff beam elements. These are extensively tested by means of relevant numerical examples.

- Chapter 3: This chapter describes our contributions to static beam-to-beam contact using a nonsmooth philosophy. The kinematics of contact and the formulation of the equilibrium conditions in the continuous setting are presented. Since we simply extend the $SE(3)$ framework, a formulation where the contact forces are expressed in the local frames emerges, and the contact element inherits some of the desirable properties from the beam model. Then, we propose two different discretizations of the contact virtual work: one by collocation and one via the so-called mortar method. The resulting set of nonlinear equations also contains inequalities. They are solved by applying an augmented Lagrangian technique and a semismooth Newton algorithm. The validity of the proposed schemes is illustrated through a selection of relevant numerical examples. In particular, we also discuss how the spatial discontinuity introduced by the rigid cross-section assumption affects the performance of the numerical scheme. To that end, we derived a novel analytic solution for a beam contact benchmark.

- Chapter 4: In the previous chapter, inertia terms were ignored, and we concentrated on spatial aspects of beam-to-beam contact. In this one, we introduce dynamic effects into the problem. As mentioned in the introduction, this demands the handling of impacts, and velocities can be discontinuous in time. At the moment of impact, accelerations are not defined in the classical sense. Therefore, a formulation of the equilibrium in terms of differential measures is introduced. This step is followed by a presentation of the nonsmooth generalized-α scheme (NSGA) applied to the beam-to-beam contact problem. We show that the combination of the mortar approach and the NSGA together with the beam finite element on $SE(3)$ offers an appropriate framework for the modeling of dynamic contact interactions among beams. As before, the discrete equations are solved by an augmented Lagrangian technique combined with a Newton method at each time step. We also explore the possibility of employing a Gauß-Seidel method as an alternative to the Newton method.

- Finally, we present the conclusions and make suggestions for future work.

Publications and Conferences

This manuscript does not stem from the work of one single author; rather, it is the result of a collaboration with Alejandro Cosimo, Olivier Brüls and Vincent Denoël from the University of Liège, and Joachim Linn, Vanessa Doerlich and Benjamin Bauer from the Fraunhofer ITWM Kaiserslautern. It led to the following full papers in journals and conference proceedings:

- Bosten, A.; Cosimo, A.; Linn, J. and Brüls, O.; "A mortar formulation for frictionless line-to-line beam contact". *Multibody System Dynamics*; 54:31-52; 2021. [51]

- Bosten, A.; Denoël, V.; Cosimo, A.; Linn, J. and Brüls, O.; "A beam contact benchmark with analytic solution". *Zeitschrift für Angewandte Mathematik und Mechanik*; 103(11):1-12; 2023. [52]

- Bauer, B.; Bosten, A.; Roller, M. and Linn, J.; "Physical validation of simulation tools for slender elastic structures". *Proceedings of ECCOMAS Multibody (Lisbon)*; 2023. [53]

Below, we provide a list of publications at scientific conferences:

- Bosten, A.; Linn, J.; Doerlich, V. and Brüls, O.; "A local frame approach for line-to-line contact between beams with circular cross-sections". *ECCOMAS WCCM Conference (Paris)*; 2020.

- Bosten, A.; Cosimo, A.; Linn, J. and Brüls, O.; "The $SE(3)$ Lie group framework for multibody systems with contact". *NumDiff-16 Conference (Halle)*; 2021.

- Bosten, A.; Cosimo, A.; Linn, J. and Brüls, O.; "A nonsmooth approach to frictionless beam-to-beam contact". *ECCOMAS Multibody Conference (Budapest)*; 2021.

- Bosten, A.; Cosimo, A.; Linn, J. and Brüls, O.; "Towards a Gauß-Seidel solver for problems involving line-to-line beam contact". *ECCOMAS WCCM Conference (Oslo)*; 2022.

- Bosten, A.; Denoël, V.; Cosimo, A.; Linn, J. and Brüls, O.; "The influence of the beam kinematic assumptions in a beam contact benchmark". *ECCOMAS WCCM Conference (Oslo)*; 2022.

- Bosten, A.; Denoël, V.; Cosimo, A.; Linn, J. and Brüls, O.; "On the nonsmoothness of beam-to-beam contact problems: analytical and numerical approaches". *ENNSD Symposium on Nonsmooth Dynamics (Toulouse)*; 2022.

- Bosten, A.; Cosimo, A.; Linn, J. and Brüls, O.; "Numerical treatment of nonsmooth frictional beam-to-beam contact". *ECCOMAS Multibody Conference (Lisbon)*; 2023.

- Brüls, O. and Bosten, A.; "On the evaluation of the tangential slip increment in quasi-static beam-to-beam contact problems". *ECCOMAS HFFS Conference (Rijeka)*; 2023.

CHAPTER 1

STATE OF THE ART & LITERATURE REVIEW

In this chapter, existing approaches for the simulation of beam-to-beam contact interactions are reviewed. Since it is difficult to fully dissociate them from the modeling of the individual beams themselves, we will start by discussing the most relevant classes of beam models and their implications. We always keep the numerical aspect in mind, i.e., a model is the combination of a continuous formulation, if there is one, a subsequent discretization, and a solution scheme. We end by pointing out gaps in the beam-to-beam contact literature and lay out our contributions to the subject as an attempt to fill some of them.

1.1 Beam Models

Our interest lies in the nonlinear theories that allow for large displacements in three dimensions and that incorporate tension, bending, and torsional deformation modes. Shear deformation in highly slender structures can generally be neglected. Hence, we do not make it a prerequisite of our potential beam model.

1.1.1 Simo-Reissner Models: On the Rigidity of Cross-Sections

The two papers by Simo and Vu-Quoc [54,55] have more than 2600 combined citations. To this day, there are still papers being published every year about how to best solve the equations Simo proposed. He must have been onto something... and who else to best explain the reasons for the excitement surrounding this beam theory than the author himself:

"*Here we proceed directly by constraining the 3-dimensional theory with the introduction of the kinematic assumption. A basic step is the formulation of the basic kinematics of the beam in terms of a 3-dimensional orthogonal moving frame defined so that one of its vectors remains normal to a typical cross-section in any configuration. The resultant force and torque acting on a typical cross-section are then resolved relative to this moving frame. ... From a computational standpoint, particularly in the context of the finite element method, such a description allows complete freedom in the best-suited parametrization of the orthogonal transformation.*".

Note that nowhere in the article does it say that cross-sections of beam-like structures remain rigid. It merely states that the equations governing the behavior of typical (or average) cross-sections under the action of resultant forces and torques resemble those describing the dynamics of a rigid body. Still, the analogy is very useful. At a coarse scale, a beam can be represented as a family of cross-sections that behave like rigid bodies, i.e., that undergo rigid body transformations (translation & rotation). In other terms, the configuration variables are elements of $\mathbb{R}^3 \times SO(3)$ or $SE(3)$, depending on the choice of kinematic description. Thus, the beam model constructed by Simo has a direct connection to the rich mathematical theory of (non-abelian, non-linear, matrix) Lie groups, which signifies the presence of invariance properties in the equilibrium equations. Just as Simo pointed out, many questions arise concerning parametrization and discretization, and this is where most of the differences between later publications on this topic lie.

At a fine scale, it is clear that cross-sections deform. The inclusion of this type of localized effect becomes necessary to derive a proper beam theory from continuum mechanics [56].

Finite Element Formulations on $\mathbb{R}^3 \times SO(3)$: These are the most widespread due to the engineering community's fondness for finite element codes. The objective is to embed the implementation into existing FE frameworks and be minimally intrusive [10, 57–62] with the assumption that translation and rotation are independent fields. As a consequence, the discretizations can also be performed separately, which leaves great flexibility in the choice of shape functions. This can be of interest if one wants to achieve a very smooth representation of the centerline in a simple manner. Oftentimes, a global parametrization of rotation is introduced [63, 64], then discretized, and finally, the equations are solved in the inertial frame of reference. Great care has to be taken to preserve invariance. Moreover, these elements are prone to locking. Generally, these two issues are addressed using clever tricks that require an advanced understanding of the physics and numerics involved. An extensive review of the literature can be found in [65].

Finite Element Formulations on $SE(3)$: Borri and Bottasso proposed a helicoidal approximation of the beam reference line in [66]. In doing so, they coupled translation and rotation variables and eliminated the locking problem. They justified it by stating that a helicoidal Ansatz is more "intrinsic" than, for example, a polynomial approximation of the centerline because it is independent of the rotation parametrization, but without giving a fully detailed explanation. Remarkably, there is no mention of Lie groups in that article, which they only started to explicitly study in [67]. The interpretation of a formulation of the kinematics on the special Euclidean group $SE(3)$ and the systematic development of flexible mechanical components for multibody systems within that theory only came twenty years later with the work of Sonneville [68], thereby giving a more precise meaning to the word "intrinsic" employed in [66]. Moreover, [68] introduces the idea of solving the equilibrium equations in the local frame. We will not go into more detail here, since chapter 3 is dedicated to that topic. The same formulation was later presented in the context of soft robotics [69]. Similar ideas have been studied in [70]. The strain and velocity-based approach discussed in [71–73], though not explicitly mentioned, is also closely related to a formulation on $SE(3)$.

Geometric Finite Difference Type Methods: A FD discretization scheme on a staggered grid was proposed by Lang et al. [74]. Rotational degrees of freedom are assumed uncoupled from translation and parametrized by unit quaternions. Such a parametrization is known to be computationally efficient and often preferred in performance-critical situations. The authors enforce the unitarity constraint via Lagrange multipliers, then apply an index reduction method to obtain simple equations. A quasi-static version that computes the solution from direct energy minimization also exists. The model has found its way into real-time applications for the automotive industry.

In [75, 76], keeping the idea of describing rotations using unit quaternions, a coupled formulation of the beam kinematics is chosen as a starting point. By this choice, locking issues are automatically circumvented, just as the models from the previous category. Both use variational integrators which are obtained by directly computing the integrals involved in the variational formulation using some quadrature rules. Instead of introducing a global parametrization of motion, so-called Lie group methods are employed which preserve the mathematical structure of the configuration space. The qualification "of FD type", albeit with special properties, stems from the fact that the discretized solution is not interpolated. Although robust and very efficient, FD methods lack a continuous representation of the beam centerline for the approximate solution, which makes them less attractive when contact interactions need to be accounted for.

1.1.2 Kirchhoff-Love Models

For very thin rods, shear deformation becomes negligible. Several authors point out that the performance of numerical solvers and time integration schemes for Simo-Reissner type beam models deteriorate as the slenderness increases because involved system matrices become ill-conditioned. Indeed, the small amplitude shear deformation modes are of much higher frequency than the bending modes. Particularly explicit time integration schemes perform poorly, as they need increasingly smaller time steps to remain stable. This is especially frustrating since this high-frequency content is seldom of interest anyway. One possible remedy is to fully take shear deformation out of the model. Basically, the beam cross-section is forced to remain orthogonal to the centerline at each point. This hypothesis is called the Kirchhoff constraint [77]. An analogous reasoning can be made for extension modes, leading to so-called inextensible Kirchhoff-Love rods. We distinguish between two families of Kirchhoff-Love models.

Constrained Simo-Reissner Models: The members of this family take the Simo-Reissner beam as a starting point with its elegant mathematical structure and then remove the superfluous degrees of freedom by adding constraints. In the continuous setting, it is straightforward. The main question is how to enforce this constraint numerically after discretization, which depends on the chosen parametrization and shape functions. Usually, it is done using Lagrange multipliers. Examples of such strategies may be found in [62,65,76,78]. In [79], shear vibrations are critically damped out inside a viscous material law, effectively making the model behave like a Kirchhoff-Love beam.

Intrinsic Kirchhoff-Love Models: Some authors are ready to abandon handy Lie groups to directly construct a beam model that only includes degrees of freedom related to centerline translation and torsion of the cross-section [28, 65, 80–82], reducing the number of required nodal parameters from 6 to 4. The Kirchhoff constraint is automatically satisfied in such cases. Here, the subtlety is generally the definition and update of a relative twist measure. Only one rotation parameter suffices, such that one does not have to deal with the nonlinearity of large rotations.

1.1.3 Rotation-Free Models

There are interesting alternatives to the previously presented beam models that do not rely on the concept of orientation of cross-sections. Their main selling point is the use of variables that exclusively live in vector spaces, which significantly simplifies their mathematical treatment. In some cases, the assumption of rigid cross-sections is too strong and has to be discarded. We briefly review two popular approaches.

ANCF Models: The Absolute Nodal Coordinate Formulation is a fully discrete theory. As its name suggests, the kinematics is described through positions and slopes at FE nodes expressed in the inertial frame of reference. It is simple and intuitive but suffers from numerous locking phenomena [83–85].

Deformable Cross-Section Models: For certain applications, the ability to include the distortion of the cross-section is critical, but a full 3D numerical model is still too computationally expensive. For example, this is the case if the Poisson effect is of importance or if local deformations due to contact interactions have a non-negligible effect on the system behavior. In such cases, the class of models proposed by Durville in [12] finds its use. The position of each particle is described via a Taylor expansion with respect to the transverse coordinates. The higher the order, the more complex deformation patterns of the cross-section may be represented. The first-order version suffices in many cases and has a nice interpretation where the position of a point on a given cross-section is given by two unconstrained variable directors. As a drawback, the number of degrees of freedom of each mode increases from 6 to 9. For a different model from the same family and a nice overview of their history, see [86].

1.1.4 Remarks on Our Choice of Beam Models

In most engineering methods, the final discretized equations that are solved involve three characteristic steps. First, the kinematic description of the body assumes that translation and rotation are independent, with configuration variables in $\mathbb{R}^3 \times SO(3)$. Second, all quantities are calculated with respect to the inertial frame. Third, the rotation group is parametrized using either a minimal or redundant set of global coordinates before discretization.

Historically, the engineering community has used this approach because it avoids abstract mathematical concepts. The equations allow for standard discretization procedures, time integration schemes, and solvers. Not all approaches reviewed in this section exhibit all these characteristics, but each has at least one, along with associated challenges. Rotation parametrizations introduce additional nonlinearity. Minimal parametrizations require reparametrization strategies to avoid singularities, while redundant parametrizations increase the number of degrees of freedom and necessitate constraint handling. The separation of translation and rotation can lead to locking issues, often addressed using reduced integration techniques. Another important aspect is defining appropriate strain measures and ensuring that the equations are invariant under superimposed rigid body motion. While issues can arise in the continuous setting, preserving invariance after discretization is particularly challenging.

The mathematical theory of Lie groups provides the necessary framework to address these challenges and naturally leads to the local frame approach. The beam finite element on $SE(3)$ introduced by Sonneville et al. [68], presented in Chapter 2, avoids parametrization singularities and locking, and invariance properties are automatically conserved. Moreover, the authors also argue that the equations of motion are less nonlinear than in other formulations, indicating potential for performance improvements. It is therefore the beam model of choice in this work.

1.2 Beam-to-Beam Contact Formulations

Now that we have discussed some of the relevant beam models, we can focus our attention on reviewing existing approaches for the simulation of contact problems involving beams undergoing large displacements. We distinguish between regularized and nonsmooth approaches. Both have their advantages and drawbacks. Interestingly, one has received much more attention in the beam-to-beam contact literature than the other.

1.2.1 Regularized Formulations

Early Point-to-Point Models: In [87], Wriggers and Zavarise derive a purely theoretical frictionless quasi-static formulation for thin cylindrical beams in the context of the finite element method. They mostly concentrate on situations with large contact angles and assume that the force the interacting components induce on each other is localized at a point. This means that the force is modeled spatially as a *Dirac delta* in the equilibrium equations, almost as if at the location of contact, the beams were replaced by rigid spheres. They propose both a penalty and a Lagrange multiplier method for the enforcement of the contact constraint. The system of nonlinear equations is solved using a Newton algorithm. Collision detection relies on a closest point projection. The same authors extend their work to the frictional case using penalty regularization in [88] and also show numerical results. Algorithmic difficulties related to the specificities of contact detection between slender objects are also discussed. Litewka obtains better behavior of the numerical scheme in the presence of sliding using a smooth representation of the centerline [89,90] and further improves it for moderate contact angles in [91].

Konyukhov and Schweizerhof propose a covariant version of a frictional point-to-point model and discuss the validity of the closest point projection in [92, 93]. Interestingly, they define a curvilinear frame of reference at the contact location and compute all quantities with respect to this local frame, which leads to computational advantages due to the effective description of kinematic measures for contact interaction. They state their preference for the penalty method when frictional contact is involved, interpreting it as an additional constitutive law at the contact interface. Also falling into this category is [94].

Collocation Line-to-Line Models with Penalty: In a large number of applications, slender structures do not simply interact at individual discrete points but rather along line segments of finite length. To cope with such situations, so-called line-to-line contact formulations have been developed. In the continuous setting, these assume distributed (lineic) contact pressures or *forces per unit length* between beams. The additional question concerning the discretization of the contact pressure arises, and there are different options. The most straightforward one is a simple collocation. The contact integral is replaced by a sum of point forces at a certain number of well-chosen locations found through a mix of geometrical calculations and numerical heuristics. A prime example is the framework developed by Durville [12, 95–97], capable of computing the static equilibrium of assemblies with an extremely large number of fibers. The algorithm is based on the definition of contact zones and the construction of an average centerline that serves as a backbone for the determination of the contact kinematics. A penalty regularization is introduced for the normal and tangential constraints. The beam model with deformable cross-sections additionally smoothes the solution. A combination with isogeometric analysis can be found in [98], and a version based on an ANCF beam model in [99, 100].

Gauß Point Line-to-Line Models with Penalty: The distributed contact pressure can also be integrated numerically, leading to Gauß point type formulations [101–103]. Meier et al. combine such a line-to-line model with a point-to-point model in an all-angle beam-to-beam contact formulation [104, 105]. In [106], a method of this type is applied to the frictional problem. A sufficient level of smoothness, typically a C^1-continuous centerline representation at element boundaries, the combination with penalty, and special segmentation algorithms are required to obtain a satisfactory precision for the integration of the contact pressure, which is necessary to preserve optimal spatial convergence rates.

1.2.2 Nonsmooth Formulations

Bertails et al. simulate hair dynamics for computer graphics applications, combining a finite difference Kirchhoff rod that uses curvatures as primary variables with a nonsmooth time integration scheme that enforces contact constraints at the velocity level [107]. Errors due to the drift of contact constraints at the position level are admissible because the interest mainly lies in the overall behavior of a large system of fibers and its visual rendering. A semismooth Newton scheme was used for finding the solution to the contact problem at each time step. Multiple contact situations can occur, which might give trouble to the Newton scheme. Indeed, in such situations, the Jacobian matrix becomes singular. Therefore, Daviet et al. developed an iterative Gauß-Seidel-like method for robustly computing the solution [49, 108]. The model can deal with many different contact configurations. However, line-to-line interactions are simply taken into account using a collocation method in which the contact points are introduced by means of smart collision detection algorithms. A similar approach is taken in [109].

1.2.3 Commercial Finite Element Codes

It is often difficult to know the exact numerical algorithms implemented in commercial codes. For the interested reader, we can mention that beam-to-beam contact problems are solved with their help [27, 110–115].

1.2.4 Remarks on Our Choice of Contact Model

As the reader may have noticed, the vast majority of beam-to-beam contact algorithms found in the computational mechanics literature are regularized penalty-type approaches. It is true that they are simpler to implement since they are non-intrusive in the sense that the nature of the governing equations does not change from the contact-free case. Thus, standard solution methods are applicable, and mature FE codes do not need to be rewritten. The interpretation of the penalty parameter (or contact stiffness) as local material compliance is a widely appreciated feature in the engineering community that turns out to be handy in practical settings. Unfortunately, the solution of the problem generally depends on the contact stiffness. The larger the stiffness, the smaller the penetration, but the more ill-conditioned the matrices become, which may compromise the convergence of Newton solvers in implicit time integration. Additionally, the time step depends on the scale of the modeled dynamic effects. It needs to be small to obtain stable results of acceptable accuracy, which contributes to the ill-conditioning of the system. Therefore, the penalty stiffness simultaneously plays the role of a numerical parameter that needs tuning to obtain a solution and a modeling parameter that affects the result. From a scientific point of view, such mixing might be controversial. Finally, the solutions resulting from such a formulation will always be smooth. Inherently nonsmooth mechanisms, such as stick-slip transitions or discontinuous velocities, cannot be represented.

In this thesis, we propose to follow a nonsmooth formalism which: avoids the use of compliance parameters, enforces the constraints exactly, and allows the use of time steps independent of the time scale of the contact interactions. As opposed to the works described in section 1.2.2, we focus on methods relevant for the simulation of mechanical systems in engineering applications as explained in the introduction.

CHAPTER 2

BEAM FINITE ELEMENT FORMULATION ON *SE(3)*

In this chapter, essential concepts concerning the local frame approach for flexible components are illustrated by deriving three beam finite elements formulated on the special Euclidean group $SE(3)$. The first one is a reformulation of the Simo-Reißner, or as it is often called, geometrically exact model as it was first presented in [68]. The other two are a Kirchhoff-Love and an inextensible Kirchhoff model obtained by imposing additional constraints. We briefly introduced these new formulations in [47], but in this chapter, we take the opportunity to give more details. We also set the framework and notations that will be employed throughout the remainder of this thesis. The existing beam model in the research code *Odin* [116] was extended by the Kirchhoff and inextensibility constraints from Eq. (2.80) in collaboration with the co-authors of [47] and its behavior in the presence of large precurvature was improved. Moreover, all numerical examples were implemented therein.

It starts with an introduction to Lie groups and the Lie group $SE(3)$ in particular in Section 2.1. We connect the mathematical theory to the kinematic description of multibody components. Section 2.2 focuses on the continuum formulation of the equilibrium equations for beams. Unlike in most approaches, the equations of motion are expressed in the local frame. Section 2.3 addresses the consistent discretization of equations written on a Lie group and on $SE(3)$. This is where the main differences lie compared to other geometrically exact formulations. For the space discretization, we employ the finite element method. The same geometric framework can be used to derive time integration schemes. In this thesis, we apply the generalized-α method. Finally, in Section 2.4, several numerical tests are performed to validate and compare the proposed beam models.

This chapter is mainly based on [68, 117–120] concerning the baseline formulation of the beam element. It is also interesting to mention that the local frame approach is not limited to beams. It has been used for the formulation and optimization of mechanical components such as rigid bodies, mechanical joints, shells, and superelements [121–124].

2.1 The Lie Group *SE(3)* and the Local Frame Philosophy

We start by recalling some fundamental notions about matrix Lie groups. We will particularize these concepts to $SO(3)$ and $SE(3)$ later. Concise overviews about this topic can be found in [125–127].

Definition: A *Lie group* is a C^∞ (smooth) manifold that is also a group such that the composition and inverse operations are C^∞.

Definition: The *general linear group*, denoted $GL(d)$, is the set of invertible $\mathbb{R}^{d\times d}$ matrices with the matrix multiplication as the composition rule.

$$GL(d) = \left\{\mathbf{A} \in \mathbb{R}^{d\times d} : \det(\mathbf{A}) \neq 0\right\}. \tag{2.1}$$

When talking about matrices, we will always assume that the matrix multiplication comes with it automatically from now on. Though Eq. (2.1) is strictly speaking written as a set, the implicit presence of the matrix multiplication makes it a (Lie) group in our eyes and we will sometimes use the terms set and group interchangeably.

Let us show that the general linear group is indeed a Lie group. Since $GL(d)$ is a smooth open subset of $\mathbb{R}^{d\times d}$, it is a manifold. The matrix multiplication and the matrix inverse are C^∞ operations. Finally, it is also a group as it verifies the four group axioms:

- Closure: the composition of two elements $\mathbf{A}_1, \mathbf{A}_2 \in GL(d)$ yields an element $\mathbf{A}_3 = \mathbf{A}_1\mathbf{A}_2 \in GL(d, \mathbb{R})$.
- Associativity: $\mathbf{A}_1(\mathbf{A}_2\mathbf{A}_3) = (\mathbf{A}_1\mathbf{A}_2)\mathbf{A}_3$.
- Existence of a neutral element $\mathbf{I} \in GL(d)$ which is the identity matrix: $\mathbf{IA} = \mathbf{AI} = \mathbf{A}, \forall \mathbf{A} \in GL(d)$.
- Existence of an inverse element $\mathbf{A}^{-1} \in GL(d) : \mathbf{A}^{-1}\mathbf{A} = \mathbf{A}\mathbf{A}^{-1} = \mathbf{I}, \forall \mathbf{A} \in GL(d)$.

In this work, we are only interested in the Lie groups $SO(3)$ and $SE(3)$, see Sections 2.1.1 and 2.1.2, or Lie groups appearing as their direct products. These are finite-dimensional Lie groups that always admit a representation as a subgroup of $GL(d)$. We will generically denote a Lie group G if the given developments hold for any such group. For the remainder of this work, the provided definitions will hold for the general linear group and its subgroups.

A special map can be defined in that case. For $\mathbf{X} \in G$ denote by $l_{\mathbf{X}} \to G, l_{\mathbf{X}}(\mathbf{A}) = \mathbf{XA}$, which we call the *left translation* by $\mathbf{X}$ on G.

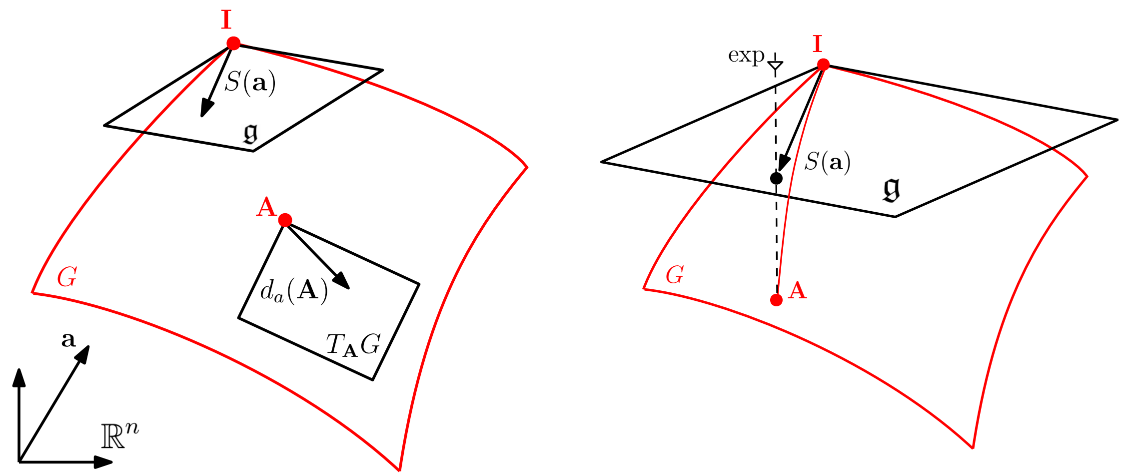

Figure 2.1: Illustration of a Lie group as a nonlinear space with its Lie algebra and the exponential map.

The element $\mathbf{A}_1^{-1}\mathbf{A}_2$, which expresses the relative transformation between two elements of G, is invariant under left translation on G. The qualification "*invariant*" stems from the fact that $\mathbf{A}_1^{-1}\mathbf{A}_2$ does not vary under left multiplication of $\mathbf{A}_1$ and $\mathbf{A}_2$ by an arbitrary $\mathbf{A}_0 \in G$. Indeed,

$$\begin{aligned}
(l_{\mathbf{A}_0}(\mathbf{A}_1))^{-1}\, l_{\mathbf{A}_0}(\mathbf{A}_2) &= (\mathbf{A}_0\mathbf{A}_1)^{-1} l_{\mathbf{A}_0}\,(\mathbf{A}_1)^{-1}\, l_{\mathbf{A}_0}\,(\mathbf{A}_2)\,\mathbf{A}_0\mathbf{A}_2 \\
&= \mathbf{A}_1^{-1}\left(\mathbf{A}_0^{-1}\mathbf{A}_0\right)\mathbf{A}_2 \\
&= \mathbf{A}_1^{-1}\mathbf{A}_2.
\end{aligned} \tag{2.2}$$

The tangent space at $\mathbf{A} \in G$ is denoted $T_{\mathbf{A}}G$. In particular, the tangent space at the identity element $\mathbf{I}$ is denoted $\mathfrak{g}$ and called the Lie algebra. It is isomorphic to $\mathbb{R}^n$

through an invertible linear map:

$$S(\bullet) : \mathbb{R}^n \to \mathfrak{g},\ \mathbf{a} \to S(\mathbf{a}), \tag{2.3}$$

where n denotes the dimension of the Lie algebra.

In Eq. (2.3), we depart from earlier publications [51,68] that used $\tilde{\bullet}$ to denote this map. We will give the tilde a different meaning in the context of the dynamic simulation of nonsmooth systems, see Chapter 4.

Owing to the composition rule, the tangent space at any element $\mathbf{A} \in G$ is directly related to the Lie algebra through a linear operation. As a consequence, the derivative of a curve $\mathbf{A}(a) \in G$ with $a \in \mathbb{R}$, denoted $d_a(\mathbf{A}) \in T_{\mathbf{A}}G$ can be written as

$$d_a(\mathbf{A}) = \mathbf{A}S(\mathbf{a}), \tag{2.4}$$

where the vector field represented by $S(\mathbf{a}) \in \mathfrak{g}$ is left invariant. In this way, the derivative is represented in the Lie algebra by $S(\mathbf{a})$ and in $\mathbb{R}^n$ by $\mathbf{a}$. Again, one verifies easily for an arbitrary $\mathbf{A}_0 \in G$ independent of the parameter a that the derivative of the curve $l_{\mathbf{A}_0}(\mathbf{A})$ is represented as

$$d_a(l_{\mathbf{A}_0}(\mathbf{A})) = l_{\mathbf{A}_0}(\mathbf{A})S(\mathbf{a})_{tr} \tag{2.5}$$

and

$$\begin{aligned} S(\mathbf{a})_{tr} &= (\mathbf{A}_0\mathbf{A})^{-1} d_a(\mathbf{A}_0\mathbf{A}) \\ &= \mathbf{A}^{-1}\left(\mathbf{A}_0^{-1}\mathbf{A}_0\right) d_a(\mathbf{A}) \\ &= \mathbf{A}^{-1} d_a(\mathbf{A}) \\ &= S(\mathbf{a}). \end{aligned} \tag{2.6}$$

A second, right-invariant, representation of the derivative exists: $d_a(\mathbf{A}) = S(\mathbf{a})\mathbf{A}$. It leads in the end to a different formulation that will not be considered in this work. Borri et al. [66] suggested this choice for a beam model formulated on $SE(3)$. The interested reader may find more details in [40].

The adjoint representation is a linear map:

$$\mathrm{Ad}_{\mathbf{A}}(\bullet) : \mathfrak{g} \to \mathfrak{g},\ S(\mathbf{a}) \to \mathrm{Ad}_{\mathbf{A}}(S(\mathbf{a})) = \mathbf{A}S(\mathbf{a})\mathbf{A}^{-1}. \tag{2.7}$$

Since $\mathfrak{g}$ is isomorphic to $\mathbb{R}^n$, we also use the following abuse of notation $\mathrm{Ad}_{\mathbf{A}}(\bullet) : \mathbb{R}^n \to \mathbb{R}^n$, i.e., the adjoint representation is seen as a map from vector to vector. This map describes the transformation rule from one representation of the derivative to the other.

Derivatives in the general case do not commute. Consider a surface $\mathbf{A}(a, b) \in G$ parametrized by $a, b \in \mathbb{R}$. The cross derivatives of the vector fields are related by a compatibility equation that is a consequence of the non-commutative nature of G:

$$d_b(S(\mathbf{a})) = d_a(S(\mathbf{b})) + [S(\mathbf{a}), S(\mathbf{b})]\,, \tag{2.8}$$

where we introduced the *Lie bracket*

$$[\bullet, \bullet] : \mathfrak{g} \times \mathfrak{g} \to \mathfrak{g}, [S(\mathbf{a}), S(\mathbf{b})] \to S(\mathbf{a})S(\mathbf{b}) - S(\mathbf{b})S(\mathbf{a}). \tag{2.9}$$

Eq. (2.8) can be expressed in terms of vectors in $\mathbb{R}^n$:

$$d_b(\mathbf{a}) = d_a(\mathbf{b}) + \widehat{\mathbf{a}}\mathbf{b}. \tag{2.10}$$

The hat operator $\widehat{\bullet}$ is a linear map that transforms a vector in $\mathbb{R}^n$ into a matrix of dimensions $\mathbb{R}^{n \times n}$.

The Exponential Map

Equation (2.4) can be seen as a first-order differential equation on G. If $\mathbf{a}$ is assumed constant and given the initial condition $\mathbf{A}(0) = \mathbf{A}_0$, its solution is

$$\mathbf{A}(a) = \mathbf{A}_0 \exp_G(aS(\mathbf{a}))\,. \tag{2.11}$$

The exponential map takes an element from the Lie algebra and projects it onto the Lie group. For matrix Lie groups, it matches the definition of the matrix exponential, i.e.,

$$\exp_G(\bullet) : \mathfrak{g} \to G,\ S(\mathbf{a}) \to \exp_G\left(S(\mathbf{a})\right), \tag{2.12}$$

with

$$\exp_G\left(S(\mathbf{a})\right) = \sum_{k=0}^{+\infty} \frac{1}{k!} S(\mathbf{a})^k. \tag{2.13}$$

From now on, we will often employ the following shortcut notation: $\exp_G(\bullet) : \mathbb{R}^n \to G$. In this way, the exponential map directly takes a vector as an entry and maps into the Lie group, skipping the notation of the $S(\bullet)$ operator. The inverse of the exponential map is the logarithm map:

$$\log_G(\bullet) : G \to \mathfrak{g},\ \mathbf{A} \to \log_G\left(\mathbf{A}\right). \tag{2.14}$$

We will also make use of the shortcut: $\log_G(\bullet) : G \to \mathbb{R}^n$. The general series expression of the logarithm map is given by

$$\log_G\left(\mathbf{A}\right) = \sum_{k=1}^{+\infty} \frac{(-1)^k}{k} \left(\mathbf{A} - \mathbf{I}\right)^k. \tag{2.15}$$

Figure 2.1 shows a graphical illustration of a Lie group with its Lie algebra and the exponential map. The exponential map defines a system of coordinates $\boldsymbol{\alpha}(a) \in \mathbb{R}^n$ (here we consider a curve parametrized by a again) around the neutral element $\mathbf{I}$ for elements of the Lie group G. By left translation, a local system of coordinates can be constructed around any $\mathbf{A}_0 \in G$ akin to Eq. (2.11) as

$$\mathbf{A} = \mathbf{A}_0 \exp_G(\boldsymbol{\alpha}). \tag{2.16}$$

Derivation of Eq. (2.16) with respect to the parameter a yields

$$d_a(\mathbf{A}) = \mathbf{A} S\left(\mathbf{T}_G(\boldsymbol{\alpha}) d_a(\boldsymbol{\alpha})\right) \tag{2.17}$$

where one identifies

$$\mathbf{a} = \mathbf{T}_G(\boldsymbol{\alpha}) d_a(\boldsymbol{\alpha}), \tag{2.18}$$

and where the tangent operator

$$\mathbf{T}_G(\bullet) : \mathbb{R}^n \to \mathbb{R}^{n\times n},\ \boldsymbol{\alpha} \to \mathbf{T}_G(\boldsymbol{\alpha}) \tag{2.19}$$

can be seen as the linearization of the exponential map. It gives a relationship between the derivative of the coordinates $\boldsymbol{\alpha}$ involved in the description of $\mathbf{A}$ and the vector $\mathbf{a}$ used for the representation of derivatives as defined in Eq. (2.4). The series expansion of the tangent operator is given by

$$\mathbf{T}_G(\boldsymbol{\alpha}) = \sum_{k=0}^{+\infty} (-1)^k \frac{\widehat{\boldsymbol{\alpha}}^k}{(1+k)!}. \tag{2.20}$$

We may invert Eq. (2.16) to obtain

$$\boldsymbol{\alpha} = \log_G \left(\mathbf{A}_0^{-1} \mathbf{A} \right). \tag{2.21}$$

Taking the derivative yields an expression equivalent to Eq. (2.18):

$$d_a(\boldsymbol{\alpha}) = \mathbf{T}_G^{-1}(\boldsymbol{\alpha}) \mathbf{a}. \tag{2.22}$$

and the inverse of the tangent operator emerges:

$$\mathbf{T}_G^{-1}(\bullet) : \mathbb{R}^n \to \mathbb{R}^{n\times n},\ \boldsymbol{\alpha} \to \mathbf{T}_G^{-1}(\boldsymbol{\alpha}). \tag{2.23}$$

Similar to the tangent operator, we may interpret its inverse as the linearization of the logarithm map. It gives the inverse relation between the derivative of the coordinates $\boldsymbol{\alpha}$ and the vector $\mathbf{a}$. The series expansion is

$$\mathbf{T}_G^{-1}(\boldsymbol{\alpha}) = \sum_{k=0}^{+\infty} (-1)^k B_k \frac{\widehat{\boldsymbol{\alpha}}^k}{k!}, \tag{2.24}$$

where the B_k are the Bernoulli numbers of the first kind [128].

The series expansions of the exponential map, the logarithm map, the tangent operator, and the inverse tangent operator are also valid for every subgroup of the general linear group, i.e., they may also be used for the Lie groups we will present in the next sections.

The Cayley Transform

The exponential map is not the only way of mapping an element from the Lie algebra to the Lie group [129]. An alternative is provided by the Cayley transform:

$$\mathrm{cay}_G(\bullet) : \mathfrak{g} \to G, S(\mathbf{a}) \to \mathrm{cay}_G(S(\mathbf{a})) \tag{2.25}$$

with

$$\mathrm{cay}_G(S(\mathbf{a})) = \left(\mathbf{I} - \frac{1}{2}S(\mathbf{a})\right)^{-1}\left(\mathbf{I} + \frac{1}{2}S(\mathbf{a})\right). \tag{2.26}$$

In the subsequent geometric discretization methods, it could be used instead of the exponential map. Since it does not involve an infinite sum or transcendental functions, its computation is cheaper and necessary derivatives have simpler expressions. Note that, unlike the exponential map, the Cayley transform is not a solution of Eq. (2.4).

2.1.1 *SO(3)*

We call $SO(3)$ the group of $3D$ rotations. It is abstractly (meaning in the geometrical, coordinate-free sense) defined as the set of direct isometries of the three-dimensional vector space $\mathcal{V}^3$, with the rotation composition, which is a geometric construction, as the group operation. In a given basis, it can be shown that there is a one-to-one bijective relation between the set of rotations and the set of 3×3 proper orthogonal matrices. Hence, we will identify $SO(3)$ with its representation as a subgroup of $GL(3)$, i.e.,

$$SO(3) = \left\{\mathbf{R} \in \mathbb{R}^{3\times3} : \mathbf{R}^T\mathbf{R} = \mathbf{I}_{3\times3},\ \det(\mathbf{R}) = +1\right\}. \tag{2.27}$$

The orthogonality conditions form a set of six quadratic constraints and $SO(3)$ is thus a nonlinear space.

The Lie algebra of $SO(3)$ is the set of skew-symmetric matrices:

$$\mathfrak{so}(3) = \left\{S(\boldsymbol{\theta}) \in \mathbb{R}^{3\times3} : S(\boldsymbol{\theta}) + S(\boldsymbol{\theta})^T = \mathbf{0}\right\}, \tag{2.28}$$

which is isomorphic to $\mathbb{R}^3$ through the linear map $S(\bullet)$:

$$\boldsymbol{\theta} = \begin{bmatrix}\theta_1\\ \theta_2\\ \theta_3\end{bmatrix} \in \mathbb{R}^3 \to \mathbf{S}(\boldsymbol{\theta}) = \begin{bmatrix} 0 & -\theta_3 & \theta_2 \\ \theta_3 & 0 & -\theta_1 \\ -\theta_2 & \theta_1 & 0 \end{bmatrix} \in \mathfrak{so}(3). \tag{2.29}$$

The hat operator $\widehat{\bullet}$ is equivalent to $S(\bullet)$ and for the adjoint representation we have:

$$\mathrm{Ad}_{\mathbf{R}}(S(\boldsymbol{\theta})) = \mathbf{R}S(\boldsymbol{\theta})\mathbf{R}^T \quad \text{or} \quad \mathrm{Ad}_{\mathbf{R}}(\boldsymbol{\theta}) = \mathbf{R}\boldsymbol{\theta}. \tag{2.30}$$

According to Eq. (2.4), the variation of an element $\mathbf{R} \in SO(3)$ is then represented by:

$$\delta(\mathbf{R}) = \mathbf{R}S(\delta\boldsymbol{\theta}), \quad S(\delta\boldsymbol{\theta}) \in \mathfrak{so}(3). \tag{2.31}$$

The series expansion of the exponential map admits an analytic expression known as the Rodrigues formula:

$$\exp_{SO(3)}(\boldsymbol{\theta}) = \mathbf{I}_{3\times 3} + \frac{\sin(\|\boldsymbol{\theta}\|)}{\|\boldsymbol{\theta}\|}S(\boldsymbol{\theta}) + \frac{1-\cos(\|\boldsymbol{\theta}\|)}{\|\boldsymbol{\theta}\|^2}S(\boldsymbol{\theta})S(\boldsymbol{\theta}). \tag{2.32}$$

Similar considerations hold for the other operators. The logarithm map can be computed as:

$$\log_{SO(3)}(\mathbf{A}) = \frac{\phi}{2\sin(\phi)}(\mathbf{A} - \mathbf{A}^T), \tag{2.33}$$

where $\phi = \arccos(1/2(\mathrm{trace}(\mathbf{A}) - 1))$. However, it is only defined in the range $-\pi < \phi < \pi$. The tangent operator can be obtained from:

$$\mathbf{T}_{SO(3)}(\boldsymbol{\theta}) = \mathbf{I}_{3\times 3} + \frac{\sin(\|\boldsymbol{\theta}\|)}{2\|\boldsymbol{\theta}\|}S(\boldsymbol{\theta}) + \frac{\|\boldsymbol{\theta}\|^2 + \cos(\|\boldsymbol{\theta}\|) - 2}{\|\boldsymbol{\theta}\|^4}S(\boldsymbol{\theta})S(\boldsymbol{\theta}) \tag{2.34}$$

and there is also a closed-form expression for the inverse:

$$\mathbf{T}^{-1}_{SO(3)}(\boldsymbol{\theta}) = \mathbf{I}_{3\times 3} + \frac{1}{2}S(\boldsymbol{\theta}) + \frac{2-\cot(\|\boldsymbol{\theta}\|/2)}{2\|\boldsymbol{\theta}\|^2}S(\boldsymbol{\theta})S(\boldsymbol{\theta}). \tag{2.35}$$

Upon inspection, one notices a singularity in Eqs.(2.32) to (2.35) when $\boldsymbol{\alpha} = \mathbf{0}$. It can be removed by replacing the above formula by a truncated version of the series in Eqs.(2.13), (2.15), (2.20), and (2.24) [130,131].

Sp(1)

A different way of representing rotations is the group of unit quaternions:

$$Sp(1) = \left\{ \bar{p} = p_0 + \mathbf{p} : p_0 \in \mathbb{R},\, \mathbf{p} \in \mathbb{R}^3,\, \|\bar{p}\| = 1 \right\}, \tag{2.36}$$

where the quaternion composition is given by $\bar{p}, \bar{q} \in Sp(1)$:

$$\bar{p}\bar{q} = p_0 q_0 - \mathbf{p}^T \mathbf{q} + p_0 \mathbf{q} + q_0 \mathbf{p} + S(\mathbf{p})\mathbf{q} \in Sp(1), \tag{2.37}$$

It is locally isomorphic to $SO(3)$. The Euler map provides a double cover of $SO(3)$:

$$\mathbf{R}(\bar{p}) = (2p_0^2 - 1)\mathbf{I}_{3\times 3} + \mathbf{p}\mathbf{p}^T + 2p_0 S(\mathbf{p}). \tag{2.38}$$

In the implementation of the Lie group methods presented in this thesis, only relative rotations are ever computed, for example, the relative rotation between two successive finite element nodes or the relative rotation between two identical nodes evaluated at successive time steps. One can assume them to be of moderate amplitudes. We therefore consider $Sp(1)$ as equivalent to $SO(3)$. Since $Sp(1)$ is isomorphic to the special unitary group $SU(2)$, which is a matrix Lie group, the principles presented in Section 2.1 can be applied when taking certain notational precautions. The Lie algebra of $Sp(1)$ is the set of pure quaternions:

$$\mathfrak{sp}(1) = \left\{ \bar{\theta} \in Sp(1) : \bar{\theta} = 0 + \boldsymbol{\theta} \right\}. \tag{2.39}$$

It is interesting to point out that the Lie algebras $\mathfrak{so}(3)$, $\mathfrak{su}(2)$, and $\mathfrak{sp}(1)$ are all isomorphic to each other and hence also isomorphic to $\mathbb{R}^3$.

Similar closed-form expressions exist for the different operators. For example, the exponential map is given by:

$$\exp_{Sp(1)}(0 + \boldsymbol{\theta}) = \cos(\|\boldsymbol{\theta}\|/2) + \frac{\boldsymbol{\theta}}{\|\boldsymbol{\theta}\|} \sin(\|\boldsymbol{\theta}\|/2). \tag{2.40}$$

Unit quaternions are very popular in practical applications due to their efficiency. For example, the open-source software *Odin* [116], to which this thesis contributes, uses them. In practice, it is always possible to transform a quaternion-based parametrization into a rotation matrix if needed. However, one has to be careful when performing the inverse operation, since for every rotation matrix there are two unit quaternions. This may be a source of bugs in software implementations.

2.1.2 *SE(3)*

The group of rigid body motions $SE(3) = \mathbb{R}^3 \rtimes SO(3)$ is defined as the group of direct isometries in Euclidean space $\mathcal{E}^3$. The symbol $\rtimes$ denotes the semidirect product. Just as for $SO(3)$, this definition is geometric and independent of any coordinate system. After the introduction of a reference frame, such a motion may be written under the form of 4×4 matrices and we make the identification:

$$SE(3) = \left\{ \mathbf{H}(\mathbf{x}, \mathbf{R}) = \begin{bmatrix} \mathbf{R} & \mathbf{x} \\ \mathbf{0}_{1\times 3} & 1 \end{bmatrix} : \mathbf{R} \in SO(3),\, \mathbf{x} \in \mathbb{R}^3 \right\}. \tag{2.41}$$

The group operation is the matrix product:

$$\mathbf{H}_1\mathbf{H}_2 = \begin{bmatrix} \mathbf{R}_1\mathbf{R}_2 & \mathbf{x}_1 + \mathbf{R}_1\mathbf{x}_2 \\ \mathbf{0}_{1\times 3} & 1 \end{bmatrix}, \quad \mathbf{H}_1, \mathbf{H}_2 \in SE(3). \tag{2.42}$$

The operation is composed of a position translation $\mathbf{x}$ and a change of orientation (or rotation) $\mathbf{R}$. In Eq. (2.42), we observe that rotation and translation are intrinsically coupled when working on $SE(3)$.

The Lie algebra of $SE(3)$ is defined as the following set of 4×4 matrices:

$$\mathfrak{se}(3) = \left\{ S(\boldsymbol{\pi}) = \begin{bmatrix} S(\boldsymbol{\theta}) & \boldsymbol{\chi} \\ \mathbf{0}_{1\times 3} & 0 \end{bmatrix} : S(\boldsymbol{\theta}) \in \mathfrak{so}(3),\, \boldsymbol{\chi} \in \mathbb{R}^3 \right\}, \tag{2.43}$$

which is isomorphic to $\mathbb{R}^6$ through the linear map $S(\bullet)$:

$$\boldsymbol{\pi} = \begin{bmatrix} \boldsymbol{\chi} \\ \boldsymbol{\theta} \end{bmatrix} \in \mathbb{R}^6 \to S(\boldsymbol{\pi}) = \begin{bmatrix} S(\boldsymbol{\theta}) & \boldsymbol{\chi} \\ \mathbf{0}_{1\times 3} & 0 \end{bmatrix} \in \mathfrak{se}(3). \tag{2.44}$$

We always write the $S(\bullet)$ in the same manner for all Lie groups. The context should be sufficient to understand the specific meaning of this operator. Indeed, it can always be deduced from the variable it takes as an entry.

The hat operator is:

$$\widehat{\boldsymbol{\pi}} = \begin{bmatrix} S(\boldsymbol{\theta}) & S(\boldsymbol{\chi}) \\ \mathbf{0}_{3\times 3} & S(\boldsymbol{\theta}) \end{bmatrix}. \tag{2.45}$$

The adjoint is given by:

$$\mathrm{Ad}_{\mathbf{H}}(S(\boldsymbol{\pi})) = \mathbf{H}S(\boldsymbol{\pi})\mathbf{H}^{-1} \quad \text{or} \quad \mathrm{Ad}_{\mathbf{H}}(\boldsymbol{\pi}) = \begin{bmatrix} \mathbf{R} & S(\mathbf{x})\mathbf{R} \\ \mathbf{0}_{3\times 3} & \mathbf{R} \end{bmatrix} \boldsymbol{\pi}. \tag{2.46}$$

The variation of an element $\mathbf{H} \in SE(3)$ is written as:

$$\delta\mathbf{H} = \mathbf{H}S(\delta\boldsymbol{\pi}),\ S(\delta\boldsymbol{\pi}) \in \mathfrak{se}(3) \Leftrightarrow \begin{bmatrix} \delta\mathbf{R} & \delta\mathbf{x} \\ \mathbf{0}_{1\times 3} & 0 \end{bmatrix} = \begin{bmatrix} \mathbf{R} & \mathbf{x} \\ \mathbf{0}_{1\times 3} & 1 \end{bmatrix} \begin{bmatrix} S(\delta\boldsymbol{\theta}) & \delta\boldsymbol{\chi} \\ \mathbf{0}_{1\times 3} & 0 \end{bmatrix}, \tag{2.47}$$

such that we can identify $\delta\boldsymbol{\chi} = \mathbf{R}^T\delta\mathbf{x}$ and $S(\delta\boldsymbol{\theta}) = \mathbf{R}^T\delta\mathbf{R}$.

Just as for $SO(3)$, the series expansions of the exponential, logarithm, and tangent operators have closed-form expressions. There is the exponential map:

$$\exp_{SE(3)}(\boldsymbol{\pi}) = \begin{bmatrix} \exp_{SO(3)}(\boldsymbol{\theta}) & \mathbf{T}^T_{SO(3)}(\boldsymbol{\theta})\boldsymbol{\chi} \\ \mathbf{0}_{1\times 3} & 1 \end{bmatrix} \tag{2.48}$$

and the logarithm map:

$$\log_{SE(3)}(\mathbf{H}) = \begin{bmatrix} S(\boldsymbol{\theta}) & \mathbf{T}^{-T}_{SO(3)}(\boldsymbol{\theta})\mathbf{x} \\ \mathbf{0}_{1\times 3} & 0 \end{bmatrix}, \tag{2.49}$$

where $S(\boldsymbol{\theta}) = \log_{SO(3)}(\mathbf{R})$.

The tangent operator on $SE(3)$ is:

$$\mathbf{T}_{SE(3)}(\boldsymbol{\pi}) = \begin{bmatrix} \mathbf{T}_{SO(3)}(\boldsymbol{\theta}) & \mathbf{T}_{\chi\theta+}(\boldsymbol{\chi}, \boldsymbol{\theta}) \\ \mathbf{0}_{3\times 3} & \mathbf{T}_{SO(3)}(\boldsymbol{\theta}) \end{bmatrix}, \tag{2.50}$$

where the off-diagonal term coupling rotation and translation is:

$$
\begin{aligned}
\mathbf{T}_{\chi\theta+}(\mathbf{a},\mathbf{b}) = & -\frac{\sin(\mathbf{b})}{2\|\mathbf{b}\|}S(\mathbf{a}) + \frac{\|\mathbf{b}\|^2+\cos(\|\mathbf{b}\|)-2}{\|\mathbf{b}\|^4}\left(S(\mathbf{a})S(\mathbf{b})+S(\mathbf{b})S(\mathbf{a})\right) \\
& + \frac{\mathbf{b}^T\mathbf{a}}{\|\mathbf{b}\|^2}\left(\frac{2-2\cos(\|\mathbf{b}\|)-\|\mathbf{b}\|\sin(\|\mathbf{b}\|)}{\|\mathbf{b}\|^2}\right)S(\mathbf{b}) \\
& + \frac{\mathbf{b}^T\mathbf{a}}{\|\mathbf{b}\|^2}\left(\frac{5\cos(\|\mathbf{b}\|)-5+3\|\mathbf{b}\|\sin(\|\mathbf{b}\|)}{\|\mathbf{b}\|^2}\right)S(\mathbf{b})S(\mathbf{b}), \quad \mathbf{a},\mathbf{b}\in\mathbb{R}^3.
\end{aligned}
\tag{2.51}
$$

Finally, the inverse tangent operator is written as:

$$
\mathbf{T}^{-1}_{SE(3)}(\boldsymbol{\pi}) = \begin{bmatrix} \mathbf{T}^{-1}_{SO(3)}(\boldsymbol{\theta}) & \mathbf{T}_{\chi\theta-}(\boldsymbol{\chi},\boldsymbol{\theta}) \\ \mathbf{0}_{3\times 3} & \mathbf{T}^{-1}_{SO(3)}(\boldsymbol{\theta}) \end{bmatrix}, \tag{2.52}
$$

where a similar coupling term as in Eq. (2.51) appears:

$$
\begin{aligned}
\mathbf{T}_{\chi\theta-}(\mathbf{a},\mathbf{b}) = & \frac{1}{2}S(\mathbf{a}) + \frac{2-\cot(\|\mathbf{b}\|/2)}{2\|\mathbf{b}\|^2}\left(S(\mathbf{a})S(\mathbf{b})+S(\mathbf{b})S(\mathbf{a})\right) \\
& + \frac{4\|\mathbf{b}\|^2+\|\mathbf{b}\|\sin(\|\mathbf{b}\|)}{2(1-\cos(\|\mathbf{b}\|))\|\mathbf{b}\|^4}\left(\mathbf{b}^T\mathbf{a}\right)S(\mathbf{b})S(\mathbf{b}), \quad \mathbf{a},\mathbf{b}\in\mathbb{R}^3.
\end{aligned}
\tag{2.53}
$$

Remarks

- The concepts presented in this section may seem rather abstract and the operators are indeed a bit complex at first glance, but they are actually always the same and reappear several times. More importantly, we gave them clear mathematical interpretations which should help reduce any initial aversion towards them. Now that we have written them down once, we have the building blocks for a powerful and flexible range of tools and discretization methods that Lie group theory can offer.
- In this thesis, we chose to do a presentation in terms of the 4×4 matrix representation of $SE(3)$ since there exists a one-to-one relation between matrices of this type and the abstract group of rigid body transformations. Other equivalent or almost equivalent representations are of course applicable such as $\mathbb{R}^3 \times SO(3)$ or $\mathbb{R}^3 \rtimes Sp(1)$. The abstract operators are general and remain the same and so do their interpretations. They simply need to be adapted to a given representation.

2.1.3 Kinematics of the Rigid Body

Let t denote time. The configuration of a rigid body can be described as the relative transformation between an inertial frame of reference $\{O\}$ and a frame $\{C(t)\}$ attached to a reference point on the rigid body, see Fig.2.2. Formally, it is given by the map $\mathbb{R} \to SE(3) : t \to \mathbf{H}(\mathbf{x}(t), \mathbf{R}(t))$.

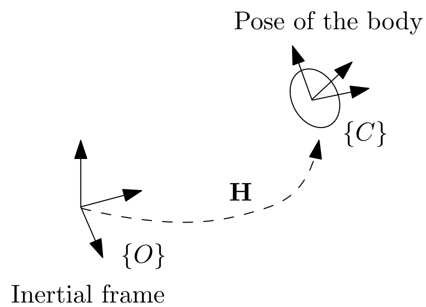

Figure 2.2: Schematic illustration of a frame transformation being used to compute the pose of a rigid body.

Any superimposed Euclidean transformation can be represented by a left multiplication on $SE(3)$ as in Eq. (2.42). The relative configuration between two rigid bodies represented by their poses $\mathbf{H}_1$ and $\mathbf{H}_2$ is an element of $SE(3)$. It is expressed as:

$$\mathbf{H}_{12} = \mathbf{H}_1^{-1}\mathbf{H}_2, \quad \mathbf{H}_1, \mathbf{H}_2 \in SE(3). \tag{2.54}$$

Owing to Eq. (2.2), it is invariant under superimposed Euclidean transformation.

We define the velocity vector $\boldsymbol{v} \in \mathbb{R}^6$ from the representation of the time derivative which we introduced in Eqs. (2.4) and (2.6) as follows:

$$S(\boldsymbol{v}) = \mathbf{H}^{-1}\dot{\mathbf{H}} \in \mathfrak{se}(3). \tag{2.55}$$

Taking the time derivative of Eq.(2.41) and solving for the velocity vector in Eq.(2.55) yields:

$$\boldsymbol{v} = \begin{bmatrix} \boldsymbol{v}_\chi \\ \boldsymbol{v}_\theta \end{bmatrix} = \begin{bmatrix} \mathbf{R}^T\dot{\mathbf{x}} \\ S^{-1}(\mathbf{R}^T\dot{\mathbf{R}}) \end{bmatrix}. \tag{2.56}$$

We recover the classical definition of the angular velocity vector $\boldsymbol{v}_\theta = S^{-1}(\mathbf{R}^T\dot{\mathbf{R}})$ and we identify $\boldsymbol{v}_\chi = \mathbf{R}^T\dot{\mathbf{x}}$ as the linear velocity of the reference point where the frame $\{C\}$ is attached with respect to the inertial frame of reference $\{O\}$ but expressed in the current frame $\{C\}$. It introduces the concept of local frame representation of the velocity. It is the only representation of the velocity that is invariant under superimposed Euclidean transformations [68].

A change of basis of the velocity is conveniently handled via the adjoint operator defined in Eq. (2.7). For example, the velocity can be expressed in the inertial frame $\{O\}$ by:

$$\boldsymbol{v}^O = \mathrm{Ad}_{\mathbf{H}}(\boldsymbol{v}). \tag{2.57}$$

To conclude, the Lie group formalism applied to the rigid body in this section gives direct access to frame-invariant velocities. These reside *in the local frame*. As will be seen in the next chapter, the same procedure can be applied to handle spatial derivatives of frames, allowing the kinematic description of flexible mechanical components.

2.2 Continuum Beam Formulation

Let t denote time and suppose the centerline of a beam to be parametrized by $s \in [0, L]$, where s is the centerline arclength coordinate in a straight reference configuration and L the total length. An orthonormal frame is attached to each of its points, as schematically represented in Fig. 2.3.

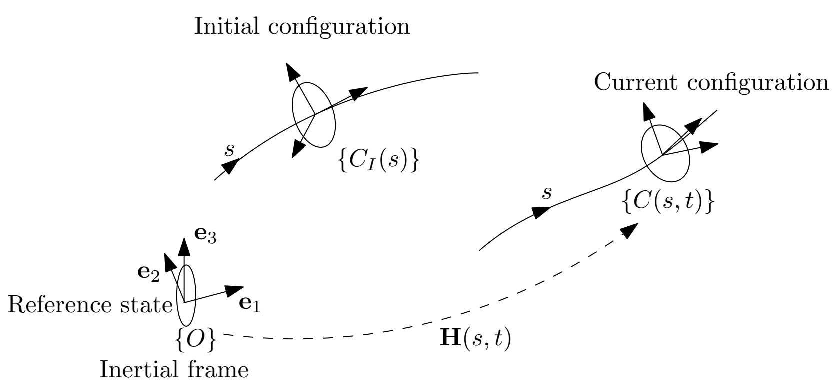

Figure 2.3: Description of beam kinematics as frame transformations from the inertial to the local frame.

The configuration is given by the map $\mathbb{R}^2 \to SE(3) : s, t \to \mathbf{H}(s,t)$, which corresponds to the transformation from the inertial frame $\{O\}$ to the local frame $\{C(s,t)\}$. Deformation measures and velocities follow from the representation of the derivative on the

Lie algebra:

$$\mathbf{H}' = \mathbf{H}S(\boldsymbol{f}) \Leftrightarrow \begin{cases} \mathbf{x}' = \mathbf{R}\boldsymbol{f}_\chi \\ \mathbf{R}' = \mathbf{R}S(\boldsymbol{f}_\theta), \quad S(\boldsymbol{f}_\theta) \in \mathfrak{so}(3), \end{cases} \tag{2.58a}$$

$$\dot{\mathbf{H}} = \mathbf{H}S(\boldsymbol{v}) \Leftrightarrow \begin{cases} \dot{\mathbf{x}} = \mathbf{R}\boldsymbol{v}_\chi \\ \dot{\mathbf{R}} = \mathbf{R}S(\boldsymbol{v}_\theta), \quad S(\boldsymbol{v}_\theta) \in \mathfrak{so}(3). \end{cases} \tag{2.58b}$$

Analogous to the kinematic description of the rigid body, the variable $S(\boldsymbol{v}) \in \mathfrak{se}(3)$ in Eq. (2.58b) is interpreted as the velocity field expressed in the local frame $\{C\}$ attached to the cross-section. In particular, $v_{\chi,1}$ is the velocity component along the reference curve and $v_{\chi,2}, v_{\chi,3}$ are the velocities in the directions of the cross-section axes. The components $v_{\theta,1}, v_{\theta,2}, v_{\theta,3}$ represent the rotational velocities of the cross-sections along the respective aforementioned directions.

In Eq. (2.58a), we constructed the deformation gradient:

$$\boldsymbol{f} = \begin{bmatrix} \boldsymbol{f}_\chi \\ \boldsymbol{f}_\theta \end{bmatrix} = \begin{bmatrix} \mathbf{R}^T\mathbf{x}' \\ S^{-1}(\mathbf{R}^T\mathbf{R}') \end{bmatrix}. \tag{2.59}$$

Just as for the velocity field, this deformation gradient is expressed in the local frame $\{C\}$ and invariant under superimposed Euclidean transformation. It can also be expressed in the inertial frame $\{O\}$ using the adjoint operator from Eq. (2.7) as follows:

$$\boldsymbol{f}^O = \mathrm{Ad}_{\mathbf{H}}(\boldsymbol{f}). \tag{2.60}$$

Interestingly, the classical sectional strains are recovered by a simple linear relation:

$$\boldsymbol{\epsilon} = \boldsymbol{f} - \boldsymbol{f}_I = \begin{bmatrix} \boldsymbol{\gamma} \\ \boldsymbol{\kappa} \end{bmatrix}. \tag{2.61}$$

The deformation gradient in the initial and undeformed configuration is denoted $\boldsymbol{f}_I$. It can be obtained by constructing the Frenet triad on a given centerline curve. We will skip the details concerning initially curved beams for the sake of conciseness and clarity. These can be looked up in [40]. Still, some numerical examples in Section 2.4 will have precurvature. For an initially straight beam, which is regularly encountered in practice, $\boldsymbol{f}_I = \begin{bmatrix}1 & 0 & 0 & 0 & 0 & 0\end{bmatrix}^T$ and we have:

$$\begin{bmatrix}\boldsymbol{\gamma} \\ \boldsymbol{\kappa}\end{bmatrix} = \begin{bmatrix}\mathbf{R}^T\mathbf{x}' - \mathbf{e}_1 \\ \mathbf{R}^T\mathbf{R}'\end{bmatrix}. \tag{2.62}$$

One recognizes γ_1 as the extensional strain along the reference curve, γ_2, γ_3 as the shear strains, κ_1 as the torsion about the reference curve, and κ_2, κ_3 as the bending curvatures. For the Kirchhoff-Love beam, shear strains are supposed to vanish:

$$\gamma_2 = \gamma_3 = 0. \tag{2.63}$$

In addition, inextensibility would be written as:

$$\gamma_1 = 0. \tag{2.64}$$

Kirchhoff-Love models and inextensible Kirchhoff models can be achieved in different ways which are often separated into two types. The first family of models were called intrinsic in the state of the art, because a minimal set of variables is defined in such a way that shear deformation and elongation modes are impossible. However, the configuration variables are not elements of $SE(3)$ in that case. These models are not considered in this thesis [28, 80–82, 132]. We will focus on the second family of models, i.e., constrained Kirchhoff-type models. These generally start from the advantageous mathematical structure of the Simo-Reißner beam model and then, as the name suggests, impose Eqs. (2.63) and (2.64) as algebraic constraints via Lagrange multipliers. The practical implementation depends on the chosen interpolation technique. Therefore, we defer this discussion after the description of the spatial discretization procedure.

The starting point for a finite element method is the weak form of the equations of motion which is deduced from Hamilton's principle and given by:

$$\delta\mathcal{W} = \int_0^L \left((\delta\boldsymbol{\pi})^T \left[\mathbf{M}\dot{\boldsymbol{v}} - \widehat{\boldsymbol{v}}^T\mathbf{M}\boldsymbol{v} - \mathbf{f}^{\text{ext}} \right] - (\delta\boldsymbol{\epsilon})^T \mathbf{K}\boldsymbol{\epsilon} \right) \mathrm{d}s = 0, \tag{2.65}$$

where $\delta\boldsymbol{\pi} \in \mathbb{R}^6$ is a virtual displacement as defined in Eq. (2.47).

In this thesis, we will exclusively work with circular cross-sections of uniform radius R and linear elastic materials. The stiffness properties of the beam are encoded in the constant and diagonal 6×6 stiffness matrix $\mathbf{K} = \text{diag}(EA, GA, GA, 2GI, EI, EI)$, where E is Young's modulus, G is the bulk or shear modulus, $A = \pi R^2$ is the cross-section area, and $I = (\pi/4)R^4$ is the moment of inertia. Off-diagonal terms related to precurvature are negligible for small to moderate cross-section radii and will always be ignored in this thesis.

The mass matrix $\mathbf{M}$ is independent of the configuration. Just as the stiffness matrix, it only depends on the initial configuration of the beam. Under the same considerations as for the stiffness matrix, it is purely diagonal and writes $\mathbf{M} = \mathrm{diag}(\rho A, \rho A, \rho A, 2\rho I, \rho I, \rho I)$, where ρ is the material density. The second term in Eq. (2.65) corresponds to gyroscopic effects. It takes a special form which is characteristic for local frame formulations. The externally applied forces $\mathbf{f}^{\mathrm{ext}}$ also have to be expressed in the local frame. Eqs. (2.58a), (2.58b), and Eq. (2.65) need to be solved. The solution also needs to verify the compatibility equation that was mentioned in Eq. (2.10):

$$\boldsymbol{v}' - \dot{\boldsymbol{\epsilon}} = \widehat{\boldsymbol{v}}\boldsymbol{\epsilon}. \tag{2.66}$$

The first two terms in Eq. (2.65) as well as Eqs. (2.58b) and (2.66) are simply ignored in the static case.

Remark

- The usual deformation measures for the Simo-Reißner beam appear naturally from the representation of the derivative by left translation on $SE(3)$ (i.e., quantities are interpreted as residing in the local frame) and not from a formulation on $\mathbb{R}^3 \times SO(3)$ in the inertial frame. The reason why they are the default deformation measures appearing in all Simo-Reißner type models is because they are invariant under a superimposed rigid body motion. They allow the definition of a quadratic potential deformation energy by making a small deformation assumption in the derivation of the beam model. All other representations of spatial derivatives contain information about large amplitude motion which makes the small deformation assumption inaccurate [40]. Most formulations solve the equations of motion expressed in the inertial frame after a separate discretization of translation and rotation.

2.3 Geometric Discretization Methods

In this section, we focus on time and space discretization of the equations of motion. This is not straightforward, as they are formulated on a non-linear and non-commutative space. As hinted at in the state of the art, the classical engineering approach is to first introduce a global parametrization of motion (rotation in particular) and then subsequently discretize the equations which raises the following issues:

- The global parametrization induces additional non-linearity.
- The global parametrization induces potential singularities.
- The strain operator is non-linear.
- There is a risk of breaking the geometric structure of the configuration space and losing invariance properties.

Modern Lie group solvers and geometric interpolation methods avoid the need for a global parametrization and ensure that the non-linear configuration space is preserved. They thereby avoid the aforementioned drawbacks.

2.3.1 Finite Elements in Space

A two-noded beam element of length L_e is defined as shown in Fig. 2.4. A frame $\{A\}$ is attached to the node at $s = 0$ and a frame $\{B\}$ is attached to the node at $s = L_e$. The configuration of the element is contained in the variable $q_e = (\mathbf{H}_A, \mathbf{H}_B) \in SE(3)^2$. We employ an interpolation scheme accounting for the nonlinearity of the configuration space. The first step is the computation of the discrete relative configuration vector:

$$S(\mathbf{d}_{AB}) = \log_{SE(3)} \left(\mathbf{H}_A^{-1}\mathbf{H}_B\right) \tag{2.67}$$

which yields an element of the Lie algebra. We distinguish between a translational part $\mathbf{d}_{AB,\chi} \in \mathbb{R}^3$ and a rotational part $\mathbf{d}_{AB,\theta} \in \mathbb{R}^3$ with $\mathbf{d}_{AB} = \begin{bmatrix}\mathbf{d}_{AB,\chi}^T & \mathbf{d}_{AB,\theta}^T\end{bmatrix}^T$. Since the Lie algebra is a vector space, scaling the relative configuration vector by a real number is allowed such that we can simply interpolate it linearly. The interpolation formula for the frame is then constructed as:

$$\mathbf{H}(s) = \mathbf{H}_A \exp_{SE(3)} \left(\frac{s}{L_e} S(\mathbf{d}_{AB})\right). \tag{2.68}$$

Equation (2.68) only depends on the relative configuration and is thus frame invariant. Taking the derivative of Eq. (2.68) with respect to s and doing some manipulations yields the elementwise strain:

$$\boldsymbol{\epsilon} = \begin{bmatrix} \boldsymbol{\gamma} \\ \boldsymbol{\kappa} \end{bmatrix} = \frac{\mathbf{d}_{AB} - \mathbf{d}_{AB,I}}{L_e}, \tag{2.69}$$

where $\mathbf{d}_{AB,I}$ is the relative configuration vector in the initial configuration. The strain $\boldsymbol{\epsilon}$ is constant along the span of the element and the discretization scheme defines helicoidal shape functions. The discretized expressions of the infinitesimal motion and the velocity are given by:

$$\delta\boldsymbol{\pi}(s) = \mathbf{Q}\left(s, \mathbf{d}_{AB}\right) \delta\boldsymbol{\pi}_e, \tag{2.70a}$$

$$\boldsymbol{v}(s) = \mathbf{Q}\left(s, \mathbf{d}_{AB}\right) \boldsymbol{v}_e, \tag{2.70b}$$

where

$$\mathbf{Q}(s, \mathbf{d}_{AB}) = \begin{bmatrix} \mathbf{I}_{6\times 6} - \mathbf{T}^*(s, \mathbf{d}_{AB}) & \mathbf{T}^*(s, \mathbf{d}_{AB}) \end{bmatrix} \tag{2.71}$$

and

$$\mathbf{T}^*(s, \mathbf{d}_{AB}) = (s/L_e)\mathbf{T}_{SE(3)}(s\mathbf{d}_{AB}/L_e)\mathbf{T}^{-1}_{SE(3)}(\mathbf{d}_{AB}). \tag{2.72}$$

For the discrete deformation, we have:

$$\delta\boldsymbol{\epsilon} = \frac{1}{L_e}\mathbf{P}\left(\mathbf{d}_{AB}\right) \delta\boldsymbol{\pi}_e \tag{2.73}$$

with

$$\mathbf{P}(\mathbf{d}_{AB}) = \begin{bmatrix} -\mathbf{T}^{-1}_{SE(3)}(-\mathbf{d}_{AB}) & \mathbf{T}^{-1}_{SE(3)}(\mathbf{d}_{AB}) \end{bmatrix}. \tag{2.74}$$

Note that the same matrix $\mathbf{Q}$ appears in both virtual displacement and velocity interpolations. Through this procedure, the kinematic relation in (2.58a) is verified by construction and also ensures compatibility of the derivatives.

The expressions for $\mathbf{Q}$ and $\mathbf{P}$ involve the tangent operator and its inverse. These

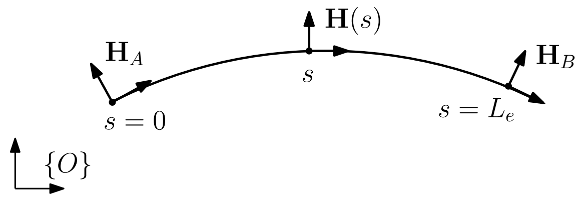

Figure 2.4: Two-noded interpolation of motion.

operators always remain the same; simply, the way they are computed differs if the exponential map in Eq. (2.68) is replaced by another local parametrization [63, 64, 68, 118, 120].

Next, the following nodal derivatives are introduced:

$$\delta\mathbf{H}_I = \mathbf{H}_I S(\delta\boldsymbol{\pi}_I), \tag{2.75a}$$

$$\dot{\mathbf{H}}_I = \mathbf{H}_I S(\boldsymbol{v}_I) \tag{2.75b}$$

where $I \in (A, B)$ and we note:

$$\delta\boldsymbol{\pi}_e = \begin{bmatrix}\delta\boldsymbol{\pi}_A \\ \delta\boldsymbol{\pi}_B\end{bmatrix}, \quad \boldsymbol{v}_e = \begin{bmatrix}\boldsymbol{v}_A \\ \boldsymbol{v}_B\end{bmatrix} \quad \in \quad \mathbb{R}^{12}. \tag{2.76}$$

Inserting Eqs. (2.70a), (2.70b), and (2.73) into Eq. (2.65) yields the equations of motion for the beam element:

$$\mathbf{M}_e\dot{\boldsymbol{v}}_e + \mathbf{f}_e = \mathbf{0}, \tag{2.77}$$

where

$$\mathbf{M}_e(\mathbf{d}_{AB}) = \int_0^{L_e} \mathbf{Q}^T\mathbf{M}\mathbf{Q}\,\mathrm{d}s, \tag{2.78a}$$

$$\mathbf{C}_e(\mathbf{d}_{AB}, \boldsymbol{v}_e) = \int_0^{L_e} \mathbf{Q}^T\left(\mathbf{M}\dot{\mathbf{Q}} - \widehat{\mathbf{Q}\boldsymbol{v}_e}^T\mathbf{M}\mathbf{Q}\right)\mathrm{d}s, \tag{2.78b}$$

$$\mathbf{f}_e(q_e, \boldsymbol{v}_e, t) = \mathbf{C}_e\boldsymbol{v}_e + \mathbf{K}_e\boldsymbol{\epsilon} - \int_0^{L_e} \mathbf{Q}^T\mathbf{f}^{\mathrm{ext}}\,\mathrm{d}s, \tag{2.78c}$$

and where $\mathbf{K}_e = \mathbf{P}^T \mathbf{K} L_e$. These equations can then be assembled in standard finite element fashion to obtain an expression of the form:

$$\mathbf{M}(q)\dot{\boldsymbol{v}} + \mathbf{f}(q, \boldsymbol{v}, t) = \mathbf{0}, \tag{2.79}$$

where $q \in SE(3)^N$ contains all nodal frames, N is the total number of nodes, and $\boldsymbol{v}$ is the vector of nodal velocities. We denote by $\circ$ the composition rule of the Lie group $SE(3)^N$, which is simply the matrix product. We reuse $\mathbf{M}$ to denote the assembled mass matrix and write the assembled damping matrix $\mathbf{C}$. The expression for $\dot{\mathbf{Q}}$ may be found in the appendix. Eq. (2.75b) and Eq. (2.79) form a set of ordinary differential equations on a Lie group which can be solved with appropriate Lie group time integration schemes which we will discuss in the next section. If the intention is to compute a sequence of static equilibria, the first terms in Eqs. (2.77) and (2.78c) are ignored.

Kirchhoff-Love Model and Inextensibility

The beam model presented in [68] includes shear and extension deformation modes. In this section, we present two novel beam models within the Lie group framework. These are a Kirchhoff-Love model that excludes shear deformation and an inextensible Kirchhoff model where we additionally exclude axial tension deformation. The motivation to develop these two beam models is that for very thin beams, the shear and extension modes may lead to numerically ill-conditioned problems. An extensive explanation of the numerical advantages of Kirchhoff-Love beam theories can be found in [65]. The Kirchhoff constraint and the inextensibility constraint can be implemented straightforwardly by simply imposing the bilateral constraints $\gamma_2 = \gamma_3 = 0$ and $\gamma_1 = 0$ for each finite element respectively using the standard Lagrangian multiplier technique described in [47]. Since these three strain measures are elementwise constant for the beam model on the special Euclidean group, this is straightforward. Let us introduce $\boldsymbol{\lambda}_e$ the elementwise Lagrange multiplier associated with the bilateral constraints. These are additional variables that will be determined as part of the solution. They can be interpreted as the forces necessary to fulfill the constraints. For the Kirchhoff-Love beam, it is of dimension 2 and for the inextensible Kirchhoff model, it is of dimension 3. The constraints are written under the form:

$$\mathbf{g}_e = \mathbf{D}\boldsymbol{\epsilon} L_e = \mathbf{0}, \tag{2.80}$$

where $\mathbf{D} = \begin{bmatrix} \mathbf{I}_{3\times 3} & \mathbf{0}_{3\times 3} \end{bmatrix}$ when inextensibility is included. Otherwise, the first row is simply removed. The constraint gradient follows as:

$$\delta \mathbf{g}_e = \underbrace{\mathbf{DP}(\mathbf{d}_{AB})}_{\mathbf{G}_e} \delta \boldsymbol{\pi}_e. \tag{2.81}$$

The equations of motion of the beam element now are:

$$\mathbf{M}_e \dot{\boldsymbol{v}}_e + \mathbf{f}_e - \mathbf{G}_e^T \boldsymbol{\lambda}_e = \mathbf{0} \tag{2.82}$$

which are to be solved together with Eq. (2.80). After assembly, the full system of equations is:

$$\begin{aligned} \mathbf{M}(q)\dot{\boldsymbol{v}} + \mathbf{f}(q, \boldsymbol{v}, t) - \mathbf{G}^T(q)\boldsymbol{\lambda} = \mathbf{0} \\ \mathbf{g}(q) = \mathbf{0}, \end{aligned} \tag{2.83}$$

with $\mathbf{g}$ and $\boldsymbol{\lambda}$ simply containing the constraints and Lagrange multipliers for the entire discretized beam.

Remarks

- In the resulting formulation, all the sectional forces, constraint forces, deformation measures, and other kinematic quantities are expressed in the local frame. Nonlinearities stemming from large amplitude rigid body motions are, in some sense, filtered out and we are left with a set of simple equations where all the complexity is hidden modularly in the local parametrization of the Lie group and the interpolation operators. In particular for $SE(3)$, closed-form expressions and robust implementations exist. These can be looked up in the literature [40,68,76].
- The exponential map serves as *local* parametrization of $SE(3)$ for the relative transformation between nodes A and B. The beam can then be described using the element of $\mathfrak{se}(3)$ constructed in Eq. (2.67). The influence of nonlinearity reduces with mesh refinement.
- As reported in [68], the coupling of translation and rotation variables which is conserved after the geometric discretization procedure circumvents the typical locking issues of classical Simo-Reissner beam implementations without the need for reduced integration techniques. More details can be found in Section 2.4.1

where we show that the Lie group framework leads to the same property for the Kirchhoff-Love and the inextensible Kirchhoff models.

- The interpolation formula with the Cayley transform would be:

$$\mathbf{H}(s) = \mathbf{H}_A \mathrm{cay}\left(\frac{s}{L_e} S(\mathbf{d}_{AB})\right), \tag{2.84}$$

  where

$$S(\mathbf{d}_{AB}) = \mathrm{cay}^{-1}\left(\mathbf{H}_A^{-1}\mathbf{H}_B\right). \tag{2.85}$$

- If unit quaternions are used for the parametrization of rotation instead of rotation matrices, the Lie group Q that is considered is $\mathbb{R}^3 \rtimes Sp(1)$. The configuration of one beam element is given by $\bar{H}_A, \bar{H}_B \in Q$ and the interpolation is performed as follows:

$$\bar{H}(s) = \bar{H}_A \circ \exp_G\left(\frac{s}{L_e} S(\mathbf{d}_{AB})\right), \quad \bar{H} \in Q,\, \mathbf{d}_{AB} \in \mathbb{R}^6, \tag{2.86}$$

  where

$$S(\mathbf{d}_{AB}) = \log_G(\bar{H}_A^{-1} \circ \bar{H}_B), \quad S(\mathbf{d}_{AB}) \in \mathfrak{q}. \tag{2.87}$$

  Here the group operation is not the matrix product, but an operation denoted $\circ$. Some notations would need to be adapted, but as mentioned before, the main interpretations and conclusions remain the same. The interested reader may refer to [76] which contains useful information about the Lie group Q in the context of beam models.

- Equation (2.83) formulates the vanishing shear and inextensibility constraints exclusively at the position level. Index reduction methods expressing constraints at position and velocity level or additionally at acceleration level have been the subject of extensive research [133–136]. These will not be considered for bilateral constraints in this thesis. In Chapter 4, we will however exploit them to deal with contact constraints as these are the main focus of this work.

2.3.2 Time Integration

Now that we have derived the equations of motion, we turn our attention towards their integration in time. The key point is the avoidance of a global parametrization of motion just as it was successfully achieved at the space discretization step. Naturally, similar principles are applicable when considering time integration, but additional criteria have to be taken into consideration. Equations resulting from the finite element discretization of structural components are stiff and implicit time integration schemes are required. This will be especially important in the next chapters, when we will add contact constraints with the wish to avoid rather small time steps. Some dissipation of artificial high-frequency vibrations that might appear for fine meshes is also desirable. Popular suitable time integration algorithms in structural mechanics are the Newmark scheme, the Hilbert-Hughes-Taylor (HHT) scheme, and the generalized-α method. They were, however, originally designed for linear spaces.

The earliest publications about Lie group solvers devised two families of methodologies. These are also based on the exponential map and the exploitation of the linear structure of the Lie algebra. In [137], local coordinates are constructed at each time step and the ordinary differential equation is reformulated in the Lie algebra. Explicit Runge-Kutta time integration methods of any order can be constructed systematically on any Lie group. However, the execution of this approach for implicit time integration schemes is complicated, because the tangent operator is involved in the integration formulae and these need to be linearized when using Newton-type solution methods. Therefore, a balance between the complexity of the implementation and the need for higher order accuracy needs to be struck in practical settings. The approach by Crouch and Grossman [138] interprets the exponential map as the solution to the differential equation for a fixed velocity field and this field is allowed to be a linear combination of velocities evaluated at different time steps. In the present work, we employ the Lie group version of the generalized-α scheme developed in [139–141] that follows the latter approach of freezing the velocity for the duration of the time step. Second-order convergence, which is sufficient for the simulation of mechanical systems, was proved, even in the presence of bilateral constraints typical for multibody system dynamics formulations, for example, to impose vanishing shear or inextensibility.

If the subscript n in t_n refers to the last time instant where the solution is known and h denotes the time step size then the solution at t_{n+1} is obtained from the following system of equations:

$$q_{n+1} = q_n \circ \exp_{SE(3)^N}\left(S(\boldsymbol{\alpha}_{n+1})\right), \tag{2.88a}$$

$$\mathbf{M}(q_{n+1})\dot{\boldsymbol{v}}_{n+1} + \mathbf{f}(q_{n+1}, \boldsymbol{v}_{n+1}, t_{n+1}) - \mathbf{G}^T(q_{n+1})\boldsymbol{\lambda}_{n+1} = \mathbf{0}, \tag{2.88b}$$

$$\mathbf{g}(q_{n+1}) = \mathbf{0} \tag{2.88c}$$

and the generalized-α integration formulae:

$$\boldsymbol{\alpha}_{n+1} = h\boldsymbol{v}_n + (1/2 - \beta)h^2\mathbf{a}_n + \beta h^2\mathbf{a}_{n+1}, \tag{2.89a}$$

$$\boldsymbol{v}_{n+1} = \boldsymbol{v}_n + (1 - \gamma)h\mathbf{a}_n + \gamma h\mathbf{a}_{n+1}, \tag{2.89b}$$

$$(1 - \alpha_m)\mathbf{a}_{n+1} + \alpha_m\mathbf{a}_n = (1 - \alpha_f)\dot{\boldsymbol{v}}_{n+1} + \alpha_f\dot{\boldsymbol{v}}_n. \tag{2.89c}$$

The numerical parameters are related to the spectral radius $\rho_\infty \in [0, 1[$ which can be tuned to achieve a desired amount of numerical dissipation:

$$\alpha_f = \frac{\rho_\infty}{\rho_\infty + 1}; \quad \alpha_m = \frac{2\rho_\infty - 1}{\rho_\infty + 1}; \quad \gamma = 1/2 + \alpha_f - \alpha_m; \quad \beta = \frac{(\gamma + 1/2)^2}{4}. \tag{2.90}$$

The acceleration-like variable $\mathbf{a}_{n+1}$ is different from the true acceleration $\dot{\boldsymbol{v}}_{n+1}$. The classical generalized-α method can be recovered by considering q in $\mathbb{R}^N$ with the simple addition as the composition operator. Note that $\dot{q}_{n+1}$ is never computed. Instead, all of the linear combinations required for the integration formulae are performed in the Lie algebra as $\boldsymbol{\alpha}_{n+1} \in \mathfrak{se}(3)^N$, where they make sense. At each time step, a nonlinear system of equations has to be solved for the unknowns $q_{n+1}, \boldsymbol{\alpha}_{n+1}, \boldsymbol{v}_{n+1}, \dot{\boldsymbol{v}}_{n+1}$ which is done by a Newton-Raphson procedure. This requires the linearized equations of motion. We note $\Delta(\bullet)$ a finite variation. The linearization of the configuration writes according to Eq. (2.18):

$$\Delta\mathbf{q}_{n+1} = \mathbf{T}_{SE(3)^N}(\boldsymbol{\alpha}_{n+1})\Delta\boldsymbol{\alpha}_{n+1}, \quad S(\Delta\mathbf{q}_{n+1}) \in \mathfrak{se}(3)^N. \tag{2.91}$$

Linearizing and combining Eqs. (2.89) gives:

$$\Delta \boldsymbol{v}_{n+1} = \gamma' \Delta \boldsymbol{\alpha}_{n+1}, \quad \Delta \dot{\boldsymbol{v}}_{n+1} = \beta' \Delta \boldsymbol{\alpha}_{n+1}, \tag{2.92}$$

with $\gamma' = \gamma/(\beta h)$ and $\beta' = (1-\alpha_m)/(\beta h^2(1-\alpha_f))$. Let us now introduce the residual function by aggregating Eqs. (2.88b) and (2.88c) into the form $\mathbf{r} = [\mathbf{r}_f^T \; \mathbf{r}_c^T]^T = \mathbf{0}$. Its linearization is:

$$D_q \mathbf{r}_f \cdot \Delta \mathbf{q}_{n+1} = \mathbf{K}_T \Delta \mathbf{q}_{n+1} = \mathbf{K}_T \mathbf{T}_{SE(3)^N}(\boldsymbol{\alpha}_{n+1}) \Delta \boldsymbol{\alpha}_{n+1}, \tag{2.93a}$$

$$D_{\boldsymbol{v}} \mathbf{r}_f \cdot \Delta \boldsymbol{v}_{n+1} = \mathbf{C}_T \Delta \boldsymbol{v}_{n+1} = \gamma' \mathbf{C}_T \Delta \boldsymbol{\alpha}_{n+1}, \tag{2.93b}$$

$$D_{\dot{\boldsymbol{v}}} \mathbf{r}_f \cdot \Delta \dot{\boldsymbol{v}}_{n+1} = \mathbf{M}_T \Delta \dot{\boldsymbol{v}}_{n+1} = \beta' \mathbf{M}_T \Delta \boldsymbol{\alpha}_{n+1}, \tag{2.93c}$$

$$D_{\boldsymbol{\lambda}} \mathbf{r}_f \cdot \Delta \boldsymbol{\lambda}_{n+1} = \mathbf{G}^T \Delta \boldsymbol{\lambda}_{n+1}, \tag{2.93d}$$

where $\mathbf{K}_T$ is the tangent stiffness matrix, $\mathbf{C}_T$ the tangent damping matrix, and $\mathbf{M}_T$ the tangent mass matrix. In the case of the beam model, $\mathbf{M}_T$ coincides with $\mathbf{M}$. We use $\mathbf{C}$ defined in Eq. (2.78b) for the tangent damping matrix and compute the tangent stiffness matrix by assembling the following elementwise contributions:

$$\mathbf{K}_{T,e} = \frac{1}{L_e^2} \mathbf{K}_e \mathbf{P}, \tag{2.94}$$

where the geometric stiffness has been neglected [68]. The constraint equation (2.88c) is linearized as:

$$D_q \mathbf{r}_c \cdot \Delta \mathbf{q}_{n+1} = \mathbf{G} \mathbf{T}_{SE(3)^N}(\boldsymbol{\alpha}_{n+1}) \Delta \boldsymbol{\alpha}_{n+1}. \tag{2.95}$$

The motion and Lagrange multiplier increments are computed at each step of the Newton-Raphson procedure by solving:

$$\mathbf{S}_t \begin{bmatrix} \Delta \boldsymbol{\alpha}_{n+1} \\ \Delta \boldsymbol{\lambda}_{n+1} \end{bmatrix} = - \begin{bmatrix} \mathbf{r}_f \\ \mathbf{r}_c \end{bmatrix} \tag{2.96}$$

where the total tangent matrix is given by:

$$\mathbf{S}_t = \begin{bmatrix} \beta'\mathbf{M}_T + \gamma'\mathbf{C}_T + \mathbf{K}_T\mathbf{T}_{SE(3)^N}(\boldsymbol{\alpha}_{n+1}) & \mathbf{G}^T \\ \mathbf{G}\mathbf{T}_{SE(3)^N}(\boldsymbol{\alpha}_{n+1}) & \mathbf{0} \end{bmatrix}. \tag{2.97}$$

Algorithm 1 computes all variables at time step t_{n+1} given their values at time step t_n.

Algorithm 1 $[q_{n+1}, \boldsymbol{v}_{n+1}, \dot{\boldsymbol{v}}_{n+1}, \boldsymbol{\lambda}_{n+1}, \mathbf{a}_{n+1}] = \text{solveGenAlphaTimeStep}(q_n, \boldsymbol{v}_n, \dot{\boldsymbol{v}}_n, \mathbf{a}_n)$

$\boldsymbol{\lambda}_{n+1} \coloneqq \mathbf{0}$
$\dot{\boldsymbol{v}}_{n+1} \coloneqq \mathbf{0}$
$\mathbf{a}_{n+1} \coloneqq (\alpha_f \dot{\boldsymbol{v}}_n - \alpha_m \mathbf{a}_n)/(1-\alpha_m)$
$\boldsymbol{v}_{n+1} \coloneqq \boldsymbol{v}_n + h(1-\gamma)\mathbf{a}_n + \gamma h \mathbf{a}_{n+1}$
$\boldsymbol{\alpha}_{n+1} \coloneqq h\boldsymbol{v}_n + (1/2-\beta)h^2\mathbf{a}_n + \beta h^2 \mathbf{a}_{n+1}$
for $k \in [1, \text{MaxIter}]$ **do**
  $\boxed{q_{n+1} = q_n \circ \exp_{SE(3)^N}(S(\boldsymbol{\alpha}_{n+1}))}$ ▷ Lie group update of the configuration
  compute $\mathbf{r}_f$, $\mathbf{r}_c$
  if Convergence($\mathbf{r}_f$) $\wedge$ Convergence($\mathbf{r}_c$) **then**
    break
  end if
  compute $\mathbf{S}_t$ ▷ Involves tangent operator: $\mathbf{T}_{SE(3)^N}(\boldsymbol{\alpha}_{n+1})$
  $\begin{bmatrix} \Delta\boldsymbol{\alpha}_{n+1} \\ \Delta\boldsymbol{\lambda}_{n+1} \end{bmatrix} \coloneqq -\mathbf{S}_t^{-1} \begin{bmatrix} \mathbf{r}_f \\ \mathbf{r}_c \end{bmatrix}$
  $\boldsymbol{\alpha}_{n+1} \coloneqq \boldsymbol{\alpha}_{n+1} + \Delta\boldsymbol{\alpha}_{n+1}$
  $\boldsymbol{v}_{n+1} \coloneqq \boldsymbol{v}_{n+1} + \gamma'\Delta\boldsymbol{\alpha}_{n+1}$
  $\dot{\boldsymbol{v}}_{n+1} \coloneqq \dot{\boldsymbol{v}}_{n+1} + \beta'\Delta\boldsymbol{\alpha}_{n+1}$
  $\boldsymbol{\lambda}_{n+1} \coloneqq \boldsymbol{\lambda}_{n+1} + \Delta\boldsymbol{\lambda}_{n+1}$
end for
$\mathbf{a}_{n+1} \coloneqq \mathbf{a}_{n+1}(1-\alpha_f)/(1-\alpha_m)\dot{\boldsymbol{v}}_{n+1}$

Remarks

- At no moment did we introduce any global parametrization of motion. The exponential map is used as a local parametrization over one time step.
- Tangent stiffness matrices enjoy invariance properties which can be exploited in view of efficient Newton-type solution methods.

2.4 Numerical Illustrations

This section aims at illustrating the behavior of the beam finite element formulated on $SE(3)$, especially its new shear-free and inextensible variants using constraints. Special attention is given to the absence of shear and membrane locking, spatial convergence rates, robustness under a large range of geometric and material parameters, predeformation, and dynamic effects.

The convergence criterion for the Newton algorithm is:

$$\text{Convergence}(\mathbf{r}_\bullet) = \text{Relative Residual} < \text{tol}_r \quad \vee \quad \text{Absolute Residual} < \text{tol}_a, \tag{2.98}$$

where the absolute residual is simply:

$$\text{Absolute Residual}(\mathbf{r}_\bullet) = \|\mathbf{r}_\bullet\| \tag{2.99}$$

and the relative residual is defined as:

$$\text{Relative Residual}(\mathbf{r}_\bullet) = \frac{\|\mathbf{r}_\bullet\|}{\frac{\sum_k \|\mathbf{r}_\bullet^k\|}{N_e} + 10^{-12}}. \tag{2.100}$$

We denote by $\mathbf{r}_\bullet^k$ the unassembled residual of element k and by tol_r and tol_a relative and absolute tolerances. Convergence is evaluated separately for the equilibrium of forces $\mathbf{r}_f$ and the constraints $\mathbf{r}_c$ such that the actual convergence criterion is given by:

$$\text{Convergence}(\mathbf{r}_f) \quad \wedge \quad \text{Convergence}(\mathbf{r}_c). \tag{2.101}$$

In all of the numerical examples, we used $\text{tol}_r = 10^{-7}$ and $\text{tol}_a = 10^{-4}$.

In all examples, we will compare and discuss each of the three beam models formulated on $SE(3)$, i.e., the Simo-Reißner (SR), Kirchhoff-Love (KL), and inextensible Kirchhoff (IK) beams.

2.4.1 Absence of Locking

A recurring subject in many works concerning displacement-based beam finite elements is their propensity for locking. This thesis will be no exception.

Pure Bending Example

Locking can be discussed considering a pure bending example which consists of a cantilever beam subject to a moment at its free end. The exact solution is characterized by vanishing shear and axial strains which should be reproduced by the numerical model. Locking occurs when the element is unable to do that. We speak of shear locking if the issue is related to shear and of membrane locking if it is related to extension modes. For classical beam elements (i.e., not the $SE(3)$ formulations), locking can occur for the following reasons:

- Shear locking for classical Simo-Reißner type beam elements: The separate interpolation of the position and rotation field coupled with a naive exact numerical integration yields an overestimation of the shear strain energy producing an element stiffer than expected. The element cannot represent the coupling between translational and rotational degrees of freedom. The problem can be removed by reduced integration or other techniques.

- Membrane locking for classical Kirchhoff type beam elements: Similar to the Simo-Reißner model, the issue appears when the element cannot handle the coupling between the axial tension mode and rotational kinematic quantities. As described in [105], membrane locking can be seen as the consequence of an overconstrained system of equations. A practical criterion based on the constraint ratio is used to predict if a given beam element is prone to locking. It is defined as the ratio between the total number of equilibrium equations and the number of constraints. In the continuum case, it is $c_{r,KL} = 3$ for the Kirchhoff-Love beam model and $c_{r,IK} = 2$ for the inextensible Kirchhoff beam. These correspond to the ideal constraint ratios which should ideally be preserved in the formulation of discrete beam elements.

Locking effects are observed in different ways. Typically, for highly slender beams, one obtains parasitic stresses that are not supposed to appear according to the exact solution. For the Simo-Reissner model on $SE(3)$, let us compute the internal forces appearing inside the finite element "by hand". In a static setting, Eq. (2.77) reduces to:

$$\mathbf{K}_e \boldsymbol{\epsilon} = \int_0^{L_e} \mathbf{Q}^T \mathbf{f}^{\text{ext}} \, \mathrm{d}s. \tag{2.102}$$

Applying a pure bending moment M produces a circular arc of curvature $k = M/(EI)$ which can be exactly represented by the interpolation formula in Eq. (2.68). The discrete relative configuration vector is $\mathbf{d}_{AB} = \begin{bmatrix} L_e & 0 & 0 & 0 & 0 & kL \end{bmatrix}^T$ which yields the discrete strain vector $\boldsymbol{\epsilon} = \begin{bmatrix} 0 & 0 & 0 & 0 & 0 & k \end{bmatrix}^T$. The nodal internal forces become:

$$\mathbf{K}_e \boldsymbol{\epsilon} = \begin{bmatrix} \mathbf{0}_{3\times 1} \\ -\mathbf{T}_{SO(3)}^T(-\mathbf{d}_{AB,\theta})\mathbf{K}_{e,\omega}\boldsymbol{\kappa} \\ \mathbf{0}_{3\times 1} \\ \mathbf{T}_{SO(3)}^T(\mathbf{d}_{AB,\theta})\mathbf{K}_{e,\omega}\boldsymbol{\kappa} \end{bmatrix} = \begin{bmatrix} \mathbf{0}_{5\times 1} \\ -EIk \\ \mathbf{0}_{5\times 1} \\ EIk \end{bmatrix} \tag{2.103}$$

matching the analytic solution. Note the absence of shear and extensional forces in the beam element. If we look at a Kirchhoff-Love or inextensible Kirchhoff models on $SE(3)$, we observe that the constraints $\epsilon_2 = \epsilon_3 = 0$ are automatically satisfied and no extensional forces appear. Let us also compute the discrete constraint ratio of our Kirchhoff-Love element on $SE(3)$:

$$\lim_{N_{el} \to +\infty} \frac{6N_{el} + 6}{2N_{el}} = 3 = c_{r,KL}. \tag{2.104}$$

A similar calculation gives exactly 2 for the inextensible Kirchhoff element on $SE(3)$. These theoretical properties are already quite convincing, but still need to be verified in a numerical test. For a numerical criterion, one checks the spatial convergence rates which deteriorate with increasing slenderness [65] for locking elements. Since the shape functions employed here describe piecewise circular arcs, the numerical solution is expected to match the analytic solution exactly, as can be seen in Fig. 2.5a, and checking spatial convergence rates does not make sense. We refer to ulterior test cases for that. Locking also affects the convergence of the Newton method in implicit schemes [68]. Figure 2.5b shows the convergence of the relative residual for a very slender beam with a square cross-section of side $b = 10^{-4}$[m], a length of $L = 1$[m], a Young's modulus of $E = 210$[GPa], an applied moment $M = Eb^4\pi/(96L)$, and an indicative discretization of 5 elements. No issue is observed in the iterative Newton process and indeed the exact solution is matched for all three studied beam models. No additional numerical trick such as, for example, reduced integration was necessary. This demonstrates that the

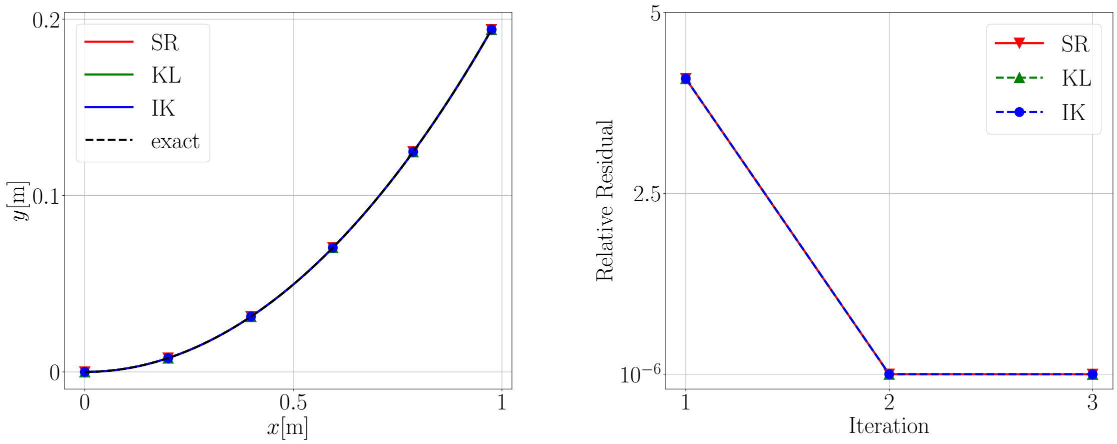

(a) Centerline position. (b) Convergence of the Newton method.

Figure 2.5: Pure bending results for a discretization of 5 elements. Color code: Simo-Reißner (red); Kirchhoff-Love (green); inextensible Kirchhoff (blue); exact solution (black).

three beam models on $SE(3)$ are inherently locking-free in the pure bending case.

Helix Under Gravity

The second test case consists of a beam lying in the xy-plane, clamped at one end, left free at the other end, and subjected to gravity in the z-direction. Its initial shape is a circle of radius $r = 0.05$[m]. It has a circular cross-section of radius $R = 0.005$[m], a length $L = 1$[m], a density $\rho = 750[\mathrm{kg/m^3}]$, a Young's modulus of $E = 6$[MPa], and a Poisson's ratio of $\nu = 0.25$. The full load is applied in 100 steps. The resulting geometry is a helix with increasing slope towards the clamped end as can be seen in Fig. 2.6a. In Fig. 2.6b, we observe for all three models the expected second-order convergence rate of the relative L^2-error [51], which is given by:

$$\text{Error} = \frac{\int_0^L \|\mathbf{x}_C - \mathbf{x}_C^{\text{ref}}\|^2 \,\mathrm{d}s}{\int_0^L \|\mathbf{x}_C^{\text{ref}}\|^2 \,\mathrm{d}s}, \tag{2.105}$$

where $\mathbf{x}_C$ is the position of the centerline. The reference is the numerical solution for a very fine mesh of 640 elements.

(a) Typical beam geometry for a discretization of 40 elements.

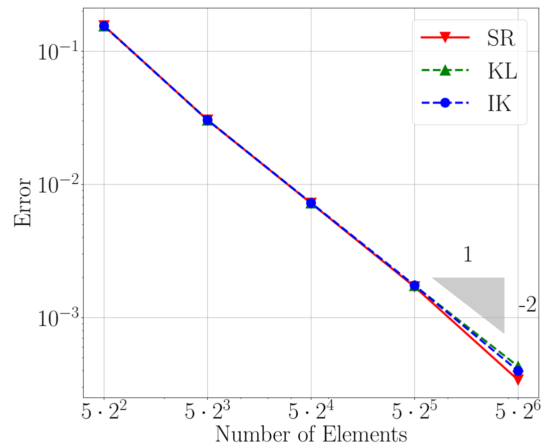

(b) Convergence of the relative L_2-error in function of the mesh size.

Figure 2.6: Helix under gravity results. Color code: Simo-Reißner (red); Kirchhoff (green); inextensible Kirchhoff (blue).

2.4.2 Physical Validation Examples

Romero et al. [142] proposed a framework consisting of four benchmark tests for physical validation of simulation tools for slender elastic structures in computer graphics. These benchmarks were specifically designed such that they may be experimentally verified in a reliable manner. Adimensional scaling laws are used to robustly check the proper physical behavior of the numerical model across a large range of geometrical and material parameter combinations. In the next two examples, we investigate within their validation framework the behavior of all three beam elements. In [53], it was only done for the unconstrained $SE(3)$ beam finite element.

The main driving force of each test case is gravity. Depending on the slenderness of the beam-like structure and the material it is composed of, the object under study will settle into a certain equilibrium shape. The situation can be summarized by one single adimensional quantity that measures the relative importance of gravitational and bending effects. It is given by:

$$\Gamma = \frac{\rho A g L^3}{EI} \tag{2.106}$$

We may interpret Γ as the ratio of the gravitational force ρALg and the internal bending moment EI/L^2. Typical values for Γ in mechanical engineering applications range from

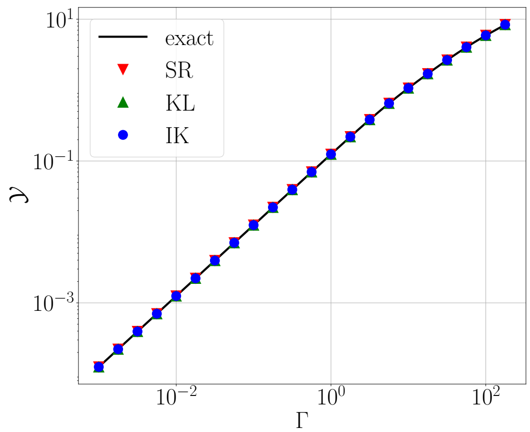

(a) Adimensional vertical position of the beam tip $\mathcal{Y}$ in function of the gravito-bending parameter Γ.

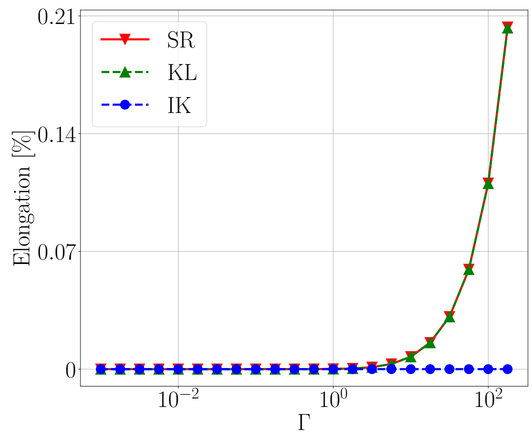

(b) Total elongation of the beam in function of the gravito-bending parameter Γ.

Figure 2.7: Cantilever results for a discretization of 50 elements. Color code: Simo-Reißner (red); Kirchhoff (green); inextensible Kirchhoff (blue); exact solution (black).

10 to 200.

Cantilever Bending

The cantilever planar bending test, first studied in detail by Bickley [143], is a standard method for obtaining elastic material parameters in soft matter physics. We clamp the object of interest at one end and leave the other end free in a straight initial configuration along the x-axis. Under the influence of gravity, the specimen bends downwards in the negative y-direction. The amount of bending is portrayed by the coordinate ratio $\mathcal{Y} = -y_C^{\text{tip}}/x_C^{\text{tip}}$ measured at the end point of the beam in the deformed state. This ratio depends on the gravito-bending parameter Γ.

A logarithmic plot of the gravito-bending parameter against the coordinate ratio is given in Fig. 2.7a. The simulations align well with the semi-analytic master curve from [142] which was derived for the inextensible Kirchhoff model. Though present in the two extensible models, the effect of elongation defined as:

$$\text{Elongation} = 100 \times \frac{L^{\text{final}} - L}{L} \tag{2.107}$$

is negligible, as shown in Fig. 2.7b. The results we provide here are for a cable made of rubber of initial length $L = 1$[m], cross-section radius $R = 0.01$[m], Young's modulus 5[MPa], density $\rho = 1100$[kg/m^3], and Poisson ratio $\nu = 0.5$. We modify the gravity g to obtain the desired values for Γ in each simulation.

For values of Γ larger than those shown in the plot, i.e., larger than 200, the downward pull becomes extremely large and the cable experiences high tension forces giving rise to unrealistic amounts of elongation for the two extensible models. The inextensible model struggles with convergence due to the ill-conditioning originating from the extremely high constraint forces that are supposed to counteract the cable's tendency to elongate.

Bend-Twist Bifurcation

Numerical simulation of the bend-twist coupling of rods is a challenging task. The present benchmark aims at verifying the ability of the $SE(3)$ beam elements to properly capture this effect. It consists of a precurved rod possibly experiencing twist under the effect of gravity. In its natural shape, the rod is a twist-free circle of radius r lying in the xz-plane. It is clamped at one end and left free at its other end while it deforms under the effect of gravity applied in the negative z-direction. Depending on the geometric and material parameters, the planar (2D) solution is stable or not and a small perturbation (as would occur in the real world) would induce the rod to buckle into a helix-like shape (3D).

Note about the involved parameters: For this benchmark, we vary the parameters $\mathcal{Y} = L/(2\pi r)$ and $\mathcal{X} = (r/L)\sqrt[3]{\Gamma}$. The first one fixes the initial geometry of the beam. The second one is obtained by tuning the gravity g and keeping the rest fixed. Realistic Γ values for this use case lie in $[10^2, 10^3]$. The corresponding $\mathcal{X}$-values are $\mathcal{Y}[2,5]/\pi$. Thus, the interesting parameters for cable simulation lie in a corridor around $\mathcal{X}\mathcal{Y} = 1$, which is a straight line in the logarithmic phase diagram connecting $(0.1, 1)$ and $(1, 10)$.

The semi-analytic reference solution from [142] separates the phase diagram into two distinct zones: one where the 2-dimensional solution is stable and one where it is not. The validation procedure consists in sweeping the $\mathcal{X}\mathcal{Y}$-plane and checking if the numerical solution is planar or not. To that end, we compute the integral of the absolute value of the Frenet torsion along the final curve. Since in the present case the deformation is elementwise constant, we may compute it as follows [40]:

$$\vartheta = \int_0^L \|\tau\| \,\mathrm{d}s = \sum_e^{N_e} L_e^{-1} \| \left(\mathbf{d}_{AB,\theta}\right)^T \mathbf{d}_{AB,\chi} \|. \tag{2.108}$$

The quantity above vanishes for a planar curve [144]. We will consider a curve to be in a 3-dimensional state when $\vartheta > 10^{-3}$. To perturb the system, we apply a gravitational acceleration in the y-direction with a magnitude of $10^{-2} \times g$, before actually switching on gravity. This perturbation is ultimately removed before considering the final deformed state of the rod.

We obtain the phase diagram shown in Fig. 2.8b. However, the results are rather sensitive to the threshold chosen for ϑ. Therefore, we also illustrate the results as a height map in Fig. 2.8a which we believe reflects the results more truthfully. We show the results for the unconstrained beam element.

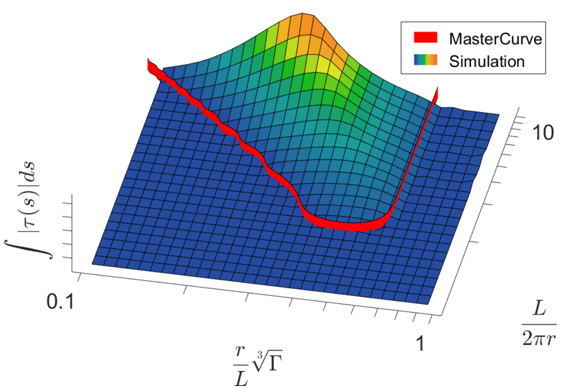

(a) Integrated torsion of the equilibrium shape displayed in a height map. The red wall corresponds to the master curve.

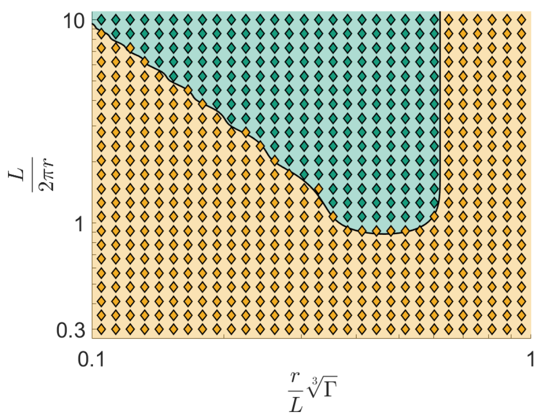

(b) Bend-Twist phase diagram with ground truth in the background and simulations as diamond shapes. Green and orange represent 3D and 2D states, respectively.

Figure 2.8: Bend-Twist results computed with $100 \times \mathcal{Y}$ elements for the unconstrained (SR) beam model. Each simulation corresponds to a given value for the aspect ratio L/r and the parameter $(r/L)\sqrt[3]{\Gamma}$. The simulations were made with a length $L = 1$[m], a cross-section radius $R = 0.0025$[m], a Poisson ratio $\nu = 0.3$, a density $\rho = 1273[\mathrm{kg/m^3}]$, a bending stiffness $EI = 1[\mathrm{Nm^2}]$, a torsion stiffness $GJ = 0.77[\mathrm{Nm^2}]$, and a tensional stiffness $EA = 16$[MN].

Similar figures can be obtained for the constrained (KL) and (IK) beam elements. The issue raised in the previous section concerning the elongation of the beam for extremely large values of Γ is still valid here.

2.4.3 Dynamic Examples

In this section, we illustrate the behavior of the proposed beam elements in a dynamic setting. We start with a planar initially undeformed example and finally, we finish this chapter with a tridimensional test case where the beam is predeformed.

Flexible Pendulum

We reproduce the same exact situation as described by Lang et al. [74]. A flexible rubber rod of length $L = 1$[m], cross-section radius $R = 0.005$[m], Young's modulus $E = 5$[MPa], Poisson ratio $\nu = 0.5$, and density $\rho = 1100$[kg/m^3] in an initially straight configuration along the x-axis is fixed by a revolute joint at one end and left free at the other. It is subject to the gravitational acceleration $g = 9.81$[m/s^2] in the negative z-direction. The beam is discretized into 10 elements of equal length. We use a time step of $\Delta t = 0.001$[s] and a spectral radius of $\rho_\infty = 0$.

The graphs provided in Fig. 2.9 show the non-trivial position and rotation components of the pendulum taken at three different locations being $s = 0$, $s = 0.5$, and $s = 1$. They very closely match the reference solution computed by *ABAQUS* [74]. It is interesting to note that the cross-section orientation of the inextensible Kirchhoff beam element slightly departs from the other two towards the end of the simulation.

In Fig. 2.10, we show non-trivial deformation measures. We make a first reassuring observation: the extensional strain in Fig. 2.10b vanishes for the inextensible beam model and the shear strains in Fig. 2.10c vanish for the two Kirchhoff models during the entirety of the simulation. We also notice that for such a long and slender structure the main deformation mode is bending, shown in Fig. 2.10a, and the three beam elements only slightly differ from one another in that regard since for such structures extension and shearing are anyways negligible.

The attentive scientist will notice discrepancies between the bending curvature and shear deformation we obtain for our unconstrained beam element and the reference solution given in [74]. Thankfully, the reason is also explained therein. Indeed, *ABAQUS* uses different deformation measures than the classical ones introduced by Simo [54, 68] which are only equivalent for extension. Figure 2.10b is therefore the only one that matches the reference closely.

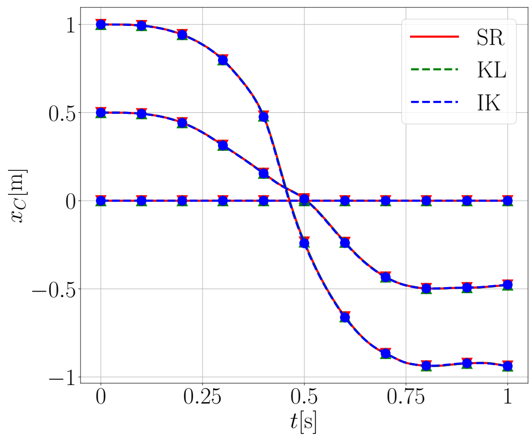

(a) Horizontal position.

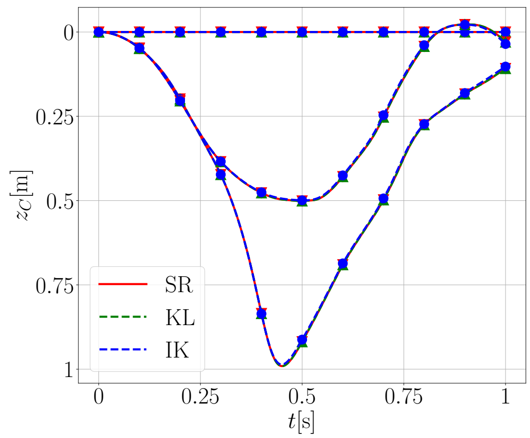

(b) Vertical position.

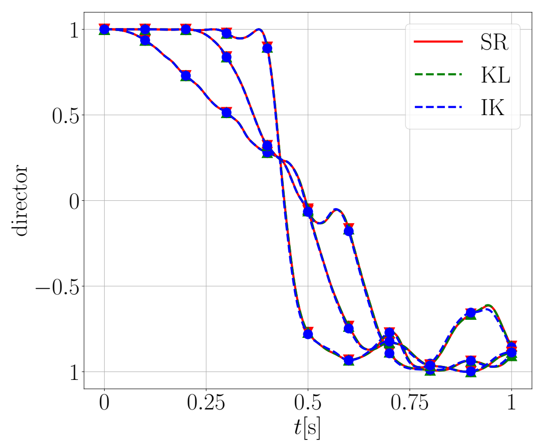

(c) Projection of the cross-section director onto the z-axis.

Figure 2.9: Results flexible pendulum for 10 elements and a time step $\Delta t = 0.001$[s]. We always show the solution at $s = 0$, $s = 0.5$, and $s = 1$. Here director means the non-trivial basis vector of the rotation matrix perpendicular to the cross-section normal. Color code: Simo-Reißner (red); Kirchhoff (green); inextensible Kirchhoff (blue).

Wilberforce Pendulum

In the spirit of a publication by Harsch et al. [62], we chose as the last example the *Wilberforce pendulum*. It is an interesting object that has been the subject of several experimental and analytical works in the past [145, 146]. It consists of a steel spring fixed at one end and loaded with a steel cylinder at the other end. The cylinder initially starts vibrating vertically under the action of gravity. Due to a coupling of bending

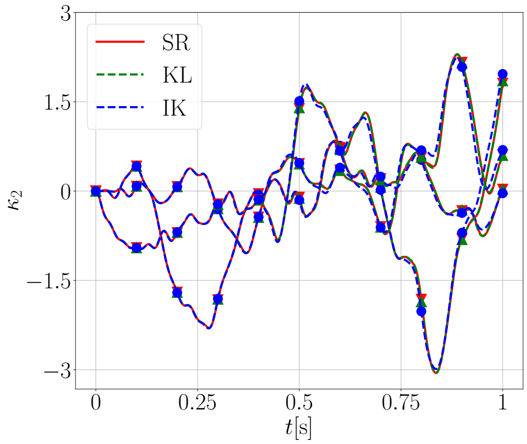

(a) Bending curvature.

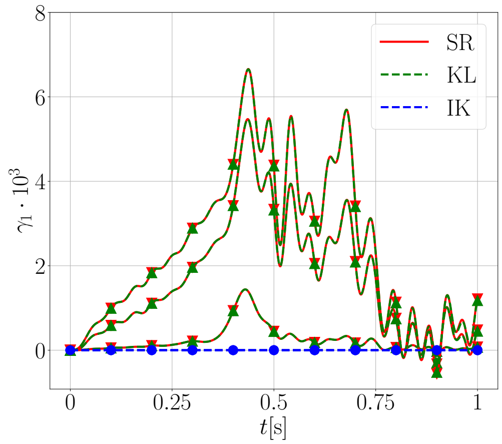

(b) Extension.

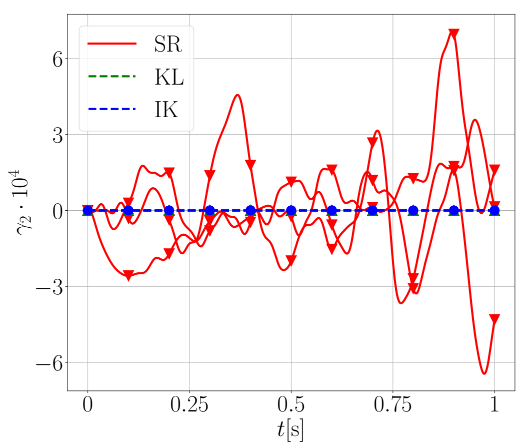

(c) Shear deformation.

Figure 2.10: Results flexible pendulum for 10 elements and a time step $\Delta t = 0.001$[s]. We always show the solution at $s = 0$, $s = 0.5$, and $s = 1$. Color code: Simo-Reißner (red); Kirchhoff (green); inextensible Kirchhoff (blue).

and torsion effects in the spring, the cylinder exhibits an additional periodic torsional motion. The material and geometry parameters may be tuned in such a way that the vertical and torsional vibrations have an exact phase shift of $\pi/2$. Thereby we can verify in a simple manner the proper behavior of the proposed beam elements in a complex situation where initial curvature, bending and torsional coupling, and dynamic effects are involved. See Fig. 2.11 for a schematic illustration of the pendulum.

We use the following parameters. The cylinder is modeled as a rigid body of mass

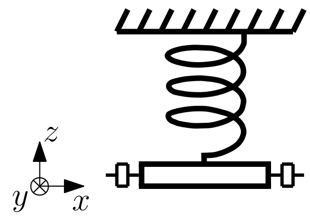

Figure 2.11: Schematic representation of the Wilberforce pendulum

$m = 0.469$[kg], and matrix of inertia $\mathbf{J} = \text{diag}(1.2, 1.2, 1.4) \times 10^{-4}$[kg m$^{\mathbf{2}}$]. The spring is made of steel with a density $\rho = 7850$[kg/m$^{\mathbf{3}}$], Young's modulus $E = 199$[GPa], bulk modulus $G = 81$[GPa]. Its initial shape is a helix made of $N_{helix} = 3$ coils, with a helix radius of $R_{helix} = 0.0016$[m], a helix pitch of $p_{helix} = 0.001$[m], and a wire cross-section radius of $R = 0.001$[m]. We use 50 Simo-Reissner-$SE(3)$ beam elements of the same length to model the spring. With these elements, the initial helicoidal geometry can be represented exactly such that no optimization procedure for the generation of the initial beam geometry, as explained in [62], is necessary.

In Fig. 2.12, the expected phase shift between the vertical and torsional oscillations can be seen. The total simulation time is $T = 9$[s], we use a time step of $\Delta = 10^{-3}$[s], and a spectral radius at infinity of $\rho_\infty = 0.8$ for the generalized-α time integration scheme.

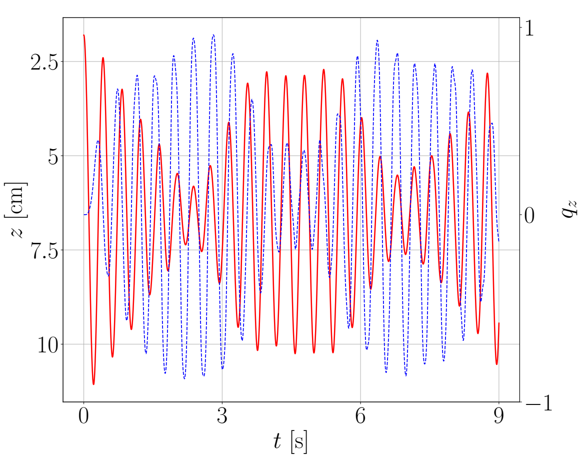

Figure 2.12: Z-component of the position and the rotation quaternion of the rigid cylinder's center of mass in function of time. The beat phenomenon typical for the Wilberforce pendulum can be observed together with a phase shift of half a period.

2.5 Concluding Remarks

Chapter 2 focuses on the development and the detailed derivation of a beam finite element on the special Euclidean group $SE(3)$, emphasizing the local frame approach for flexible components. It is a reformulation of the classical Simo-Reißner model. The chapter builds on earlier research by highlighting important properties, setting notations for subsequent chapters as well as extending the $SE(3)$ formalism to the Kirchhoff-Love and the inextensible Kirchhoff models.

The chapter begins with an introduction to Lie groups, particularly $SE(3)$, connecting them to the kinematic descriptions of the rigid body and the flexible beam. The deformation measures are interpreted as being expressed in the local frames attached to the cross-sections and are invariant under a superimposed Euclidean transformation. Consequently, the equilibrium equations enjoy the same interpretation and invariance property. A key aspect to preserve these properties lies in the consistent spatial and temporal discretization of these equations on the Lie group using the finite element method, paired with the Lie group generalized-α time integration scheme which we have described in this chapter.

Various numerical tests validate and compare the proposed beam models, exploring their convergence and behavior under different conditions. The examples include the investigation of locking phenomena, helix deformation under gravity, and cantilever bending tests. They demonstrate the absence of locking phenomena and highlight the models' robustness and accuracy.

CHAPTER 3

STATIC BEAM-TO-BEAM CONTACT

In this chapter, frictional contact between the $SE(3)$ beam elements derived in chapter 2 is considered. The common point between all application examples and also in particular in the case of wire harnesses in the automotive industry in Fig. 1 we presented in the introduction of this thesis is the following: the structures of interest are slender rods with circular cross-sections. We will exploit this fact to simplify the contact kinematics. Under certain conditions the full formulation can even be done in terms of relative positions of the beam centerlines only. The extension to arbitrary cross-section shapes does not fundamentally change the nature of the methodologies presented in this chapter. However, it can potentially complexify the contact kinematics. Inertia effects are ignored for now, but there are already enough subtleties to study in the (quasi) static case. For a treatment of dynamic effects the reader is referred to chapter 4.

Computational contact mechanics for general deformable bodies has been studied extensively in the literature. For an introduction and an overview see [147–153]. The most popular approaches, due to their solid mathematical foundation and advantageous numerical properties, are probably the mortar method and its variants. These are characterized by contact constraints enforced in a weak sense and a saddle point formulation of the problem. It began as a method for ensuring optimal information transfer between non-matching finite element grids [154–156]. It turned out that similar principles are applicable in the context of contact problems. Thus the mortar method found its way into computational contact mechanics [157–179]. Mathematical proofs of stability and convergence properties can be found in [180–184]. Some research has also been done on efficient implementation strategies [185].

Contact interactions between purely rigid bodies historically has also received significant attention[1]. As we saw in the state-of-the-art (1.2), publications on beam-to-beam contact however remain rather scarce, even though their number has been increasing in recent years. Nonsmooth formulations based on Lagrangian multipliers are especially rare. One of the reasons is the complexity of the topic which boils down to the following reason: the beam model we presented in the previous chapter lies somewhere in between a fully deformable and a rigid object. It is potentially highly flexible, but there is some rigidity in the model due to the presence of the kinematic restriction on the cross-section. Unfortunately, the beam-to-beam contact problem inherits many of the difficulties that arise in both classes of models.

Additionally, due to the particular geometric features, modeling contact between thin beams with circular cross-sections has many specificities. For example the appearance of contact forces of different nature. In the region of large contact angles, i.e. when two beams cross each other, interactions can be understood as point-to-point contact and the situation ressembles rigid body contact at first glance. However, the beam elements deform under the action of the contact forces and finding the location of contact points is much more difficult than for purely rigid bodies. Questions about the existence and uniqueness of the contact points arise. Beams also have the ability to slide over each other and deform at the same time. When the contact angle is sufficiently small along larger beam segments, the interaction should rather be described as a distributed force per unit length.

Let us look again at Figs. 1 and 2 from the introduction to help us guide our choice of beam-to-beam contact model. The cables or fibers are generally closely packed and touch each other along the majority of their length. We therefore assume that so called line-to-line contact models are the most appropriate. Our main focus will be on the latter type of contact description. Therefore it makes sense to draw inspiration from contact mechanics for general deformable bodies and attempt the use of mortar methods for beam-to-beam contact. Since those are not the easiest to implement, we also explore a simpler collocation-type approach.

The kinematics of contact and the space continuous formulation of the equilibrium conditions are given in section 3.2. As teased by the title of the thesis, we opt for a nonsmooth formulation in terms of inequality constraints enforced via Lagrangian multipliers playing the role of the distributed contact forces. This then raises the question of discretization which is adressed in section 3.3. As mentioned before, we propose two approaches. The first one is a collocation method. The distributed contact force is sim-

[1]Since the issues related to rigid body contact are mainly encountered in the dynamic case, we postpone its literature review to the relevant chapter.

ply replaced by a set of point forces at well chosen locations. The second one is a mortar finite element method. The non-penetration constraints become weighted integrals that involve the interpolation functions of the Lagrangian multiplier field. In section 3.4, an augmented Lagrangian method combined with a semismooth Newton algorithm is applied to obtain a solution to the system of nonlinear discretized equations. Finally, in section 3.5, the numerical performance of the proposed methodology is studied. We show optimal spatial convergence rates as expected for the mortar method, without the need for envolved integration schemes, nor a smooth representation of beam centerlines, even in the presence of spatial discontinuities in the distributed contact force. Interestingly, the combination with the geometrically exact beam formalism on the Lie group $SE(3)$ leads to a constraint gradient and a tangent stiffness invariant under rigid body transformations for the contact element.

This chapter is based on the author's own work in [51]. Compared to that publication, derivations have been simplified and streamlined, yielding a more robust implentation. Moreover, the formulation is extended to the frictional case and the comparison with the collocation approach was added. A similar mortar algorithm was later also studied for static frictionless beam-to-beam contact by Tomec and Jelenic in [186].

3.1 Contact kinematics

Let us start with some notations. We will do all the developments for a two-beam system, but they may be generalized to an arbitrary number of beams. The configuration of each individual beam is given by the frame variables $(\mathbf{H}_C(s_1), \mathbf{H}_F(s_2)) \in SE(3)^2$ which are defined at their respective centerlines. We introduce their variations from the left trivialized derivative on $SE(3)$ as

$$\delta\mathbf{H}_C = \mathbf{H}_C S(\delta\boldsymbol{\pi}_C), \quad S(\delta\boldsymbol{\pi}_C) \in \mathfrak{se}(3), \tag{3.1}$$

$$\delta\mathbf{H}_F = \mathbf{H}_F S(\delta\boldsymbol{\pi}_F), \quad S(\delta\boldsymbol{\pi}_F) \in \mathfrak{se}(3) \tag{3.2}$$

and which we collect in the vector

$$\delta\boldsymbol{\pi}(s_1, s_2) = \begin{bmatrix} \delta\boldsymbol{\pi}_C(s_1) \\ \delta\boldsymbol{\pi}_F(s_2) \end{bmatrix} \in \mathbb{R}^{12}. \tag{3.3}$$

Intuitively everyone understands that contact interactions exclusively happen at the

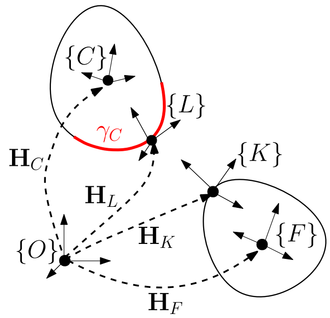

Figure 3.1: Graphical illustration of contact kinematics between two flexible beams: cross-section view for a given centerline coordinate.

surface of the two bodies of interest, in our case beams. Therefore, one of our goals in a later stage will be to construct the contact frames $q = (\mathbf{H}_L, \mathbf{H}_K) \in SE(3)^2$ which are variables that express the configuration on the boundary of the beams under study. These will be handy for introducing the appropriate kinematic quantities used in the description of frictional contact. We write their variations

$$\delta\mathbf{H}_L = \mathbf{H}_L S(\delta\boldsymbol{\pi}_L), \quad S(\delta\boldsymbol{\pi}_L) \in \mathfrak{se}(3), \tag{3.4}$$

$$\delta\mathbf{H}_K = \mathbf{H}_K S(\delta\boldsymbol{\pi}_K), \quad S(\delta\boldsymbol{\pi}_K) \in \mathfrak{se}(3). \tag{3.5}$$

At every location of the potential contact surface γ_C, which is defined on the so-called "slave" body, a location on the opposing "master" body is defined by means of a geometrical projection, see Fig. 3.1. This association of two points that might enter into contact can be straightforward or rather complex depending on the shape of the cross-section and the degree of precision that we desire to achieve. In the next section we shall profit from the fact that we restrict ourselves to thin circular cross-sections to keep the formulation simple.

For the remainder of this thesis the pair of frames $(\{L\}, \{K\})$ will always be considered as associated via the above-mentioned projection. They are thus functions of the slave surface centerline coordinate i.e. we have $q = q(s_1)$ and also $\delta\boldsymbol{\pi} = \delta\boldsymbol{\pi}(s_1)$.

The configuration of the individual beams are given by the variables defined in the local frames $(\mathbf{H}_C, \mathbf{H}_F)$ attached to the beam centerlines and not the surface, where variables related to contact i.e. $(\mathbf{H}_L, \mathbf{H}_K)$ are expressed. However, by means of well-defined operations on $SE(3)$ we can switch from one representation to the other effortlessly.

A non-penetration constraint is a unilateral restriction of relative motion that we write in its most general form as

$$g_N(\mathbf{H}_{LK}) \geq 0. \tag{3.6}$$

It is a pointwise condition that has to hold for every point on the potential contact surface. The function g_N is called the *normal gap* and serves as a signed measure of proximity between the two bodies. When the normal gap equals zeros, the two beams touch, when it is strictly positive, there is no contact and penetration i.e. a strictly negative gap function is mathematically prohibited by Eq. (3.6). The subscript N labels variables defined along a direction perpendicular to the potential contact surface. If no friction is considered these are the only ones that matter.

The second important kinematic quantity involved in friction models is the *tangential slip velocity* $\mathbf{u}_T(\mathbf{H}_{LK}, \boldsymbol{v}_{LK})$. It only truly intervenes when the two bodies are already in contact. They are said to *stick* to each other when the tangential slip velocity vanishes and *slip*/*slide* otherwise. Since in this chapter we are concerned with quasi-static simulations, talking about velocities does not make sense. But, we can simply replace the slip velocity $\mathbf{u}_T$ by a *tangential slip increment* [187] over a pseudo-time interval Δt as

$$\triangle \mathbf{g}_T(t - \triangle t, t) = \int_{t-\triangle t}^{t} \mathbf{u}_T(\tau)\,\mathrm{d}\tau. \tag{3.7}$$

and we also define its infinitesimal counterpart

$$\mathrm{d}\mathbf{g}_T = \lim_{\triangle t \to 0} \triangle \mathbf{g}_T = \mathbf{u}_T \mathrm{d}\tau. \tag{3.8}$$

In Eq. (3.8) note the appearance of the tangential gap $\mathrm{d}\mathbf{g}_T(\mathbf{H}_{LK}, \mathrm{d}\boldsymbol{\pi}_{LK})$. This effectively shifts the description of contact states from velocities to position increments. Next to being necessary in the present quasi-static case, it also has some importance for the time integration schemes discussed in chapter 4.

Let us list all possible kinematic contact states in terms of the values taken by the normal gap and the tangential slip increment:

- No contact. There is a finite distance between the two objects: $g_N > 0$.
- Contact. The bodies touch and the distance is zero at these locations: $g_N = 0$.
  - The two bodies stick: $\|\mathrm{d}\mathbf{g}_T\| = 0$.

– Two two bodies slide over each other $\|\mathrm{d}\mathbf{g}_T\| > 0$.

The quantity $\mathbf{H}_{LK} = \mathbf{H}_L^{-1}\mathbf{H}_K$ describes the relative configuration (or transformation) between the two contact frames. We call $\mathbf{x}_{LK}$ the *contact vector*. It is the translation part of $\mathbf{H}_{LK}$, which appears as the difference between the position of frame $\{L\}$ and frame $\{K\}$ expressed in frame $\{L\}$. Later, when we will introduce the virtual work we will be in need of its arbitrary variation

$$\delta\mathbf{x}_{LK}^{K} = \mathbf{G}(\mathbf{H}_{LK})\delta\boldsymbol{\pi} = \begin{bmatrix}\mathbf{G}_N \\ \mathbf{G}_T\end{bmatrix}\delta\boldsymbol{\pi}. \tag{3.9}$$

This implicitly introduces the constraint gradient $\mathbf{G}$ as the direction of the contact force expressed in the local frames $\{C\}$ and $\{F\}$ attached to the respective centerlines, since these serve as primary variables of our problem. Thanks to the Lie group framework its derivation is straightforward. The term constraint gradient in the present case is an abuse of language that we use to align with vocabulary from the field of Multibody Dynamics with bilateral constraints.

In the previous chapter we saw that a relative configuration between frames is frame invariant and hence any constraint gradient of the form Eq. (3.9) will be so too. This property should naturally carry through the discretization process. We have split the constraint gradient into a normal part $\mathbf{G}_N$ and a tangential part $\mathbf{G}_T$ which will be useful in later developments. Note that in Eq. (3.9) the variation of the contact vector is expressed in terms of arbitrary motions of the reference frames $\{C\}$ and $\{F\}$. Thus the constraint gradient incorporates the information relating $\delta\boldsymbol{\pi}_L$ and $\delta\boldsymbol{\pi}_K$ to $\delta\boldsymbol{\pi}$. One could imagine less common contact mechanisms explicitely involving rotational degrees of freedom, for example when formulating specialized joints with clearance. These would be incorporated easily into the above formalism.

3.1.1 Friction between thin beams with circular cross-sections

The purpose of this section is to construct $\mathbf{H}_{LK}$ and deduce all relevant variables for the formulation of frictional contact. To keep notations as simple as possible without losing the most essential features of the formulation we restrict ourselves to thin beams with circular cross-sections. R_1 and R_2 denote the two cross-section radii. We consider them constant here and shearing is neglected in the kinematics of contact. An analogous procedure can be applied to arbitrarly shaped beams. We start by explaining the projection procedure we hinted at in the previous section.

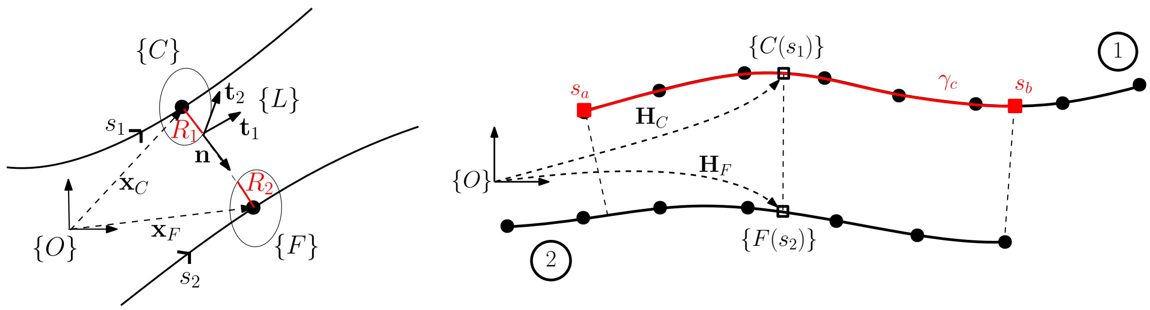

Figure 3.2: Notations for beam-to-beam contact.

Projection

Everytime contact forces have to be computed, two points on the two beams have to be associated. Generally a point $s_1 \in [0, L]$ at the position $\mathbf{x}_C(s_1)$ on the slave beam is known. For example because we are evaluating an integral at a Gauß point on the slave beam. We then seek to determine a point $\bar{s}_2$ on the master beam located at $\overline{\mathbf{x}}_F(s_2)$. The overbar means that it is a quantity that was found by the projection step and satisfies the following condition:

$$\mathcal{P}_m(\bar{s}_2) = \left(\overline{\mathbf{x}}_F(\bar{s}_2) - \mathbf{x}_C(s_1)\right)^T \mathbf{m}(s_1) = 0, \tag{3.10}$$

where $\mathbf{m} = \mathbf{R}_C \mathbf{e}_1$ is the normal of the cross-section on the slave beam and $\mathbf{e}_1 = \begin{bmatrix} 1 & 0 & 0 \end{bmatrix}^T$. Thus, given a point on the slave beam, the associated point on the master side will be the intersection between the plane defined by the cross-section on the slave side and the centerline curve of the master beam. Eq. (3.10) is solved by a Newton-Raphson procedure. To that end the derivative with respect to the unknown s_2 is computed as:

$$\frac{\partial \mathcal{P}_m}{\partial s_2} = \left(\mathbf{R}_F \mathbf{N} \boldsymbol{f}_F\right)^T \mathbf{m}, \tag{3.11}$$

where $\mathbf{N} = \begin{bmatrix} \mathbf{I}_{3\times 3} & \mathbf{0}_{3\times 3} \end{bmatrix}$. It can be generalized to more complex cross-section shapes by introducing additional terms in the $\mathbf{N}$ matrix.

Integration boundaries

The potential contact region $\gamma_C = [s_a, s_b] \in [0, L_C]$ is defined by the set of values s_1 such that Eq. (3.12) has a solution where $\bar{s}_2 \in [0, L_F]$. Therefore, as represented on Fig. 3.2, an integration boundary s_k with $k = a, b$, is either given by a node of the slave beam or by the projection of a master node onto the slave depending on what is most restrictive. This projection is given by:

$$\mathcal{P} = (\mathbf{x}_\beta - \mathbf{x}_C(s_k))^T \mathbf{m}(s_k) = 0, \quad \beta = D, E \tag{3.12}$$

where $\mathbf{x}_\beta$ denotes the position of a master node. The solution to Eq. (3.12) is again obtained via a Newton-Raphson scheme. Contrary to the previous case the unknown here is a point on the slave beam. Thus the Jacobian required for numerical method is

$$\frac{\partial \mathcal{P}}{\partial s_1} = -(\mathbf{R}_C \mathbf{N} \boldsymbol{f}_C)^T \mathbf{m} + (\mathbf{x}_F - \mathbf{x}_C)^T (\mathbf{R}_C S(\mathbf{N} \boldsymbol{f}_C)) \, \mathbf{e}_1. \tag{3.13}$$

Note that this way of computing the potential contact region fails when the two beam elements are perfectly orthogonal. The overbar will be dropped from now on.

The local contact frame

The next step is the definition the local contact frame $\{L\}$ on the surface of the slave beam as shown in Fig. 3.2 and described by the variable

$$\mathbf{H}_L = \begin{bmatrix} \mathbf{R}_L & \mathbf{x}_L \\ \mathbf{0}_{1\times 3} & 1 \end{bmatrix} \in SE(3), \tag{3.14}$$

where $\mathbf{R}_L = \begin{bmatrix} \mathbf{n} & \mathbf{t}_1 & \mathbf{t}_2 \end{bmatrix}$. The normal vector $\mathbf{n}$ is introduced as

$$\mathbf{n} = \frac{\mathbf{x}_F - \mathbf{x}_C}{\|\mathbf{x}_F - \mathbf{x}_C\|}. \tag{3.15}$$

This normal is well-suited when beams are almost parallel along the potential contact region. It might become problematic in the range of large contact angles. In such a case an alternative definition of the contact normal is necessary, an aspect that has been studied in detail in [12]. The frame $\{L\}$ is located at

$$\mathbf{x}_L = \mathbf{x}_C + R_1 \mathbf{n}. \tag{3.16}$$

One needs to be careful when defining the first tangent vector $\mathbf{t}_1$. It should be perpendicular to $\mathbf{n}$. Looking at Eq. (3.10) a natural candidate would be $\mathbf{m}$. To ensure that the first tangent vector is truly perpendicular to $\mathbf{n}$ we slightly correct it by projecting it onto the plane perpendicular to $\mathbf{n}$. Hence it is give by the formula

$$\mathbf{t}_1 = \mathbf{m} - \left(\frac{\mathbf{m}^T\mathbf{n}}{\|\mathbf{n}\|^2}\right)\mathbf{n}. \tag{3.17}$$

The second tangent vector is simply the cross product between Eqs. (3.15) and (3.17)

$$\mathbf{t}_2 = -\frac{S(\mathbf{n})\mathbf{t}_1}{\|S(\mathbf{n})\mathbf{t}_1\|}. \tag{3.18}$$

We introduce the frame

$$\mathbf{H}_K = \begin{bmatrix} \mathbf{R}_L & \mathbf{x}_K \\ \mathbf{0}_{1\times3} & 1 \end{bmatrix} \in SE(3), \tag{3.19}$$

which is simply the frame $\mathbf{H}_L$, but translated onto the surface of the master beam with the position vector

$$\mathbf{x}_K = \mathbf{x}_F - R_2\mathbf{n}. \tag{3.20}$$

The relative configuration between the two contact frames is

$$\mathbf{H}_{LK} = \begin{bmatrix} \mathbf{R}_{LK} & \mathbf{x}_{LK} \\ \mathbf{0}_{1\times3} & 1 \end{bmatrix} = \begin{bmatrix} \mathbf{I}_{3\times3} & \mathbf{R}_L^T(\mathbf{x}_K - \mathbf{x}_L) \\ \mathbf{0}_{1\times3} & 1 \end{bmatrix} \in SE(3). \tag{3.21}$$

A scalar measure of proximity is given by the signed distance function, also called normal gap. It is immediately obtained as the first component of the translation part of $\mathbf{H}_{LK}$

$$g_N = \mathbf{e}_1^T\mathbf{x}_{LK} = \mathbf{n}^T(\mathbf{x}_F - \mathbf{x}_C) - R_1 - R_2, \tag{3.22}$$

where we recognize the usual expression for thin circular beams [102]. Due to their geometric shape, pure normal (or frictionless) contact can be entirely written in terms of variables located at the centerline without performing additional transformations. This is no longer true in the presence of friction. The main difficulty is the proper construction of the tangential slip increment. The advantage of embedding the formulation in a Lie group setting is the direct access to any kinematic information.

An infinitesimal perturbation of the frame defined in Eq. (3.21) is given by

$$\begin{aligned}\mathrm{d}\mathbf{H}_{LK} &= \mathbf{H}_{LK} S\left(\mathrm{d}\boldsymbol{\pi}_{LK}^{K}\right)\\ &= S\left(\mathrm{d}\boldsymbol{\pi}_{LK}^{L}\right)\mathbf{H}_{LK}, \quad S\left(\mathrm{d}\boldsymbol{\pi}_{LK}^{K}\right), S\left(\mathrm{d}\boldsymbol{\pi}_{LK}^{L}\right) \in \mathfrak{se}(3),\end{aligned} \tag{3.23}$$

where the superscript indicates in which frame the infinitesimal perturbation is represented. This is the only time we make it appear explicitely. A left trivialized representation of the frame derivative yields tangential slip measures and contact forces computed in frame $\{K\}$. Chosing a right trivialized representation produces a formulation in frame $\{L\}$. When the two beams are in contact both approaches are equivalent. To be consistent with what was done in chapter 2 we go for the left trivialized representation here.

For an infinitesimal motion, the tangential slip increment is simply identified as the second and third translational components of the infinitesimal translation perturbations

$$\mathrm{d}\mathbf{g}_T = \begin{bmatrix}\mathrm{d}g_{T_1}\\ \mathrm{d}g_{T_2}\end{bmatrix} = \begin{bmatrix}\mathbf{e}_2^T\\ \mathbf{e}_3^T\end{bmatrix}\mathrm{d}\mathbf{x}_{LK}^{K} = \begin{bmatrix}\mathbf{e}_2^T\\ \mathbf{e}_3^T\end{bmatrix}\mathbf{N}\mathrm{d}\boldsymbol{\pi}_{LK}^{K} = \mathbf{N}_T\mathrm{d}\boldsymbol{\pi}_{LK}^{K}, \tag{3.24}$$

where

$$\mathbf{N}_T = \begin{bmatrix}\mathbf{e}_2^T\\ \mathbf{e}_3^T\end{bmatrix}\mathbf{N} = \begin{bmatrix}0 & 1 & 0 & 0 & 0 & 0\\ 0 & 0 & 1 & 0 & 0 & 0\end{bmatrix}. \tag{3.25}$$

We can relate the infinitesimal tangential slip to perturbations of the centerline frames as

$$\mathrm{d}\mathbf{x}_{LK}^{K} = \underbrace{\mathbf{N}\left[-\mathrm{Ad}_{\mathbf{H}_{KC}} \quad \mathrm{Ad}_{\mathbf{H}_{KF}}\right]}_{=\mathbf{G}}\mathrm{d}\boldsymbol{\pi}. \tag{3.26}$$

The adjoint was defined in section 2.1.2. Its presence here is not surprising since it is the operator that relates derivatives expressed in different reference frames which is also precisely how we defined the constraint gradient in Eq. (3.9).

For the sake of completeness we also provide the expression in the frame $\{L\}$

$$\mathrm{d}\mathbf{x}_{LK}^{L} = \mathbf{N}\left[-\mathrm{Ad}_{\mathbf{H}_{LC}} \quad \mathrm{Ad}_{\mathbf{H}_{LF}}\right]\mathrm{d}\boldsymbol{\pi}. \tag{3.27}$$

We will not use it in the actual implementation.

Invariance of the constraint gradient

Let us write down the constraint gradient from Eq. (3.26) explicitly:

$$\mathbf{G}(\mathbf{H}_{LK}) = \left[\underbrace{-\mathbf{R}_K^T\mathbf{R}_C}_{\mathcal{T}_1} \quad \underbrace{S\left(\mathbf{R}_K^T(\mathbf{x}_C - \mathbf{x}_K)\right)}_{\mathcal{T}_2} \quad \underbrace{\mathbf{R}_K^T\mathbf{R}_F}_{\mathcal{T}_3} \quad \underbrace{S\left(\mathbf{R}_K^T(\mathbf{x}_F - \mathbf{x}_K)\right)}_{\mathcal{T}_4} \right]. \tag{3.28}$$

One rapidly verifies the invariance to a left translation of the involved matrices and vectors (see section 2.1). Indeed, applying an arbitrary transformation $\mathbf{H}_0 \in SE(3)$ to the term $\mathcal{T}_1$ yields

$$\begin{aligned}
\mathcal{T}_{1,tr} &= -\mathbf{R}_K^T\left(\mathbf{R}_0^T\mathbf{R}_0\right)\mathbf{R}_C \\
&= -\mathbf{R}_K^T\mathbf{R}_C \\
&= \mathcal{T}_1
\end{aligned} \tag{3.29}$$

and to the term $\mathcal{T}_2$ yields

$$\begin{aligned}
\mathcal{T}_{2,tr} &= S\left(\mathbf{R}_K^T\mathbf{R}_0^T(\mathbf{R}_0(\mathbf{x}_C - \mathbf{x}_0) - \mathbf{R}_0(\mathbf{x}_K - \mathbf{x}_0))\right) \\
&= S\left(\mathbf{R}_K^T\left(\mathbf{R}_0^T\mathbf{R}_0\right)(\mathbf{x}_C - \mathbf{x}_K + (\mathbf{x}_0 - \mathbf{x}_0))\right) \\
&= S\left(\mathbf{R}_K^T(\mathbf{x}_C - \mathbf{x}_K)\right) \\
&= \mathcal{T}_2
\end{aligned} \tag{3.30}$$

Similar operations may be performed on the third and fourth term such that we indeed have the constraint gradient $\mathbf{G}_{tr}$ after left translation that verifies

$$\mathbf{G}_{tr} = \mathbf{G}. \tag{3.31}$$

3.2 Space continuum formulation

The attention now turns towards formulating the equilibrium equations. The distributed contact force $\boldsymbol{\lambda}(s_1, t)$ which has the dimensions of a force per unit length is defined over the potential contact region γ_c on the slave beam. We decompose it in the local contact frame $\{L\}$ as $\boldsymbol{\lambda} = \begin{bmatrix}\lambda_N & \lambda_{T_1} & \lambda_{T_2}\end{bmatrix}^T$. It plays the role of Lagrange multiplier in the formulation and has to be determined as part of the solution. The virtual work produced by the contact force is

$$\begin{aligned}\delta\mathcal{W}_c &= \int_{\gamma_c} \left(\delta\mathbf{x}_{LK}^K\right)^T \boldsymbol{\lambda}\,\mathrm{d}\gamma \\ &= \int_{\gamma_c} (\delta\boldsymbol{\pi})^T\,\mathbf{G}^T\boldsymbol{\lambda}\,\mathrm{d}\gamma.\end{aligned} \tag{3.32}$$

This contribution is to be equilibrated by the weak form of the equilibrium equations in Eq. (2.65):

$$\delta\mathcal{W} = \delta\mathcal{W}_c. \tag{3.33}$$

Equation (3.33) holds for all admissible $\delta\boldsymbol{\pi}$ and hence we identify the contribution of the contact interaction to the equilibrium of forces and moments as

$$\begin{aligned}\mathbf{f}^{\mathrm{con}}(\mathbf{H}_{LK}, \boldsymbol{\lambda}) &= \left(\mathbf{G}(\mathbf{H}_{LK})\right)^T \boldsymbol{\lambda} \\ &= \begin{bmatrix} -\mathbf{R}_K^T\mathbf{R}_C\boldsymbol{\lambda} \\ S\left(\mathbf{R}_K^T(\mathbf{x}_C - \mathbf{x}_K)\right)\boldsymbol{\lambda} \\ \mathbf{R}_K^T\mathbf{R}_F\boldsymbol{\lambda} \\ S\left(\mathbf{R}_K^T(\mathbf{x}_F - \mathbf{x}_K)\right)\boldsymbol{\lambda}\end{bmatrix}.\end{aligned} \tag{3.34}$$

Under this form the interpretation of the individual terms should be clear. The first and third terms are the contact force acting on the translational degrees of freedom of the two beams respectively. They are expressed in the local frames attached to the beam centerlines. The second and fourth terms are moments resulting from the action of the contact force at the surface of the beam with respect to a point on the centerline. This effect only matters in the presence of friction. Indeed, a purely normal contact force is of the form $\boldsymbol{\lambda} = \lambda_N\mathbf{n}$. Introducing it into Eq. (3.34) and writing out the moment acting on the slave beam in that case yields

$$S(\mathbf{n}^T(\mathbf{x}_C - \mathbf{x}_K))\lambda_N \mathbf{n} = \mathbf{0}, \tag{3.35}$$

since the cross-product of parallel vectors is the null vector[2]. This explains why in the frictionless case surface effects may be ignored and a fully centerline-based formulation is possible [102, 186]. Strictly speaking, this is no longer true when adding friction forces to the problem. One could however argue that the moments induced by tangential contact forces are negligeable for very thin beams, since the lever arm is small.

3.2.1 Mathematical preliminaries

Convex analysis is devoted to the study of convex functions and convex sets. It helps with the understanding of set valued force laws as they appear in contact mechanics and explains how to express them as inclusions. Convex analysis also encompasses convex minimization theory which opens the door to powerful solution algorithms. In this section we quickly introduce the terminology relevant for the formulation of the Coulomb contact law [188–191].

We denote by $\psi_{\mathcal{S}}$ the *indicator function* of a set $\mathcal{S}$. It is zero when an element $\mathbf{x}$ belongs to the set $\mathcal{S}$ and infinite otherwise. In particular, the indicator function of the real half line $\mathcal{S} = \mathbb{R}^+$, shown in fig. 3.3a, is defined as

$$\psi_{\mathbb{R}^+}(x) = \begin{cases} 0 & \text{if } x \geq 0 \\ +\infty & \text{if } x < 0 \end{cases}. \tag{3.36}$$

The *subdifferential*, a generalization of the derivative to convex functions which are not necessarily differentiable everywhere, is a set valued function denoted $\partial\psi_{\mathcal{S}}$. The subdifferential of $\psi_{\mathbb{R}^+}$ has the expression

$$\partial\psi_{\mathbb{R}^+}(x) = \begin{cases} 0 & \text{if } x > 0 \\ ]-\infty, 0] & \text{if } x = 0 \\ \emptyset & \text{if } x < 0 \end{cases}. \tag{3.37}$$

[2]The same calculation can be made for the master beam.

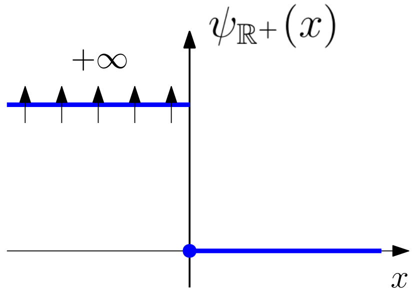

(a) Indicator function of the real half line.

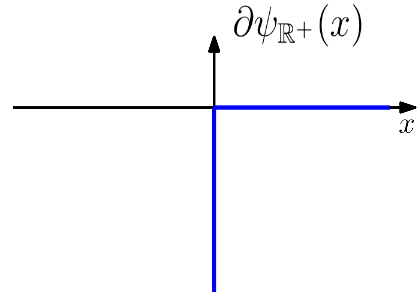

(b) Subdifferential of the indicator function of the real half line.

Figure 3.3: Graphs of $\psi_{\mathbb{R}^+}$ and $\partial\psi_{\mathbb{R}^+}$.

When its argument x is strictly positive, $\partial\psi_{\mathbb{R}^+}$ returns the value 0, when its argument is exactly 0 the subdifferential can take any negative value. Negative values of x are not allowed and $\partial\psi_{\mathbb{R}^+}$ is thus the empty set in that case. The graph of $\partial\psi_{\mathbb{R}^+}$ exactly describes, up to the minus sign, the normal contact force law that we hinted at in the introduction in Fig. 4.

The Coulomb disk section of the Coulomb cone is defined as

$$C(\lambda_N) = \{\boldsymbol{\lambda}_T : \|\boldsymbol{\lambda}_T\| \leq \mu\lambda_N\}\,, \tag{3.38}$$

where $\mu \in \mathbb{R}^+$. Hence, $\psi_{C(x_N)}$ shown in Fig. 3.4a is the indicator function of the Coulomb disk and the subdifferential, illustrated in Fig. 3.4b, is the set-valued function

$$\partial\psi_{C(\lambda_N)}(\boldsymbol{\lambda}_T) = \begin{cases} \mathbf{0} & \text{if } \mu\lambda_N - \|\boldsymbol{\lambda}_T\| > 0 \\ ]-\boldsymbol{\infty}, \mathbf{0}] & \text{if } \mu\lambda_N - \|\boldsymbol{\lambda}_T\| = 0 \\ \emptyset & \text{if } \mu\lambda_N - \|\boldsymbol{\lambda}_T\| < 0 \end{cases}. \tag{3.39}$$

3.2.2 Coulomb frictional contact law

In Sect. 3.1.1 it was stated that two bodies cannot penetrate. This kinematic condition is ensured by the appearance of a purely compressive reaction force per unit length. A vanishing normal gap with a finite compressive contact force and a vanishing contact force when the normal gap is strictly positive are mutually exclusive states. Hence,

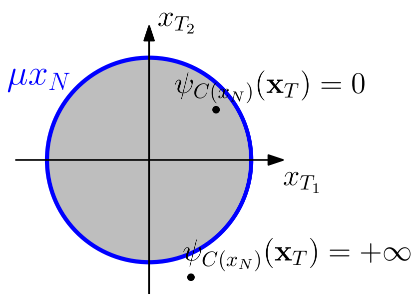

(a) Indicator function of the Coulomb disc.

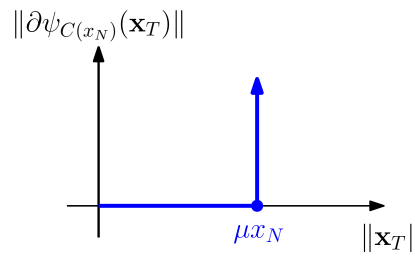

(b) Subdifferential of the indicator function of the Coulomb disc.

Figure 3.4: Graphical illustrations of $\psi_{C(x_N)}$ and $\partial\psi_{C(x_N)}$.

impenetrability in its strong, pointwise form is written

$$\lambda_N \geq 0, \quad g_N \geq 0, \quad \lambda_N g_N = 0, \quad \forall s_1. \tag{3.40}$$

This multivalued contact law is sometimes called Signorini or Karush-Kuhn-Tucker (KKT) condition. A graphical illustration is given in Fig. 4. The last equation is the complementarity condition. Equivalently, one can write a variational inequality of the type [183]

$$\lambda_N \in \mathcal{M}_N, \quad \delta\mathcal{W}_N = \int_{\gamma_C} (\delta\lambda_N - \lambda_N) g_N \,\mathrm{d}\gamma \geq 0, \quad \forall \delta\lambda_N \in \mathcal{M}_N \tag{3.41}$$

Such a weak form opens the door to mortar discretization schemes[3] that we will discuss in subsequent sections. $\mathcal{M}_N$ is a functional space that expresses that its elements have to be positive in a weak sense on the potential contact surface. For a formal definition see [173, 183]. It may also be shown that the KKT conditions in Eq. (3.40) derive from non-smooth pseudo-potentials which allows for alternative compact notations using inclusions

$$-g_N \in \partial\psi_{\mathbb{R}^+}(\lambda_N) \quad \text{or} \quad -\lambda_N \in \partial\psi_{\mathbb{R}^+}(g_N). \tag{3.42}$$

where $\psi_{\mathbb{R}^+}$ and $\partial\psi_{\mathbb{R}^+}$ were defined in the previous section. Eqs. (3.40), (3.41) and (3.42) are equivalent formulations of the contact conditions valid in the absence of friction.

In Coulomb's model additional tangential effects are taken into account. If the two beams are in contact i.e. if $g_N = 0$ they can either fully stick to each other, in which

[3] Also called variationally consistent discretization schemes

case lateral movement has to be prevented by an opposing tangential force smaller than the friction treshold. Or, the beams slide over each other while the tangential contact force equals the friction treshold. Again, these states are mutually exclusive such that they are expressed similarly to Eq. (3.40) with a complementarity condition as depicted in Fig. 6

$$\mu\lambda_N - \|\boldsymbol{\lambda}_T\| \geq 0, \quad \|\mathrm{d}\mathbf{g}_T\| \left(\mu\lambda_N - \|\boldsymbol{\lambda}_T\|\right) = 0, \quad \forall s_1 \tag{3.43a}$$

$$\mathrm{d}\mathbf{g}_T \|\boldsymbol{\lambda}_T\| = -\|\mathrm{d}\mathbf{g}_T\| \boldsymbol{\lambda}_T, \tag{3.43b}$$

where Eq. (3.43b) forces the tangential reaction to oppose movement. One important aspect of the Coulomb model, is that the friction treshold is proportional to the normal contact force. The coefficient of proportianality is the friction coefficient μ. Here we present the quasi-static formulation of the Coulomb model in terms of the slip increment. In the original version its place is actually taken by the relative velocity.

As for the frictionless case, we can write an equivalent variational inequality [183]

$$\boldsymbol{\lambda}_T \in \mathcal{M}_T, \quad \delta\mathcal{W}_T = \int_{\gamma_C} \left[\left(\delta\boldsymbol{\lambda}_T - \boldsymbol{\lambda}_T\right)^T \mathrm{d}\mathbf{g}_T \right] \mathrm{d}\gamma \geq 0, \quad \delta\boldsymbol{\lambda}_T \in \mathcal{M}_T. \tag{3.44}$$

$\mathcal{M}_T$ is a functional space that ensures that the tangential Langrange multipliers satisfy the Coulomb model in a weak sense [173, 183]. In terms of inclusions Eq. (3.43) are written [188–191]

$$\mathrm{d}\mathbf{g}_T \in \partial\psi_{C(\lambda_N)}(\boldsymbol{\lambda}_T) \quad \text{or} \quad \boldsymbol{\lambda}_T \in \partial\psi^*_{C(\lambda_N)}(\mathrm{d}\mathbf{g}_T). \tag{3.45}$$

The contact laws that were formulated in this section, be it their pointwise explicit form in Eqs. (3.40) and (3.43), the inclusions from Eqs. (3.42) and (3.45) or the weak variational inequalities (3.41) and (3.44) have to be verified by the solution while satisfying the equilibrium in Eq. (3.33).

3.2.3 Numerical treatment of the slip increment

In quasi-static simulations a pseudo-time $t \in \mathbb{R}^+$ is introduced and the solution procedure consists in finding static equilibria at each discrete pseudo-time instant $t_0, t_1, ...t_f$. Given a known contact configuration from a previous equilibrium $\mathbf{H}_{LK,n} = \mathbf{H}_{LK}(t_n)$

we construct the tangential gap at a current load step t_{n+1} by applying a simple finite difference scheme that assumes the contact velocity $\mathbf{v}_{LK}^{K}$ constant for the duration of the load step. Starting from the definition in Eq. (3.7) and introducing Eq. (3.24):

$$\triangle\mathbf{g}_T(t_n, t_{n+1}) = \int_{t_n}^{t_{n+1}} \mathrm{d}\mathbf{g}_T = \mathbf{N}_T \int_{t_n}^{t_{n+1}} \mathrm{d}\boldsymbol{\pi}_{LK}^{K}. \tag{3.46}$$

The motion increment is related to the change in $\mathbf{H}_{LK}$ by the geometric finite difference formula involving the logarithm map akin to Eq. (2.67). This results in the following expression for the discretized tangential gap:

$$\begin{aligned}
&\triangle\mathbf{g}_T(t_n, t_{n+1}) \\
&\approx \mathbf{N}_T \log_{SE(3)}\left(\mathbf{H}_{LK,n}^{-1}\mathbf{H}_{LK,n+1}\right) \\
&= \mathbf{N}_T \log_{SE(3)}\left(\mathbf{H}_{LK,n}^{-1}\right) \\
&= -\begin{bmatrix}\mathbf{e}_2^T \\ \mathbf{e}_3^T\end{bmatrix} \mathbf{T}_{SO(3)}^{-T}(\boldsymbol{\theta})\mathbf{R}_{LK,n}^{T}\mathbf{x}_{LK,n}
\end{aligned} \tag{3.47}$$

where $\boldsymbol{\theta} = \log_{SO(3)}\left(\mathbf{R}_{LK,n}^{T}\right)$. Since the tangential gap only needs to be computed when the normal gap is closed we made use of the fact that $g_{N,n+1} = 0$ implies $\mathbf{H}_{LK,n+1} = \mathbb{I}_{4\times4}$. This can be shown by combining Eqs. (3.15), (3.16), (3.20) and setting Eq. (3.22) to zero.

Note that $\mathbf{H}_{LK,n}$ denotes the relative configuration between the two contact frames $\{L\}$ and $\{K\}$ evaluated at the current material points s_1 and s_2. These material points are defined from the projection Eq. (3.10) at instant t_{n+1}. It is computed as follows

$$\mathbf{H}_{LK,n} = \mathbf{H}_{L,n+1}^{-1}\mathbf{H}_{C,n+1}\mathbf{H}_{C,n}^{-1}\mathbf{H}_{F,n}\mathbf{H}_{F,n+1}^{-1}\mathbf{H}_{K,n+1}. \tag{3.48}$$

Equation (3.48) takes a simple form for small load steps. In that case one can assume that $\mathbf{R}_{C,n} = \mathbf{R}_{C,n+1}$ and $\mathbf{R}_{F,n} = \mathbf{R}_{F,n+1}$ which yields:

$$
\begin{aligned}
\mathbf{H}_{LK,n} &= \begin{bmatrix} \mathbf{R}_{LK,n} & \mathbf{x}_{LK,n} \\ \mathbf{0}_{1\times 3} & 1 \end{bmatrix} \\
&= \begin{bmatrix} \mathbb{I}_{3\times 3} & \mathbf{R}_{L,n+1}^T \left[(\mathbf{x}_{C,n+1} - \mathbf{x}_{F,n+1}) - (\mathbf{x}_{C,n} - \mathbf{x}_{F,n}) \right] \\ \mathbf{0}_{1\times 3} & 1 \end{bmatrix}.
\end{aligned} \tag{3.49}
$$

Introducing Eq. (3.49) into Eq. (3.47) and using the definition of $\mathbf{R}_L$ in Eq. (3.14) we can write a simplified expression for the tangential gap at the level of the centerlines as

$$
\triangle \mathbf{g}_T = \begin{bmatrix} \mathbf{t}_{1,n+1}^T \left[(\mathbf{x}_{F,n+1} - \mathbf{x}_{C,n+1}) - (\mathbf{x}_{F,n} - \mathbf{x}_{C,n}) \right] \\ \mathbf{t}_{2,n+1}^T \left[(\mathbf{x}_{F,n+1} - \mathbf{x}_{C,n+1}) - (\mathbf{x}_{F,n} - \mathbf{x}_{C,n}) \right] \end{bmatrix}. \tag{3.50}
$$

By inspection we indeed notice that if the relative contact location has not moved along a given tangential direction the associated component of $\triangle \mathbf{g}_T$ vanishes. Conversely, if relative motion occured between two load steps, it will be captured by the quantity defined in Eq. (3.47). In what follows we will denote the discrete tangential gap $\triangle \mathbf{g}_T$ simply as $\mathbf{g}_T$ to lighten the presentation, but it should be kept in mind that it is a motion increment that depends on the previous and the current time step. From a practical point of view, we noticed that keeping $\mathbf{t}_{1,n+1}$ and $\mathbf{t}_{2,n+1}$ for the duration resulted in a more stable algorithm.

3.2.4 Slip-free rolling of two discs

In this section we do a simplified analysis to convince ourselves that a finite difference formula on $SE(3)$ provides an appropriate measure for the tangential slip for beams with circular cross-sections of equal radii. Let us consider two discs of radii $R_1 = R_2 = R$ and suppose a pure rolling motion. In such a case the tangential gap always remains zero. We will define $\tau = t_{n+1}$ and $\tau - \Delta\tau = t_n$.

A schematic drawing of the situation is given in Fig. 3.5a. At time τ the unique contact point where the frames $\{L\}$ and $\{K\}$ coincide is taken as the origin of the inertial frame. Without loss of generality we assume that body 1, on which the frame $\{L\}$ is attached, is fixed. Hence we have $\{L\}(\tau) = \{L\}(\tau - \Delta\tau) = \{K\}(\tau)$, located at the origin and with the same orientation. Therefore, we have

$$
\mathbf{H}_{LK}(\tau) = \mathbf{I}_{4\times 4}. \tag{3.51}
$$

The only non trivial information that we still need for the computation of a tangential slip is the location and orientation of the frame $\{K\}(\tau - \Delta\tau)$. It corresponds to the material point on body 2 that is in contact at time τ, but evaluated at a previous time instant $\tau - \Delta\tau$. If body 2 has rolled over body 1 by an angle θ over the duration $\Delta\tau$, the location of $\{K\}(\tau - \Delta\tau)$ is given by

$$\mathbf{x}_K(\tau - \Delta\tau) = \begin{bmatrix} -R - 2R\cos(\theta) + R\cos(\pi - 2\theta) \\ -2R\sin(\theta) + R\sin(\pi - 2\theta) \\ 0 \end{bmatrix} \tag{3.52}$$

and the relative orientation of the contact frames at the previous step is simply

$$\mathbf{R}_{LK}(\tau - \Delta\tau) = \exp_{SO(2)}(2\theta)\,. \tag{3.53}$$

We compare three different tangential slip measures to this exact analytical solution. These are the approximation $\Delta\mathbf{x}_{LK}$ in Eq. (3.50), the geometric finite difference for on $SE(3)$ formulation in frame $\{K\}$ as defined in Eq. (3.47) and the alternative $SE(3)$ formulation expressed in frame $\{K\}$ which can be obtained through a similar discretization procedure. Results are shown in Fig. 3.5b. There are two important points to highlight here. As expected, for small rotation increments all slip measures collapse onto the exact one and hence the simplification in Eq. (3.50) is justified. Unlike the approximation $\Delta\mathbf{x}_{LK}$ the tangential slip measures obtained from a finite difference on $SE(3)$ as computed in Eq. (3.47) match the exact one for two circular discs with equal cross-section radii also in the large rotation case.

3.3 Spatial discretization

In this section we present two methods for discretizing the contact forces and constraints such that they may be implemented in a computer algorithm. We start in Sec. 3.3.1 by a straighforward collocation method. Such an approach is attractive due to its simplicity and modularity. However, it suffers from certain drawbacks:

- Potential locking or over-constraint.
- High sensitivity to the number and distribution of contact points.
- Difficulties to deal with sliding over nonsmooth surfaces.

Still, when employed with some precautions it yields reasonable results that would

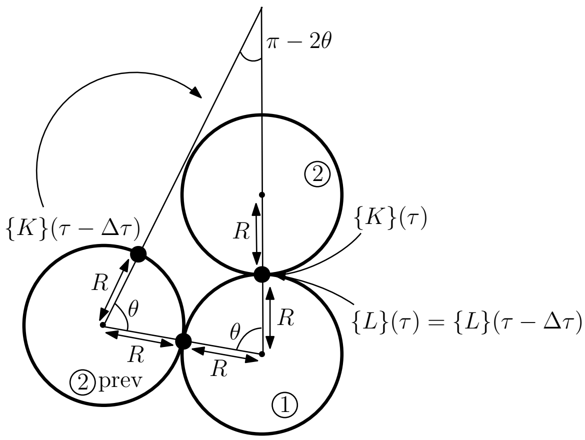

(a) Geometry and notations considered for analytic example. Two discs of equal radii.

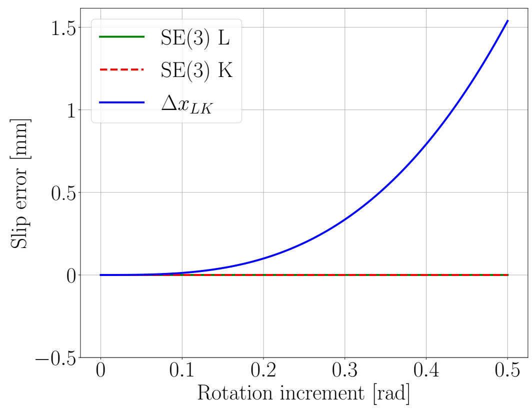

(b) Comparison of different ways of computing the slip increment. Here for a cross-section radius of $R = 1$[cm].

Figure 3.5: Pure rolling example.

probably be sufficiently accurate for many practical applications. Collocation techniques have already been employed for line-to-line contact [49, 97], but never in the context of the local frame approach.

The simple collocation also opens the door towards more sophisticated discretization schemes that do not have the above mentioned issues, like the mortar finite element method that we present in Sec. 3.3.2. As mentioned in the introduction, mortar methods can be considered as the state of the art in the field of contact mechanics for general deformable bodies, but their application to beam-to-beam contact has not been attempted before.

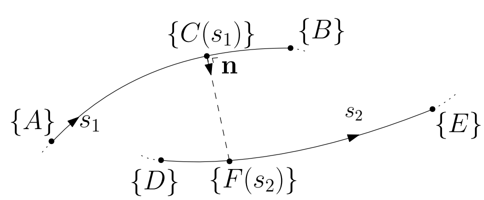

Figure 3.6: Notations for the contact element.

Suppose the two beams are discretized using the two-noded beam elements presented in the previous chapter, as seen in Figs. 3.2 and 3.6. We denote by q the set of all nodal variables. One contact element is composed of two beam elements i.e. of four nodes with six degrees of freedom each. Its configuration is given by a subset of q denoted

$$q_e = (\mathbf{H}_A, \mathbf{H}_B, \mathbf{H}_D, \mathbf{H}_E) \in SE(3)^4. \tag{3.54}$$

The infinitesimal motions are discretized as follows

$$\delta\boldsymbol{\pi}_C(s_1) = \underbrace{\mathbf{Q}(s_1, \mathbf{d}_{AB})}_{\mathbf{Q}_C} \delta\boldsymbol{\pi}_{e_1}, \tag{3.55a}$$

$$\delta\boldsymbol{\pi}_F(s_2) = \underbrace{\mathbf{Q}(s_2, \mathbf{d}_{DE})}_{\mathbf{Q}_F} \delta\boldsymbol{\pi}_{e_2} \tag{3.55b}$$

and collected in a 24×1 dimensional vector. We write the field of infinitesimal motion

$$\delta\boldsymbol{\pi}(s_1, s_2) = \mathbf{Q}_e \delta\boldsymbol{\pi}_e, \quad \mathbf{Q}_e = \begin{bmatrix} \mathbf{Q}_C & \mathbf{0} \\ \mathbf{0} & \mathbf{Q}_F \end{bmatrix}, \quad \delta\boldsymbol{\pi}_e = \begin{bmatrix} \boldsymbol{\pi}_A \\ \boldsymbol{\pi}_B \\ \boldsymbol{\pi}_D \\ \boldsymbol{\pi}_E \end{bmatrix}. \tag{3.56}$$

3.3.1 Collocation method

For ease of presentation and implementation, but also to decrease the risk of over-constraint we restrict ourselves to one single contact point per contact element located at $s_1 = s^c_{1,e}$ on the slave beam and $s_2 = s^c_{2,e}$ on the master. The question of how to obtain these contact points is deferred to a later section. Introducing Eq. (3.56) into Eq. (3.32) and evaluating the integral at the chosen collocation point yields after assembly

$$\begin{aligned}
\delta\mathcal{W}_c &= \sum_e (\delta\boldsymbol{\pi}_e)^T \mathbf{Q}_e^T(s^c_{1,e}, s^c_{2,e})\mathbf{G}^T(s^c_{1,e}, s^c_{2,e})\boldsymbol{\lambda}_e \\
&= \sum_e (\delta\boldsymbol{\pi}_e)^T \mathbf{G}_e^T \boldsymbol{\lambda}_e \\
&= \sum_e (\delta\boldsymbol{\pi}_e)^T \mathbf{f}_e^{\text{con}} \\
&= \delta\boldsymbol{\Pi}^T \mathbf{B}^T \boldsymbol{\Lambda} \\
&= \delta\boldsymbol{\Pi}^T \mathbf{f}^{\text{con}},
\end{aligned} \tag{3.57}$$

where $\boldsymbol{\lambda}_e = \begin{bmatrix} \lambda_N^e & \boldsymbol{\lambda}_T^e \end{bmatrix}^T$ is a discrete Lagrange multiplier associated to the elementwise constraint and $\boldsymbol{\Lambda}$ its assembled analogue. It gives the magnitude of the contact reaction forces (and moments). The orientation of these forces, expressed in the respective local frames of the beams, is given by what we identified as the elementwise discrete interpolated constraint gradient

$$\mathbf{G}_e = \mathbf{G}(s_{1,e}^c, s_{2,e}^c)\mathbf{Q}_e(s_{1,e}^c, s_{2,e}^c). \tag{3.58}$$

The vector $\delta\boldsymbol{\Pi}$ regroups all arbitrary nodal variations of the beam elements associated to the contact elements and $\mathbf{B}$ is the assembled constraint gradient matrix. The vector $\mathbf{f}^{\text{con}} = \mathbf{B}^T\boldsymbol{\Lambda}$ represents the discretized contact forces in the local frame. They enter the global equilibrium of forces in Eq. (2.79). Ignoring inertia terms yields the following equilibrium equations to be solved at each load step

$$\mathbf{f}(q) = \mathbf{f}^{\text{con}}(q, \boldsymbol{\Lambda}). \tag{3.59}$$

The normal contact law becomes

$$g_N^j \geq 0, \quad \lambda_N^j \geq 0, \quad g_N^j \lambda_N^j = 0, \quad \forall j = 1, 2, ..., N_C, \tag{3.60}$$

where N_C is the total number of discrete contact constraints. Note that here, since we only allow for a maximum of one contact constraint per beam element pair we have $j = e$. This switch of indices is introduced to match ulterior unified notations. The tangential constraints are: if $g_N^j \leq 0$, enforce

$$\mu\lambda_N^j - \|\boldsymbol{\lambda}_T^j\| \geq 0, \quad \|\mathbf{g}_T^j\| \left(\mu\lambda_N^j - \|\boldsymbol{\lambda}_T^j\|\right) = 0, \quad \forall j = 1, 2, ..., N_C \tag{3.61a}$$

$$\mathbf{g}_T^j \|\boldsymbol{\lambda}_T^j\| = -\|\mathbf{g}_T^j\| \boldsymbol{\lambda}_T^j. \tag{3.61b}$$

Contact point search

One simple choice of contact point is to fix $s_{1,e}^c = L_e/2$ on the slave beam and then find $s_{2,e}^c$ by projection onto the master beam for example as in Eq. (3.10). The procedure may be further simplified by considering the beam centerline as elementwise straight segments, in which case $s_{2,e}^c$ may be computed explicitely [192]. Although rather crude, this approach is often sufficient for test cases of moderate complexity, robust and fast. The literature on collision detection is vast and the intricacies of finding the best algorithms tailored to slender flexible structures are out of the scope of this thesis. However, their importance should not be underestimated. Actually, it is our belief that one of the secrets to large scale reliable simulations lies in proper collision detection. To that purpose we refer the interested reader to [12, 107, 193, 194].

3.3.2 Mortar method

In the mortar method, a key question is the choice of interpolation functions for the Lagrange multiplier field. The main criterion is the verification of the discrete inf-sup condition that guarantees stability of the saddle point formulation [156, 183]. Rigorous mathematical proofs for friction free small displacement contact problems exist showing that combining linear finite elements with linear interpolation functions for the Lagrange multipliers yields a stable mortar method [180]. Beyond that, the right interpolation functions are found by what scientists call "intuition informed trial and error". Since we use a first order interpolation in the Lie algebra in Eq. (2.68) we also use linear shape functions for the Lagrange multipliers. These are defined over the slave beam. In this thesis, the nodes of the slave beam and the nodes of the Lagrange multiplier field coincide as depicted in Fig. 3.2 and the notation is simplified accordingly. For one contact element one writes:

$$\boldsymbol{\lambda}(s_1) = \boldsymbol{\phi}_e(s_1)\boldsymbol{\lambda}_e, \tag{3.62a}$$

$$\delta\boldsymbol{\lambda}(s_1) = \boldsymbol{\phi}_e(s_1)\delta\boldsymbol{\lambda}_e, \tag{3.62b}$$

where $\boldsymbol{\lambda}_e = \begin{bmatrix}\lambda_{N,A} & \boldsymbol{\lambda}_{T,A}^T & \lambda_{N,B} & \boldsymbol{\lambda}_{T,B}^T\end{bmatrix}^T$ and $\delta\boldsymbol{\lambda}_e = \begin{bmatrix}\delta\lambda_{N,A} & \delta\boldsymbol{\lambda}_{T,A}^T & \delta\lambda_{N,B} & \delta\boldsymbol{\lambda}_{T,B}^T\end{bmatrix}^T$ are vectors that collect the nodal values of the Lagrange multipliers for contact element e and their variations respectively. The interpolation matrix is given by

$$\boldsymbol{\phi}_e(s_1) = \begin{bmatrix} 1-\dfrac{s_1}{L_e} & 0 & 0 & \dfrac{s_1}{L_e} & 0 & 0 \\ 0 & 1-\dfrac{s_1}{L_e} & 0 & 0 & \dfrac{s_1}{L_e} & 0 \\ 0 & 0 & 1-\dfrac{s_1}{L_e} & 0 & 0 & \dfrac{s_1}{L_e} \end{bmatrix}. \tag{3.63}$$

The discretized version of the virtual work produced by the contact forces is obtained by replacing the continuous fields involved in formulation (3.32) by their finite dimensional counterparts. The contribution of one element writes

$$
\begin{aligned}
\delta\mathcal{W}_{c,e} &= (\delta\boldsymbol{\pi}_e)^T \left[\int_{\gamma_c} \mathbf{Q}_e^T \mathbf{G}^T \boldsymbol{\phi}_e \,\mathrm{d}\gamma\right] \boldsymbol{\lambda}_e \\
&= (\delta\boldsymbol{\pi}_e)^T \, \mathbf{G}_e^T \boldsymbol{\lambda}_e \\
&= (\delta\boldsymbol{\pi}_e)^T \, \mathbf{f}_e^{\mathrm{con}}.
\end{aligned} \tag{3.64}
$$

These are assembled in standard finite element fashion

$$
\begin{aligned}
\delta\mathcal{W}_c &= \sum_e \delta\mathcal{W}_{c,e} \\
&= \delta\boldsymbol{\Pi}^T \mathbf{B}^T \boldsymbol{\Lambda} \\
&= \delta\boldsymbol{\Pi}^T \mathbf{f}^{\mathrm{con}}.
\end{aligned} \tag{3.65}
$$

The local (weak) constraint gradient of the contact element was identified as

$$
\mathbf{G}_e^T = \int_{\gamma_c} \mathbf{Q}_e^T \mathbf{G}^T \boldsymbol{\phi}_e \,\mathrm{d}\gamma \tag{3.66}
$$

and we denoted the global weighted constraint gradient $\mathbf{B}$. Similar to the collocation approach, it expresses the orientation of the weighted nodal contact forces and moments in the respective local frames of the beam centerlines. As a consequence, $\mathbf{f}^{\mathrm{con}} = \mathbf{B}^T\boldsymbol{\Lambda}$ represents the associated weighted forces and moments. They are simply added to Eq. (2.79). We reused the definition of the vector $\delta\boldsymbol{\Pi}$ that contains all the arbitrary nodal position and rotation variations and of $\boldsymbol{\Lambda}$ that collects the nodal values of the Lagrange multiplier field. Note that here their unit is a force per unit length.

Numerical integration of the constraint gradient

The integral in (3.66) has moving boundaries. Indeed $\gamma_c = [s_a, s_b]$, is configuration dependent. In this section we show how to compute this integral using Gauß points. First the mapping $\zeta(\eta) : [-1, 1] \to [s_a, s_b] : \eta \to s_1$ is introduced to rescale the integral. Its expression is

$$
\zeta(\eta) = \frac{1}{2}(1-\eta)\, s_a^e + \frac{1}{2}(1+\eta)\, s_b^e \tag{3.67}
$$

and the associated jacobian is given by

$$J_{nat} = \frac{s_b^e - s_a^e}{2}. \tag{3.68}$$

Integral (3.66) is then computed as

$$\begin{aligned}\mathbf{G}_e &= \int_{-1}^{1} \mathbf{Q}_e^T\left(\zeta\left(\eta\right)\right)\mathbf{G}^T\left(\zeta\left(\eta\right)\right)\boldsymbol{\phi}_e\left(\zeta\left(\eta\right)\right) J_{nat}\left(s_a, s_b, \eta\right)\, \mathrm{d}\eta & (3.69)\\ &\approx \sum_{k=1}^{N_{G_p}} w_k \mathbf{Q}_e^T\left(\zeta\left(\eta_k\right)\right)\mathbf{G}^T\left(\zeta\left(\eta_k\right)\right)\boldsymbol{\phi}_e\left(\zeta\left(\eta_k\right)\right) J_{nat}. & (3.70)\end{aligned}$$

The integration boundaries s_a and s_b are found through the projection procedure described in Eq. (3.12). Similarly, in Eq. (3.70), the projection explained in Eq. (3.10) is used to associate points on the master beam to Gauss points on the slave beam, where the integration is performed. In practice a number of integration points $N_{G_p} = 2$ is sufficient as it allows for exact integration of polynomials up to order 3. Other integrals involved in the formulation are computed in the same manner.

Discrete mortar kinematics

Now that we know how to compute the contact forces we turn our attention to the contact kinematics. To derive the normal mortar gap one starts from the weak variational inequality in Eq. (3.41) and introduces the discrete fields therein

$$\begin{aligned}\delta\mathcal{W}_N &= \sum_e \left(\delta\boldsymbol{\lambda}_{N,e} - \boldsymbol{\lambda}_{N,e}\right)^T \left[\int_{\gamma_c} \boldsymbol{\phi}_{N,e}^T g_N \,\mathrm{d}\gamma_c\right]\\ &= \sum_e \left(\delta\boldsymbol{\lambda}_{N,e} - \boldsymbol{\lambda}_{N,e}\right)^T \mathbf{g}_{N,e}^{\mathrm{con}}\\ &= \left(\delta\boldsymbol{\Lambda}_N - \boldsymbol{\Lambda}_N\right)^T \mathbf{g}_N^{\mathrm{con}} \geq 0, \quad \forall\delta\boldsymbol{\Lambda}_N \in \mathcal{M}_N, \end{aligned} \tag{3.71}$$

where we reused $\mathcal{M}_N$ to denote the space of admissible discrete normal Lagrange multiplier. For a formal definition see [173, 183]. Since the shape functions are linear, each contact element has exactly two contributions to the global (assembled) normal vector of weighted normal constraints $\mathbf{g}_N^{\text{con}}$

$$\mathbf{g}_{N,e}^{\text{con}} = \int_{\gamma_c} \boldsymbol{\phi}_{N,e}^T g_N \, \mathrm{d}\gamma_c. \tag{3.72}$$

With $\boldsymbol{\phi}_{N,e} = \left[1 - \dfrac{s_1}{L_e} \quad \dfrac{s_1}{L_e}\right]$, the block of shape functions associated to the normal Lagrange multipliers of element e is meant. The vectors $\boldsymbol{\Lambda}_N$ and $\delta\boldsymbol{\Lambda}_N$ are the complementary global nodal vectors of normal Lagrange multipliers and their arbitrary variations. Eq. (3.71) is a finite dimensional variational inequality [195]. It can equivalently be broken down into individual conditions of the exact same form as Eq. (3.60). The subtle differences are the following:

- The g_N^j are the components of $\mathbf{g}_N^{\text{con}}$. The discrete normal gaps that the mortar method wants to set to zero in the case of contact are weighted integrals. Locally penetration is allowed. Instead of checking penetration at certain localized points, the information is smeared over the element. This ensures a variationally consistent enforcement of constraints and gives the mortar method its theoretical advantageous numerical properties, such as the preservation of spatial convergence rates in the presence of contact.

- The λ_N^j are the components of $\boldsymbol{\Lambda}_N$. They are the nodal values of the Lagrange multipliers. Since we interpolate with linear shape functions, a sufficient condition for the normal Lagrange multiplier field to be positive everywhere is for the nodal values to be positive which is what the normal discrete mortar constraint expresses.

- As opposed to the collocation method, the number of constraints N_C is not arbitrary. Rather it is a consequence of the finite element space chosen for the discretisation of the Lagrange multipliers. This makes sure that the right amount of constraints are enforced by the method to avoid locking and over-constraint. In the present case N_C is simply the number of slave beam nodes.

We proceed exactly the same way to derive the tangential mortar slip increment. Eq. (3.44) becomes

$$
\begin{aligned}
\delta\mathcal{W}_T &= \sum_e \left(\delta\boldsymbol{\lambda}_{T,e} - \boldsymbol{\lambda}_{T,e}\right)^T \left[\int_{\gamma_c} \boldsymbol{\phi}_{T,e}^T \mathbf{g}_T \,\mathrm{d}\gamma\right] \\
&= \sum_e \left(\delta\boldsymbol{\lambda}_{T,e} - \boldsymbol{\lambda}_{T,e}\right)^T \mathbf{g}_{T,e}^{\text{con}} \\
&= \left(\delta\boldsymbol{\Lambda}_T - \boldsymbol{\Lambda}_T\right)^T \mathbf{g}_T^{\text{con}} \geq 0, \quad \forall \delta\boldsymbol{\Lambda}_T \in \mathcal{M}_T.
\end{aligned} \tag{3.73}
$$

The introduced notations have the same meaning as for the normal case, but adapted to the tangential components of the different vectors and matrices. In particular, $\mathcal{M}_T$ denotes the space of admissible discrete tangential Lagrange multipliers. The attention is brought to the fact that the discrete tangential slip measure is also an integrated and assembled quantity within the mortar method. Each element contributes with

$$
\mathbf{g}_{T,e}^{\text{con}} = \int_{\gamma_c} \boldsymbol{\phi}_{T,e}^T \mathbf{g}_T \,\mathrm{d}\gamma. \tag{3.74}
$$

The vector $\mathbf{g}_T^{\text{con}}$ contains the assembled weighted tangential slip and we stack the two components associated to the slave node j in $\mathbf{g}_T^j$. Likewise, $\boldsymbol{\lambda}_T^j$ contains the two tangential components of $\boldsymbol{\Lambda}_T$ associated to node j and we defined tangential shape functions as

$$
\boldsymbol{\phi}_{T,e} = \begin{bmatrix} 1 - \dfrac{s_1}{L_e} & 0 & \dfrac{s_1}{L_e} & 0 \\ 0 & 1 - \dfrac{s_1}{L_e} & 0 & \dfrac{s_1}{L_e} \end{bmatrix}.
$$

The finite dimensional variational inequality in Eq. (3.73) is equivalent to the discrete KKT-conditions of the same form as Eq. (3.61).

Additional notations concerning the constraint gradient matrix

The assembled (weighted in the case of mortar) constraint gradient matrix $\mathbf{B}^T$ has dimensions $6N_{Sl,C} \times 3N_C$, where $N_{Sl,C}$ is the total number of slave nodes involved in the beam elements for which contact elements were created. Each beam finite element node has 6 degrees of freedom and the Lagrange multipliers associated to each constraint have 3 components. The number of discrete contraints N_C is arbitrary in the case of the collocation method. For the mortar method with linear shape functions it is exactly equal to the number of slave beam finite element nodes $N_C = N_{Sl,C}$ included in the potential contact region.

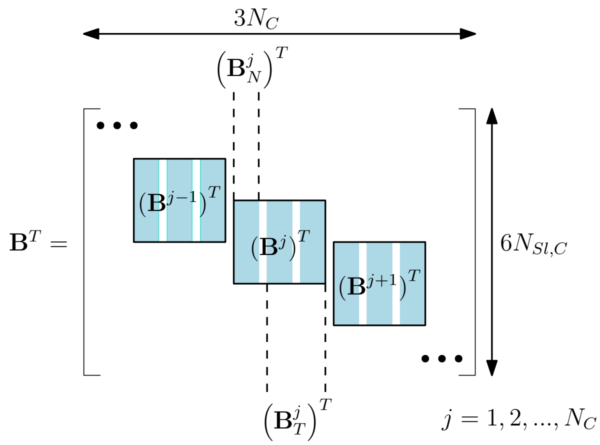

Figure 3.7: Structure of the assembled constraint gradient matrix and notations.

The Lagrange multiplier $\boldsymbol{\lambda}^j$ is associated to the gaps[4] $\mathbf{g}^{\text{con},j} = \left[g_N^j \quad \left(\mathbf{g}_T^j\right)^T\right]^T$, which we regrouped in the vector $\mathbf{g}^{\text{con}}$, and are related to a certain number of nodal degrees of freedom schematically illustrated via the non-vanishing vertical overlap of the assembled constraint gradient matrix blocks $\left(\mathbf{B}^j\right)^T$ as depicted in Fig. 3.7. The extension of the overlap depends upon which beam elements contribute to a given mortar constraint. We also split the individual blocks into normal $\left(\mathbf{B}_N^j\right)^T$ and tangential parts $\left(\mathbf{B}_T^j\right)^T$.

For the collocation approach we simply have $\mathbf{B}^j = \mathbf{G}_e$ and we consider $j = e$. It is slightly more complicated for the mortar method. In that case we have

$$\left(\mathbf{B}^j\right)^T = \int_{\gamma_C} \left(\mathbf{Q}^j\right)^T \mathbf{G}^T \boldsymbol{\phi}^j \, \mathrm{d}\gamma. \tag{3.75}$$

In what follows the reader has to be aware of some notational subtleties. We write $\boldsymbol{\phi}^j$ the shape function of the Lagrange multiplier field associated to the slave node j which is not exactly the same as $\boldsymbol{\phi}_e$ which is the shape function associated to the Lagrange multiplier field over the contact finite element e. It has local support over slave elements adjacent to node j, meaning that the contribution to the integral of non-adjacent elements is always zero. Similarly, using a slight abuse of notation, by $\mathbf{Q}^j$ the interpolation functions of the beam elements involved in the assembly of the constraint at slave node j is meant. At each load step a system of nonlinear equations with inequality constraints has to be solved for the unknowns q and $\boldsymbol{\Lambda}$.

[4] assembled in the case of mortar

Compact notation of the discrete contact problem

Using the notation in terms of inclusions introduced in Eqs. (3.42) and (3.45) the discrete contact to be solved a each load step can be written

$$
\begin{aligned}
&\mathbf{f}(q) + \mathbf{f}^{\text{con}}(q, \boldsymbol{\Lambda}) = \mathbf{0}, \\
&g_N^{\text{con},j} \in \partial\psi_{\mathbb{R}^-}(\lambda_N^j), \\
&\mathbf{g}_T^{\text{con},j} \in \partial\psi_{C(\lambda_N^j)}(\boldsymbol{\lambda}_T^j), \quad \forall j = 1, 2, ..., N_C.
\end{aligned} \tag{3.76}
$$

with $\mathbf{f}^{\text{con}}(q, \boldsymbol{\Lambda}) = \mathbf{B}^(q)\boldsymbol{\Lambda}$ Note that in the dynamic case a similar discrete contact problem appears after time discretization. It is thus a fundamental building block of any contact solution algorithm.

3.4 Contact solvers

At this stage it is still possible to regularize, or smoothen, the problem by introducing penalty type constitutive laws at the contact interface. The main advantage being the removal of the inequality constraints which allows the use of standard nonlinear equation solvers. This is especially useful in practical (meaning industrial) applications, as most of the time new developments in simulation codes should be non intrusive, for example when adding contact to an existing code, and robust i.e. one rarely implements a solver by oneself. For smoothed formulations of beam-to-beam contact see [97, 102, 104, 105] and for an implementation of a regularized approach in the context of mortar finite elements with beam-to-beam contact see [196].

In this work we follow a different philosophy. The contact remains unregularized, or nonsmooth, and specialized solution algorithms need to be applied. As loosely shown through in the previous section there are different equivalent mathematical formulations of the discrete contact problem. We started with an explicit formulation of the contact constraints. These could be equivalently written as variational inequalities and inclusion problems. Other equivalent formulations exist, such as quasi-variational inequalities, nonsmooth equations and optimization problems. Each allows the use of different types of solution schemes with their advantages and disadvantages. Usually a choice is made through a tradeoff between speed, robustness and ease of implementation. Sometimes, the existence of certain mathematical properties is also a criterion. Mathematicians did extensive research in the linearized case. Indeed, such a simplified setting helps to prove well-posedness of formulations and convergence of different algorithms. For a review on these methods the reader is referred to [197] and the references therein. Part I of Daviet's thesis [108] is also an interesting read on this topic. The study of linear methods is highly relevant to us, since oftentimes nonlinear solvers are based on iterative schemes where a sequence of *linearized equations* is solved. Thus the core of every approach is finding the solution to a linearized discrete contact problem. Alternatively, certain methods that only have convergence proofs when applied to linear problems are still applicable in the nonlinear case, there is simply no guarantee that a solution will be found.

The exact derivation and the linearized equations that are ultimately solved may differ from approach to approach. For information and because it opens the door to the application of the tools in the references above, let us derive the reduced linearized version of Eq. (3.76) in the next section.

3.4.1 Linearized discrete contact problem

Given an equilibrium configuration $(q_k, \mathbf{\Lambda}_k)$ at iteration k of an iterative method, we are looking for a solution $(q_{k+1}, \mathbf{\Lambda}_{k+1})$. The subscript k denotes a function evaluation at step k. For example: $\mathbf{f}^{\text{con}}_k = \mathbf{f}^{\text{con}}(q_k, \mathbf{\Lambda}_k)$. First, the contact force is linearized around $(q_k, \mathbf{\Lambda}_k)$:

$$\begin{aligned} \mathbf{f}^{\text{con}}_{k+1} &= \mathbf{f}^{\text{con}}_k + \cancel{\left(\frac{\partial \mathbf{B}}{\partial q}\right)^T_k} \mathbf{\Lambda}_k \mathbf{T}_k \Delta \boldsymbol{\alpha}_{k+1} + \mathbf{B}^T_k (\mathbf{\Lambda}_{k+1} - \mathbf{\Lambda}_k) \\ &= \mathbf{B}^T_k \mathbf{\Lambda}_{k+1}, \end{aligned} \tag{3.77}$$

where we used the expression of the contact force in Eq. (3.57) or Eq. (3.65) and where the crossed out term which represents the second derivative of the constraints is neglected and considered zero in linearized dynamics. We also observe the emergence of the tangent operator of the exponential map on $SE(3)^N$ evaluated at iteration k and denoted $\mathbf{T}_k = \mathbf{T}_{SE(3)^N}(\boldsymbol{\alpha}_k)$ as a consequence of Eq. (2.18). The second step is the linearization of the internal and external forces around q_k:

$$\mathbf{f}_{k+1} = \mathbf{f}_k + \mathbf{K}_{T,k} \mathbf{T}_k \Delta \boldsymbol{\alpha}_{k+1} \tag{3.78}$$

and finally the linearization of the constraint vector around q_k:

$$\mathbf{g}_{k+1}^{\text{con}} = \mathbf{g}_k^{\text{con}} + \mathbf{B}_k \mathbf{T}_k \Delta\boldsymbol{\alpha}_{k+1}. \tag{3.79}$$

Introducing these linearized expressions back into Eq. (3.76) yields the following linearized frictional contact problem:

$$\begin{aligned}
&\mathbf{f}_k + \mathbf{K}_{T,k}\mathbf{T}_k\Delta\boldsymbol{\alpha}_{k+1} + \mathbf{B}_k^T\boldsymbol{\Lambda}_{k+1} = \mathbf{0},\\
&\mathbf{g}_{k+1}^{\text{con}} = \mathbf{g}_k^{\text{con}} + \mathbf{B}_k\mathbf{T}_k\Delta\boldsymbol{\alpha}_{k+1},\\
&g_{N,k+1}^{\text{con},j} \in \partial\psi_{\mathbb{R}^-}(\lambda_{N,k+1}^j),\\
&\mathbf{g}_{T,k+1}^{\text{con},j} \in \partial\psi_{C(\lambda_N^j)}(\boldsymbol{\lambda}_{T,k+1}^j), \quad \forall j = 1,2,...,N_C.
\end{aligned} \tag{3.80}$$

where $\mathbf{K_T}$ is the tangent stiffness matrix (see Chapter 2). We call this formulation the linearized frictional contact problem. To be exact, only the equilibrium equation and the contact kinematics are linearized. The contact laws are kept in their nonlinear form. The system of equations needs to be solved for $\mathbf{g}_{k+1}^{\text{con}}$, $\boldsymbol{\Lambda}_{k+1}$ and $\Delta\boldsymbol{\alpha}_{k+1}$. In the following we list the main classes of techniques applicable to the statement in Eq. (3.80):

- **Facetted friction cone**: The friction cone $C(\lambda_N^j)$ is approximated by a facetted pyramid such that the frictional contact laws become linear which allows for a simplified treatment. The reformulation results in a linear complementarity problem (LCP) and can then be solved by a variety of techniques [198]. The obvious drawback is the modification of the model. A solution to the facetted Coulomb problem is not always a good approximation of the original one. Moreover, the number of constraints increases with the number of facets. Note that the frictionless problem is also an LCP.

- **Optimization**: The discrete Coulomb friction problem in Eq. (3.80) can be reformulated into a nonsmooth and nonconvex optimization problem. Since it is difficult to solve, the general idea of optimization based methods is to find associated, well-posed and well-understood optimization sub-problems that are solved sequencially [199–201].

- **Fixed point methods for variational inequalities**: Eq. (3.80) is equivalently written as a variational inequality. Then, an associated nonsmooth function is introduced whose roots correspond to solutions of said variational inequality and a classical fixed point algorithm is applied [202, 203].

- **Semismooth Newton methods**: One introduces a nonsmooth function whose roots correspond to the solution of Eq. (3.80) and applies a Newton method. Since the function is nonsmooth, the Jacobian from the standard Newton-Raphson method is replaced by the generalized Jacobian. The most popular are the complementarity function used by Wohlmuth [179, 183], the Fischer-Burmeister [204] function and the one introduced by Alart and Curnier [187]. These functions are also applicable when the equilibrium equations are nonlinear as in the formulation in Eq. (3.76). In that case, the Newton method solves the nonlinearity stemming from the equilibrium of forces and the Coulomb constraints monolithically. The latter methodology is often employed in the field of computational mechanics when dealing with contact between general deformable bodies.

In this section we have derived the linearized frictional contact problem as it opens the door to a wide range of well-studied solution algorithms. We will present two methods in the following sections that solve Eq. (3.76). In Sec. 3.4.2 we present the dual formulation of the linearized contact problem which would allow the use of a robust Gauß-Seidel algorithm. In Sec. 3.4.3 we present a Augmented Lagrangian formulation of the fully nonlinear system combined with an efficient monolithic nonsmooth Newton method which is described in Sec. 3.4.4.

3.4.2 Dual formulation and Gauß-Seidel algorithm

In [49] Daviet et al. argue that a highly robust solution strategy is necessary for the upscaling of beam-to-beam contact problems to a large number of fibers. Prior tests led them to conclude that a monolithic nonsmooth Newton methods works well for systems with a limited number of contacts, but often fails to converge in the case of over-constraint systems such as densely packed fiber assemblies [107]. Therefore, they developed a specialized hybrid Gauß-Seidel algorithm which splits the solution procedure into a series of local one-contact Coulomb friction problems. They solve the local Coulomb friction problem by applying a Fischer-Burmeister formulation with an analytical fail-safe to ensure the robustness of the method. In the following we will develop the theoretical framework necessary for the application of the Gauß-Seidel algorithm to our formulation of beam-to-beam contact. To that end, we will cast the system in Eq. (3.80) into a form that is suitable for a Gauß-Seidel type approach. See appendix 4.5 for a description of the classical Gauß-Seidel technique for linear systems of equations.

Premultiplying Eq. (3.80) by $\mathbf{B}_k \mathbf{K}_{T,k}^{-1}$ to eliminate $\Delta\boldsymbol{\alpha}_{k+1}$ and the tangent operator yields the following dual frictional contact problem:

$$
\begin{aligned}
&\mathbf{g}_{k+1}^{\text{con}} = \mathbf{D}_k \boldsymbol{\Lambda}_{k+1} + \mathbf{b}_k, \\
&g_{N,k+1}^{\text{con},j} \in \partial \psi_{\mathbb{R}^-}(\lambda_{N,k+1}^j), \\
&\mathbf{g}_{T,k+1}^{\text{con},j} \in \partial \psi_{C(\lambda_N^j)}(\boldsymbol{\lambda}_{T,k+1}^j), \quad \forall j = 1, 2, ..., N_C.
\end{aligned} \tag{3.81}
$$

We have defined the Delassus operator

$$
\mathbf{D} = -\mathbf{B}\mathbf{K}_T^{-1}\mathbf{B}^T \tag{3.82}
$$

and the vector

$$
\mathbf{b} = \mathbf{g}^{\text{con}} - \mathbf{B}\mathbf{K}_T^{-1}\mathbf{f}. \tag{3.83}
$$

These two depend on q_k and are thus fixed. The problem may now be solved for $\mathbf{g}_{k+1}^{\text{con}}$ and $\boldsymbol{\Lambda}_{k+1}$ directly.

The Delassus operator has a sparse block structure where each block $\mathbf{D}^{ij}$ describes the change of relative motion at contact number i due to a force applied at contact number j, see Fig. 3.7. This structure can be exploited by decomposing the Delassus operator as $\mathbf{D} = \mathbf{D}_L + \mathbf{D}_U$ where the lower diagonal part of the Delassus operator is $\mathbf{D}_L = \mathbf{D}_{i>=j}$ and its upper part $\mathbf{D}_U = \mathbf{D}_{i<j}$. The equations associated to the lower diagonal part are solved implicitly and the equations associated to the upper diagonal part of the Delassus operator are solved explicitly by a fixed point iteration:

$$
\begin{aligned}
&\mathbf{g}_{k+1}^{\text{con},j} = \mathbf{D}^{jj}\boldsymbol{\Lambda}_{k+1}^j + \sum_{i<j} \mathbf{D}^{ji}\boldsymbol{\Lambda}_{k+1}^i + \sum_{i>j} \mathbf{D}^{ji}\boldsymbol{\Lambda}_k^i + \mathbf{b}_k^j \\
&g_{N,k+1}^{\text{con},j} \in \partial \psi_{\mathbb{R}^-}(\lambda_{N,k+1}^j), \\
&\mathbf{g}_{T,k+1}^{\text{con},j} \in \partial \psi_{C(\lambda_N^j)}(\boldsymbol{\lambda}_{T,k+1}^j), \quad \forall j = 1, 2, ..., N_C.
\end{aligned} \tag{3.84}
$$

Moreover, each contact is resolved individually and then substituted into the yet unresolved equations. This results in a sequence of "one-contact problems" of the form:

$$
\begin{aligned}
\mathbf{g}^{\text{con},j} &= \mathbf{D}^{jj}\boldsymbol{\Lambda}^j + \bar{\mathbf{b}}^j \\
g_N^{\text{con},j} &\in \partial\psi_{\mathbb{R}^-}(\lambda_N^j), \\
\mathbf{g}_T^{\text{con},j} &\in \partial\psi_{C(\lambda_N^j)}(\boldsymbol{\lambda}_T^j).
\end{aligned} \tag{3.85}
$$

where $\mathbf{D}^{jj}$ is a 3×3 matrix. The solution to the problem statement in Eq. (3.85) is easier to find. Any of the methods mentioned in the previous section can be applied.

Daviet et al. implemented their hybrid Gauß-Seidel algorithm into their open source software so-bogus [205]. Odin features a connection to so-bogus which is adapted to rigid body contact elements. These contact elements are created dynamically via the third party collision detection software bullet [206]. Algorithm 2 describes the methodology we propose for solving the beam-to-beam contact problem. It combines Odin's Lie group framework with so-bogus' contact solver and has shown promising results for rigid body contact [207]. Odin currently lacks a dynamic collision detection algorithm for beam-to-beam contact. Beam-to-beam contact elements are created at the onset of the simulation and persist for the full duration of the simulation similar to the finite elements of the mechanical components. Therefore, a change in the datastructure of Odin's current beam-to-beam contact elements necessary before coding the actual Gauß-Seidel beam-to-beam contact elements. This could be addressed in future work.

Algorithm 2 $[q_{n+1}, \boldsymbol{\Lambda}_{n+1}] = \text{solveStaticLoadStepGS}(q_n)$

```
Λ_{n+1} := 0
α_{n+1} := 0                                              ▷ q_{n+1} = q_n
for k ∈ [1, MaxIter] do
    q_{n+1} := q_n exp_{SE(3)^N}(S(α_{n+1}))     ▷ Lie group update of the configuration
    compute r_f, r_c
    if Convergence(r_f) ∧ Convergence(r_c) then
        break
    end if
    compute D, b                                   ▷ Eqs. (3.82) and (3.83)
    Λ_{n+1} := so-bogus(D, b, MaxIterGS)           ▷ Use hybrid local solver in [49]
    compute Δα_{n+1}                               ▷ Eq. (3.80)
    α_{n+1} := α_{n+1} + Δα_{n+1}
end for
```

3.4.3 Augmented Lagrangian formulation

Introduced by Rockafellar [208] in the context of constrained optimization the augmented Lagrangian is a popular technique for solving variational inequalities such as they appear in computational contact mechanics applications [136, 171, 175, 187, 203, 209–211]. The reason is most likely that it has a sufficiently solid mathematical foundation, while at the same time allowing an intuitive and systematic treatment of contact constraints in mechanical systems. Indeed, it may simply be understood as additional nonsmooth energy terms contributing to the total potential energy of the system and where the final equations elegantly derive from. In a numerical context scaling and penalty parameters permit tuning to improve algorithmic performance without influencing the converged solution.

We will ignore the contributions not related to contact interactions from now on. To set up the augmented Lagrangian, we start by defining the augmented multipliers for normal and tangential directions.

$$\xi_N^j = k\lambda_N^j - p g_N^j, \quad \boldsymbol{\xi}_T^j = k\boldsymbol{\lambda}_T^j - p\mathbf{g}_T^j. \tag{3.86}$$

The original Lagrange multipliers are scaled by a factor $k > 0$ and p is a penalty coefficient whose meaning will become apparent right after. These parameters do not have to be identical in the normal and tangential direction, but we will consider them so for ease of presentation. The augmented Lagrangian functional is

$$\begin{aligned}\mathcal{L}(q, \boldsymbol{\Lambda}) = \sum_{j=1}^{N_C} &- k g_N^j \lambda_N^j + \frac{p}{2}(g_N^j)^2 - \frac{1}{2p}\mathrm{dist}^2\left[\xi_N^j, \mathbb{R}^+\right] \\ &- k\mathbf{g}_T^j \cdot \boldsymbol{\lambda}_T^j + \frac{p}{2}\|\mathbf{g}_T^j\|^2 - \frac{1}{2p}\mathrm{dist}^2\left[\boldsymbol{\xi}_T^j, C_{\xi_N^j}\right],\end{aligned} \tag{3.87}$$

where it is understood that the dependence on q is hidden in the gap and slip functions and the dependence on $\boldsymbol{\Lambda}$ is in the augmented multiplier. The function $\mathrm{dist}(\mathbf{a}, Z)$ computes the distance between a point $\mathbf{a} \in \mathbb{R}^n$ and a convex set Z [212]. The penalty terms proportional to p convexify the functional far from its optimum which improves convergence properties of iterative solution methods. The scaling factor k aims at improving the conditioning of the involved system matrices. For the normal direction we have

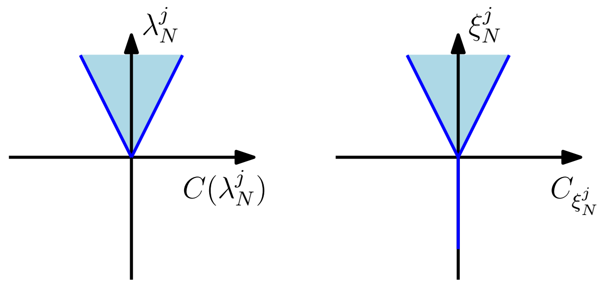

Figure 3.8: Schematic representation of the friction cone and the augmented friction cone.

$$\operatorname{dist}\left[\xi_N^j, \mathbb{R}^+\right] = \begin{cases} -\xi_N^j & \text{if } \xi_N^j < 0 \quad \text{no contact} \\ 0 & \text{if } \xi_N^j \geq 0 \quad \text{contact} \end{cases}. \tag{3.88}$$

In Eq. (3.87), $C_{\xi_N^j}$ is an augmented convex set allowing ξ_N^j to take negative values [187], see Fig. 3.8. In the tangential direction the term related to the distance function explicitly writes

$$\operatorname{dist}\left[\boldsymbol{\xi}_T^j, C_{\xi_N^j}\right] = \begin{cases} \boldsymbol{\xi}_T^j & \text{if } \xi_N < 0 \quad \text{no contact} \\ \boldsymbol{\xi}_T^j - \mu \xi_N^j \boldsymbol{\tau}^j & \text{if } \|\boldsymbol{\xi}_T^j\| \geq \mu \xi_N^j \quad \text{slip} \\ \mathbf{0} & \text{if } \|\boldsymbol{\xi}_T^j\| < \mu \xi_N^j \quad \text{stick} \end{cases}, \tag{3.89}$$

where $\boldsymbol{\tau}^j = \dfrac{\boldsymbol{\xi}_T^j}{\|\boldsymbol{\xi}_T^j\|}$ is the direction of tangential contact force which is opposed to the sliding motion.

A solution $(q, \boldsymbol{\Lambda})$ to Eq. (3.76)[5] is characterized by the stationarity condition:

$$\delta \mathcal{L}(q, \boldsymbol{\Lambda}) = 0. \tag{3.90}$$

The computation of the variation of the Lagrangian functional includes taking the variation of squared distance terms. These are in the normal direction

[5]Ignoring $\mathbf{f}$

$$\delta\left(\frac{1}{2p}\mathrm{dist}^2\left[\xi_N^j,\mathbb{R}^+\right]\right)=\begin{cases}\xi_N^j\delta\xi_N^j & \text{if } \xi_N^j<0 \quad \text{no contact}\\ 0 & \text{if } \xi_N^j\geq 0 \quad \text{contact}\end{cases}. \tag{3.91}$$

and in the tangential direction

$$\delta\left(\frac{1}{2p}\mathrm{dist}^2\left[\boldsymbol{\xi}_T^j,C_{\xi_N^j}\right]\right)=\begin{cases}\boldsymbol{\xi}_T^j\cdot\delta\boldsymbol{\xi}_T^j & \text{if } \xi_N<0 \quad \text{no contact}\\ \left(\|\boldsymbol{\xi}_T^j\|-\mu\xi_N^j\right)\boldsymbol{\tau}^j\cdot\delta\boldsymbol{\xi}_T^j & \text{if } \|\boldsymbol{\xi}_T^j\|\geq\mu\xi_N^j \quad \text{slip}\\ 0 & \text{if } \|\boldsymbol{\xi}_T^j\|<\mu\xi_N^j \quad \text{stick}\end{cases}. \tag{3.92}$$

Hence Eq. (3.90) becomes:

$$\begin{aligned}\delta\mathcal{L}(q,\boldsymbol{\Lambda})&=\sum_{j=1}^{N_C}\left[(\delta\boldsymbol{\pi}^j)^T \quad \lambda_N^j \quad \left(\delta\boldsymbol{\lambda}_T^j\right)^T\right]\mathbf{F}^{\mathcal{L},j}\\ &=\left[(\delta\boldsymbol{\Pi})^T \quad (\delta\boldsymbol{\Lambda})^T\right]\mathbf{F}^{\mathcal{L}}\\ &=0.\end{aligned} \tag{3.93}$$

Eq. (3.90) has to hold for all $(\delta\boldsymbol{\Pi},\delta\boldsymbol{\Lambda})$, which is true if

$$\mathbf{F}^{\mathcal{L}}(q,\boldsymbol{\Lambda})=\mathbf{0}. \tag{3.94}$$

The vector of generalized contact forces and constraints $\mathbf{F}^{\mathcal{L},j}$ is conjugated to the variation of the generalized degrees of freedom $\left[(\delta\boldsymbol{\pi}^j)^T \quad \lambda_N^j \quad \left(\delta\boldsymbol{\lambda}_T^j\right)^T\right]$ associated to the contact number j. It is assembled into the total vector of generalized forces and constraints $\mathbf{F}^{\mathcal{L}}$. We identified it as

$$
\mathbf{F}^{\mathcal{L},j}(q,\boldsymbol{\Lambda}) = \begin{bmatrix} \mathbf{F}^j \\ F_N^j \\ \mathbf{F}_T^j \end{bmatrix} = \begin{cases} \begin{bmatrix} \mathbf{0} \\ -\dfrac{k^2}{p}\lambda_N^j \\ -\dfrac{k^2}{p}\boldsymbol{\lambda}_T^j \end{bmatrix} & \text{if } \xi_N < 0 \quad \text{no contact} \\ \begin{bmatrix} -\left(\mathbf{B}_N^j\right)^T \xi_N^j - \mu \xi_N^j \left(\mathbf{B}_T^j\right)^T \boldsymbol{\tau}^j \\ -k g_N^j \\ -\dfrac{k}{p}\left(k\boldsymbol{\lambda}_T^j - \mu \xi_N^j \boldsymbol{\tau}^j\right) \end{bmatrix} & \text{if } \|\boldsymbol{\xi}_T^j\| \geq \mu \xi_N^j \quad \text{slip} \\ \begin{bmatrix} -\left(\mathbf{B}_N^j\right)^T \xi_N^j - \left(\mathbf{B}_T^j\right)^T \boldsymbol{\xi}_T^j \\ -k g_N^j \\ -k \mathbf{g}_T^j \end{bmatrix} & \text{if } \|\boldsymbol{\xi}_T^j\| < \mu \xi_N^j \quad \text{stick} \end{cases} . \tag{3.95}
$$

Eq. (3.94) is a nonlinear algebraic equation which has to be solved at each load step. The operator $\mathbf{F}^{\mathcal{L}}$ is only piecewise continuous, or semismooth, and therefore not differential everywhere [187]. Indeed, depending on the state of $\boldsymbol{\xi}^j$ it takes different values.

For instance, when the contact law number j indicates that there is no contact, no contribution is added to the equilibrium of forces and the scaled Lagrange multiplier in the normal and tangential direction are set to zero. When the contact is in a sliding state, a generalized normal contact force of magnitude ξ_N^j and in the direction of $\mathbf{B}_N^j$ contributes to the equilibrium of forces together with a friction force of a magnitude exactly equal to the friction treshold $\mu\xi_N^j$ and oriented along the direction $\mathbf{B}_T^j$. The scaled normal gap is forced to zero and the tangential Lagrange multipliers to the value taken by the frictional contact force. Finally, if the status of the constraint is stick, the full vectorial gap is zero and a contact force perpendicular to the constraints enters the equilibrium of forces.

At the singular points where the derivative of $\mathbf{F}^{\mathcal{L}}$ does not exist in the classical sense it possesses a so-called *generalized Jacobian*. The existence of this weaker notion of differentiability suffices to construct Newton type methods that solve Eq. (3.94) as we will show in Sec. 3.4.4.

3.4.4 Nonsmooth Newton Method

Many popular methods for solving constrained optimization problems such as the one derived in the previous section, decouple primal and dual variables such as Uzawa's algorithm [213] for example. They are based on a double loop in which the (augmented) Lagrange multiplier is kept fixed during an iteration of the outer loop to solve the nonlinear equation in the inner loop. Once the inner loop has converged the (augmented) Lagrangian multiplier is updated. These methods are stable, but converge rather slowly.

In this thesis, we go for a monolithic treatment of the primal and dual variables by means of a Newton type approach. As nicely explained by Qi and Sun in [214], the Newton-Raphson method for solving a set of nonlinear equations can be generalized to a nonsmooth setting by using the generalized Jacobian instead of the derivative. They also prove local convergence of order $p \in]1, 2]$ for such a nonsmooth Newton method when applied to augmented Lagrangian formulations.

Algorithm 3 $[q_{n+1}, \boldsymbol{\Lambda}_{n+1}] = \text{solveStaticLoadStep}(q_n)$

$\boldsymbol{\Lambda}_{n+1} \coloneqq \mathbf{0}$
$\boldsymbol{\alpha}_{n+1} \coloneqq \mathbf{0}$ ▷ $q_{n+1} = q_n$
for $k \in [1, \text{MaxIter}]$ **do**
 $\boxed{q_{n+1} \coloneqq q_n \exp_{SE(3)^N}(S(\boldsymbol{\alpha}_{n+1}))}$ ▷ Lie group update of the configuration
 compute $\mathbf{r}_f$, $\mathbf{r}_c$
 if Convergence($\mathbf{r}_f$) $\wedge$ Convergence($\mathbf{r}_c$) **then**
  break
 end if
 $\boxed{\text{compute } \mathbf{S}_t \in \partial \mathbf{F}^{\mathcal{L}}}$ ▷ Generalized Jacobian in subdifferential of $\mathbf{F}^{\mathcal{L}}$
 $\begin{bmatrix} \Delta\boldsymbol{\alpha}_{n+1} \\ \Delta\boldsymbol{\Lambda}_{n+1} \end{bmatrix} \coloneqq -\mathbf{S}_t^{-1} \begin{bmatrix} \mathbf{r}_f \\ \mathbf{r}_c \end{bmatrix}$
 $\boldsymbol{\alpha}_{n+1} \coloneqq \boldsymbol{\alpha}_{n+1} + \Delta\boldsymbol{\alpha}_{n+1}$
 $\boldsymbol{\Lambda}_{n+1} \coloneqq \boldsymbol{\Lambda}_{n+1} + \Delta\boldsymbol{\Lambda}_{n+1}$
end for

Alg. 3 describes a Lie group version of the nonsmooth Newton method applicable in the context of the static simulation of multibody systems with rotational degrees of freedom involving contact constraints. Given the configuration at the previous load step $q_n = q(t_n)$ it computes the current configuration $q_{n+1} = q(t_{n+1})$ and the Lagrange multiplier $\boldsymbol{\Lambda}_{n+1} = \boldsymbol{\Lambda}(t_{n+1})$. Here, the residual for the equilibrium of forces $\mathbf{r}_f$ is obtained by stacking the $\mathbf{F}^j$ in Eq. (3.95)

$$\mathbf{r}_f = \begin{bmatrix} \vdots \\ \mathbf{F}^j(q_{n+1}, \boldsymbol{\Lambda}_{n+1}) \\ \vdots \end{bmatrix} \tag{3.96}$$

and the residual for the constraints is

$$\mathbf{r}_c = \begin{bmatrix} \vdots \\ F_N^j(q_{n+1}, \boldsymbol{\Lambda}_{n+1}) \\ \mathbf{F}_T^j(q_{n+1}, \boldsymbol{\Lambda}_{n+1}) \\ \vdots \end{bmatrix}. \tag{3.97}$$

The remaining part of this section will exclusively be concerned with computing the generalized Jacobian $\mathbf{S}_t$. Roughly speaking it is obtained by simply taking the classical derivative where $\mathbf{F}^{\mathcal{L}}$ is differentiable and picking the derivatives of one of the differentiable branches adjacent to a non-differentiable singularity. For the remainder of this section we will write the linearization of the configuration $\boldsymbol{\Delta\pi} = \mathbf{T}_{SE(3)^{N_C}}(\boldsymbol{\alpha}_{n+1})\boldsymbol{\Delta\alpha}_{n+1}$. We define the Jacobian for individual constraint j from the linearization of Eq. (3.95)

$$\Delta\mathbf{F}^{\mathcal{L},j} = \begin{bmatrix} \Delta\mathbf{F}^j \\ \Delta F_N^j \\ \Delta\mathbf{F}_T^j \end{bmatrix} = \mathbf{S}_t^j \begin{bmatrix} \Delta\boldsymbol{\pi}^j \\ \Delta\Lambda_N^j \\ \Delta\boldsymbol{\Lambda}_T^j \end{bmatrix}. \tag{3.98}$$

Let us start by writing the linearization of the generalized forces $\mathbf{F}^j$:

$$\Delta\mathbf{F}^j = \begin{cases} \mathbf{0} & \text{if } \xi_N < 0 \quad \text{no contact} \\ -\Delta\left(\mathbf{B}_N^j\right)^T \xi_N^j - \left(\mathbf{B}_N^j\right)^T \Delta\xi_N^j - \mu\Delta\xi_N^j \left(\mathbf{B}_T^j\right)^T \boldsymbol{\tau}^j \cdots & \\ -\mu\xi_N^j \Delta\left(\mathbf{B}_T^j\right)^T \boldsymbol{\tau}^j - \mu\xi_N^j \left(\mathbf{B}_T^j\right)^T \Delta\boldsymbol{\tau}^j & \text{if } \|\boldsymbol{\xi}_T^j\| \geq \mu\xi_N^j \quad \text{slip} \\ -\Delta\left(\mathbf{B}_N^j\right)^T \xi_N^j - \left(\mathbf{B}_N^j\right)^T \Delta\xi_N^j - \Delta\left(\mathbf{B}_T^j\right)^T \boldsymbol{\xi}_T^j - \left(\mathbf{B}_T^j\right)^T \Delta\boldsymbol{\xi}_T^j & \text{if } \|\boldsymbol{\xi}_T^j\| < \mu\xi_N^j \quad \text{stick} \end{cases}. \tag{3.99}$$

We continue with the linearization of the normal contact law F_N^j:

$$\Delta F_N^j = \begin{cases} -\dfrac{k^2}{p}\Delta\lambda_N^j & \text{if } \xi_N < 0 \quad \text{no contact} \\ -k\Delta g_N^j & \text{if } \|\boldsymbol{\xi}_T^j\| \geq \mu\xi_N^j \quad \text{slip} \\ -k\Delta g_N^j & \text{if } \|\boldsymbol{\xi}_T^j\| < \mu\xi_N^j \quad \text{stick} \end{cases} \tag{3.100}$$

and finally the linearization of the tangential contact law $\mathbf{F}_T^j$:

$$\Delta\mathbf{F}_T^j = \begin{cases} -\dfrac{k^2}{p}\Delta\boldsymbol{\lambda}_T^j & \text{if } \xi_N < 0 \quad \text{no contact} \\ -\dfrac{k}{p}\left(k\Delta\boldsymbol{\lambda}_T^j - \mu\Delta\xi_N^j\boldsymbol{\tau}^j - \mu\xi_N^j\Delta\boldsymbol{\tau}^j\right) & \text{if } \|\boldsymbol{\xi}_T^j\| \geq \mu\xi_N^j \quad \text{slip} \\ -k\Delta\mathbf{g}_T^j & \text{if } \|\boldsymbol{\xi}_T^j\| < \mu\xi_N^j \quad \text{stick} \end{cases} . \tag{3.101}$$

In what follows we will only provide the detailed expressions for the mortar method, as they are the most intricate. The same procedure and hypotheses hold for the collocation approach.

One fundamental building block of the total linearized form is the linearization of the augmented multiplier given by

$$\Delta\xi_N^j = k\Delta\lambda_N^j - p\Delta g_N^j, \quad \Delta\boldsymbol{\xi}_T^j = k\Delta\boldsymbol{\lambda}_T^j - p\Delta\mathbf{g}_T^j, \tag{3.102}$$

which makes the linearization of the normal and tangential gap appear. In the normal direction we have

$$\begin{aligned} \Delta g_N^j &= \cancel{\int_{-1}^{1} \Delta\left(\boldsymbol{\phi}_N^j\right)^T g_N J_{nat}\,\mathrm{d}\eta} + \int_{-1}^{1} \left(\boldsymbol{\phi}_N^j\right)^T \Delta g_N J_{nat}\,\mathrm{d}\eta + \cancel{\int_{-1}^{1} \left(\boldsymbol{\phi}_N^j\right)^T g_N \Delta J_{nat}\,\mathrm{d}\eta}, \\ &\approx \mathbf{B}_N^j\Delta\boldsymbol{\pi}^j. \end{aligned} \tag{3.103}$$

where the integral has already been rescaled. The first term involves the linearization of the Lagrange multiplier shape functions

$$\Delta\left(\boldsymbol{\phi}_N^j\right)^T = \frac{\mathrm{d}\left(\boldsymbol{\phi}_N^j\right)^T}{\mathrm{d}\zeta}\Delta\zeta. \tag{3.104}$$

ζ is a quantity related to the slave beam and its linearization can immediately be obtained from Eq. (3.67) as

$$\Delta\zeta = \frac{1}{2}(1-\eta)\Delta s_a^e + \frac{1}{2}(1+\eta)\Delta s_b^e. \tag{3.105}$$

Thereby, it is linked to the linearizations of the integration boundaries. The same holds for the jacobian of the natural transformation. Its linearization is given by

$$\Delta J_{nat} = \frac{\Delta s_b^e - \Delta s_a^e}{2}. \tag{3.106}$$

Δs_a^e and Δs_b^e come from the varying domain of the integral. They can be expressed in terms of the configuration increments $\Delta\boldsymbol{\pi}$. As detailed in the section discussing the projection procedure, the integration boundaries may be slave nodes, in which case we have $\Delta s_k^e = 0$, where $k = a, b$. In the applications we have in mind this is the case most of the time. Therefore we neglect their contribution in Eq. (3.103) altogether, but provide the expressions in the non-vanishing case for completeness.

If the integration boundaries are implicitly defined by the projection of a master node onto a slave beam, Eq. (3.12) is linearized. The aim is to find the operator that links the linearization of the the boundary to the linearization of the configuration as $\Delta s_k^e = \mathbf{A}_k\Delta\boldsymbol{\pi}$, where $k = a, b$. The projection condition is of the form

$$\mathcal{P} = \mathcal{P}\left(q_e, s_k(q_e)\right) = 0. \tag{3.107}$$

By the implicit function theorem its linearization is given by

$$\Delta\mathcal{P} = \mathcal{P}_q\Delta\boldsymbol{\pi} + \left.\frac{\partial\mathcal{P}}{\partial s_1}\right|_{s_1 = s_k^e}\Delta s_k^e = 0, \tag{3.108}$$

where $\mathcal{P}_q$ is the derivative of $\mathcal{P}$ with respect to the configuration variables. Solving for

Δs_k^e gives

$$\Delta s_k^e = -\left(\left.\frac{\partial \mathcal{P}}{\partial s_1}\right|_{s_1=s_k^e}\right)^{-1} \mathcal{P}_q \Delta \boldsymbol{\pi} \tag{3.109}$$

and thus $\mathbf{A}_k = -\left(\left.\frac{\partial \mathcal{P}}{\partial s_1}\right|_{s_1=s_k^e}\right)^{-1} \mathcal{P}_q$. Finally, the derivatives are computed as

$$\frac{\partial \mathcal{P}}{\partial s_1} = \begin{bmatrix} -\mathbf{e}_x \\ S(\mathbf{e}_x)\mathbf{x}_{CF}^C \end{bmatrix}^T \boldsymbol{f}_C \tag{3.110}$$

and

$$\mathcal{P}_q = \begin{bmatrix} -\mathbf{e}_x & S(\mathbf{e}_1)\mathbf{x}_{CF}^C & \mathbf{R}_F^T\mathbf{R}_C\mathbf{e}_1 & \mathbf{0} \end{bmatrix}, \tag{3.111}$$

where $\mathbf{x}_{CF}^C = \mathbf{R}_C^T(\mathbf{x}_F - \mathbf{x}_C)$ is the relative configuration vector expressed in the local frame of the slave beam.

Similar considerations yield for the linearization of the tangential constraints

$$\Delta \mathbf{g}_T^j = \int_{-1}^{1} \left(\boldsymbol{\phi}_T^j\right)^T \Delta \mathbf{g}_T J_{nat}\, \mathrm{d}\eta \tag{3.112}$$

for the tangential gap. The linearization of Eq. (3.47) gives

$$\Delta \mathbf{g}_T = \mathbf{N}_T \mathbf{T}_{SE(3)}^{-1}(\mathbf{x}) \begin{bmatrix} -\mathrm{ad}_{\mathbf{H}_{KC}} & \mathrm{ad}_{\mathbf{H}_{KF}} \end{bmatrix} \Delta \boldsymbol{\pi}, \tag{3.113}$$

where $\mathbf{x} = \log_{SE(3)}\left(\mathbf{H}_{LK,n}^{-1}\mathbf{H}_{LK,n+1}\right)$. For small load increments we can assume

$$\mathbf{T}_{SE(3)}^{-1}(\mathbf{x}) \approx \begin{bmatrix} \mathbb{I}_{3\times 3} & \mathbb{I}_{3\times 3} \end{bmatrix} \tag{3.114}$$

such that

$$\Delta \mathbf{g}_T^j \approx \mathbf{B}_T^j \Delta \boldsymbol{\pi}^j. \tag{3.115}$$

Then there is the term related to the sliding direction for which linearizes as

$$\Delta \boldsymbol{\tau}^j = \left(\mathbb{I}_{3\times 3} - \boldsymbol{\tau}^j \otimes \boldsymbol{\tau}^j\right) \frac{\Delta \boldsymbol{\xi}_T^j}{\|\boldsymbol{\xi}_T^j\|}. \tag{3.116}$$

The discrete weighted constraint gradient is linearized as follows

$$\begin{aligned}
\Delta \mathbf{B}^j = & \int_{-1}^{1} \left(\Delta \mathbf{Q}^j\right)^T \mathbf{G}^T \boldsymbol{\phi}^j J_{nat} \, \mathrm{d}\eta \\
& + \int_{-1}^{1} \left(\mathbf{Q}^j\right)^T \Delta \mathbf{G}^T \boldsymbol{\phi}^j J_{nat} \, \mathrm{d}\eta \\
& + \int_{-1}^{1} \left(\mathbf{Q}^j\right)^T \mathbf{G}^T \Delta \boldsymbol{\phi}^j J_{nat} \, \mathrm{d}\eta \\
& + \int_{-1}^{1} \left(\mathbf{Q}^j\right)^T \mathbf{G}^T \boldsymbol{\phi}^j \Delta J_{nat} \, \mathrm{d}\eta,
\end{aligned} \tag{3.117}$$

where $\Delta \boldsymbol{\phi}^j$ and ΔJ_{nat} have already been derived previously and are neglected as before. A closed form expression for $\Delta \mathbf{Q}^j$ may be found in [68]. However, as suggested therein, it is negligeable for moderate curvatures. Finally, the linearization of the term $\mathbf{G}$ involves taking the derivative of the orientation of the contact frame $\mathbf{R}_L$ which is advised against in [12]. Indeed, in our experience the inclusion of this term in $\mathbf{S}_t^j$ almost never accelerates convergence. Moreover, the procedure was found to be more robust in absence of this term. Similar arguments are put forward when considering bilateral constraints stemming from the formulation of mechanical joints in [40]. For all the reasons mentioned above all numerical examples shown in this thesis consider

$$\Delta \mathbf{B}_N^j \approx \mathbf{0}, \quad \Delta \mathbf{B}_T^j \approx \mathbf{0}. \tag{3.118}$$

Remarks

- The use of Lie group tools streamlined the derivation of the contact kinematics. In particular, the use of a left invariant representation on $SE(3)$ yielded a local frame formulation of the beam-to-beam contact problem. It also led to an exact slip increment for beams with circular cross-sections of equal radii.
- We proposed a simple collocation method and a mortar discretization method.

The latter enforces weak normal and tangential constraints to ensure variational consistency of the numerical scheme.

- In Sec. 3.4.3 we propose to solve the discrete friction problem using a combination of an augmented Lagrangian formulation with a nonsmooth Newton method. In practice, it boils down to an active set method, where the augmented multiplier $\boldsymbol{\xi}^j$ is used to distinguish between active and inactive sets, as can be observed in Eq. (3.95). According to Brüls et al. [140] this is more robust than directly using $\boldsymbol{\Lambda}^j$. Other solution methods such as those briefly introduced in Sec. 3.4.1 could also be applied.

- The expressions of the Jacobian are rather involved. However, due to the particularity of beam-to-beam contact and the local frame approach, many terms could be ignored without worsening the convergence of the Newton method.

- The Gauß-Seidel algorithm can be used as an alternative to the nonsmooth Newton solver. Notably, it does not require the computation of the generalized Jacobian $\mathbf{S}_t$ which simplifies the implementation of the contact element.

3.5 Numerical examples

This section aims at illustrating proper behaviour of the beam-to-beam contact finite elements formulated on $SE(3)$ in a quasi-static setting by studying four test cases. It starts with a classical sliding patch test in Sec. 3.5.1. In Sec. 3.5.2 we present a benchmark made of a cantilever beam in frictionless contact with rigid wall. The third example is the twisting of two initially underformed beams in Sec. 3.5.3. Finally in Sec. 3.5.4, we look at an example that reproduces the loadcase of the Mesomics machine described in the introduction of this thesis. The machine performs torsion and bending tests which we both present here.

The collocation and the mortar method were implemented in the software Odin, along with all the examples presented in this section.

The convergence criterion for the Newton algorithm is:

$$\text{Convergence}(\mathbf{r}_\bullet) = \text{Relative Residual} < \text{tol}_r \quad \vee \quad \text{Absolute Residual} < \text{tol}_a, \tag{3.119}$$

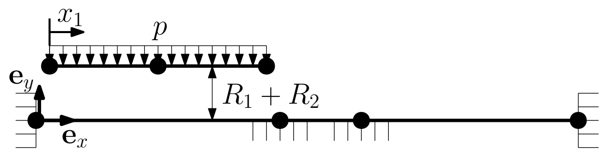

Figure 3.9: Schematic description of the sliding patch test.

where the absolute residual is simply

$$\text{Absolute Residual}(\mathbf{r}_\bullet) = \|\mathbf{r}_\bullet\| \tag{3.120}$$

and the relative residual is defined as

$$\text{Relative Residual}(\mathbf{r}_\bullet) = \frac{\|\mathbf{r}_\bullet\|}{\frac{\sum_k \|\mathbf{r}_\bullet^k\|}{N_e} + 10^{-12}}. \tag{3.121}$$

We denote by $\mathbf{r}_\bullet^k$ the unassembled residual of element k and by tol_r and tol_a relative and absolute tolerances. Convergence is evaluated separately for the equilibrium of forces $\mathbf{r}_f$ and the constraints $\mathbf{r}_c$ such that the actual convergence criterion is given by:

$$\text{Convergence}(\mathbf{r}_f) \quad \wedge \quad \text{Convergence}(\mathbf{r}_c). \tag{3.122}$$

In all of the numerical examples we used $\text{tol}_r = 10^{-7}$ and $\text{tol}_a = 10^{-4}$.

3.5.1 Frictional sliding patch test

A frictionless version of this test was described in [102, 186]. As shown in Fig. 3.9, it consists of two beams of cross-section radii $R_1 = R_2 = 5$[mm], Young moduli $E_1 = E_2 = 10^{10}$[Pa], Poisson ratios $\nu_1 = \nu_2 = 0.3$ and densities $\rho_1 = \rho_2 = 1200$[kg/m^3]. The lower beam is kept fixed and discretized into three elements of lengths 0.9[m], 0.3[m] and 0.8[m]. The top one is discretized into two elements of length 0.4[m] and moved, by imposing the horizontal position $x_1(t) = t/100$[m] of its first node. It is also subjected to a constant distributed vertical load of magnitude $p = 1$[N/m] that presses it onto the lower beam. The total simulation time is $T = 100$[s]. In the exact solution, the gap function remains zero everywhere and at all times. The lower beam exerts an upward distributed contact force of magnitude $\lambda = p$ on the top beam. Fig. 3.10 shows the evolution of the relative position error in function of time as it is defined in Eq. (2.105).

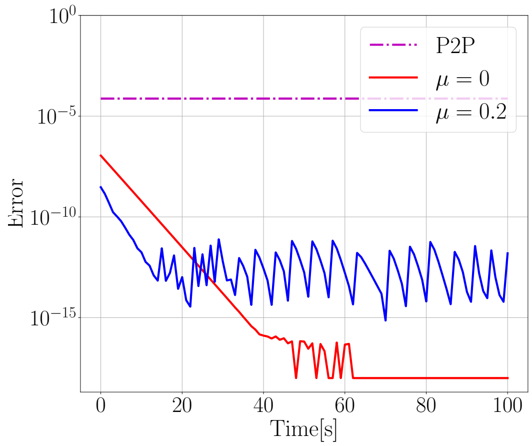

(a) Relative error.

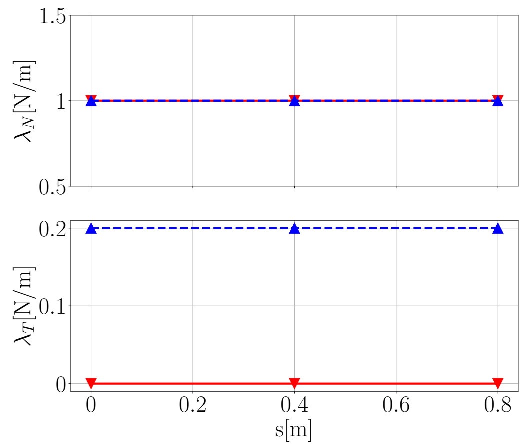

(b) Contact reaction forces.

Figure 3.10: Left: Relative error on the gap for different combinations of models and parameters. Right Top: Vertical distributed contact force. Right bottom: Tangential distributed contact force. Red: Mortar, $\mu = 0$. Blue: Mortar, $\mu = 0.2$, Other: Collocation, $\mu = 0$.

We give results for static simulations in the absence and in the presence of friction with $\mu = 0.2$. The relative error quickly drops to extremely small values independent of the number of Gauß points used, as long as it is more than one. For comparison we also provide results for a collocation method where the collocation points are chosen at locations $s_c^j = L_{e,1}/2$. Here, the relative error is modulated by the chosen relative tolerance for the constraints, which is $\mathrm{tol}_r = 10^{-4}$ for this example. The distributed contact force obtained via the mortar algorithm perfectly matches the exact solution for all t. The interpretation of the Lagrange multiplier computed by collocation is less immediate. It has the dimensions of a force as opposed to a force per unit length. Dividing it by the length of the associated beam element yields a value of the order of magnitude of p.

3.5.2 Frictionless contact of a cantilever with a rigid wall

In [47] we presented a benchmark for static frictionless beam-to-beam contact with an analytic solution. The main goal was to explain the origin of spatial discontinuities induced by a Simo-Reißner and a Kirchhoff-Love beam model in the solution of a beam-to-beam contact problem and how finite element implementations based on such models behave in their presence. We compared our mortar finite element implementation to novel analytic solutions for a cantilever beam in contact with a rigid wall. We derived this solution for the linear $2D$ versions of the above mentioned beam theories. In this section we reproduce these developments in detail and complete the analysis by also showing the results obtained with the collocation method.

Description of the benchmark

Fig. 3.11a shows a semi-infinite cantilever beam clamped at $x = 0$ and left free at the other end. It is subjected to a constant vertical distributed load p[N/m] and a contact reaction force $r(x)$[N/m]. The applied forces are counted positively in the upward direction. The vertical displacement is denoted by $w(x)$ and the initial gap by g[m]. They are taken positive in the downward direction. The beam enters in contact with the rigid substrate at $x = d$. The length of the free region, d, is a priori unknown. It separates the problem into two domains: the free region, where $x \in [0, d]$ and the contact region where $x \in [d, +\infty]$.

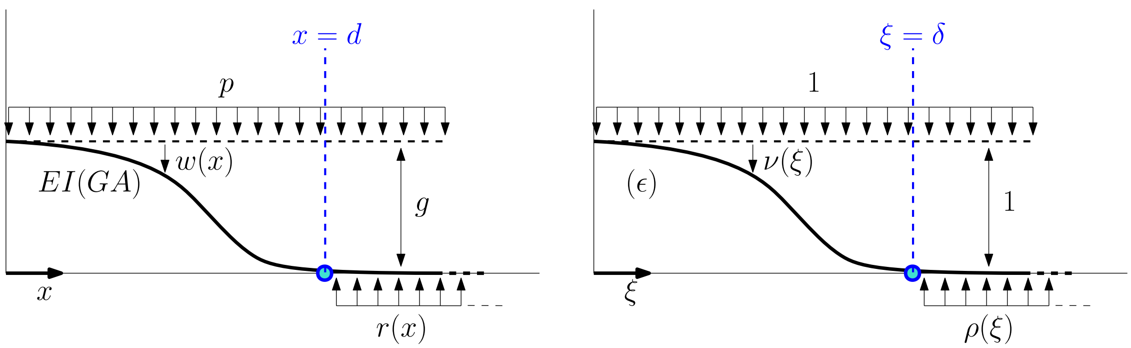

(a) Dimensional variables (b) Dimensionless variables

Figure 3.11: Schematic illustration of the proposed benchmark.

Euler-Bernoulli model

In the linear, small displacement setting, the equation governing the Euler-Bernoulli beam [39] is

$$w''''(x) = \frac{p}{EI}, \tag{3.123}$$

where EI[Nm^2] is the constant bending stiffness. It combines the equilibrium of the beam in the free region with a linear constitutive law. After solving Eq. (3.123) the internal bending moment and the shear force are computed as

$$M(x) = -EIw''(x), \quad T(x) = -EIw'''(x). \tag{3.124}$$

In our conventions the internal bending moment is positive in the clockwise direction and the shear force in the vertical upward direction. Note that the equation for the shear force follows from the equilibrium of moments and thus only holds at equilibrium. Equation (3.123) needs to be solved in the free region, where the applied load is known. The boundary conditions at the clamp are $w(0) = w'(0) = 0$. We enforce continuity of the displacement and its slope at the transition point, i.e. $w(d) = g$ and $w'(d) = 0$, since the beam geometry is imposed by the rigid wall in the contact region. The length of the free region is obtained by imposing the continuity of the bending moment, $M(d) = 0$, since the bending moment in the contact region is zero.

Timoshenko model

Under the same hypotheses as in the previous section, but allowing for shear deformation, the equations to be solved in the free region are [39]

$$w''''(x) = \frac{p}{EI}, \quad \theta'''(x) = \frac{p}{EI}, \quad w'(x) = \theta(x) - \frac{EI}{GA}\theta''(x), \tag{3.125}$$

where θ is the cross-section rotation angle and GA[N] is the constant shear stiffness. The last equation is a kinematic condition that combines constitutive equations for the bending moment and the shear force with the equilibrium equations. The boundary conditions on the transverse displacement, $w(0) = w'(d) = 0$, $w(d) = g$, are complemented by $\theta(0) = 0$ at the fixed end and $\theta(d) = \theta_d$. The quantity θ_d was introduced to explicitly translate the continuity of the beam angle through the transition point. In the contact region, where $\bar{w}(x) = 0$, the governing equations are

$$\bar{\theta}'''(x) = \frac{p - r(x)}{EI}, \quad \bar{\theta}(x) - \frac{EI}{GA}\bar{\theta}''(x) = 0, \tag{3.126}$$

which have to be solved for θ and r together with the boundary conditions $\bar{\theta}(d) = \theta_d$ and $\bar{\theta} \to 0$ as $x \to +\infty$. A technical difference to the Euler-Bernoulli model concerning the solution approach is that a governing equation has to be solved in the contact region where not all kinematic quantities are trivially obtained. Notice that the overhead bar refers to variables in the contact region. As before, the extent d of the free region is determined by enforcing the continuity of the bending moment at $x = d$. The shear forces and bending moments at equilibrium are given by

$$M(x) = -EI\theta'(x), \quad T(x) = -EI\theta''(x), \quad \bar{M}(x) = -EI\bar{\theta}'(x), \quad \bar{T}(x) = -EI\bar{\theta}''(x), \tag{3.127}$$

in each region respectively.

Dimensionless variables

The problem is characterized by the following two length scales

$$u_1^* = g, \quad u_2^* = \left(\frac{gEI}{p}\right)^{1/4}. \tag{3.128}$$

The first one is the initial gap. It is the maximal transverse deflection of the beam. The second one is a longitudinal lengthscale, which is a characteristic beam length with maximal transverse displacement g for given bending stiffness and applied load. Therefore, it is natural to scale the variables of the problem as $\xi = x/u_2^*$ and $\delta = d/u_2^*$. The dimensionless transverse displacement of the beam is defined as

$$\nu(\xi) = \frac{w[x(\xi)]}{u_1^*}. \tag{3.129}$$

The angle $\theta(x)$ is related to the slope $w'(x)$ of the neutral axis. It is thus naturally scaled by

$$\theta^* = \frac{u_1^*}{u_2^*} = \left(\frac{pg^3}{EI}\right)^{1/4} \tag{3.130}$$

such that the dimensionless angles

$$\vartheta(\xi) = \frac{\theta[x(\xi)]}{\theta^*}, \quad \bar{\vartheta}(\xi) = \frac{\bar{\theta}[x(\xi)]}{\theta^*} \tag{3.131}$$

are of order 1. The characteristic bending moment and shear force are chosen as $T^* = pu_2^*$ and $M^* = pu_2^{*^2}$, such that the dimensionless analogue of Eq. (3.124) is

$$\mathcal{M}(\xi) = \frac{M[x(\xi)]}{M^*} = -\nu''(\xi), \quad \mathcal{T}(\xi) = \frac{T[x(\xi)]}{T^*} = -\nu'''(\xi) \tag{3.132}$$

and for Eq. (3.127) we get

$$\mathcal{M}(\xi) = -\vartheta'(\xi), \quad \mathcal{T}(\xi) = -\vartheta''(\xi), \quad \bar{\mathcal{M}}(\xi) = -\bar{\vartheta}'(\xi), \quad \bar{\mathcal{T}}(\xi) = -\bar{\vartheta}''(\xi). \tag{3.133}$$

In the Timoshenko model, the reaction $r(x)$ along the wall plays an important role. It is naturally scaled by p. Thus, we define its adimensional counterpart as $\rho(\xi) = r[x(\xi)]/p$. Finally, the dimensionless relative shear deformability of the Timoshenko beam will naturally appear as

$$\epsilon^2 = \frac{EI}{GAu_2^{*2}} = \frac{(EIgp^3)^{1/4}}{GA}. \tag{3.134}$$

An illustration of the problem with adimensional variables is given in Fig. 3.11b.

Analitical solution of the Euler-Bernoulli model

Under the change of variables introduced in section 3.5.2 the Euler-Bernoulli beam is governed by

$$\nu''''(\xi) = 1, \quad \xi \in [0, \delta] \tag{3.135}$$

with $\nu(0) = \nu'(0) = \nu'(\delta) = 0, \nu(\delta) = 1$. The solution is

$$\nu(\xi) = \frac{\xi^4}{24} - \left(\frac{2}{\delta^3} + \frac{\delta}{12}\right)\xi^3 + \left(\frac{3}{\delta^2} + \frac{\delta^2}{24}\right)\xi^2. \tag{3.136}$$

The continuity of the bending moment yields $\delta = 72^{1/4}$. The dimensionless shear force has the following simple expression

$$\mathcal{T}(\xi) = -\xi + \delta\left(\frac{1}{2} + \frac{12}{\delta^4}\right). \tag{3.137}$$

such that at the boundaries one has

$$\mathcal{T}(0) = \frac{2}{3}\delta, \quad \mathcal{T}(\delta) = -\frac{1}{3}\delta. \tag{3.138}$$

Since $\bar{\nu}(\xi) = 1$ in the contact region, the shear force at the boundary is given by

$$\bar{\mathcal{T}}(\delta) = 0. \tag{3.139}$$

Unlike the bending moment, the shear force is thus discontinuous at $\xi = \delta$. As a consequence, the contact reaction includes a point load of magnitude

$$f_\delta = \bar{\mathcal{T}}(\delta) - \mathcal{T}(\delta) = \frac{1}{3}\delta. \tag{3.140}$$

Hence, one third of the distributed load applied to the beam in the free region ends up as a point contact reaction force at the contact boundary. The other two thirds are transmitted into the clamp. The distributed contact force in the region $\xi > \delta$ is simply $\rho(\xi) = 1$.

Analytical solution of the Timoshenko model

Free region: After the change of variables Eqs. (3.125) become

$$\nu''''(\xi) = 1, \quad \vartheta'''(\xi) = 1, \quad \nu'(\xi) = \vartheta(\xi) - \epsilon^2\vartheta''(\xi) \tag{3.141}$$

and the boundary conditions are $\nu(0) = \nu'(\delta) = 0$, $\nu(\delta) = 1$ for the adimensional transverse displacement and $\vartheta(0) = 0$, $\vartheta(\delta) = \vartheta_\delta$ for the adimensional beam angle. From the first two equations and the clamping conditions one knows that the deflection is of the form

$$\nu(\xi) = \frac{\delta^4}{24}\left(\left(\frac{\xi}{\delta}\right)^4 + A\left(\frac{\xi}{\delta}\right)^3 + B\left(\frac{\xi}{\delta}\right)^2 + C\left(\frac{\xi}{\delta}\right)\right), \tag{3.142}$$

and that the beam angle is of the form

$$\vartheta(\xi) = \frac{\delta^3}{6}\left(\left(\frac{\xi}{\delta}\right)^3 + D\left(\frac{\xi}{\delta}\right)^2 + E\left(\frac{\xi}{\delta}\right)\right). \tag{3.143}$$

The five constants A, B, C, D and E may be obtained using the two boundary conditions at the contact interface, together with the third equation in (3.141). These are

$$A = -2\Delta\left(1+\frac{24}{\delta^4}\right), \tag{3.144a}$$

$$B = -\frac{3}{\delta}\left(1+\frac{8}{\delta^3}\right) + 4\Delta\left(1+\frac{24}{\delta^4}\right), \tag{3.144b}$$

$$C = -2\left(1+\frac{24}{\delta^4}\right)(\Delta-1), \tag{3.144c}$$

$$D = -\frac{3}{2}\Delta\left(1+\frac{24}{\delta^4}\right), \tag{3.144d}$$

$$E = -\frac{5}{2} + \frac{1}{\Delta} + 2\Delta + \frac{12}{\delta^4}(4\Delta-1), \tag{3.144e}$$

where we defined an additional adimensional parameter $\Delta = \dfrac{\delta^2}{\delta^2+6\epsilon^2}$. The shear force and the bending moment may now be computed

$$\mathcal{T}(\xi) = -\xi - \frac{\delta}{3}D, \quad \mathcal{M}(\xi) = -\frac{\xi^2}{2} - \frac{\delta}{3}D\xi - \frac{\delta^2}{6}E \tag{3.145}$$

Note that one can verify that $\mathcal{T}(0)-\mathcal{T}(\delta)=\delta$, such that vertical equilibrium is satisfied.

Contact region: The adimensional equations are

$$\bar{\vartheta}'''(\xi) = 1-\rho(\xi), \quad \bar{\vartheta}(\xi) - \epsilon^2\bar{\vartheta}''(\xi) = 0. \tag{3.146}$$

We start by solving the third equation for $\vartheta(\xi)$ together with the boundary conditions $\bar{\vartheta}(\delta) = \vartheta_\delta$ and $\bar{\vartheta} \to 0$ as $\xi \to +\infty$. The solution is given by

$$\bar{\vartheta}(\xi) = \vartheta_\delta e^{(\delta-\xi)/\epsilon}. \tag{3.147}$$

The internal bending moment and shear force in the contact region follow as

$$\bar{\mathcal{T}}(\xi) = -\frac{\vartheta_\delta}{\epsilon^2}e^{(\delta-\xi)/\epsilon}, \quad \bar{\mathcal{M}}(\xi) = \frac{\vartheta_\delta}{\epsilon}e^{(\delta-\xi)/\epsilon} \tag{3.148}$$

Finally, from the second equation in (3.146) the adimensional distributed contact force exerted on the beam is computed as

$$\rho(\xi) = \frac{\vartheta_\delta}{\epsilon^3} e^{(\delta-\xi)/\epsilon} - 1. \tag{3.149}$$

The total contact reaction force over a region $\xi \in [\delta, \mathcal{L}]$ is

$$f_c = \int_\delta^{\mathcal{L}} \rho(\xi)\,\mathrm{d}\xi = \frac{\vartheta_\delta}{\epsilon^2}\left(1 - e^{(\delta-\mathcal{L})/\epsilon}\right) + (\mathcal{L} - \delta). \tag{3.150}$$

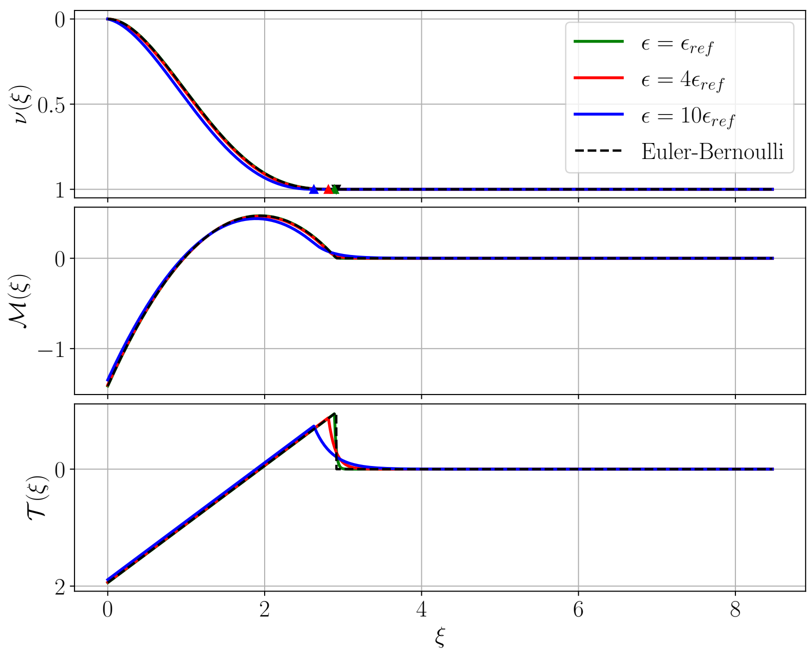

Figure 3.12: Transverse displacement, bending moment, shear force. The markers denote the first contact point.

Subtracting the constant part of the contact force and taking $\mathcal{L} \to \infty$ yields an equivalent contact force in the transition region which may be compared to the point force from the Euler-Bernoulli case in Eq. (3.140). It is equal to

$$f_\delta = \frac{\vartheta_\delta}{\epsilon^2}. \tag{3.151}$$

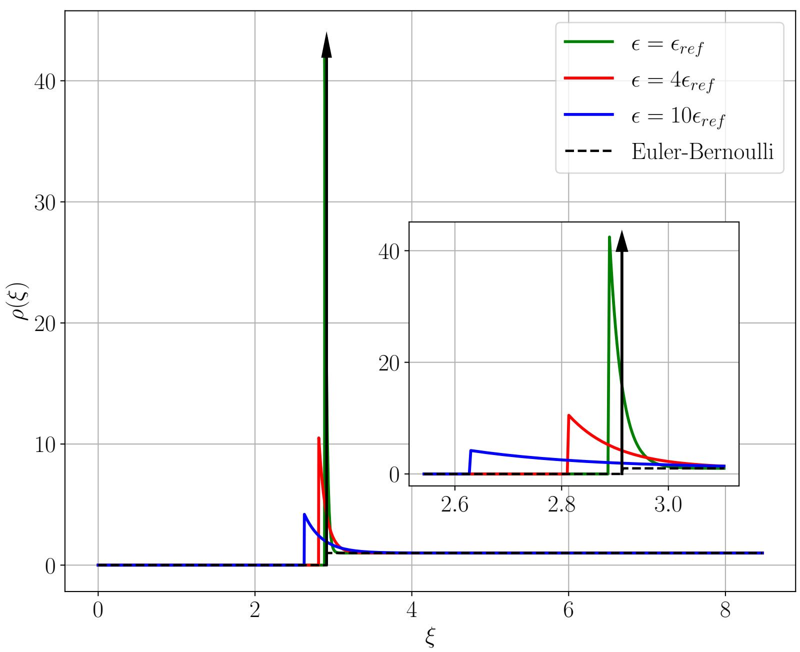

Figure 3.13: Distributed contact force.

For small ϵ, this resultant force is concentrated in a thin boundary layer of length ϵ and located close to the transition point [215].

Transition point: The beam angle at the transition point is

$$\vartheta_\delta = \frac{\epsilon^2 \Delta}{2\delta^3} \left(\delta^4 + 12\delta^2\epsilon^2 - 24\right). \tag{3.152}$$

The continuity of the bending moment is used to derive the following equation for the adimensional free length

$$\delta^6 + 6\epsilon\delta^5 + 30\epsilon^2\delta^4 + 72\epsilon^3\delta^3 + 72(\epsilon^4 - 1)\delta^2 - 144\epsilon(\delta + \epsilon) = 0 \tag{3.153}$$

By Descartes' rule of signs the above equation has a unique positive solution. The value of δ from the Euler-Bernoulli model may be used as initial guess for an iterative solution procedure. Interestingly, it can be verified that $\mathcal{T}(\delta) - \bar{\mathcal{T}}(\delta) = 0$ and thus, unlike in the Euler-Bernoulli case, the shear force is continuous and no additional point load at the contact boundary appears.

Figure 3.12 shows the transverse displacement, bending moment and shear force for different values of the relative shear deformability ϵ. We can already observe that increasing ϵ shortens the length of the free region, which is bounded from above by its value taken in the Euler-Bernoulli case. For a better understanding of the magnitude of the quantities involved, realistic dimensional parameters were chosen. These are given in table 3.1 and represent a thin circular steel rod.

To judge the shear stiffness of the Timoshenko beam we may compute a slenderness ratio of the beam in the free region as $R/d_{Tym} = 0.0097$. Notice that L denotes the finite beam length considered in the numerical models, whereas $L \to \infty$ in the analytic case. We assume that boundary effects are negligeable such that both solutions can be compared. The resulting reference value for the shear deformability is $\epsilon_{ref} = 0.023$. The value of ϵ is increased by chosing a larger shear stiffness G, while keeping all other parameters fixed. The same parameter set will be used for all remaining figures throughout this section.

Parameter	Value	Unit
R	1	mm
g	0.01	mm
L	0.3	m
p	1	N/m
I	0.79	mm^4
E	200	GPa
A	3.1	mm^2
G_{ref}	77	GPa

Table 3.1: Numerical values of the dimensional quantities used to generate all figures throughout this section.

The distributed contact reaction force ρ for different values of the relative shear deformability, is represented in Fig. 3.13. It is also compared to the Euler-Bernoulli model. As ϵ decreases, the contact force gets more concentrated around the transition region and tends towards a point load. Indeed, one can show analytically that when ϵ becomes negligeable

$$\lim_{\epsilon \to 0} \rho(\delta) = +\infty. \tag{3.154}$$

Numerical results and discussion

A good agreement between the exact and the numerically computed transverse displacement, ν_h, is obtained for both beam models and both contact discretization methods, as may be seen in Figs. 3.14. This stays true for a small number of finite elements, as shown by the discretization error in Fig. 3.15a, which is defined as

$$e_d = \sqrt{\frac{\int_0^{\mathcal{L}} |\nu_h(\xi) - \nu(\xi)|^2 \, \mathrm{d}\xi}{\int_0^{\mathcal{L}} \nu(\xi)^2 \, \mathrm{d}\xi}}. \tag{3.155}$$

The spatial convergence rate of 2, characteristic for constant deformation elements, is conserved for all cases.

Since the mortar formulation assumes distributed contact forces and interpolates them, in this case with linear shape functions, the method cannot represent the point contact force that appears in the exact solution of the Euler-Bernoulli case. To compare with the collocation method directly on the same graph, we divided the pointwise contact forces by the length of the associated beam finite element. The point forces are always located in the middle of the slave element. Far from the transition region the simple collocation method yields satisfying results, but it also suffers from the oscillation phenomenon close to the discontinuity. One possible explanation is that that the location of the first contact point rarely coincides with the location of the discontinuity and when it does, it is in the middle of an element that is incapable to represent a discontinuous curvature.

Similarly, the discontinuity followed by a potentially sharp gradient in the Timoshenko case induces oscillations in the interpolated contact force. Note that this does not affect the optimal spatial convergence rate. As may be seen in Figs. 3.14, these oscillations may be reduced by mesh refinement. An important parameter is the ratio between the element length h and the characteristic length of the boundary layer, which is given by the relative shear deformability ϵ. When the latter is decreased, the peak in the distributed contact force is sharper, resulting in a problem with more numerical difficulties.

Discretizations too coarse to represent the short spatial scales in the boundary layer, i.e. such that $h > \epsilon$ (see Fig. 3.14c), will result in a poor approximation of the distributed contact force. Outside this transition region, the distributed contact force is equal to the applied load and the numerical solution agrees with the exact one. Another interesting quantity to look at is the numerical resultant contact force acting on the beam and denoted f_{c_h}, obtained by integrating the distributed contact force along the

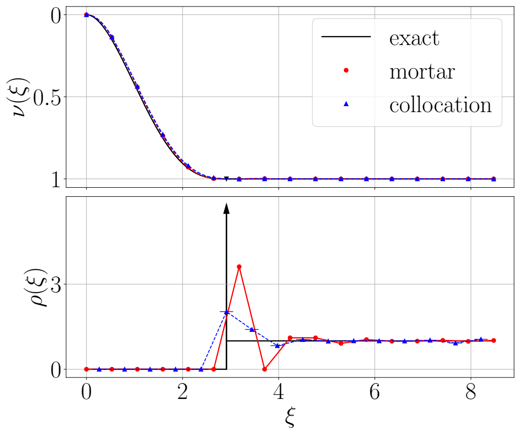

(a) Euler-Bernoulli with $h = 0.53$.

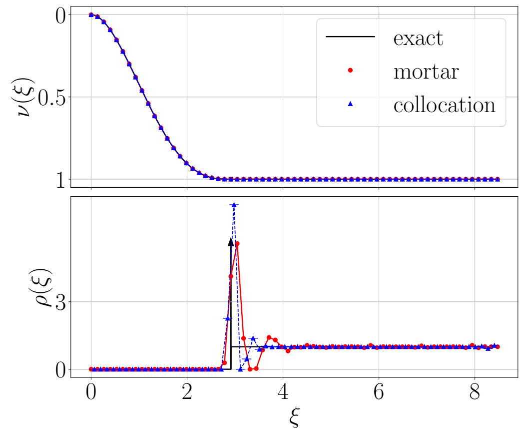

(b) Euler-Bernoulli with $h = 0.13$.

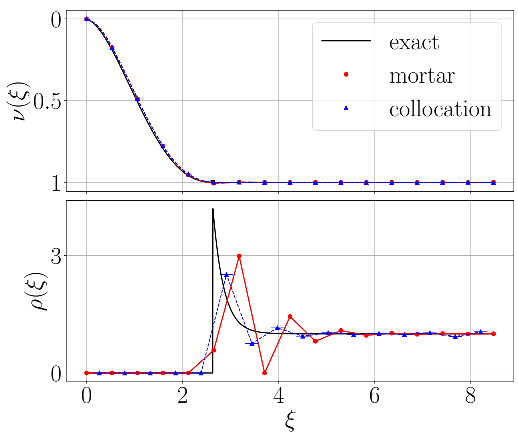

(c) Timoshenko with $\epsilon = 10\epsilon_{ref}$ and $h = 0.53 > \epsilon$.

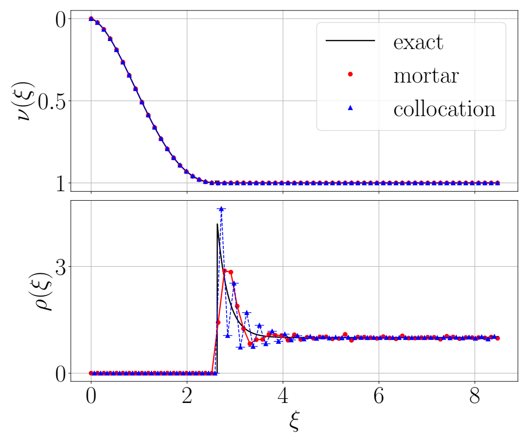

(d) Timoshenko with $\epsilon = 10\epsilon_{ref}$ and $h = 0.13 < \epsilon$.

Figure 3.14: Comparison between analytic and numerical solutions of the transverse displacement and distributed contact reaction force for a coarse and a fine mesh.

contact region.

Figure 3.15b shows the relative error with respect to the analytic solution which is defined as

$$e_f = \frac{|f_{c_h} - f_c|}{f_c}. \tag{3.156}$$

We observe second order convergence only for the mortar method. Since the represen-

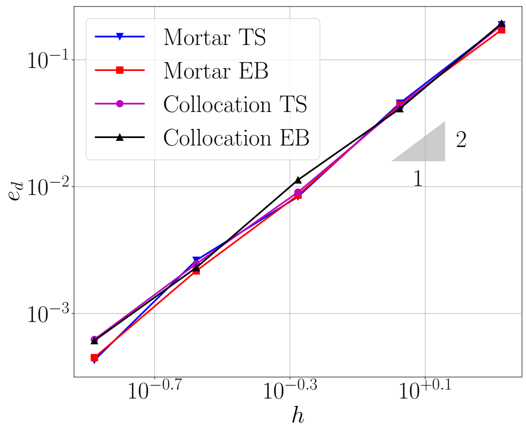

(a) Error on the vertical displacement.

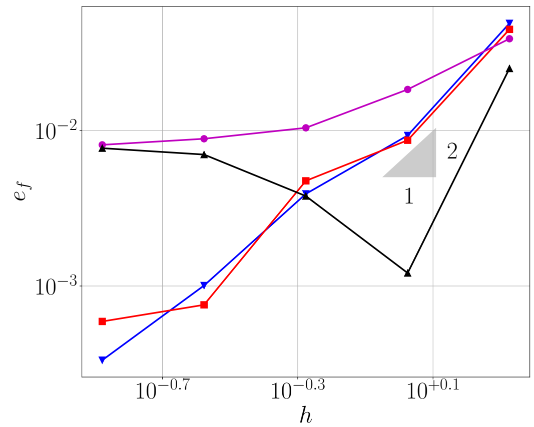

(b) Error on the integrated contact force.

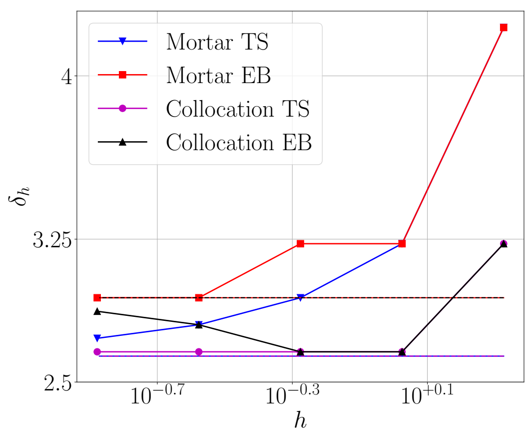

(c) Length of the free region.

Figure 3.15: Convergence analysis for different quantities of interest. The horizontal lines represent the analytic value.

tation of contact forces is highly dependent on the number and location of the contact points in the case of the collocation approach, it is difficult to conclude about convergence. There is no doubt however, that the convergence behaviour is not as good as for the mortar method.

Figure 3.15c shows the evolution of the numerical free length δ_h as the mesh is refined. We take it as the average location of the first non-vanishing node and the maximum in the distributed contact force.

Remarks

- The Euler-Bernoulli model leads to a point contact force at the boundary of the contact region and the shear force is discontinuous. For the Timoshenko beam however, a purely distributed load is exerted by the wall, and the shear force is continuous. The observed spike in the distributed contact force increases when the shear deflection decreases, such that the solution for the Timoshenko model tends towards the solution of the Euler-Bernoulli model.

- The discontinuity and high intensity of the contact forces at the contact boundary are difficult to be captured by a numerical model, since they occur over extremely short spatial scales. Indeed, the typical size of these short boundary layers is ϵ in the Timoshenko model and 0 in the Euler-Bernoulli model. As was shown in other works, these local effects are a consequence of the selected kinematic hypothesis of the underlying beam model and would not occur if a 3D continuum model of the beam was adopted. Generally, such local effects are of no importance to multibody system simulations, where reduced beam models, as they were studied here, are often employed. For such applications, the interest lies in the overall behaviour of assemblies of components. From that point of view, both the collocation and the mortar approach provide a reasonable approximation of the distributed contact forces. Indeed, the optimal spatial convergence rates for the displacements are not affected.

- On the displacement graphs the solution for the collocation and mortar approaches are indistinguishable. The same holds for distributed contact forces far from the transition region. A major difference may be observed in the convergence behaviour of the total contact force, where the collocation method does not perform as good as the mortar method while still yielding reasonable results in absolute terms.

3.5.3 Twisting of two initially undeformed cantilever beams

In this example the twisting of two beams as described by Tomec et al. in [186] is studied. Similar variants were also proposed in [51, 102]. The beams are both initially straight, of length $L = 5$[m] and cross-section radii $R_1 = R_2 = R = 10^{-2}$[m], and they are separated by a distance of $H = 10^{-3}$[m]. Their Young's modulus is 1[GPa] and they have a Poisson ratio of 0.3. We fully clamp them on one end and fix them to a common rigid body on the other end of which we control the movement. First some pretension is applied by imposing an axial displacement of $d = 0.05$[m] to prevent the two beams from buckling as soon as the twisting motion is applied. Then the rigid body is rotated around the same axial direction by an angle $\phi = 2\pi$. In that manner the end nodes of the beam travel on an imposed circular path. The two beams take a shape that approaches a double helix and contact occurs along a continuous line. A graphical representation of the load case can be found in Fig. 3.16 and some snapshots of the simulation at relevant time instants are given in Fig. 3.19.

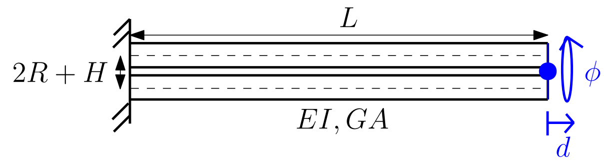

Figure 3.16: Schematic description of the twisting example.

Frictionless case

We will start by analyzing the frictionless case in detail. The results are summarized in Fig. 3.17. We compare the distributed contact force in Fig. 3.17a. Oscillations are observed near the transitions between contact and no-contact states, which can be attributed to the presence of a discontinuity in the exact contact pressure as in the previous test case. These are less pronounced for the collocation method. Due to the absence of interpolation in the Lagrange multipliers and the fact that, in the collocation method, constraints are imposed at discrete points rather than through integrated, assembled quantities, the degrees of freedom are less coupled. As a result, the influence of any discontinuity in the exact solution becomes more localized, reducing the propagation of numerical oscillations across the domain. Far away from the the influence of the transition region both solutions match perfecly. The proposed method is able to handle the nonsmooth distributed contact force at the cost of oscillations. These can be reduced by tuning numerical parameters, but will never fully disappear. Note that the symmetry of the problem is well reflected in the result.

In Figs. 3.17b and 3.17c we study the number iterations of the Newton algorithm in function of the number of elements and the number of load steps. As an indication the average number of Newton iterations using 100 elements within 100 load steps is a reasonable 1.96 in the case of mortar and 2.72 for the collocation approach. For this study the terms related to the linearization of the shape functions and the normal vector were neglected in the tangent stiffness matrix.

In the present example a spatial convergence rate slightly above 2 is obtained, see Fig. 3.17d. This superconvergence could be due to the $SE(3)$ interpolation scheme, which approximates the beam centerline by piecewise helices [66, 68]. These are particularly well-suited for this kind of problem. We also highlight the fact that the convergence rate slightly deteriorates when number of contact points is high for the collocation method. The reference solution is simply the result obtained for a very fine discretization of 1600 elements.

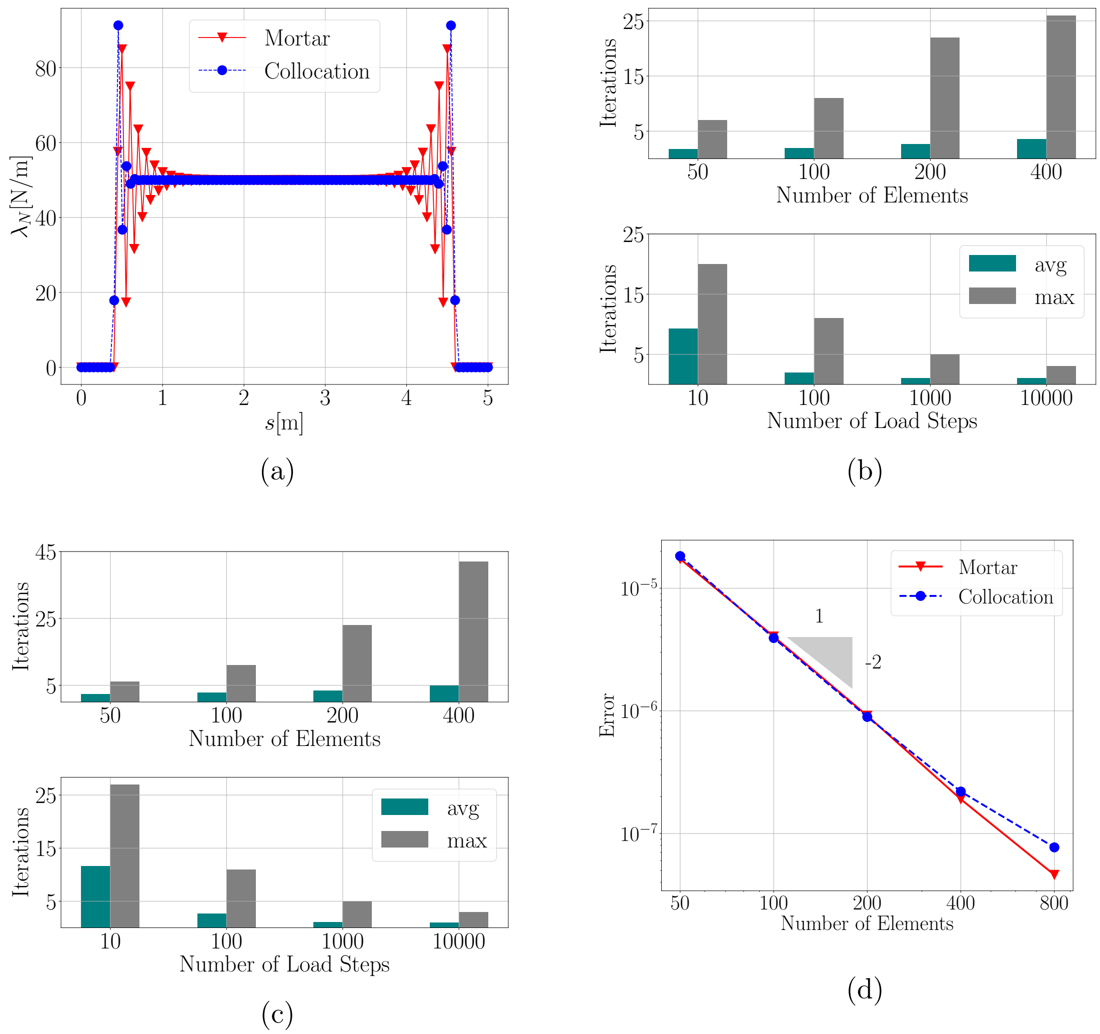

Figure 3.17: (a) Distributed contact force for the $3D$ twisting example using 100 finite elements for each beam. Color code: Mortar (red); Collocation (blue) (b) Average and maximum number of Newton iterations for the mortar method.(c) Average and maximum number of Newton iterations for the collocation method. For the influence of the discretization the number of load steps is set to 100. For the influence of the load step the number of elements is set to 100. For both analyses the beams are submitted to one turn. (d) Spatial convergence study.

Frictional case

We redo the same simulation, but this time the friction coefficient is set to $\mu = 0.3$. Our current implementation of the mortar method suffers from robustness issues and convergence of the Newton algorithm could only be obtained for very specific combinations of numerical, material and geometric parameters. Therefore, we only provide results for the collocation method in this section which can be seen in Fig. 3.18. Extrapolating conclusions from earlier results, we do not expect major differences between the two methods. In Fig. 3.18a a spatial convergence rate of 2 can be observed. Here the reference solution was obtained using a discretization of 250 elements.

Fig. 3.18b shows the final normal and tangential distributed contact force. We notice that the normal contact force is very similar to the normal contact force in the friction free case. Frictional effects are concentrated at the two extremities of the contact region. The tangential contact force almost vanish in the central region away from the boundaries. The absolute value of the tangential contact forces are always strictly below the sliding treshold indicating that all elements are in a sticking state. The tangential contact force along the direction of the centerline tangent (in blue in Fig. 3.18b) also suffers from numerical oscillations in the transition region. It is more pronounced close to the fixed boundary. Such oscillations are not observed for the tangential contact force in the transverse direction.

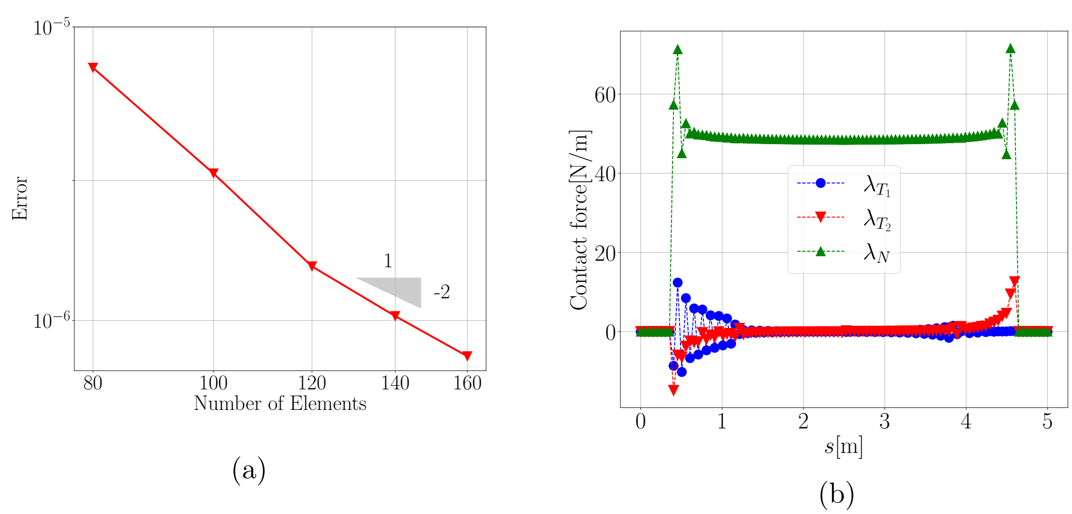

Figure 3.18: Results for the twisting example with a friction coefficient of $\mu = 0.3$ using the collocation method. (a) Spatial convergence study. (b) Final distributed contact force as a function of the arc length parameter using 100 finite beam elements.


(a) First twist (b) Second twist

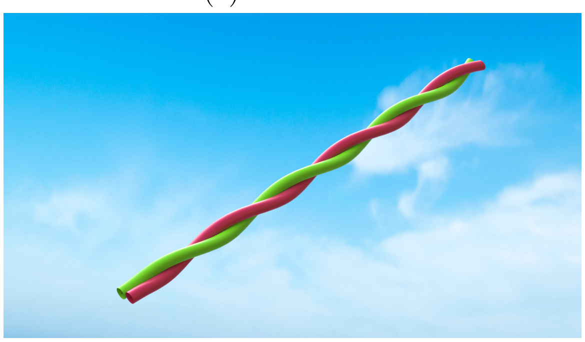
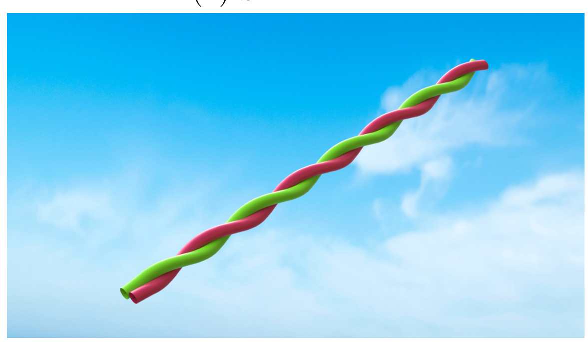

(c) Third twist (d) Fourth twist

Figure 3.19: Graphical illustration of the results obtained for the twisting of two beams. Here we show a simulation with up to four twists.

3.5.4 The twisted pair

The goal of this chapter's final section is to demonstrate our method's ability to simulate a torsion and a geometrically nonlinear bending experiment akin to the load cases of the MESOMICS machine developed at the Fraunhofer Institute for Industrial Mathematics in Kaiserslautern. The purpose of the machine is the robust measurement of mechanical properties of cable bundles and hoses. Numerical simulations have been carried out by Hawwash et al. in [114, 115, 216]. These experiments involve the torsion and bending of a so-called unshielded twisted pair [217]. Twisted pairs consist of two intertwined conductors. Their particular structure reduces electromagnetic radiation and cross-interference. Commonly used in wire harnesses of automotive onboard electronics, the electrical properties of twisted pairs are negatively affected by torsion, tensile strain or accute bending deformation [218] which explains the interest of car manufacturers in understanding their mechanical properties.

Figure 3.20: Typical specimen of a twisted pair.

A typical specimen used in the experiments can be seen in Fig. 3.20. One additional complication stems from the initial deformation of the specimen. We model it as a perfect double helix with radius $r_h = 0.65$[mm] and pitch $p_h = 20$[mm].

Torsion

A pure torsion test is performed on the twisted pair. At one end both wires are fully clamped. At the other end they are connected to a revolute joint that imposes a rotation θ_x along the x-axis. A schematic description of the experiment can be seen in Fig. 3.21. A cyclic procedure is applied where the torsion angle is increased up to 12° and then goes back to its original value of 0°. The reaction torque M_x is measured as a function of θ_x. The following material and geometric parameters were used in the simulation of the torsion test:

Parameter	Value	Unit
E	5610	[MPa]
G	1870	[MPa]
ρ	6.03	[g/cm³]
r	0.65	[mm]
l	10	[cm]

We start by analyzing the case without frictional forces. Figure 3.25 compares the normal contact force obtained from the collocation method with the distributed contact forces resulting from the mortar method at the maximum applied rotation. These results were obtained using 150 elements for each wire. For the collocation method the contact patch was discretized into 50 contact points for stability reasons. We find good agreement between the solutions resulting from both methods. All constraints are active along the span of the contact line.

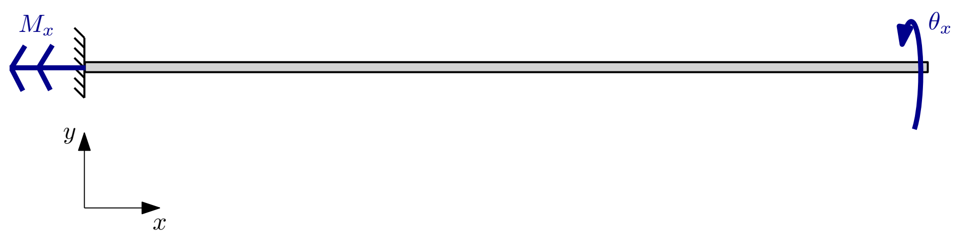

Figure 3.21: Schematic description of the torsion test.

We redo the same simulation, but this time the friction coefficient is set to $\mu = 0.2$. Our implementation of the mortar method suffers from robustness issues. Therefore, we only provide results for the collocation method in this section which can be seen in Fig. 3.26. Frictional interactions occur at the extremities of the contact region. The tangential contact forces are almost always strictly below the sliding treshold, thus indicating that most elements are in a sticking state.

In Fig. 3.22c, we present the torque-angle curves for the mortar method and the collocation method with and without friction. We make the following observation. The torsional stiffness of a single fiber with helicoidal initial shape is slightly higher than an initially straight fiber. The torsional stiffness of the twisted pair when ignoring contact interactions is exactly twice the stiffness of the single helicoidal fiber. The presence of contact interactions between the two fibers results in an increase of the torsional stiffness of the twisted pair.

A second observation is related to hysteresis. In their comparative study between Ansys simulations and experimental results, Hawwash et al. successfully reproduced hysteresis effects of similar magnitude to those observed in the experiments with their numerical model [216]. Notably, their model did not include material plasticity, leading them to conclude that hysteresis is primarily dominated by interwire friction. In contrast, our friction model exhibits only negligible amounts of hysteresis. As can be seen in Fig. 3.22d, the difference of the reaction force ΔM_x between a simulation including and excluding frictional effects is of the order of 10^{-3}. The discrepancy between our results and those from the literature may be attributed to the nonsmooth nature of our

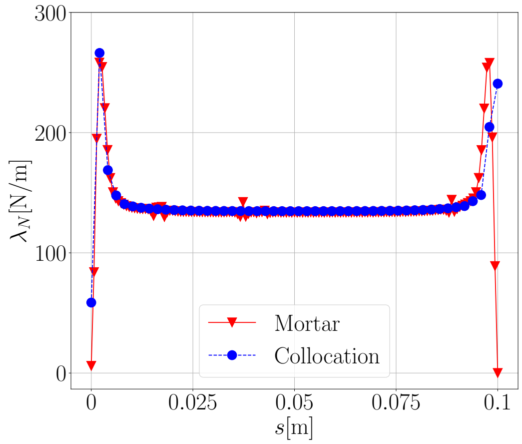

(a) Normal distributed contact force at maximum applied rotation.

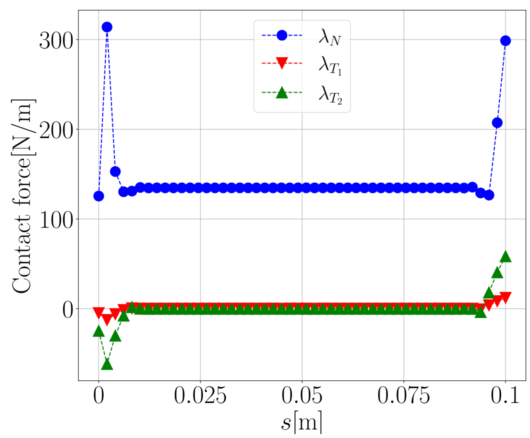

(b) Tangential distributed contact force at maximum applied rotation.

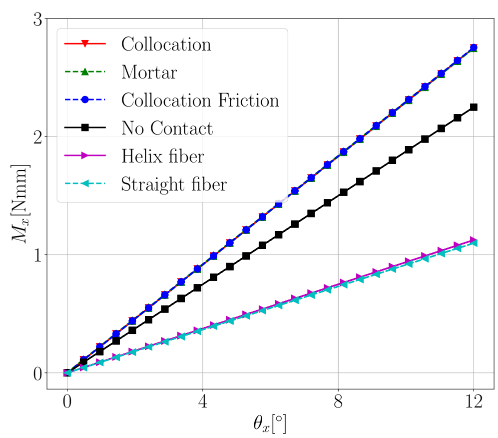

(c) Reaction torque M_x[Nmm] in function of the applied angle θ_x[°].

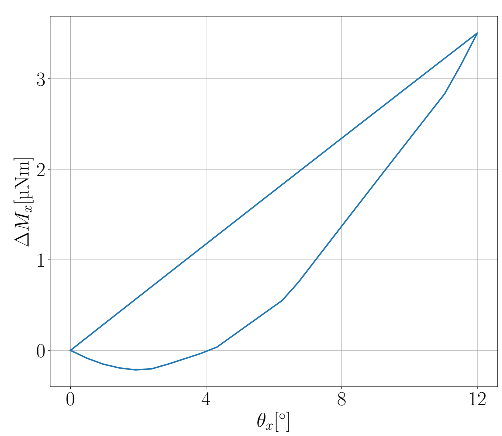

(d) Difference between the reaction torque for the collocation method with and without friction ΔM_x[µNm] in function of the applied rotation θ_x[°].

Figure 3.22: Top: Contact forces along the span of the contact line at maximum applied rotation of the torsion of the twisted pair simulation. Bottom: Analysis of the reaction torque. We use 150 finite elements per beam. The full simulation is split into 100 load steps. The Newton method converged after 1.92 iterations on average for $\mu = 0.2$.

friction model, where all contacts remain in a sticking state throughout the simulation, resulting in no energy dissipation. It is important to note that a regularized approach cannot accurately represent sticking. Consequently, all contacts in such an approach are perpetually in a sliding state.

Geometrically nonlinear bending

The bending test emulates the load case of the MESOMICS machine. The boundary conditions for this bending experiment are derived from the second case of Euler buckling [219] applied to a multiwire system. At one end both wires are rigidly connected to a fixed revolute joint and at the other end they are connected to a sliding revolute joint. The experiment has two phases to bypass the critical Euler buckling load:

- **Initial Phase**: A volumic load F_0 is applied in the negative y-direction to the specimen to induce buckling, displacing the roller-supported joint on the right side slightly by Δx_0. In practice, this is done by hand on the MESOMICS machine. Then the right side joint is kept fixed while the vertical load is removed.
- **Cyclic Phase**: A displacement in the negative x-direction Δx is imposed incrementally on the righ side joint in steps reaching a maximum of 3 times the diameter of the twisted pair assembly, followed by an unloading back to the initial position Δx_0. We use a total of 100 load steps.

This setup creates a symmetric bending configuration, with zero bending moments at the supports and maximum moments at the midpoint. The final evaluation of the experiment consists in measuring the horizontal reaction force F_x necessary to achieve the displacement Δx. A schematic description of the test case can be found in Fig. 3.23. Fig. 3.24 shows snapshots of the simulation at different time instants.

The following material and geometric parameters were used in simulation of the geometrically nonlinear bending test:

Parameter	Value	Unit
E	1050	[MPa]
ν	0.50	[MPa]
ρ	6.03	[g/cm³]
r	0.65	[mm]
l	10	[cm]

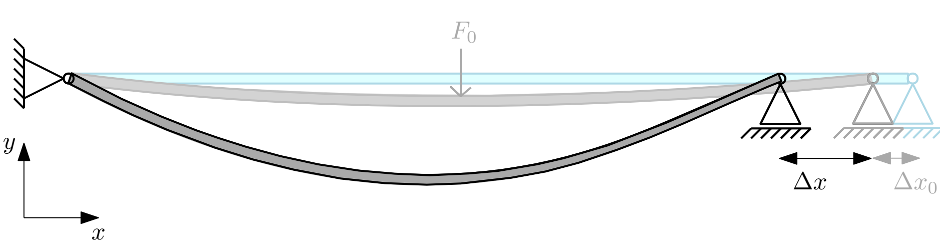

Figure 3.23: Schematic description of the bending test.

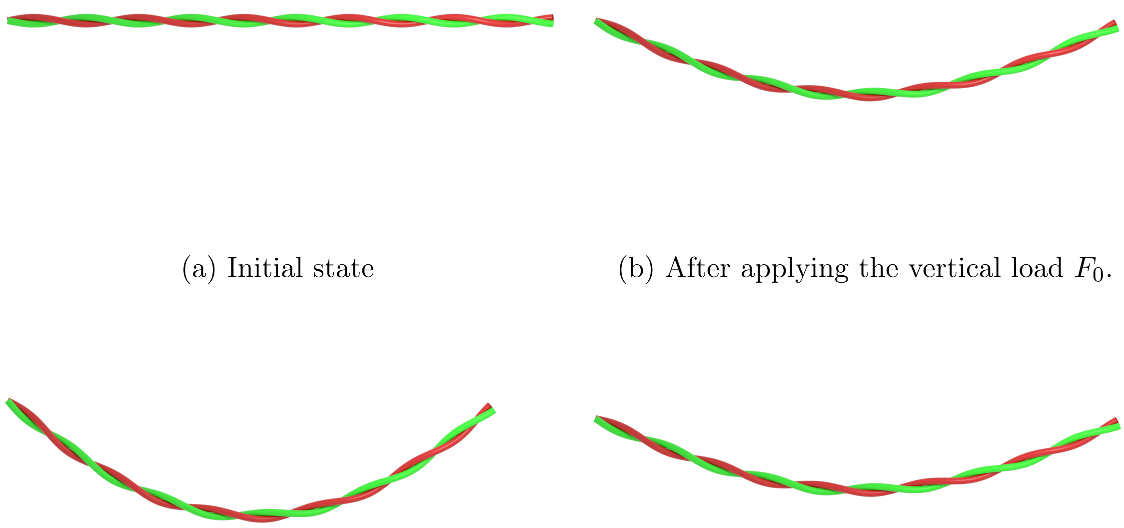

(a) Initial state

(b) After applying the vertical load F_0.

(c) Max displacement reached after 50 load steps.

(d) Final state

Figure 3.24: Snapshots of the bending of the twisted pair simulation at relevant time instants. We use 150 finite elements per beam. The full simulation is split into 250 load steps. The Newton method converged after 3.25 iterations on average for $\mu = 0.2$. The transverse dimensions of the wires have been scaled in these pictures for graphical illustration purposes.

As for the previous example, we start by analyzing the case without frictional forces. Figure 3.25 compares the normal contact force obtained from the collocation method with the distributed contact forces resulting from the mortar method. These results were obtained using 150 elements for each wire. For the collocation method the contact patch was discretized into 50 contact points. Fig. 3.25a shows the contact forces at the moment the vertical load F_0 is applied which match for both methods. All constraints are active along the span of the contact line. On the contrary, during the cyclic phase of the experiment, contact interactions concentrate on the boundaries, as can be seen in Fig. 3.25b. Amplitude peaks are more pronounced for the mortar method. This could simply be due to the finer discretization of the contact patch.

We redo the same simulation, but this time the friction coefficient is set to $\mu = 0.2$. As for the torsion test, our implementation of the mortar method suffers from robustness

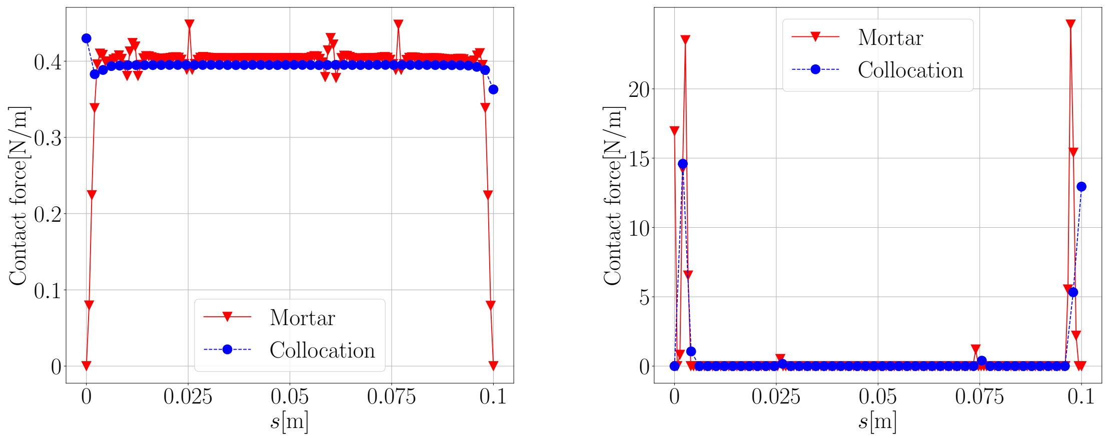

(a) Initial phase: Application of the vertical acceleration F_0.

(b) Cyclic phase: Sliding of the right joint. Here at maximum horizontal displacement.

Figure 3.25: Contact forces along the span of the contact line at different time instants during the bending of twisted pair simulation.

issues. Therefore, we only provide results for the collocation method in this section which can be seen in Fig. 3.26. Similar conclusions can be drawn. The normal contact force is indistinguishable from the normal contact force in the friction free case and tangential contact forces are almost always strictly below the sliding treshold, thus indicating that most elements are in a sticking state.

In Fig. 3.26c, we present the force-displacement curves for the mortar method and the collocation method with and without friction. For the same reasons as for the torsion experiment, our friction model exhibits only negligible amounts of hysteresis. As can be seen in Fig. 3.26d, the difference of the reaction force ΔF_x between a simulation including and excluding frictional effects is of the order of 10^{-6}.

3.6 Concluding remarks

This chapter presented a formulation of frictional beam-to-beam contact within the $SE(3)$ Lie group framework. The contact kinematics was expressed in the local frame of reference attached to the beam centerline. A finite difference formula on $SE(3)$ provided an exact measure of tangential slip for beams with circular cross-sections. The resulting contact elements depend only on the relative motion of the two beams ensuring that the constraint gradient and the tangent operator are invariant under rigid body transformations.

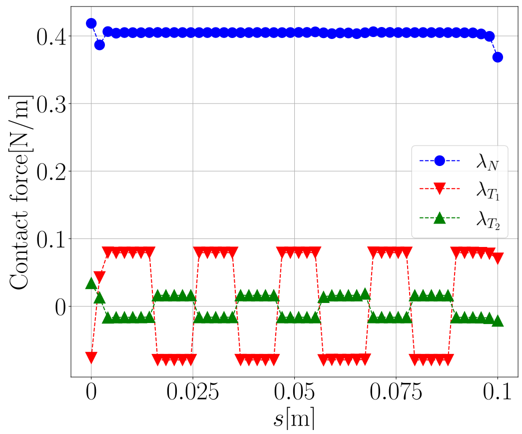

(a) Initial phase: Application of the vertical acceleration F_0.

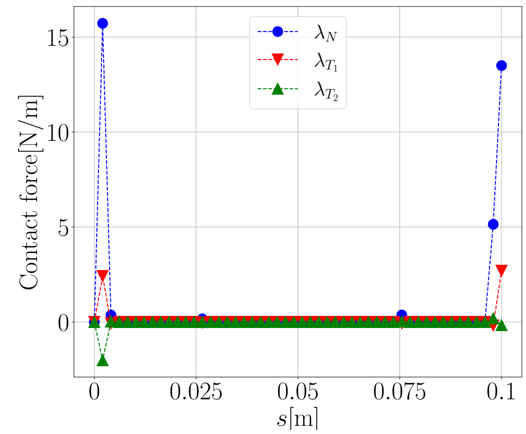

(b) Cyclic phase: Sliding of the right joint. Here at maximum horizontal displacement.

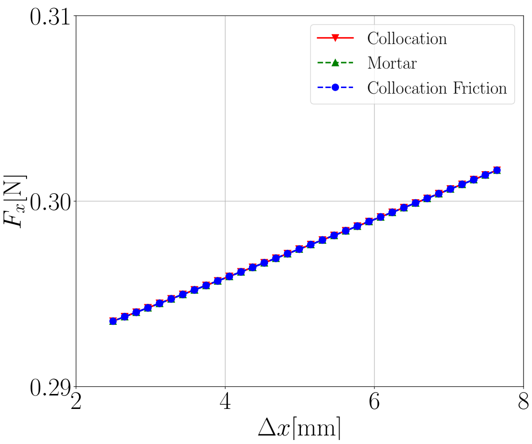

(c) Cyclic phase: Horizontal reaction force F_x[N] in function of the horizontal displacement Δx[mm].

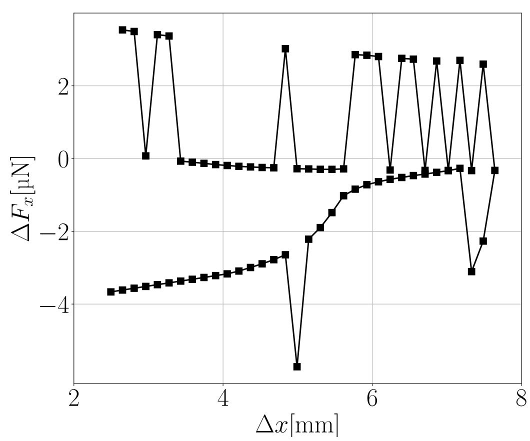

(d) Cyclic phase: Difference between the horizontal reaction force for the collocation method with and without friction ΔF_x[µN] in function of the horizontal displacement Δx[mm].

Figure 3.26: Top: Contact forces along the span of the contact line at different time instants during the bending of the twisted pair simulation. Bottom: Analysis of the reaction force.

Two spatial discretization strategies were introduced for the contact line: a collocation technique that enforces the contact law at discrete locations and is straightforward to implement and a mortar finite element method that enforces the contact law in a weak sense through integration over the contact region. The resulting discrete nonsmooth problem was addressed using an augmented Lagrangian formulation combined with a semismooth Newton method. In parallel, progress was made towards incorporating a Gauss-Seidel algorithm to enable contact-by-contact resolution strategies.

Numerical examples, including benchmark tests and beam twisting, were used to assess the behavior and accuracy of the proposed approaches. Novel analytic solutions were derived to that end. We conclude that the Euler-Bernoulli model leads to a point contact force at the boundary of the contact region and the shear force is discontinuous. For the Timoshenko beam however, a purely distributed load is excerted by the wall, and the shear force is continuous. We show optimal spatial convergence rates as expected for our frictionless mortar implementation.

CHAPTER 4

DYNAMIC BEAM-TO-BEAM CONTACT

Chapter 3 was concerned with the spatial aspects of discretizing contact. Now, the semi-discretized system is chosen as a starting point and we turn our attention towards time integration. We take the same beam elements as before and we make the same assumptions on the kinematics of contact. As discussed in the introduction, situations might occur, where impacts between beams cause instantaneous jumps in the velocity. These modeling effects are well understood in the field of rigid body dynamics. They have been studied extensively and specialized numerical methods have been devised to handle these challenges, see [188–191, 212, 220, 221]. The case of beam-to-beam contact is less obvious. These discontinuities in time have different origins. Two are in the model and due to the radial rigidity of our chosen beam formulation or result from frictional stick-slip transitions. A third one is a consequence of the finite element space discretization. When contact occurs exactly at the location of nodes, the numerical model becomes analoguous to the impact of rigid bodies. Indeed, finite element nodes have finite mass associated to them. We therefore speak of numerical impacts. In any case, the conclusion is the same. At the moment of impact, the acceleration is not defined in the classical sense.

For that reason, a general nonsmooth formalism that has its roots in the nonsmooth rigid body dynamics literature and valid both for the smooth parts of motion and at impact time is appropriate. Such a formulation was first introduced by Moreau and Jean in [222–224]. The equilibrium equations are written as equalities of measures instead of ODEs, which opens the door to time stepping schemes for nonsmooth mechanical systems. The Paoli and Schatzman scheme in [225, 226] is also very popular. In section 4.2 we present the formulation in the particular case of beam-to-beam contact. In the Moreau-Jean time integration scheme, the non-penetration constraints are only enforced at velocity level. As a consequence, this scheme suffers from numerical drift. Moreover, it cannot capture vibration phenomena accurately, since it only uses first order numerical approximations of the involved differential operators. For the simulation of flexible multibody systems these are major issues. Indeed, vibrations play an important role in many systems that contain flexible components and though not the subject of this thesis, the presence of bilateral constraints for the modeling of joints should not be forgotten. Time integrators allowing numerical drift are not well suited at all in such situations. The recent trend has been the development of integrators that impose position, velocity and potentially also acceleration constraints simultaneously and that use higher order approximations for the free part of the motion. These start from a Gear-Gupta-Leimkühler (GGL) type stabilization of the equations of motion.

The decoupled nonsmooth generalized-α (NSGA) scheme by Cosimo et al. [136] is one example, see section 4.3. It is particularly well suited for systems involving flexible components and is therefore the method of choice in this work. Not only does it remedy the drifting problem, it also allows for second order integration of the smooth part of the motion and fine control over numerical dissipation. Two properties which are appreciated in the structural mechanics community. The generalized-α scheme was initially constructed for solving the equations of free motion [227] and later extented to constrained mechanical systems [228] and formulations on Lie groups [139–141]. Most recent efforts were dedicated to the inclusion of unilateral constraints, beginning with frictionless contact [134, 135, 229], and then allowing for multiple impacts and friction [209, 210, 230–232]. This lead to the development of a few different versions of the NSGA. They are all characterized by a suitable splitting of the variables into smooth and impulsive (nonsmooth) contributions. The main difference between the different NSGA methods is the choice of this splitting. In the version by Cosimo et al. the resulting algorithm solves a sequence of three uncoupled problems at each time step, starting by a smooth prediction that excludes any contact constraints and followed by two projection steps. One that corrects for the non-penetration constraint at position level and one for the velocity jump.

The chapter starts by introducing the nonsmooth formalism for contact dynamics in Sec. 4.1. In this first formulation, non penetration constraints are expressed at position level. In Sec. 4.2 we describe the formulation at velocity level and the derivation of the NSGA follows in Sec. 4.3. In section 4.3.5 we discuss the augmented Lagrangian formulation with a semismooth Newton method and a direct linear solver. Finally, in section 4.4, we show the validity of the proposed algorithms by means of some numerical examples. The goal of this chapter is to demonstrate that together with the $SE(3)$ local frame approach, these methods can deal with all the difficulties related to the simulation of beam-to-beam contact in an elegant manner.

4.1 Formulation at position level

Here, we introduce the basic ideas underlying nonsmooth contact mechanics. The final goal is to present a first formulation of the dynamics with contact constraints simply appearing as an extension of the position contraints we encountered in the previous chapter. This version of the equations of motion will be our starting point for constructing the nonsmooth algorithm.

4.1.1 Mathematical preliminaries

We start by introducing some important mathematical concepts necessary for the understanding of nonsmooth formalisms [190, 191, 197, 222].

Definition: A function $\mathbf{f} : \mathbf{I} \to \mathbb{R}^n$ is *absolutely continuous* on the interval $\mathbf{I}$ if, for every $\epsilon > 0$, there exists a $\delta > 0$ such that,

$$\sum_{i=1}^{m} \|\mathbf{f}(b_i) - \mathbf{f}(a_i)\| \leq \epsilon \tag{4.1}$$

for any m and every finite collection of pairwise disjoint intervals $[a_i, b_i] \in \mathbf{I}$ satisfying

$$\sum_{i=1}^{m} (b_i - a_i) < \delta. \tag{4.2}$$

For a real valued function $\mathbf{f}$ on an interval $I = [a, b]$ the following statements are equivalent:

- $\mathbf{f}$ is absolutely continuous.
- The derivative of $\mathbf{f}$, written $\mathbf{f}'$, exists almost everywhere and is Lebesgue integrable, and we have

$$\mathbf{f}(t) = \mathbf{f}(a) + \int_a^t \mathbf{f}'(\tau)\,\mathrm{d}\tau \tag{4.3}$$

for all $t \in I$.

Definition: A function $\mathbf{f} : \mathbf{I} \to \mathbb{R}^n$ is called a *step function* when it takes a finite number of values on the domain $\mathbf{I}$, such that it can be written as

$$\mathbf{f}(t) = \sum_{i=1}^{m} \alpha_i \Psi_{Z_i}(t), \tag{4.4}$$

where $m \in \mathbb{N}$, $\alpha_i \in \mathbb{R}$ and Ψ_{Z_i} is the indicator function of the set Z_i that takes the value 1 if $t \in Z_i$ and is zero otherwise. A graphical example of a step function is shown in fig. 4.1a.

For illustrative purposes let us briefly study the simple example shown in fig. 4.1c: the Heaviside or unit step function. All step functions can be written as a linear combination of the Heaviside function. We define it as

$$H(t) \coloneqq \begin{cases} 1, & t > 0 \\ 0, & t < 0 \end{cases} . \tag{4.5}$$

In some definitions, the value of $H(0)$ is left unspecified or defined as $H(0) = 1$. We will use $H(0) = 0.5$. It is also defined as the derivative of the ramp function

$$H(t) \coloneqq \frac{\mathrm{d}}{\mathrm{d}t} \max(t, 0) \quad \text{for } t \neq 0. \tag{4.6}$$

The derivative of the Heaviside function vanishes everywhere except at the origin where it is infinite, which is exactly one of the properties of the Dirac Delta function $\delta(t)$. To make sure that the integral of the Dirac Delta function is indeed the Heaviside function its definition contains a normalization condition such that we write

$$\delta(t) = \begin{cases} +\infty & \text{if } t = 0 \\ 0 & \text{if } t \neq 0 \end{cases}, \quad \int_{-\infty}^{+\infty} \delta(t)\,\mathrm{d}t = 1 \tag{4.7}$$

and we can hence also write the Heaviside function as

$$H(t) := \int_{-\infty}^{t} \delta(\tau)\,\mathrm{d}\tau. \tag{4.8}$$

Definition: A function $\mathbf{f} : \mathbf{I} \to \mathbb{R}^n$ is of *locally bounded variation* if and only if

$$\sup \sum_{i=1}^{n} \|\mathbf{f}(t_i) - \mathbf{f}(t_{i-1})\| < \infty \tag{4.9}$$

for every compact subinterval $[a, b] \in \mathbf{I}$.

For a function of a single variable it can be visualized as the vertical distance travelled by a point that follows the graph always remains finite. This also means that the function is allowed to exhibit jumps as long as these are finite. Fig. 4.1b shows a classical counter example.

A function of locally bounded variation f may be decomposed as

$$\mathbf{f} = \mathbf{f}_{sg} + \mathbf{f}_{st} + \mathbf{f}_{ac}, \tag{4.10}$$

where

- $\mathbf{f}_{sg}$ is a singular function. It is continuous, non-constant and has a vanishing derivative almost everywhere.
- $\mathbf{f}_{st}$ is a step function.
- $\mathbf{f}_{ac}$ is absolutely continuous.

4.1.2 Nonsmooth mechanical systems

As discussed in the introduction of this chapter contact interactions between beams can cause jumps in the velocity and accelerations that are not defined in the classical sense. As a consequence we cannot write the equations of motion as DAEs since they are not valid at the precise moments where impacts occur.

We will see below that the equations of motion can be written in terms of measure differential inclusions. Solutions of measure differential inclusions are defined as functions of locally bounded variation i.e. solutions of measure differential inclusions contain the contribution of a step function, which can account for jumps in the evolution of

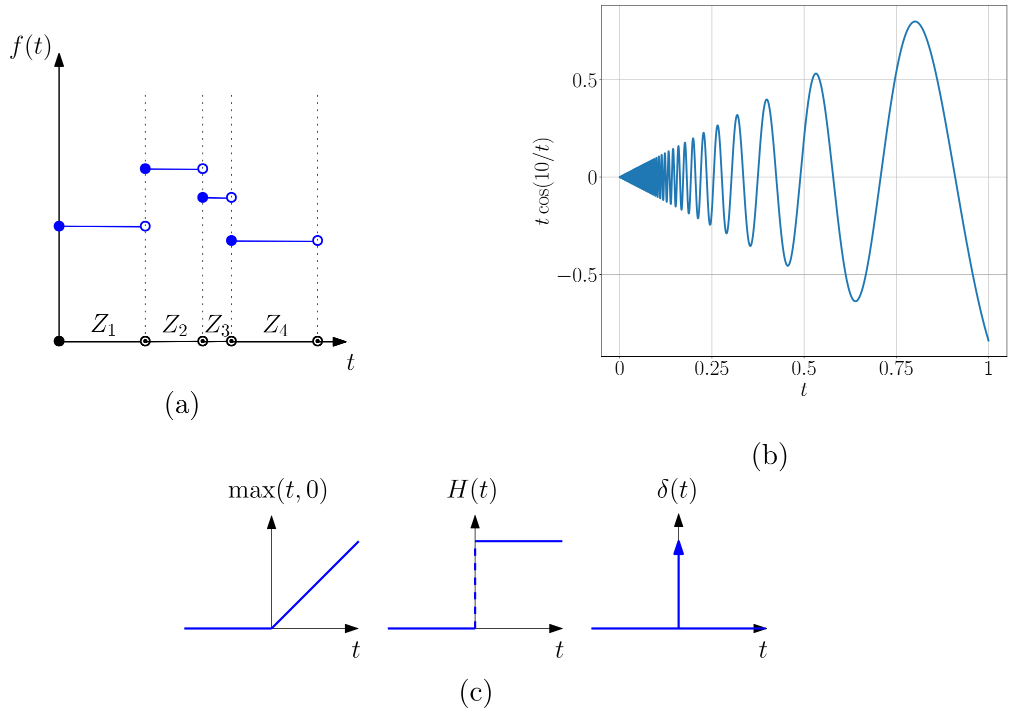

Figure 4.1: (a) Example of a step function. (b) Example of a continuous function that is not of locally bounded variation: $f(t) = t\cos(10/t)$ for $t \in]0, 1]$. (c) Graph of the ramp function, the Heaviside function and the Dirac Delta function.

the state variables such as for example the velocity. Hence, they are the appropriate mathematical framework to express the dynamics our mechanical system.

The pose of a space discretized mechanical system q is assumed absolutely continuous in time. The velocity is of locally bounded variation. Therefore it admits a decomposition analogous to Eq. (4.10)

$$\boldsymbol{v} = \boldsymbol{v}_{st} + \boldsymbol{v}_{ac}. \tag{4.11}$$

The smooth part of motion is contained in $\boldsymbol{v}_{ac}$ whereas the nonsmooth part related to impact effects is contained in $\boldsymbol{v}_{st}$, see fig. 4.2. The singular function was left out as it is not necessary in the context of mechanical systems. Moreover, the velocity always admits a right and a left limit

$$\boldsymbol{v}^{+}(t) = \lim_{\tau \to t, \tau > t} \boldsymbol{v}(\tau), \quad \boldsymbol{v}^{-}(t) = \lim_{\tau \to t, \tau < t} \boldsymbol{v}(\tau). \tag{4.12}$$

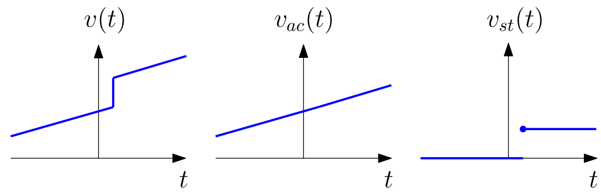

Figure 4.2: Decomposition of the velocity into a step function and an absolutely continuous function.

To simplify notations we will consider $\boldsymbol{v}(t) = \boldsymbol{v}^+(t)$ from now on.

In a nonsmooth formalism, the time derivative of the velocity is replaced by the differential measure $\mathrm{d}\boldsymbol{v}$. Similarly, the contact force becomes the impulse measure $\mathrm{d}\mathbf{i}$. Following Eq. (4.11) the velocity measure is decomposed as

$$\begin{aligned}\mathrm{d}\boldsymbol{v} &= \mathrm{d}\boldsymbol{v}_{st} + \mathrm{d}\boldsymbol{v}_{ac} \\ &= \dot{\boldsymbol{v}}\mathrm{d}t + \sum_i \left(\boldsymbol{v}(t_i) - \boldsymbol{v}^-(t_i)\right)\delta_{t_i}\end{aligned} \tag{4.13}$$

We denote δ_{t_i} the Dirac delta supported at impact time t_i and $\mathrm{d}t > 0$ is the standard Lebesgue measure for time. In a similar fashion the impulse measure is split as

$$\mathrm{d}\mathbf{i} = \boldsymbol{\Lambda}\mathrm{d}t + \sum_i \mathbf{p}_i\delta_{t_i}, \tag{4.14}$$

The variable $\boldsymbol{\Lambda}$ is a Lagrange multiplier associated to smooth motion and the $\mathbf{p}_i$ is the impulse reaction force caused by an impact at time t_i. The equilibrium equations of a system of beams with contact conditions in terms of differential measures are

$$\mathbf{M}\mathrm{d}\boldsymbol{v} - \mathbf{B}^T\mathrm{d}\mathbf{i} + \mathbf{f}\mathrm{d}t = \mathbf{0} \tag{4.15}$$

under the contact laws formulated at position level:

$$\begin{aligned} & g_N^j \in \partial\psi_{\mathbb{R}^-}(\mathrm{d}i_N^j), \\ \text{if } g_N^j \leq 0: \quad & \boldsymbol{v}_T^j + e_T^j\boldsymbol{v}_T^{j,-} \in \partial\psi_{C(\mathrm{d}i_N^j)}(\mathrm{d}\mathbf{i}_T^j), \quad \forall j = 1, 2, ..., N_C. \end{aligned} \tag{4.16}$$

At impact time t_i we prescribe the change of velocity using the Newton impact law. In the normal direction it writes

$$v_N^j = -e_N^j v_N^{j,-}, \tag{4.17}$$

where the normal contact velocity is defined as

$$v_N^j = \mathbf{B}_N^j \boldsymbol{v}. \tag{4.18}$$

In the tangential direction it is

$$\boldsymbol{v}_T^j = -e_T^j \boldsymbol{v}_T^{j,-}, \tag{4.19}$$

where the tangential contact velocity is defined as

$$\boldsymbol{v}_T^j = \mathbf{B}_T^j \boldsymbol{v}. \tag{4.20}$$

The restitution coefficients express the amount of energy that is lost during an impact. They take values between 0 and 1 for e_N and between -1 and 1 for e_T. They can be measured experimentally or derived through analytic considerations. For flexible bodies one usually takes $e_N^j = e_T^j = 0$. This means that if the pre-impact velocity is finite, the change in velocity is sudden i.e. $\boldsymbol{v}(t_i) - \boldsymbol{v}^-(t_i) \neq \mathbf{0}$. We speak of a velocity jump.

Remarks

- The kinematic equations in Eq. (2.75b) also hold for every nodal frame.
- Particularizing notations to a two-beam system we introduce the following definitions. $\mathbf{M}(q) = \mathrm{diag}(\mathbf{M}_1, \mathbf{M}_2)$ is the total mass matrix, which depends on the relative configuration between the nodal frames. $\mathbf{M}_1$ and $\mathbf{M}_2$ are the assembled mass matrices of the slave and master beam respectively, as they are found in Eq. (2.79). Similarly, $\mathbf{f}(q, \boldsymbol{v}, t) = \begin{bmatrix} \mathbf{f}_1 \\ \mathbf{f}_2 \end{bmatrix}$ is total force vector. Akin to Eq. (2.78c), it contains the assembled internal, external and gyroscopic forces of both beams.
- $\mathrm{d}\boldsymbol{v} = \begin{bmatrix} \mathrm{d}\boldsymbol{v}_1 \\ \mathrm{d}\boldsymbol{v}_2 \end{bmatrix}$ contains the differential measure associated to the velocity of every node.

- The $g_N^j(q)$ are simply the normal (weighted) gaps, $\mathbf{g}_T^j(q)$ are the tangential (weighted) gaps and $\mathbf{B}(q)$ is the assembled constraint gradient as it was defined in Chapter 3, which has a normal contribution $\mathbf{B}_N^j$ and a tangential contribution $\mathbf{B}_T^j$ to a given contact j.

- $\mathrm{d}\mathbf{i} = \begin{bmatrix} \mathrm{d}i_N \\ \mathrm{d}\mathbf{i}_T \end{bmatrix}$ denotes the impulse measures of the contact force associated to the whole set of contacts.

- As in the previous chapter, $\psi_{\mathbb{R}^+}$ is the indicator function of $\mathbb{R}^+$ and $\partial\psi_{\mathbb{R}^+}$ its subdifferential. Moreover, $\psi_{C(\mathrm{d}i_N)}$ is the indicator function of a section of the Coulomb friction cone such that Eq. (4.16) represents frictional contact conditions. The inclusions in Eq. (4.16) are shortcuts for $\partial\psi_{\mathbb{R}^+}(\lambda_N^j)$ and $\partial\psi_{C(\lambda_N^j)}(\boldsymbol{\lambda}_T^j)$ during the smooth part of motion and $\partial\psi_{\mathbb{R}^+}(p_{iN}^j)$ and $\partial\psi_{C(p_{iN}^j)}(\mathbf{p}_{iT}^j)$ at impact time t_i.

- N_C is the total number of discrete constraints. For the mortar formulation it is related to the order of the shape functions used to interpolate the distributed contact pressure. For a collocation type approach it is simply the number of collocation points.

4.2 Formulation at velocity level

The Newton impact law can be directly embedded into into the equations of motion by writing the constraints at velocity level [209, 210, 222–224]. From now on, the developments are particularized to the case $e_N = e_T = 0$, which is usually accepted for contacts between flexible bodies. The equivalence between the velocity formulation and the formulation presented in the previous section is ensured by Moreau's viability Lemma. The equations write:

$$\mathbf{M}\mathrm{d}\boldsymbol{v} - \mathbf{B}^T\mathrm{d}\mathbf{i} + \mathbf{f}\mathrm{d}t = \mathbf{0}, \tag{4.21}$$

under the contact laws at velocity level:

$$-v_N^j \in \partial\psi_{\mathbb{R}^+}(\mathrm{d}i_N^j), \quad \text{if } g_N^j \leq 0, \quad \forall j = 1, 2, ..., N_C \tag{4.22a}$$

$$-\boldsymbol{v}_T^j \in \partial\psi_{C(\mathrm{d}i_N^j)}(\mathrm{d}\mathbf{i}_T^j), \quad \text{if } g_N^j \leq 0 \quad \forall j = 1, 2, ..., N_C. \tag{4.22b}$$

Let us write the explicit form of the contact laws for clarity. The impenetrability in Eq. (4.22a) are expressed at the level of the normal contact velocity: if $g_N^j \leq 0$

$$v_N^j \geq 0, \quad \mathrm{d}i_N^j \geq 0, \quad v_N^j \mathrm{d}i_N^j = 0. \tag{4.23}$$

In the time-continuum setting it is equivalent to the normal position constraints in Eq. (4.16) [189, 190] together with the impact law in Eqs. (4.17) and (4.19).

Note that at velocity level we have the inequality $g_N^j \leq 0$ in Eq. (4.22a) and not the equality $g_N^j = 0$ as one could expect. It appears as part of Moreau's proof of his viability Lemma.

Coulomb's law in Eq. (4.22b) is most naturally expressed in terms of the tangential contact velocity. Explicitly it writes:

$$\boldsymbol{v}_T^j \|\mathrm{d}\mathbf{i}_T^j\| = -\|\boldsymbol{v}_T^j\| \mathrm{d}\mathbf{i}_T^j, \quad \mu \mathrm{d}i_N^j - \|\mathrm{d}\mathbf{i}_T^j\| \geq 0, \quad \|\boldsymbol{v}_T^j\| \left(\mu \mathrm{d}i_N^j - \|\mathrm{d}\mathbf{i}_T^j\|\right) = 0. \tag{4.24}$$

In the smooth part of the motion the friction conditions are

$$\boldsymbol{v}_T^j \|\boldsymbol{\lambda}_T^j\| = -\|\boldsymbol{v}_T^j\| \boldsymbol{\lambda}_T^j, \quad \mu \lambda_N^j - \|\boldsymbol{\lambda}_T^j\| \geq 0, \quad \|\boldsymbol{v}_T^j\| \left(\mu \lambda_N^j - \|\boldsymbol{\lambda}_T^j\|\right) = 0 \tag{4.25}$$

and when $g_N^j = 0$ at impact time $t = t_i$ a friction law of similar form holds:

$$\boldsymbol{v}_T^j \|\mathbf{p}_{iT}^j\| = -\|\boldsymbol{v}_T^j\| \mathbf{p}_{iT}^j, \quad \mu p_{iN}^j - \|\mathbf{p}_{iT}^j\| \geq 0, \quad \|\boldsymbol{v}_T^j\| \left(\mu p_{iN}^j - \|\mathbf{p}_{iT}^j\|\right) = 0. \tag{4.26}$$

4.2.1 Particular cases of the equations of motion

In the static case, the first term in Eq. (4.21) is ignored and the impulse measure boils down to its smooth contribution as $\mathrm{d}\mathbf{i} = \boldsymbol{\Lambda}\mathrm{d}t$ such that the equilibrium of forces is given by

$$\left(\mathbf{f} - \mathbf{B}^T \boldsymbol{\Lambda}\right) \mathrm{d}t = \mathbf{0}, \tag{4.27}$$

which is true when the expression in brackets vanishes. The frictional contact constraints are expressed by Eq.(4.25), but $\boldsymbol{v}_T^j$ is replaced by the slip increment $\mathrm{d}\mathbf{g}_T^j$ as we showed in Chapter 3. Hence we recover quasi-static algorithms as a particular case of the present formulation.

In the absence of impacts the equilibrium equations fall back to traditional ordinary differential equations

$$\mathbf{M}\dot{\boldsymbol{v}} - \mathbf{B}^T\boldsymbol{\Lambda} + \mathbf{f} = \mathbf{0}, \tag{4.28}$$

that hold together with Eqs (4.25). In many computational mechanics applications it is the above model that is considered [147–149, 153, 160, 183]. These are also covered as a particular case of the formulation in terms of measure differential equations.

4.3 NSGA time integration scheme

The nonsmooth generalized-α method we will present in this section is an extension of the classical algorithm by Chung and Hulbert [227]. It is designed for an absolutely continuous configuration variable that is part of a Lie group. In this thesis we follow the works of Cosimo et al. [210]. Let us also mention a version of the NSGA that includes constraints at acceleration level by Brüls et al. [135] and Capobianco [232] and the progress made by Wang [233] in introducing the mortar method in a nonsmooth framework.

4.3.1 Representation of motion

Since in the present case the configuration q is an element of a Lie group $G = SE(3)^N$ and we work with a representation of derivatives in the Lie algebra by left translation, a slight adaptation of the derivation presented in [134] is necessary, as briefly presented in discrete form in [210]. Here, we present a complete derivation of the NSGA for mechanical systems on a Lie group starting from the continuous time formulation. We consider a time interval $\mathcal{I} =]t_n, t_{n+1}]$ and suppose that the variables $q(t_n)$ and $\boldsymbol{v}(t_n)$ are known at $t = t_n$. In chapter 2 we saw that the configuration q at some time $t \in \mathcal{I}$ may be represented by an increment vector $\boldsymbol{\alpha}$ making use of the exponential map

$$q(t) = q(t_n)\exp_G\left(S(\boldsymbol{\alpha}(t))\right), \tag{4.29}$$

The time derivative of the increment vector is related to the velocity

$$\dot{\boldsymbol{\alpha}} = \mathbf{T}_G^{-1}(\boldsymbol{\alpha})\boldsymbol{v}. \tag{4.30}$$

Eqs. (4.29) and (4.30) are kinematic equations that always hold for the duration of the considered time interval.

4.3.2 Velocity splitting

Following [134–136,209], we introduce a splitting of variables to separate impulsive from smooth contributions to the motion. In the considered time interval $\mathcal{I}$, let $\dot{\tilde{\boldsymbol{v}}}(t)$ be a function of bounded variations. It plays the role of a smooth acceleration. The smooth part of the velocity field, written $\tilde{\boldsymbol{v}}(t)$, is obtained by integrating it with the initial value $\tilde{\boldsymbol{v}}(t_n) = \boldsymbol{v}(t_n)$. The velocity measure is decomposed as

$$\mathrm{d}\boldsymbol{v} = \mathrm{d}\boldsymbol{w} + \dot{\tilde{\boldsymbol{v}}}\mathrm{d}t. \tag{4.31}$$

The variable $\mathrm{d}\boldsymbol{w}$ contains all discontinuous contributions to the velocity resulting from any impacts during the considered time interval. The smooth configuration $\tilde{q}(t)$ and velocity $\tilde{\boldsymbol{v}}(t)$ are defined as the solution to the following contact free initial value problem

$$\tilde{q} = q(t_n)\exp_G\left(S(\tilde{\boldsymbol{\alpha}})\right), \tag{4.32a}$$

$$\dot{\tilde{\boldsymbol{\alpha}}} = \mathbf{T}_G^{-1}(\tilde{\boldsymbol{\alpha}})\tilde{\boldsymbol{v}}, \tag{4.32b}$$

$$\mathbf{M}(\tilde{q})\dot{\tilde{\boldsymbol{v}}} - \mathbf{f}(\tilde{q}, \tilde{\boldsymbol{v}}, t) = \mathbf{0}. \tag{4.32c}$$

with initial values $\tilde{q}(t_n)$ and $\tilde{\boldsymbol{v}}(t_n)$. Note that the problem defined above only includes smooth variables. It is independent of the total configuration and the total velocity which will naturally result in a time integration scheme where the different subproblems are uncoupled. Eq. (4.32b) is a consequence of Eq. (4.32a). These two equations are thus not independent, but we write them down explicitly here to show that these relations must hold for the smooth motion. Isolating $\mathrm{d}\mathbf{w}$ in Eqs. (4.31), (4.32) and

(4.21) yields an equation for the nonsmooth variables

$$\mathbf{M}(q)\mathrm{d}\mathbf{w} - \mathbf{B}^T\mathrm{d}\mathbf{i} - \mathbf{f}^*(q, \boldsymbol{v}, \tilde{q}, \tilde{\boldsymbol{v}}, \dot{\tilde{\boldsymbol{v}}}, t)\mathrm{d}t = \mathbf{0}. \tag{4.33}$$

together with the contact constraints in Eqs. (4.22a) and (4.22b) and with the vector of forces of which smooth contributions were subtracted as

$$\mathbf{f}^*(q, \boldsymbol{v}, \tilde{q}, \tilde{\boldsymbol{v}}, \dot{\tilde{\boldsymbol{v}}}, t) = \mathbf{f}(q, \boldsymbol{v}, t) - \mathbf{f}(\tilde{q}, \tilde{\boldsymbol{v}}, t) + (\mathbf{M}(\tilde{q}) - \mathbf{M}(q))\,\dot{\tilde{\boldsymbol{v}}}. \tag{4.34}$$

4.3.3 Gear-Gupta-Leimkühler formulation

The impenetrability constraints in Eq. (4.22a) are written at velocity level. As mentioned in the section 4.2, the exact solution of the problem as formulated in Eqs. (4.21) and (4.22) also satisfies the constraints at position level in Eq. (4.16). This is no longer true after time discretization. A time integration algorithm based on the problem formulation presented in the previous section with constraints only enforced at velocity level will not satisfy the position constraints due to a numerical drift effect. For that reason Brüls et al. [134] proposed a Gear-Gupta-Leimkühler type reformulation [133] of the equations of motion that includes the velocity and position constraints explicitly. This strategy leads to a discretization procedure that simulatneously satisfies impenetrability at position and velocity level. It can be interpreted as an index reduction operation for systems with inequality constraints. A similar technique can be applied to add information about the contact problem at acceleration level. [135, 232].

The idea is to add the constraints at position level to the kinematic equation above. To keep a well posed problem, we relax Eq. (4.32b) by multiplying both sides by the mass matrix and introducing an additional Lagrange multiplier $\boldsymbol{\zeta}$ analogous to $\boldsymbol{\Lambda}$

$$\mathbf{M}(q)\mathbf{T}_G(\boldsymbol{\alpha})\dot{\boldsymbol{\alpha}} - \mathbf{B}^T\boldsymbol{\zeta} = \mathbf{M}(q)\boldsymbol{v}. \tag{4.35}$$

For the exact solution, $\boldsymbol{\zeta}$ is supposed to vanish since the velocity and position constraints are redundant. Eq. (4.30) is thus technically not satisfied if $\boldsymbol{\zeta} = \mathbf{0}$. However, we have

$$\boldsymbol{\alpha}(t) = \boldsymbol{\alpha}(t_n) + \int_{t_n}^{t} \dot{\boldsymbol{\alpha}}(\tau)\,\mathrm{d}\tau. \tag{4.36}$$

The full set of EOMs now is (i) an equation for the smooth motion

$$\mathbf{M}(\tilde{q})\dot{\tilde{\boldsymbol{v}}} - \mathbf{f}(\tilde{q}, \tilde{\boldsymbol{v}}, t) = \mathbf{0}, \tag{4.37}$$

(ii) a problem at position level

$$\mathbf{M}(q)\mathbf{T}_G(\boldsymbol{\alpha})\dot{\boldsymbol{\alpha}} - \mathbf{B}^T\boldsymbol{\zeta} = \mathbf{M}(q)\boldsymbol{v}, \tag{4.38}$$

with associated position constraints

$$-g_N^j \in \partial\psi_{\mathbb{R}^+}(\zeta_N^j), \quad \forall j = 1, 2, ..., N_C \tag{4.39a}$$

$$-\mathbf{g}_T^j \in \partial\psi_{C(\zeta_N^j)}(\boldsymbol{\zeta}_T^j), \quad \forall j = 1, 2, ..., N_C \tag{4.39b}$$

and (iii) an equation for the nonsmooth contributions

$$\mathbf{M}(q)\mathrm{d}\mathbf{w} - \mathbf{B}^T\mathrm{d}\mathbf{i} - \mathbf{f}^*(q, \boldsymbol{v}, \tilde{q}, \tilde{\boldsymbol{v}}, \dot{\tilde{\boldsymbol{v}}}, t)\mathrm{d}t = \mathbf{0}, \tag{4.40}$$

with the original constraints at velocity level

$$-v_N^j \in \partial\psi_{\mathbb{R}^+}(\mathrm{d}i_N^j), \quad \text{if } g_N^j \leq 0, \quad \forall j = 1, 2, ..., N_C \tag{4.41a}$$

$$-\boldsymbol{v}_T^j \in \partial\psi_{C(\mathrm{d}i_N^j)}(\mathrm{d}\mathbf{i}_T^j), \quad \text{if } g_N^j \leq 0 \quad \forall j = 1, 2, ..., N_C. \tag{4.41b}$$

The representation of motion in Eq. (4.29) also still holds. When setting $\boldsymbol{\zeta} = \mathbf{0}$ Eqs. (4.37) to (4.41b) are equivalent to Eqs. (4.31) to (4.33) together with the kinematic relation in Eq. (4.30) and the constraints at velocity level in Eq. (4.22a) and (4.22b). When all constraints are active, the equations reduce to Gear-Gupta-Leimkühler formalism for DAEs. Analogous to the position constraints in the quasi-static setting, the tangential position constraints in Eq. (4.39b) are written in terms of increments to be able to capture the irreversible nature of friction.

4.3.4 Time integration method

Now that all preparations have been made we can turn our attention towards the actual time discretization. The idea is that since by construction $\tilde{q}(t)$ and $\tilde{\boldsymbol{v}}(t)$ are sufficiently smooth to be integrated by a higher-order time integration formula. In our case we employ the generalized-α scheme which is of order two. Then nonsmooth correction terms are defined such that the contact constraints are satisfied. We start with the velocity jump which is defined by

$$\mathbf{W}(t_n;t) = \int_{t_n}^{t} \mathrm{d}\mathbf{w}, \tag{4.42}$$

which satisfies

$$\mathbf{W}(t_n;t) = \boldsymbol{v}(t) - \cancel{\boldsymbol{v}_n} - \tilde{\boldsymbol{v}}(t) + \cancel{\tilde{\boldsymbol{v}}_n} = \boldsymbol{v}(t) - \tilde{\boldsymbol{v}}(t). \tag{4.43}$$

The terms cancel out due to our assumptions on the initial configuration and the intial velocity. The position correction is defined as

$$\mathbf{U}(t_n;t) = \int_{t_n}^{t} \left[\dot{\boldsymbol{\alpha}} - \mathbf{T}_G^{-1}(\tilde{\boldsymbol{\alpha}})\tilde{\boldsymbol{v}}\right] \mathrm{d}\tau, \tag{4.44}$$

satisfies

$$\begin{aligned}
\mathbf{U}(t_n;t) &= \boldsymbol{\alpha}(t) - \boldsymbol{\alpha}(t_n) - \int_{t_n}^{t} \mathbf{T}_G^{-1}(\tilde{\boldsymbol{\alpha}})\tilde{\boldsymbol{v}}\,\mathrm{d}\tau \\
&= \boldsymbol{\alpha}(t) - \cancel{\boldsymbol{\alpha}(t_n)} - \tilde{\boldsymbol{\alpha}}(t) + \cancel{\tilde{\boldsymbol{\alpha}}(t_n)} \\
&= \boldsymbol{\alpha}(t) - \tilde{\boldsymbol{\alpha}}(t),
\end{aligned} \tag{4.45}$$

where we used Eqs. (4.36) and (4.32b) and we have $\mathbf{W}(t_n;t_n) = \mathbf{U}(t_n;t_n) = \mathbf{0}$. We additionally define the multipliers

$$\boldsymbol{\Lambda}(t_n;t) = \int_{t_n}^{t} \mathrm{d}\mathbf{i}, \tag{4.46}$$

and

$$\boldsymbol{\nu}(t_n;t) = \int_{t_n}^{t} [\boldsymbol{\zeta}(\tau) + \boldsymbol{\Lambda}(t_n;\tau)] \, \mathrm{d}\tau. \tag{4.47}$$

The time step size is written $h = t_{n+1} - t_n$ and discretized approximations of the variables are denoted by a subscript as in $q_{n+1} \approx q(t_{n+1})$, $\boldsymbol{v}_{n+1} \approx \boldsymbol{v}(t_{n+1})$ etc. We also introduce the discrete nonsmooth variable $\mathbf{W}_{n+1} \approx \mathbf{W}(t_n;t_{n+1})$ (and $\mathbf{U}_{n+1} \approx \mathbf{U}(t_n;t_{n+1})$, $\boldsymbol{\Lambda}_{n+1} \approx \boldsymbol{\Lambda}(t_n;t_{n+1})$, $\boldsymbol{\nu}_{n+1} = \boldsymbol{\nu}(t_n;t_{n+1})$ respectively) and $\boldsymbol{\Lambda}_{n+1} = \boldsymbol{\Lambda}(t_{n+1})$ (and $\boldsymbol{\nu}_{n+1} \approx \boldsymbol{\nu}(t_{n+1})$ respectively).

The time integration scheme is based on a discrete approximation of Eqs. (4.38) and (4.40). We start by Eq. (4.40) which is discretized as:

$$\mathbf{M}(q(t_{n+1}))\mathbf{W}_{n+1} = \mathbf{B}_{n+1}^{T}\boldsymbol{\Lambda}_{n+1} + h\mathbf{f}_{n+1}^{*} + \mathcal{O}(h). \tag{4.48}$$

Indeed, integrating Eq. (4.40) over $]t_n, t]$ and keeping in mind that q is continuous gives

$$\begin{aligned} \mathbf{0} &= \int_{t_n}^{t} \mathbf{M}(q) \, \mathrm{d}\mathbf{w} - \int_{t_n}^{t} \mathbf{B}^T \, \mathrm{d}\mathbf{i} - \int_{t_n}^{t} \mathbf{f}^* \, \mathrm{d}\tau \\ &= \mathbf{M}(q) \underbrace{\int_{t_n}^{t} \mathrm{d}\mathbf{w}}_{=\mathbf{W}} - \mathbf{B}^T \underbrace{\int_{t_n}^{t} \mathrm{d}\mathbf{i}}_{=\boldsymbol{\Lambda}} - h\mathbf{f}^* + \mathcal{O}(h) \quad \forall t \in \mathcal{I}. \end{aligned} \tag{4.49}$$

Then, Eq. 4.48 is obtained by setting $t = t_{n+1}$. Note the appearance of the velocity jump $\mathbf{W}_{n+1}$ in Eq. (4.48). Now we focus our attention to the discretization of Eq. (4.38) for which the following holds:

$$\mathbf{M}(q_{n+1})\mathbf{U}_{n+1} = \mathbf{B}_{n+1}^{T}\boldsymbol{\nu}_{n+1} + h^2\mathbf{f}_{n+1}^{*} + \mathcal{O}(h^2). \tag{4.50}$$

This property is obtained by integrating Eq. (4.38) over the time step $\mathcal{I}$ and introducing Eq. (4.50) and Eq. (4.43) as follows:

$$
\begin{aligned}
\mathbf{0} &= \int_{t_n}^{t_{n+1}} \left(\mathbf{M}(q)\mathbf{T}_G(\boldsymbol{\alpha})\dot{\boldsymbol{\alpha}} - \mathbf{B}^T\boldsymbol{\zeta} - \mathbf{M}(q)\boldsymbol{v}\right) \,\mathrm{d}t \\
&= \int_{t_n}^{t_{n+1}} \left(\mathbf{M}(q)\mathbf{T}_G(\boldsymbol{\alpha})\left(\dot{\boldsymbol{\alpha}} - \mathbf{T}_G^{-1}(\boldsymbol{\alpha})\tilde{\boldsymbol{v}}\right) - \mathbf{B}^T\boldsymbol{\zeta} - h\mathbf{f}^*\right) \,\mathrm{d}t \\
&= \int_{t_n}^{t_{n+1}} \left(\mathbf{M}(q)\mathbf{T}_G(\boldsymbol{\alpha})\left(\dot{\boldsymbol{\alpha}} - \mathbf{T}_G^{-1}(\boldsymbol{\alpha})\tilde{\boldsymbol{v}}\right) - \mathbf{B}^T\left(\boldsymbol{\zeta} + \boldsymbol{\Lambda}\right) - h\mathbf{f}^* + \mathcal{O}(h)\right) \,\mathrm{d}t \\
&= \mathbf{M}(q_{n+1}) \underbrace{\int_{t_n}^{t_{n+1}} \left(\dot{\boldsymbol{\alpha}} - \mathbf{T}_G^{-1}(\tilde{\boldsymbol{\alpha}})\tilde{\boldsymbol{v}}\right) \,\mathrm{d}t}_{=\mathbf{U}_{n+1}} - \mathbf{B}_{n+1}^T \underbrace{\int_{t_n}^{t_{n+1}} \left(\boldsymbol{\zeta} + \boldsymbol{\Lambda}\right) \,\mathrm{d}t}_{=\boldsymbol{\nu}_{n+1}} - h^2\mathbf{f}^* + \mathcal{O}(h^2).
\end{aligned}
\tag{4.51}
$$

In the final step of the derivation we used $\mathbf{M}(q) = \mathbf{M}_{n+1} + \mathcal{O}(h)$, $\mathbf{B}(q) = \mathbf{B}_{n+1} + \mathcal{O}(h)$, $\mathbf{T}_G(\boldsymbol{\alpha}) = \mathbb{I} + \mathcal{O}(h)$ and $\mathbf{T}_G(\boldsymbol{\alpha}) = \mathbf{T}_G(\tilde{\boldsymbol{\alpha}}) + \mathcal{O}(h)$ which is a consequence of the continuity of q. The three terms in the equation above are interpreted as nonsmooth contributions since they appear as the difference between the total and the smooth motion. For the first term it is obvious. The second term contains $\boldsymbol{\Lambda}$ which is the discrete multiplier associated to the nonsmooth velocity problem. As shown by Eq. (4.34) the third term also involves the difference between contributions from the full and the smooth motion.

Smooth motion

The smooth motion, we simply solve Eq. (4.37) using the generalized-α scheme, as in Sec. 2.3.2

$$
\tilde{q}_{n+1} = q_n \exp_G\left(S(\tilde{\boldsymbol{\alpha}}_{n+1})\right), \tag{4.52a}
$$

$$
\mathbf{M}(\tilde{q}_{n+1})\dot{\tilde{\boldsymbol{v}}}_{n+1} - \mathbf{f}(\tilde{q}_{n+1}, \tilde{\boldsymbol{v}}_{n+1}, t_{n+1}) = \mathbf{0}. \tag{4.52b}
$$

Unsurprisingly, it is the exact same set of equations as described in Eq. (2.88). The equations only involve the smooth variables $\tilde{q}_{n+1}$, $\tilde{\boldsymbol{\alpha}}_{n+1}$, $\tilde{\boldsymbol{v}}_{n+1}$ and $\dot{\tilde{\boldsymbol{v}}}_{n+1}$. They can hence be solved completely independently of any information about the contact state stored in the position correction $\mathbf{U}_{n+1}$, the velocity jump $\mathbf{W}_{n+1}$ or the full kinematic variables q_{n+1} and $\boldsymbol{v}_{n+1}$.

Position correction

After the computation of the smooth motion the configuration of the system is corrected using Eq. (4.44) evaluated at t_{n+1} as

$$\boldsymbol{\alpha}_{n+1} = \tilde{\boldsymbol{\alpha}}_{n+1} + \mathbf{U}_{n+1}, \tag{4.53}$$

where $\mathbf{U}_{n+1}$ is obtained by solving a discrete contact problem satisfying the normal and tangential constraints at position level. This position correction step ensures the absence of numerical drift that notoriously plagues velocity based time integration schemes.

The dependence of $\mathbf{f}^*$ on $\boldsymbol{v}$ in Eq. (4.50) signifies a coupling between the equation above that we intend to solve for $\mathbf{U}_{n+1}$ and the problem at velocity level. Cosimo et al. [136, 210] argue that the $\mathbf{f}^*$ operator is much more sensitive to changes in q than $\boldsymbol{v}$ such that the actual equation they propose to solve for the position correction is

$$\mathbf{M}(\tilde{q}_{n+1})\mathbf{U}_{n+1} - h^2\mathbf{f}^p_{n+1} - \mathbf{B}^T\boldsymbol{\nu}_{n+1} = \mathbf{0}. \tag{4.54}$$

where $\mathbf{f}^p_{n+1} = \mathbf{f}(q_{n+1}, \tilde{\boldsymbol{v}}_{n+1}, t_{n+1}) - \mathbf{f}(\tilde{q}_{n+1}, \tilde{\boldsymbol{v}}_{n+1}, t_{n+1})$, effectively neglecting inertial effects and fixing the velocity to its smooth contribution while computing the position correction. This modification gave satisfying results on academic test cases including flexible systems. Therefore we will employ the same simplification.

As in [134, 210] we impose discrete position contraints based on the integrated quantity $\boldsymbol{\nu}_{n+1}$ and with the gap functions evaluated at q_{n+1}

$$-g^j_{N,n+1} \in \partial\psi_{\mathbb{R}^+}(\nu^j_{N,n+1}), \quad \forall j = 1, 2, ..., N_C \tag{4.55a}$$

$$-\mathbf{g}^j_{T,n+1} \in \partial\psi_{C(\nu^j_{N,n+1})}(\boldsymbol{\nu}^j_{T,n+1}), \quad \forall j = 1, 2, ..., N_C. \tag{4.55b}$$

If contact occurs during the time interval $\mathcal{I}$, $\zeta^j_{N,n+1} > 0$ and $\Lambda^j_{N,n+1} > 0$, hence from Eq. (4.47) we also have that $\nu^j_{N,n+1} > 0$. Similar considerations are true in the tangential direction. This justifies the use of Eqs. (4.55). Eq. (4.54) implies that if $\boldsymbol{\nu}_{n+1} \neq \mathbf{0}$ then $\mathbf{U}_{n+1} \neq \mathbf{0}$ i.e. if the constraints in Eqs. (4.55) are activated, then a non-vanishing position correction will be computed and the motion will deviate from the smooth trajectory as expected.

We could have opted for discrete versions of ζ_N and $\boldsymbol{\zeta}_T$ as suggested by the actual time continuum constraints in Eqs. (4.39). Since they are not immediately accessible by the algorithm which uses integrated values they need to be computed through a numerical integration step which is polluted by large numerical errors in the presence of impacts. This choice is thus not recommended.

Eq. (4.54) with the constraints (4.55) is to be solved for the unknows $\mathbf{U}_{n+1}$ and $\boldsymbol{\nu}_{n+1}$. The problem has the same mathematical structure as the quasi-static discrete friction problem presented in Eq. (3.76) and we can reuse the same solution algorithms, see Sec. 3.4. In this thesis we employ the augmented Lagrangian method. The augmented Lagrangian for the unilateral position constraints is given by

$$\begin{aligned}\mathcal{L}_p(\mathbf{U}_{n+1},\boldsymbol{\nu}_{n+1}) = \sum_{j=1}^{N_C} &- k_p g^j_{N,n+1}\nu^j_{N,n+1} + \frac{p_p}{2}(g^j_{N,n+1})^2 - \frac{1}{2p_p}\text{dist}^2\left[\xi^j_{N,n+1},\mathbb{R}^+\right] \\ &- k_p \mathbf{g}^j_{T,n+1}\cdot\boldsymbol{\nu}^j_{T,n+1} + \frac{p_p}{2}\|\mathbf{g}^j_{T,n+1}\|^2 - \frac{1}{2p_p}\text{dist}^2\left[\boldsymbol{\xi}^j_{T,n+1}, C_{\xi^j_{N,n+1}}\right],\end{aligned} \tag{4.56}$$

where we introduced the augmented multipliers $\xi^j_{N,n+1} = k_p\nu^j_{N,n+1} - p_p g^j_{N,n+1}$ and $\boldsymbol{\xi}^j_{T,n+1} = k_p\boldsymbol{\nu}^j_{T,n+1} - p_p\mathbf{g}^j_{T,n+1}$. As already detailed in Chap. 3 the solution to the position contact problem is then obtained by stationarity of the augmented Lagrangian:

$$\delta\mathcal{L}_p(\mathbf{U}_{n+1},\boldsymbol{\nu}_{n+1}) = 0. \tag{4.57}$$

Dual formulation for the position subproblem

In Sec. 3.4.2 we discussed the possility to solve discrete frictional contact problems using a Gauß-Seidel type technique as presented in [49]. Therefore we provide linearized dual form of the position contact problem in Eqs. (4.54) and (4.55) here. Following the same procedure as in Sec. 3.4.1 and 3.4.2 we obtain the following expressions.

The Delassus operator for the position subproblem is

$$\mathbf{D}_p = \mathbf{B}\left[\mathbf{M}(\tilde{q}_{n+1}) - h^2\mathbf{K}^p_T\right]^{-1}\mathbf{B}^T, \tag{4.58}$$

where

$$D\mathbf{f}^p_{n+1} \cdot \Delta \mathbf{q}_{n+1} = \mathbf{K}^p_T \Delta \mathbf{q}_{n+1} \tag{4.59}$$

and we define the vector

$$\mathbf{b}_p = -\mathbf{B}\left[\mathbf{M}(\tilde{q}_{n+1}) - h^2\mathbf{K}^p_T\right]^{-1}\left[\mathbf{M}(\tilde{q}_{n+1})\mathbf{U}_{n+1} - h^2\mathbf{f}^p_{n+1}\right] + \mathbf{g}^{\mathrm{con}}_{n+1}. \tag{4.60}$$

Just as in the quasi-static setting, the vector $\mathbf{g}^{\mathrm{con}}_{n+1}$ stacks all the normal and tangential gaps evaluated at time $t = t_{n+1}$. The linearizion of Eq. (4.54) yields an expression for the position correction analogous to Eq. (3.80):

$$\Delta\mathbf{U}_{n+1} = -\left[\mathbf{M}(\tilde{q}_{n+1}) - h^2\mathbf{K}^p_T\mathbf{T}_G\right]^{-1}\left[\mathbf{M}(\tilde{q}_{n+1})\mathbf{U}_{n+1} - h^2\mathbf{f}^p_{n+1} - \mathbf{B}^T\boldsymbol{\nu}_{n+1}\right]. \tag{4.61}$$

Velocity jump

After finding the pose q_{n+1} of the system, the velocity jump $\mathbf{W}_{n+1}$ is computed. To that end we solve the approximation of Eq. (4.48):

$$\mathbf{M}(q_{n+1})\mathbf{W}_{n+1} = \mathbf{B}^T_{n+1}\boldsymbol{\Lambda}_{n+1} + h\mathbf{f}^*_{n+1}(\boldsymbol{v}_{n+1}) \tag{4.62}$$

while enforcing the following discrete constraints at velocity level

$$-v^j_{N,n+1} \in \partial\psi_{\mathbb{R}^+}(\Lambda^j_{N,n+1}), \quad \forall j = 1,2,...,N_C \tag{4.63a}$$

$$-\boldsymbol{v}^j_{T,n+1} \in \partial\psi_{C(\Lambda^j_{N,n+1})}(\boldsymbol{\Lambda}^j_{T,n+1}), \quad \forall j = 1,2,...,N_C. \tag{4.63b}$$

The augmented multipliers for the augmented Lagrangian technique are $\sigma^j_{N,n+1} = k_v\Lambda^j_{N,n+1} - p_v v^j_{N,n+1}$ and $\boldsymbol{\sigma}^j_{T,n+1} = k_v\boldsymbol{\Lambda}^j_{T,n+1} - p_v\boldsymbol{v}^j_{T,n+1}$. Different scaling and penalty factors may be employed for the velocity and the position problem. The augmented Lagrangian functional associated to the velocity problem writes

$$\mathcal{L}_v(\mathbf{W}_{n+1}, \boldsymbol{\Lambda}_{n+1}) = \sum_{j=1}^{N_C} - k_v v^j_{N,n+1}\sigma^j_{N,n+1} + \frac{p_v}{2}(v^j_{N,n+1})^2 - \frac{1}{2p_v}\mathrm{dist}^2\left[\sigma^j_{N,n+1}, \mathbb{R}^+\right]$$
$$- k_v \boldsymbol{v}^j_{T,n+1}\cdot\boldsymbol{\sigma}^j_{T,n+1} + \frac{p_v}{2}\|\boldsymbol{v}^j_{T,n+1}\|^2 - \frac{1}{2p_v}\mathrm{dist}^2\left[\boldsymbol{\sigma}^j_{T,n+1}, C_{\sigma^j_{N,n+1}}\right] \tag{4.64}$$

and the solution is obtained by requiring:

$$\delta\mathcal{L}_v(\mathbf{W}_{n+1}, \boldsymbol{\sigma}_{n+1}) = 0. \tag{4.65}$$

Dual formulation for the velocity subproblem

Again, we can write the dual formulation introduced in Sec. 3.4.2 of the velocity problem allowing the use of the solution algorithms in [49].

The Delassus operator is

$$\mathbf{D}_v = \mathbf{B}\left[\mathbf{M}(q_{n+1}) - h\mathbf{K}^v_T\right]^{-1}\mathbf{B}^T, \tag{4.66}$$

where

$$D\mathbf{f}^*_{n+1}\cdot\Delta\mathbf{q}_{n+1} = \mathbf{K}^v_T\Delta\mathbf{q}_{n+1} \tag{4.67}$$

and we define the vector

$$\mathbf{b}_v = -\mathbf{B}\left[\mathbf{M}(q_{n+1}) - h\mathbf{K}^v_T\right]^{-1}\left[\mathbf{M}(q_{n+1})\mathbf{W}_{n+1} - h\mathbf{f}^*_{n+1}\right] + \boldsymbol{v}^{\mathrm{con}}_{n+1}. \tag{4.68}$$

The vector $\boldsymbol{v}^{\mathrm{con}}_{n+1}$ stacks all the normal velocities $v^j_{N,n+1}$ and tangential velocities $\boldsymbol{v}^j_{T,n+1}$. The linearizion of Eq. (4.54) yields an expression for the velocity jump analogous to Eq. (3.80):

$$\Delta\mathbf{W}_{n+1} = -\left[\mathbf{M}(q_{n+1}) - h\mathbf{K}^v_T\mathbf{T}_G\right]^{-1}\left[\mathbf{M}(q_{n+1})\mathbf{W}_{n+1} - h\mathbf{f}^v_{n+1} - \mathbf{B}^T\boldsymbol{\Lambda}_{n+1}\right]. \tag{4.69}$$

4.3.5 Numerical implementation of the NSGA

The three subproblems in Eq. (4.52), Eq. (4.57) and Eq. (4.65) have to be solved at each time step. These correspond to a smooth prediction, a position correction and a velocity jump and are computed sequentially in a fully decoupled manner. For each subproblem we employ a semismooth Newton solution scheme as presended in Chap. 3. The algorithm is summarized in Alg. 4. The smooth motion is integrated using the generalized-α formulas. Therefore, the corrections $\Delta\dot{\tilde{\boldsymbol{v}}}_{n+1}$ and $\Delta\boldsymbol{\alpha}_{n+1}$ can be expressed in terms of $\Delta\tilde{\boldsymbol{v}}_{n+1}$, $\mathbf{W}_{n+1}$ and $\mathbf{U}_{n+1}$ as

$$\Delta\boldsymbol{v}_{n+1} = \Delta\tilde{\boldsymbol{v}}_{n+1} + \Delta\mathbf{W}_{n+1}, \tag{4.70a}$$

$$\Delta\dot{\tilde{\boldsymbol{v}}}_{n+1} = (1-\alpha_m)/\left((1-\alpha)\gamma h\right)\Delta\tilde{\boldsymbol{v}}_{n+1}, \tag{4.70b}$$

$$\Delta\boldsymbol{\alpha}_{n+1} = 1/\gamma'\Delta\tilde{\boldsymbol{v}}_{n+1} + \Delta\mathbf{U}_{n+1}. \tag{4.70c}$$

We denote the residuals of the different subproblems $\mathbf{r}_f^i$ for the force equilibrae, $\mathbf{r}_c^p, \mathbf{r}_c^v$ for the constraints and the tangent matrices $\mathbf{S}_t^i$, where $i = s, p, v$. The criterion used for checking the Newton scheme convergence in each sub-problem is denoted simply as

$$\mathbf{r}_f^i < \text{tol, for}\, i = s, p, v, \tag{4.71}$$

where *tol* is a composed tolerance. It is given by

$$\text{tol} = \text{tol}_r \left(\sum_k \|\mathbf{r}_{f,k}^i\| + \text{tol}_f \right), \tag{4.72}$$

where tol_r is a relative tolerance set by the user, $\mathbf{r}_{f,k}^i$ is the kth term contributing to the residual $\mathbf{r}_f^i$, tol_f is a reference tolerance and $\|\cdot\|$ denotes the L_2 norm.

The solution does not depend on the value of parameters k_s, k_p, k_v, p_s, p_p and p_v. However, the conditioning and consequently the convergence rate do depend on them. Therefore, the iteration matrices are scaled as follows [234]:

$$k_s = p_s = \frac{\bar{m}}{h}, k_p = p_p = \bar{m}, k_v = p_v = \bar{m} \tag{4.73}$$

where $\bar{m}$ is a characteristic mass of the problem.

We also provide a description of the solution scheme when replacing the nonsmooth Newton solver by the Gauß-Seidel algorithm in Alg. 5.

4.4 Numerical examples

We present four numerical examples to show the potential of combining the beam-to-beam contact finite element formulated on $SE(3)$ with the NSGA time integration scheme and the semismooth Newton method. We start by a dynamic version of the sliding patch test in Sec 4.4.1. The second example is the bouncing of a flexible beam on a rigid substrate in Sec. 4.4.2 which is followed by the bouncing of two flexible beams in Sec. 4.4.3. Finally, in Sec. 4.4.4 we study the twisting of two beams.

4.4.1 Sliding patch test

We redo the exact same test as for the quasi-static case in Sec. 3.5.1 with an imposed constraint at velocity level and show the results in Fig. 4.3. Similar conclusions can be drawn.

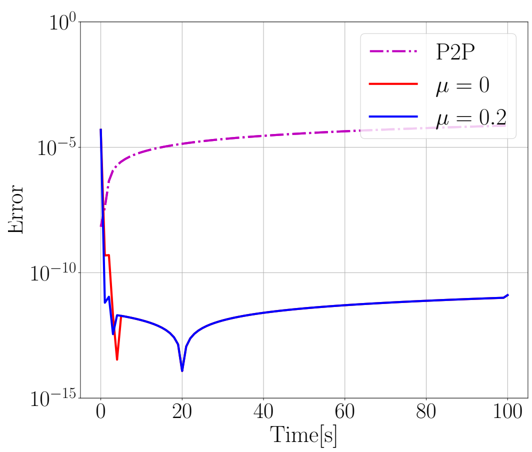

(a) Relative error.

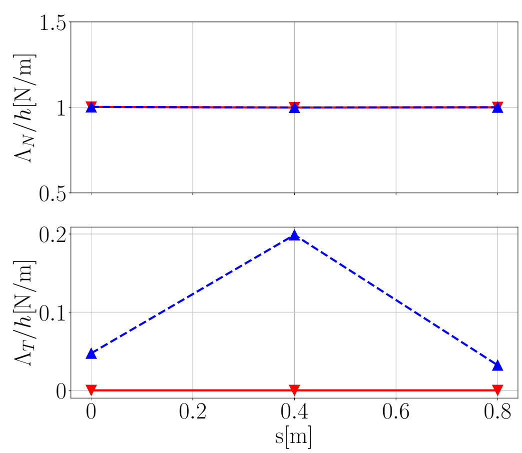

(b) Contact reaction forces.

Figure 4.3: Left: Relative error on the gap for different combinations of models and parameters. Right Top: Vertical distributed contact force. Right bottom: Tangential distributed contact force. Red: mortar with $\mu = 0$. Blue: mortar with $\mu = 0.2$, Other: Collocation with $\mu = 0.2$ (only on the left).

Algorithm 4 $[q_{n+1}, \boldsymbol{\Lambda}_{n+1}] = \text{solveNonsmoothGenAlphaTimeStep}(q_n)$

$\dot{\tilde{\boldsymbol{v}}}_{n+1} \coloneqq \mathbf{0}$, $\boldsymbol{\nu}_{n+1} \coloneqq \mathbf{0}, \boldsymbol{\Lambda}_{n+1} \coloneqq \mathbf{0}$, $\mathbf{U}_{n+1} \coloneqq \mathbf{0}$, $\mathbf{W}_{n+1} \coloneqq \mathbf{0}$
$\mathbf{a}_{n+1} \coloneqq (\alpha_f \dot{\tilde{\boldsymbol{v}}}_n - \alpha_m \mathbf{a}_n)/(1-\alpha_m)$
$\boldsymbol{v}_{n+1} \coloneqq \tilde{\boldsymbol{v}}_{n+1} \coloneqq \boldsymbol{v}_n + h(1-\gamma)\mathbf{a}_n + \gamma h \mathbf{a}_{n+1}$
$\boldsymbol{\alpha}_{n+1} \coloneqq h\boldsymbol{v}_n + (1/2-\beta)h^2\mathbf{a}_n + \beta h^2 \mathbf{a}_{n+1}$
Step 1 *(smooth motion)*:
for $k \in [1, \text{MaxIter}]$ **do**
    $q_{n+1} = q_n \exp_{SE(3)^N}(S(\boldsymbol{\alpha}_{n+1}))$
    compute $\mathbf{r}_f^s$
    if Convergence($\mathbf{r}_f^s$) **then** break **end if**
    compute $\mathbf{S}_t^s$
    $\Delta\boldsymbol{\alpha}_{n+1} \coloneqq -\mathbf{S}_t^{-1}\mathbf{r}_f^s$
    $\boldsymbol{\alpha}_{n+1} \coloneqq \boldsymbol{\alpha}_{n+1} + \Delta\boldsymbol{\alpha}_{n+1}$
    $\tilde{\boldsymbol{v}}_{n+1} \coloneqq \tilde{\boldsymbol{v}}_{n+1} + \gamma' \Delta\boldsymbol{\alpha}_{n+1}$
    $\dot{\tilde{\boldsymbol{v}}}_{n+1} \coloneqq \dot{\tilde{\boldsymbol{v}}}_{n+1} + \beta' \Delta\boldsymbol{\alpha}_{n+1}$
end for
Step 2 *(position correction)*:
for $k \in [1, \text{MaxIter}]$ **do**
    $q_{n+1} = q_n \exp_{SE(3)^N}(S(\boldsymbol{\alpha}_{n+1}))$
    compute $\mathbf{r}_f^p$, $\mathbf{r}_c^p$
    If Convergence($\mathbf{r}_f^p$) $\wedge$ Convergence($\mathbf{r}_c^p$) **then** break **end if**
    compute $\mathbf{S}_t^p$
    $\begin{bmatrix} \Delta\mathbf{U}_{n+1} \\ \Delta\boldsymbol{\nu}_{n+1} \end{bmatrix} \coloneqq -\left(\mathbf{S}_t^p\right)^{-1} \begin{bmatrix} \mathbf{r}_f^p \\ \mathbf{r}_c^p \end{bmatrix}$
    $\mathbf{U}_{n+1} \coloneqq \mathbf{U}_{n+1} + \Delta\mathbf{U}_{n+1}$
    $\boldsymbol{\alpha}_{n+1} \coloneqq \boldsymbol{\alpha}_{n+1} + \Delta\mathbf{U}_{n+1}$
    $\boldsymbol{\nu}_{n+1} \coloneqq \boldsymbol{\nu}_{n+1} + \Delta\boldsymbol{\nu}_{n+1}$
end for
Step 3 *(velocity jump)*:
for $k \in [1, \text{MaxIter}]$ **do**
    $q_{n+1} = q_n \exp_{SE(3)^N}(S(\boldsymbol{\alpha}_{n+1}))$
    compute $\mathbf{r}_f^v$, $\mathbf{r}_c^v$
    If Convergence($\mathbf{r}_f^v$) $\wedge$ Convergence($\mathbf{r}_c^v$) **then** break **end if**
    compute $\mathbf{S}_t^v$
    $\begin{bmatrix} \Delta\mathbf{W}_{n+1} \\ \Delta\boldsymbol{\Lambda}_{n+1} \end{bmatrix} \coloneqq -\left(\mathbf{S}_t^v\right)^{-1} \begin{bmatrix} \mathbf{r}_f^v \\ \mathbf{r}_c^v \end{bmatrix}$
    $\mathbf{W}_{n+1} \coloneqq \mathbf{W}_{n+1} + \Delta\mathbf{W}_{n+1}$
    $\boldsymbol{v}_{n+1} \coloneqq \tilde{\boldsymbol{v}}_{n+1} + \Delta\mathbf{W}_{n+1}$
    $\boldsymbol{\Lambda}_{n+1} \coloneqq \boldsymbol{\Lambda}_{n+1} + \Delta\boldsymbol{\Lambda}_{n+1}$
end for
$\mathbf{a}_{n+1} \coloneqq \mathbf{a}_{n+1} + (1-\alpha_f)/(1-\alpha_m)\dot{\tilde{\boldsymbol{v}}}_{n+1}$

Algorithm 5 $[q_{n+1}, \boldsymbol{\Lambda}_{n+1}] = \text{solveNonsmoothGenAlphaTimeStepGS}(q_n)$

$\dot{\tilde{\boldsymbol{v}}}_{n+1} \coloneqq \mathbf{0}$, $\boldsymbol{\nu}_{n+1} \coloneqq \mathbf{0}, \boldsymbol{\Lambda}_{n+1} \coloneqq \mathbf{0}$, $\mathbf{U}_{n+1} \coloneqq \mathbf{0}$, $\mathbf{W}_{n+1} \coloneqq \mathbf{0}$

$\mathbf{a}_{n+1} \coloneqq (\alpha_f \dot{\tilde{\boldsymbol{v}}}_n - \alpha_m \mathbf{a}_n)/(1-\alpha_m)$

$\boldsymbol{v}_{n+1} \coloneqq \tilde{\boldsymbol{v}}_{n+1} \coloneqq \boldsymbol{v}_n + h(1-\gamma)\mathbf{a}_n + \gamma h \mathbf{a}_{n+1}$

$\boldsymbol{\alpha}_{n+1} \coloneqq h\boldsymbol{v}_n + (1/2-\beta)h^2\mathbf{a}_n + \beta h^2 \mathbf{a}_{n+1}$

Step 1 *(smooth motion)*:

for $k \in [1, \text{MaxIter}]$ **do**

  $q_{n+1} = q_n \exp_{SE(3)^N}(S(\boldsymbol{\alpha}_{n+1}))$

  compute $\mathbf{r}_f^s$

  if Convergence($\mathbf{r}_f^s$) **then** break **end if**

  compute $\mathbf{S}_t^s$

  $\Delta\boldsymbol{\alpha}_{n+1} \coloneqq -\mathbf{S}_t^{-1}\mathbf{r}_f^s$

  $\boldsymbol{\alpha}_{n+1} \coloneqq \boldsymbol{\alpha}_{n+1} + \Delta\boldsymbol{\alpha}_{n+1}$

  $\tilde{\boldsymbol{v}}_{n+1} \coloneqq \tilde{\boldsymbol{v}}_{n+1} + \gamma' \Delta\boldsymbol{\alpha}_{n+1}$

  $\dot{\tilde{\boldsymbol{v}}}_{n+1} \coloneqq \dot{\tilde{\boldsymbol{v}}}_{n+1} + \beta' \Delta\boldsymbol{\alpha}_{n+1}$

end for

Step 2 *(position correction)*:

for $k \in [1, \text{MaxIter}]$ **do**

  $q_{n+1} = q_n \exp_{SE(3)^N}(S(\boldsymbol{\alpha}_{n+1}))$

  compute $\mathbf{r}_f^p$, $\mathbf{r}_c^p$

  If Convergence($\mathbf{r}_f^p$) $\wedge$ Convergence($\mathbf{r}_c^p$) **then** break **end if**

  compute $\mathbf{D}_p, \mathbf{b}_p$ ▷ Eqs. (4.58) and (4.60)

  $\boldsymbol{\nu}_{n+1} \coloneqq \text{so-bogus}\,(\mathbf{D}_p, \mathbf{b}_p, \text{MaxIterGS})$ ▷ Use hybrid local solver in [49]

  compute $\Delta\mathbf{U}_{n+1}$ ▷ Eq. (4.61)

  $\mathbf{U}_{n+1} \coloneqq \mathbf{U}_{n+1} + \Delta\mathbf{U}_{n+1}$

  $\boldsymbol{\alpha}_{n+1} \coloneqq \boldsymbol{\alpha}_{n+1} + \Delta\mathbf{U}_{n+1}$

end for

Step 3 *(velocity jump)*:

for $k \in [1, \text{MaxIter}]$ **do**

  $q_{n+1} = q_n \exp_{SE(3)^N}(S(\boldsymbol{\alpha}_{n+1}))$

  compute $\mathbf{r}_f^v$, $\mathbf{r}_c^v$

  If Convergence($\mathbf{r}_f^v$) $\wedge$ Convergence($\mathbf{r}_c^v$) **then** break **end if**

  compute $\mathbf{D}_v, \mathbf{b}_v$ ▷ Eqs. (4.66) and (4.68)

  $\boldsymbol{\Lambda}_{n+1} \coloneqq \text{so-bogus}\,(\mathbf{D}_p, \mathbf{b}_p, \text{MaxIterGS})$ ▷ Use hybrid local solver in [49]

  compute $\Delta\mathbf{W}_{n+1}$ ▷ Eq. (4.69)

  $\mathbf{W}_{n+1} \coloneqq \mathbf{W}_{n+1} + \Delta\mathbf{W}_{n+1}$

  $\boldsymbol{v}_{n+1} \coloneqq \tilde{\boldsymbol{v}}_{n+1} + \Delta\mathbf{W}_{n+1}$

end for

$\mathbf{a}_{n+1} \coloneqq \mathbf{a}_{n+1} + (1-\alpha_f)/(1-\alpha_m)\dot{\tilde{\boldsymbol{v}}}_{n+1}$

4.4.2 Frictionless bouncing flexible beam

This example intends to study the ability of the proposed methods to deal with dynamic impacts and to compare the behaviour of the mortar discretization and the collocation approach in such a situation. To that end a beam discretized by 21 elements is simply supported at both ends above a rigid ground and we define one single contact element at the central beam element. The material parameters are the following: Young's modulus $E = 210$[MPa], beam length $L = 1$[m], Poisson ratio $\nu = 0.3$, density $\rho = 7200[\mathrm{kg/m^3}]$, the beam has a circular cross-section of area $A = 10^{-4}[\mathrm{m^2}]$ and the centerline is initially located at a height $H = 4R$. The friction coefficient is set to $\mu = 0$. At the onset of the simulation the full gravitational load is applied and then maintained until the end of the simulation at $T = 1.5$ [s]. The time step is $h = 0.001$[s]. As an indication, the maximum number of Newton iterations per subproblem did not exceed 3.

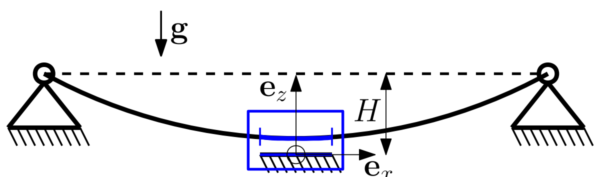

Figure 4.4: Bouncing flexible beam.

In a first phase the motion is fully unconstrained and smooth as can be observed in Fig. 4.5a showing the vertical position of the reference node on the beam centerline. Therefore it overlaps with the contact free case. Then a first impact occurs where the vertical velocity of the reference node, depicted in Fig. 4.5b, instantly drops from a finite value to zero. The beam enters into a contact phase where the position and velocity constraint is switched on and off, before the beam fully takes off again. Initially the collocation method and the mortar method provide very similar results for the position, velocity and acceleration, but as the simulation progresses discrepancies appear and increase with time. The contact reaction forces computed by division of the impulse $\mathbf{\Lambda}$ by the time step h are shown in Fig. 4.5d. For the mortar method these are obtained by integrating the position Lagrange multipliers along the element. They indicate that indeed several impacts occur during the contact phases.

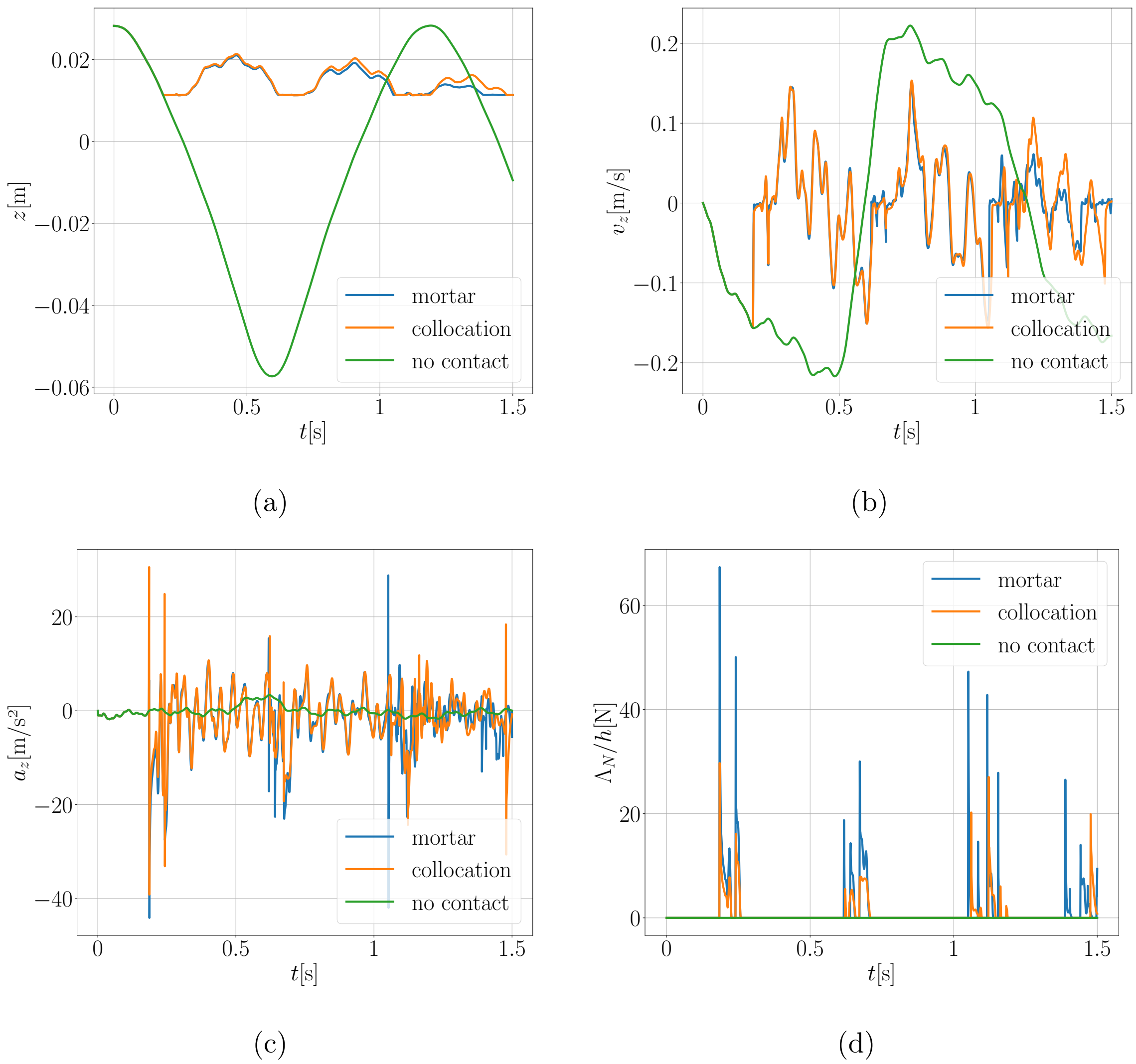

Figure 4.5: Frictionless bouncing flexible beam results. The reference node is the first beam finite element node used in the contact element. It is located slightly to left of the beam middle point: (a) Vertical position of the reference node. (b) Vertical velocity of the reference node. (c) Vertical acceleration of the reference node. (d) Contact reaction force.

4.4.3 Bouncing flexible on flexible beams

The previous examples showed the correct treatment of contact forces for non-matching grids and as nodes slide over each other, which did not deteriorate in the presence of friction nor dynamic effects, as well as the ability of the algorithm to handle the impact of a beam with a rigid ground. The present one focuses on the dynamic behaviour of two flexible beams that bounce on each other with the intention to verify the proper modeling of impacts in a line-to-line contact configuration using the mortar and the collocation approach. To that end, we take inspiration from [235] and set up the following example: two initially straight beams of lengths $L_1 = L_2 = 0.5$[m], radii $R_1 = R_2 = 5$[mm], Young moduli $E_1 = E_2 = 10^9$[Pa], Poisson ratios $\nu_1 = \nu_2 = 0.3$ and densities $\rho_1 = \rho_2 = 7200$[kg/m^3] are placed such that the initial gap is $g_0 = 10$[mm]. The lower beam is clamped at both ends while the upper one drops down under the effect of gravity. We first study the frictionless case with a friction coefficient $\mu = 0$, then we apply $\mu = 0.2$. We use a time step of $h = 10^{-4}$[s] and spectral radius at infinity of $\rho_\infty = 0.8$.

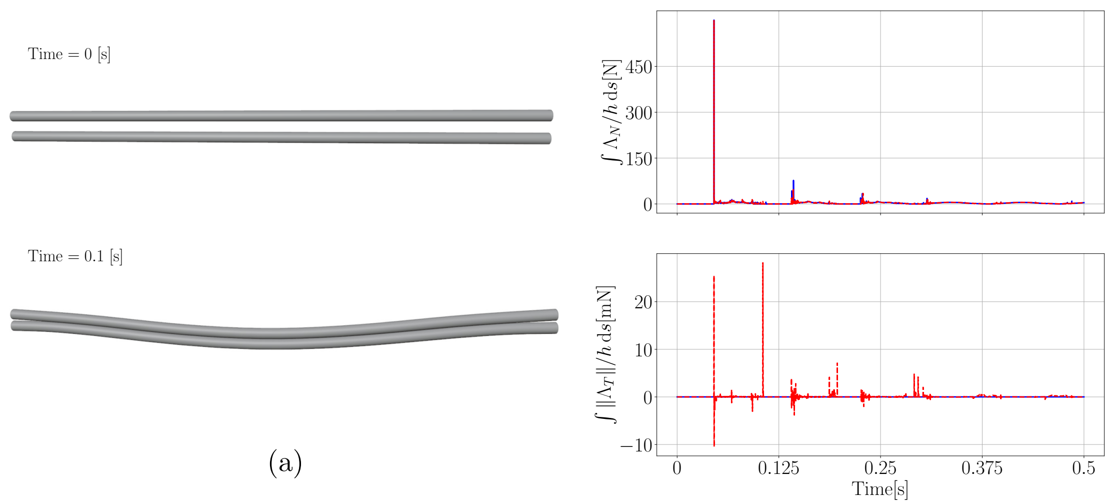

(a)

(b)

Figure 4.6: Results for the bouncing flexible on flexible beams example. (a) Deformation at the first impact. (b) Top figure: Integrated normal contact force: $\int \Lambda_N/h\,\mathrm{d}s$ [N]. Bottom figure: Integrated tangential contact force: $\int \|\mathbf{\Lambda}_T\|/h\,\mathrm{d}s$ [N]. Blue: $\mu = 0$. Red: $\mu = 0.2$.

Fig. 4.6a shows the initial configuration and the state of the system same time after the first impact. The evolution of the integrated contact force can be observed in Fig. 4.6b. At the moment of impact the weighted gap in Fig. 4.7 and the weighted relative velocity suddenly vanish which can also be highlighted by the kink in the displacement field or the instantaneous jump of the velocities in Fig. 4.7. This generates an impulse in the normal direction. One then observes an alteration of separation and contact phases. After some time, the system settles and both beams vibrate in phase. The addition of friction by setting $\mu = 0.2$ does not greatly affect the overall motion as expected for this test case. However, as can be observed in Fig. 4.6b the tangential contact force is non-zero due to the different bending curvatures of the two beams.

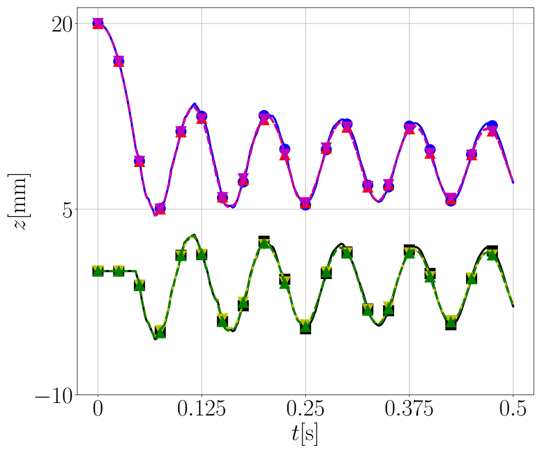

(a)

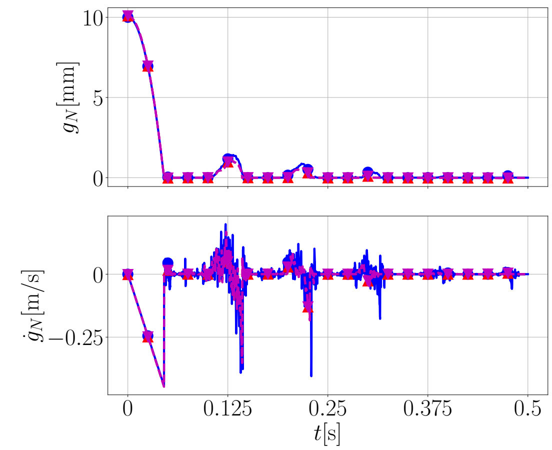

(b)

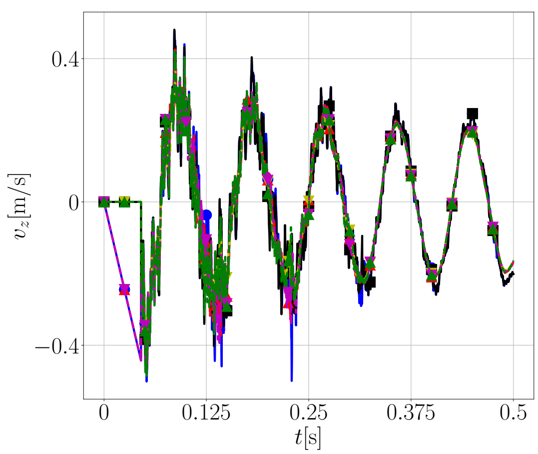

(c)

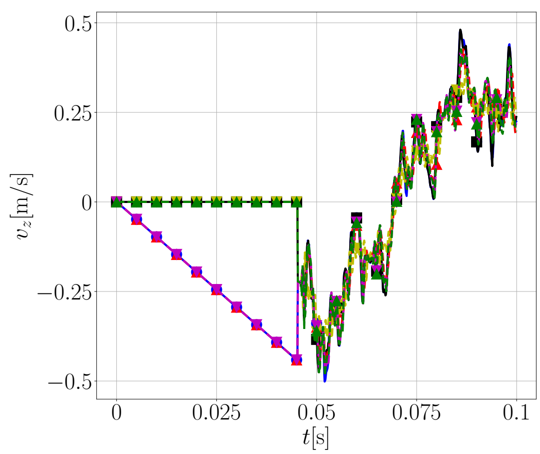

(d)

Figure 4.7: Results for the bouncing flexible on flexible beams example. (a): Position of the beam middle points. Blue: Top beam, collocation with $\mu = 0$ Red: Top beam, mortar with $\mu = 0$. Magenta: Top beam, mortar with $\mu = 0.2$. Black: Lower beam, collocation with $\mu = 0$. Yellow: Lower beam, mortar with $\mu = 0$. Green: Lower beam, mortar with $\mu = 0.2$. (b): Imposed position and velocity constraints associated to the slave middle node i.e. the weighted gap and the weighted relative velocity are divided by the element length for better comparison between the mortar and the collocation method. (c): Velocity of the beam middle points. (d): Zoom on the instants of impact.

4.4.4 Two-fiber dynamic twisting

The goal of this test case is to illustrate the ability of the method to deal with complex three dimensional deformations, inertial effects, friction and impacts. To that end we take inspiration from the quasi-static twisting example in Sec. 3.5.3. Two initially undeformed beams are clamped at one end and position controlled at the other end. These are of length $L_1 = L_2 = 1$[m], cross-section radii $R_1 = R_2 = R = 1$[mm], Young moduli $E_1 = E_2 = 5 \cdot 10^6$, Poisson ratios $\nu_1 = \nu_2 = 0.3$ and densities $\rho_1 = \rho_2 = 1100$[kg/m^3]. We use a time step of $h = 0.001$[s] and a spectral radius at infinity $\rho_\infty = 0.8$. The beams are discretized into 12 finite elements each. The time step is $h = 0.001$[s].

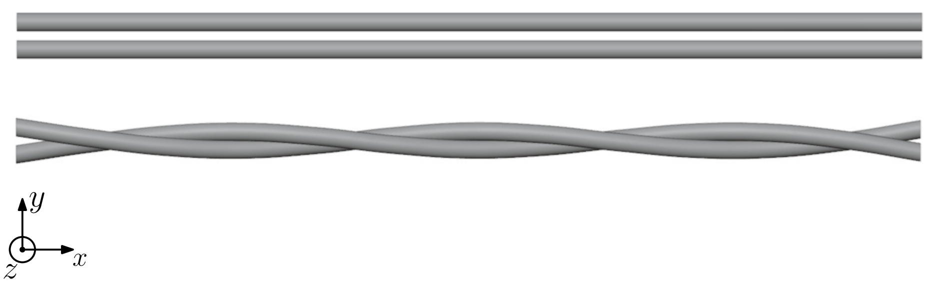

Figure 4.8: Initial and final configuration of the two-fiber twistig example.

The two beams are initially placed apart by a distance of R. During the simulation, the moving end nodes travel on a circular path of radius $R_{traj} = 1.5R$. They do a full revolution within 12[s]. We apply some physical damping to stabilize the simulation.

Fig. 4.9 shows the vertical position component of the top and lower middle beam point. Fig. 4.10 shows its velocity and Fig. 4.11 its smooth acceleration component. The beams demonstrate intricate dynamics attributed to the combination of frictional forces and inertial effects as can be observed in Fig. 4.12. A wave propagates within the slender structure due the imposed displacement at one extremity. Then, the first impact occurs after a simulation time of 3 seconds and we observe successive contact and detachement phenomena. Consequently, the middle points of the structure do not return to their initial positions by the conclusion of the simulation. The effect of the presence of friction in the model is more prominent for the collocation method than for the mortar approach. The mortar method distributes the contact constraints and forces more smoothly across the contact interface which is necessary for variational consistency [158]. The present example is highly non-linear. Our results indicate that the the global response of the beams is sensitive to the differences in the distribution of the frictional contact force between the collocation and the mortar method.

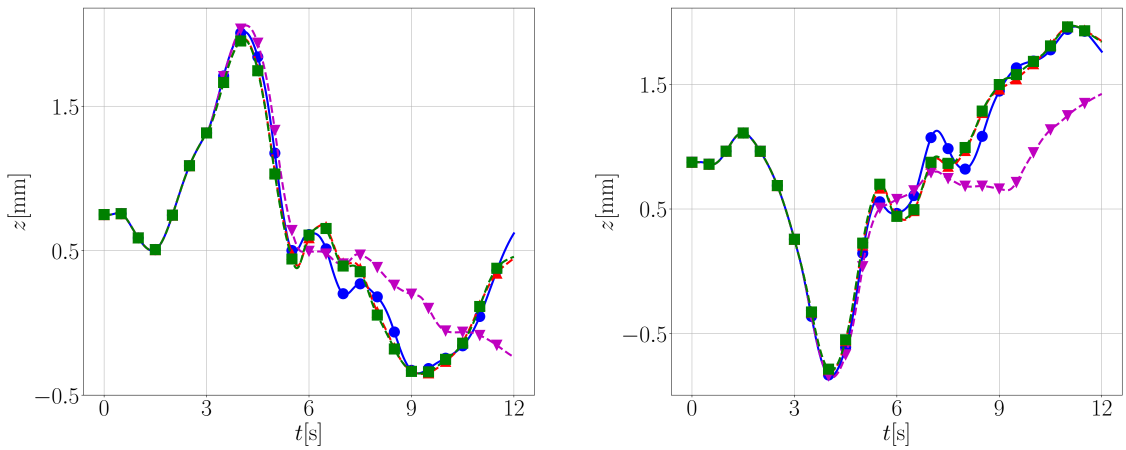

(a) (b)

Figure 4.9: Results for the two-fiber twisting example. (a) z-component of the top beam middle point position. (b) z-component of the lower beam middle point position. Blue: Collocation with $\mu = 0$. Red: Mortar with $\mu = 0$. Magenta: Collocation with $\mu = 0.2$. Green: Mortar with $\mu = 0.2$.

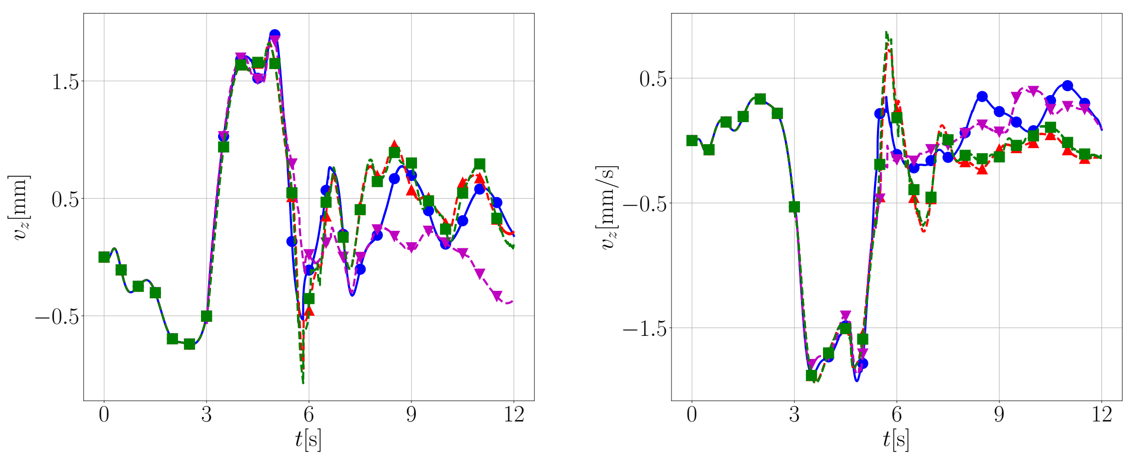

(a) (b)

Figure 4.10: Results for the two-fiber twisting example. (a) z-component of the top beam middle point velocity. (b) z-component of the lower beam middle point velocity. Blue: Collocation with $\mu = 0$. Red: Mortar with $\mu = 0$. Magenta: Collocation with $\mu = 0.2$. Green: Mortar with $\mu = 0.2$.

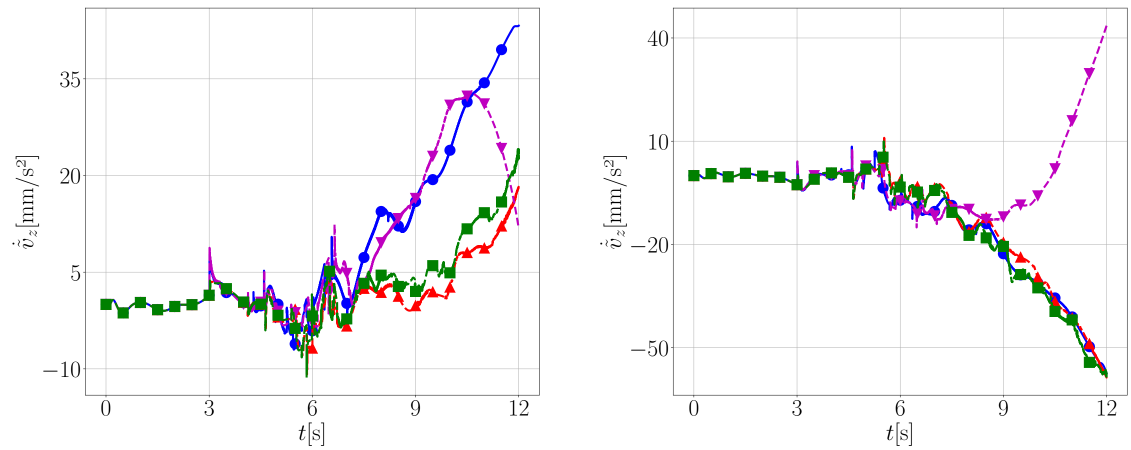

(a) (b)

Figure 4.11: Results for the two-fiber twisting example. (a) z-component of the top beam middle point smooth acceleration. (b) z-component of the lower beam middle point smooth acceleration. Blue: Collocation with $\mu = 0$. Red: Mortar with $\mu = 0$. Magenta: Collocation with $\mu = 0.2$. Green: Mortar with $\mu = 0.2$.

4.5 Concluding remarks

Chapter 4 is dedicated to the simulation of dynamic beam-to-beam contact. Due to the presence of nonsmooth effects in the model, accelerations are not defined in the classical sense. To address this, we develop a nonsmooth mechanical framework using measure differential inclusions to describe able to deal with the smooth and nonsmooth components of the motion.

Time integration is performed using the nonsmooth generalized-α (NSGA) scheme, which separates smooth and impulsive contributions and applies two projection steps to enforce contact constraints at position and velocity levels. We redevelop the NSGA for systems on a Lie group, starting from the continuous time formulation. Then, within this framework, we developed the contact elements using the collocation and mortar discretization presented in the previous chapter for the position and the velocity subproblems.

The discrete frictional contact problem, arising at the position and velocity subproblems at each time step share an identical mathematical structure as one load step in quasi-static analysis. We chose an augmented Lagrangian formulation of the discrete constraints paired with a monolithic nonsmooth Newton solver for its efficiency.

Several numerical examples were performed to make a first evaluation of the approach.

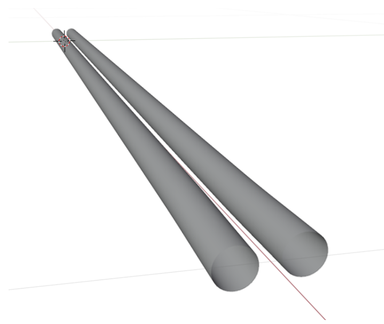

(a) $t = 0$[s]

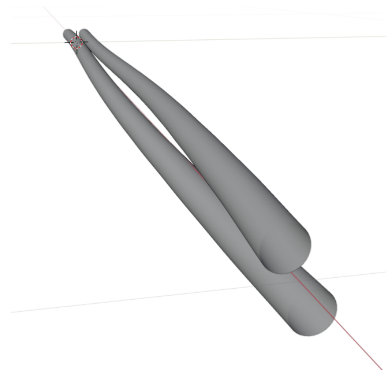

(b) $t = 2$[s]

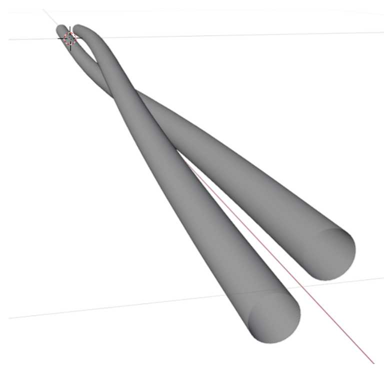

(c) $t = 4$[s]

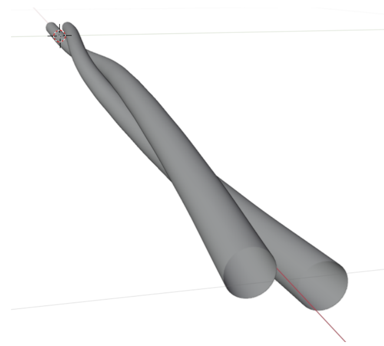

(d) $t = 6$[s]

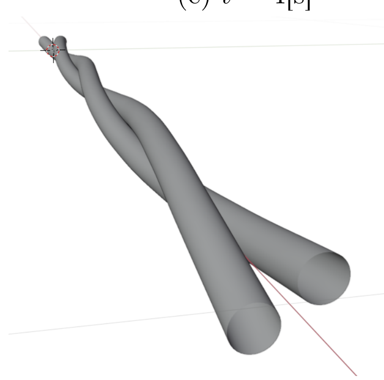

(e) $t = 10$[s]

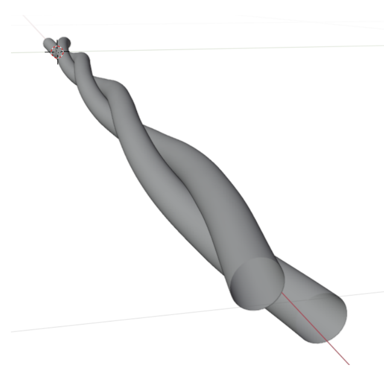

(f) $t = 12$[s]

Figure 4.12: Snapshots of the two-fiber dynamic twisting simulation. We use 12 finite elements per beam. Simulation time is $T = 12$[s] with a time step $h = 0.001$[s]. The transverse dimensions of the wires have been scaled in these pictures for graphical illustration purposes.

The full numerical procedure was implemented and we show credible results. These demonstrated the handling of impacts, friction, non-matching meshes, and three-dimensional beam deformations. This chapter shows the potential of combining Lie group methods, the NSGA formalism, and the either the collocation or mortar discretization approach to address the nonlinear and nonsmooth effects in dynamic beam contact problems. The next step would be to validate the approach by performing convergence analyses on test cases with an analytic solution.

CONCLUSION

In this thesis, we have investigated mathematical modeling and numerical algorithms for the simulation of mechanical systems involving highly flexible slender structures and their contact interactions. Throughout our exploration, we have advocated for the integration of both geometric finite element techniques and nonsmooth contact mechanics to address the complexities brought about by frictional interactions in such systems. The following discussion summarizes the contributions of this work, and outlines potential future directions for research.

Summary

The thesis starts by a detailed review of existing beam models and beam-to-beam contact algorithms. We highlighted the strengths and weaknesses of the most prominent approaches and identified how a nonsmooth local frame formulation complements what can be found in the scientific literature. The main contributions are:

- **Kirchhoff-Love and inextensible Kirchhoff beam model**: Building upon the established local frame philosophy for geometrically exact beams (Chapter 2), which utilizes rigrous Lie group concepts, this thesis presents extensions to a Kirchhoff-Love and an inextensible Kirchhoff beam model. These formulations inherit the advantages of the underlying framework – as demonstrated numerically, these include locking-free behaviour, reduced non-linearity, no need for reparametrization, and simple handling of initial deformation.
- **Local contact formulation on $SE(3)$**: We presented the development of frictional beam-to-beam contact kinematics within the local frame approach. Ex-

ploiting the $SE(3)$ Lie group framework, the contact conditions are formulated as unilateral restrictions on the relative motion between beams. The direction of contact forces, including friction, in the local frame is determined by the associated constraint gradient, which depends solely on relative motion. As a consequence, the equations benefit from the expected frame invariance properties.

- **A beam contact benchmark with analytic solution**: We derived a closed-form solution for a semi-infinite cantilever beam under a constant distributed load in frictionless contact with a rigid substrate. In the Euler-Bernoulli model, the contact force equals the applied load except at the boundary. In the Timoshenko model, the substrate exerts a distributed load that decays exponentially from the contact point, with a rate dependent on shear deformability. The transverse shear force, discontinuous in the Euler-Bernoulli model, becomes continuous in the Timoshenko model.

- **The mortar technique for static beam-to-beam contact**: Drawing inspiration from the field of contact mechanics for general deformable bodies a mortar method was developed for beam-to-beam contact interactions involving a distributed force per unit length. The non-penetration constraint is formulated in a weak sense and becomes a set of weighted integrals in the discretized setting. Interestingly, the combination with the geometrically exact beam formalism on the Lie group $SE(3)$ leads to a frame invariant tangent stiffness for the contact element. For the frictionless case, we show numerical experiments with optimal spatial convergence rates as expected for the mortar method, even in the presence of spatial discontinuities in the distributed contact force. While the frictionless implementation shows promising results, the current implementation in the frictional case lacks robustness when curved beams are involved.

- **The collocation approach for static beam-to-beam contact**: We also developed a simple and easier-to-implement collocation method to discretize the contact region. This method, provided the location density of the contact points is well chosen, yielded a robust scheme that delivered satisfying results, even when including friction. We discussed our numerical results for the collocation method compared to the mortar method in the presence and absence of frictional effects. In particular, we compared our numerical results to our analytic solution of the beam contact benchmark, and to experimental results of the torsion and bending of a twisted pair.

- **NSGA combined with the mortar and collocation technique for dynamic problems**: When non-penetration conditions are strictly enforced, the acceleration is not defined in the classical sense at the moment of impact. To address this challenge, this thesis employs a general nonsmooth formalism rooted in rigid body dynamics. We employ the nonsmoothe generalized-α scheme (NSGA) initially proposed flexible multibody systems with impacts. It uses anevaluation of the smooth part of the motion followed by the evaluation of two nonsmooth contributions: a position correction and a velocity jump. This prevents constraint drifting and ensures second-order accuracy of the smooth motion. To that end, we developed the collocation and mortar beam-to-beam contact elements at position and velocity levels within the NSGA framework. This includes the derivation of the discrete equilibrium equations and constraints at both levels and the computation of the tangent operators.

- **Augmented Lagrangian formulation and nonsmooth Newton solver**: The discrete frictional contact problems, arising at each load step in quasi-static analysis and for the position and velocity subproblems at each time step in the dynamic simulation, shares an identical mathematical structure. To solve this problem, we developed and implemented an augmented Lagrangian formulation of the discrete constraints paired with a monolithic nonsmooth Newton solver for its efficiency.

- **Towards a Gauß-Seidel–type solver**: A prerequesite for large-scale simulations is a robust solution scheme, motivating our exploration of an alternative Gauß-Seidel–type algorithm which yielded promising results for solving friction problems in rigid body dynamics. All the necessary derivations to adapt it to beam-to-beam contact have been performed in this thesis, which paves the way for a future implementation in simulation codes.

- **Implementation in the open source software Odin**: All the formulated contact elements developed within this thesis have been implemented in the open-source software Odin. These are the collocation and mortar discretizations of the beam-to-beam contact element both in the quasi-static and dynamic settings. Our contributions are thereby connected to a wide library of finite elements for the simulation of flexible multibody systems. We have performed various numerical experiments including: a quasi-static and a dynamic sliding patch test and the twisting of two fibers with and without frictional effects, the static frictionless contact of a cantilever with a rigid wall, the quasi-static nonlinear bending of a twisted pair with friction, the frictionless bouncing of flexible beam on a rigid wall and the bouncing of two flexible beams. The examples show the potential of combining all the previously mentioned concepts to form an appropriate framework for handling geometric non-linearities, discontinuities, and complex frictionless and frictional contact configurations exhibited by cable assemblies.

Further work

In this thesis, we focus on distributed contact interactions between slender rods with rigid circular cross-sections. We chose a nonsmooth Lie group formalism to capture the kinematics and dynamics to model such systems. The following aspects could be improved in future developments.

- The implementations of the beam-to-beam contact elements presented in this thesis lack an efficient collision detection algorithm which slows down performance considerably. A specialized contact search for slender objects would open the door to large scale simulation involving an increased number of fibers such as full wire harnesses or textile braiding machines.

- All the derivations adapted to our beam-to-beam contact elements for offering an alternative to Odin's nonsmooth Newton method with so-bogus' Gauss-Seidel (GS) type algorithm have been presented in this thesis. Implementation efforts to connect the datastructure of Odin's beam-to-beam contact elements to so-bogus are necessary before coding the actual GS beam-to-beam contact elements. These will be simpler, since the computation of the generalized Jacobian is not required.

- The bending load case from the MESOMICS experimental setup for a twisted pair with complex initial geometry has been implemented and the simulated deformed configurations passed the eye-test. No significant hysteresis effects were observed. The experimentally observed hysteresis is therefore not explained by our simulations. This point deserves further investigation.

- We focused on beam models with rigid cross-sections and restricted the contact model to circular beams. Though these hypotheses are justified in many practical situations and are a good place to start any investigation related to beam-to-beam contact, they might face limitations at some point. Non-circular cross-sections would complexify the contact search, but not fundamentally change the approach. The additional compliance provided by models with deformable cross-section might add robustness to the model. Such more detailed models may also permit to better investigate hysteresis within wire harnessess.

- The robustness and results obtained from the frictional mortar method for non-trivial three dimensional test cases are not satisfactory and calls for deeper analysis. In particular the implementation of the weighted tangential contact constraints deserves more detailed investigations.

- The general validation of the robustness and accuracy of the proposed contact element in the dynamic case could be further investigated by performing a wider range of test cases for which reference solutions would be available.

APPENDIX

Odin

Odin is a research code developed by Cosimo et. al. [116] for the simulation of nonsmooth flexible multibody systems which uses geometric methods for the description of the motion, for the spatial discretization of flexible components and for the time integration. The contact elements were implemented into a seperate development branch that is currently not available to the public.

DOI: https://zenodo.org/records/7468114

Public Gitlab repository: https://gitlab.uliege.be/am-dept/odin

Documentation: https://obruls.gitlabpages.uliege.be/doc4odin/

Example of the two-fiber twist

```
from odin4py import *
import numpy as np
import json

initialize_odin()

json_file = json.load(open("BeamContactTwist.json"))

ps = create_physical_system()
analysis = ps.get_mech_analysis_ref()
```

```
nodes_list = ps.get_nodes_list_ref()

r = 0.001
l = 1
A = 3.141516 * r * r
E = 200e9
mu = 0.2
G = E / (2 * (1 + mu))
I = 0.25 * 3.141516 * r**4

params = prepro.BeamParams_EA()
params.EA = E * A
params.GA_1 = G * A
params.GA_2 = G * A
params.GJ = G * 2 * I
params.EI_1 = E * I
params.EI_2 = E * I

prop_ground = RigidBodyProps()

# create beam elements' properties
beam_props = prepro.create_Beam_Props_from_parameters(params)
beam_props.with_tg_operator = True
beam_props.with_geom_stiffness = True

num_ele_A = 32 # num_ele_A >= num_ele_B
num_ele_B = 32
n_0 = np.array([0, 1, 0])
b_0 = np.array([0, 0, 1])

# first beam
eps = 0.5 * r
start_point = np.array([0, 0, 0])
end_point = np.array([l, 0, 0])
id_start = 0
elabel = 0

prepro.straight_beam(start_point, end_point, num_ele_A, elabel, id_start, n_0,
```

```
                     b_0, beam_props, ps, -1)
elabel += num_ele_A

nodes_list.insert_nodal_frame(num_ele_A + 1 + num_ele_B + 2, l, 0, 0)
ps.create_element("Rigid_Body", elabel, [num_ele_A + 1 + num_ele_B + 2],
                  prop_ground)
elabel += 1

s_prop_A1 = SphericalJProps()
s_prop_A1.s = ScalingNonsmooth(1, 1, 1)
s_prop_A1.position = end_point
ps.create_element("SphericalJ", elabel,
                  [num_ele_A, num_ele_A + 1 + num_ele_B + 2], s_prop_A1)
elabel += 1

h = json_file["Time_Integrator"]["parameters"]["time_increment"]
hinge_propA = DrivenRevoluteJProps()
hinge_propA.alpha_imposed = lambda t: np.array([h])
hinge_propA.axis = np.array([1, 0, 0])
hinge_propA.position = np.array([l, 0, r + 0.5 * eps])
ps.create_element("Driven_Ground_RevoluteJ", elabel,
                  [num_ele_A + 1 + num_ele_B + 2], hinge_propA)
elabel += 1

# second beam
start_point = np.array([0, 0, 2 * r + eps])
end_point = np.array([l, 0, 2 * r + eps])
id_start = num_ele_A + 1

prepro.straight_beam(start_point, end_point, num_ele_B, elabel, id_start, n_0,
                     b_0, beam_props, ps, deg_ele)
elabel += num_ele_B

nodes_list.insert_nodal_frame(id_start + num_ele_B + 1, l, 0, 2 * r + eps)
ps.create_element("Rigid_Body", elabel, [id_start + num_ele_B + 1],
                  prop_ground)
elabel += 1
s_prop_B1 = SphericalJProps()
```

```
s_prop_B1.s = ScalingNonsmooth(1, 1, 1)
s_prop_B1.position = end_point
ps.create_element("SphericalJ", elabel,
                  [id_start + num_ele_B, id_start + num_ele_B + 1], s_prop_B1)
elabel += 1

hinge_prop = DrivenRevoluteJProps()
hinge_prop.alpha_imposed = lambda t: np.array([h])
hinge_prop.axis = np.array([1, 0, 0])
hinge_prop.position = np.array([l, 0, r + 0.5 * eps])
ps.create_element("Driven_Ground_RevoluteJ", elabel,
                  [id_start + num_ele_B + 1], hinge_prop)
elabel += 1

# creation of contact pairs
contact_prop = BeamContactProps()
contact_prop.r_1 = r
contact_prop.r_2 = r

for i in range(0,num_ele_A,1):
    ps.create_element("Beam_Contact", elabel,
                      [i + num_ele_A + 1, i + num_ele_A + 2, i, i + 1],
                      contact_prop)
    elabel += 1

# Boundary conditions
bc_clamp = BCValue(0, 0, 0)
bc = analysis.get_essential_bcs()
bc.insert(0, BC.Motion,
          [bc_clamp, bc_clamp, bc_clamp, bc_clamp, bc_clamp, bc_clamp])
bc.insert(num_ele_A + 1, BC.Motion,
          [bc_clamp, bc_clamp, bc_clamp, bc_clamp, bc_clamp, bc_clamp])

# compute for the solution
analysis.set_analysis_type(AnalysisType.NonSmoothMortarStatic)
analysis.compute_solution(json_file)

finalize_odin()
```

Gauß-Seidel algorithm

The Gauß-Seidel algorithm [236] is an iterative method to solve linear systems of equations of the type:

$$\mathbf{A}\mathbf{x} = \mathbf{b}, \tag{4.74}$$

where $\mathbf{A}$ is a known square n-dimensional matrix, $\mathbf{b}$ is a known vector and $\mathbf{x}$ is the unknown. The convergence of the Gauß-Seidel algorithm is guaranteed if $\mathbf{A}$ is symmetric positive-definite or strictly diagonally dominant, which is typically the case in beam-to-beam contact applications.

The matrix is decomposed into a lower triangular and a strictly upper triangular part $\mathbf{A} = \mathbf{A}_L + \mathbf{A}_U$. Let us use the subscript k to denote the k-th iteration of $\mathbf{x}$. The solution is obtained by a fixed point iteration via

$$\mathbf{x}_{k+1} = \mathbf{A}_L^{-1} \left(\mathbf{b} - \mathbf{A}_U \mathbf{x}_k\right) \tag{4.75}$$

and using forward substitution to compute each row j of $\mathbf{x}_{k+1}$ sequentially with the most up-to-date values:

$$x_{k+1}^j = \frac{1}{a_{jj}} \left(b_j - \sum_{i<j} a_{ji} x_{k+1}^i - \sum_{i>=j} a_{ji} x_k^i \right), \quad j = 1, 2, ..., n. \tag{4.76}$$

The algorithm ends when a criterion is met on the residual is met. It is detailed in Alg. 6

Algorithm 6 Gauss-Seidel Method

```
Input: A, b, ϵ, MaxIter
Initialize x_0 with an initial guess
for k ∈ [0, MaxIter] do
    for j ∈ [1, n] do
        σ := 0
        for i ∈ [1, n] do
            if i ≠ j then
                σ := σ + a_ji x_k^i
            end if
        end for
        x_{k+1}^j := (b_j − σ)/a_jj
    end for
    if ‖x_{k+1} − x_k‖ < ϵ then
        break
    end if
end for
```

LIST OF FIGURES

LIST OF TABLES

LIST OF SYMBOLS

We list here all relevant symbols in the order of their first occurence in the text.

G	Lie group
$\mathfrak{g}$	Lie algebra of G
$SO(3)$	special orthogonal group
$\mathfrak{so}(3)$	Lie algebra of $SO(3)$
$Sp(1)$	group of unit quaternions
$\mathfrak{sp}(1)$	Lie algebra of $SP(1)$
$\mathbb{R}^3 \times SO(3)$	Lie group that considers translation and rotation seperately
$SE(3)$	special Euclidean group
$\mathfrak{se}(3)$	Lie algebra of $SE(3)$
q	configuration of the system
q_e	configuration of one finite element
$\mathbf{S}(\bullet)$	element of a Lie algebra
$\exp_G$	exponential map of Lie group G

$\log_G$	logarithm map of Lie group G
$\mathbf{T}_G$	tangent operator of Lie group G
cay	Cayley transform
$\{\bullet\}$	a frame
$\mathbf{R}_\bullet$	rotation matrix giving the relative orientation between $\{O\}$ and $\{\bullet\}$ expressed in $\{O\}$
$\mathbf{H}_\bullet$	4×4 matrix giving the relative configuration between $\{O\}$ and $\{\bullet\}$ expressed in $\{O\}$
$\delta\boldsymbol{\pi}_\bullet$	arbitrary variation of $\{\bullet\}$ expressed in $\{\bullet\}$
$\boldsymbol{f}$	deformation gradient
$\boldsymbol{\epsilon}$	sectional strain
$\boldsymbol{v}$	velocity
$\delta\mathcal{W}$	virtual work of the contact free system
$\mathbf{K}$	sectional stiffness matrix
$\mathbf{M}$	mass matrix
$\mathbf{C}$	assembled damping matrix
$\mathbf{f}^{\text{ext}}$	vector of externally applied loads
$\mathbf{d}_{AB}$	discrete relative configuration vector
$\mathbf{Q}$	interpolation matrix for arbitrary perturbations of the beam configuration
$\mathbf{P}$	interpolation matrix for arbitrary perturbation of the beam deformation
ρ_∞	spectral radius at infinity (generalized-α method)
$\alpha_f, \alpha_m, \gamma, \gamma', \beta, \beta'$	numerical parameters (generalized-α method)
$\mathbf{K}_T$	tangent stiffness matrix
$\mathbf{S}_T$	full tangent matrix or Jacobian matrix

$\mathbf{H}_C, \mathbf{H}_F$	local (material) frames located at the beam centerline
$\mathbf{H}_L, \mathbf{H}_K$	local (material) contact frames located at the beam surface
γ_C	potential contact region
$\mathbf{H}_{LK}$	relative contact configuration
g_N	normal gap function
$\mathbf{u}_T$	tangential slip velocity
$\triangle\mathbf{g}_T$	tangential slip increment
$\mathbf{x}_{LK}$	contact vector expressed in $\{L\}$
$\mathbf{G}, \mathbf{G}_N, \mathbf{G}_T$	full, normal and tangential constraint gradient
$\mathbf{m}$	normal to the slave cross-section
$\mathbf{n}$	contact normal
$\mathbf{t}_1$	first contact tangent
$\mathbf{t}_2$	second contact tangent
R_1, R_2	beam radii
$\delta\mathcal{W}_C$	virtual work produced by contact forces
$\boldsymbol{\lambda}, \lambda_N, \boldsymbol{\lambda}_T$	full, normal and tangential Lagrange multiplier
$\mathbf{f}^{\text{con}}$	forces and moments induced by contact interactions
$\mathcal{M}_N$	functional space expressing the constraint on the normal Lagrange multiplier in a weak sense
$\mathcal{M}_T$	functional space expressing the constraint on the tangential Lagrange multiplier in a weak sense
$\psi_{\mathbb{R}^{+/-}}, \partial\psi_{\mathbb{R}^{+/-}}$	indicator function of the positive/negative real line and its subdifferential
μ	friction coefficiant
$C(\lambda_N)$	Coulomb disc

$\psi_{C(\lambda_N)}, \psi^*_{C(\lambda_N)}, \partial\psi_{C(\lambda_N)}$	indicator function of the Coulomb disc, its conjugate and its subdifferential
$\delta\boldsymbol{\Pi}$	total vector of arbitrary nodal variations
$\mathbf{B}, \mathbf{B}_N, \mathbf{B}_T$	total, normal and tangential discretized assembled constraint gradient matrix
$\boldsymbol{\Lambda}, \boldsymbol{\Lambda}_N, \boldsymbol{\Lambda}_T$	total, normal and tangential vector of discrete Lagrange multipliers
$\mathbf{f}^{\text{con}}$	discretized and assembled vector of contact forces and moments
$\boldsymbol{\phi}_e, \boldsymbol{\phi}_{N,e}, \boldsymbol{\phi}_{T,e}$	full, normal and tangential elementwise shape functions for Lagrange multipliers
$\mathbf{g}^{\text{con}}, \mathbf{g}_N^{\text{con}}, \mathbf{g}_T^{\text{con}}$	full, normal and tangential vector of discrete (assembled) constraints
$\mathbf{B}^j, \mathbf{B}_N^j, \mathbf{B}_T^j$	total, normal and tangential discretized assembled constraint gradient matrix associated to constraint j
$\mathbf{D}$	Delassus operator
$\mathbf{b}$	load vector involved in the linearized reduced formulation of the discrete frictional contact problem
$\xi_N^j, \boldsymbol{\xi}_T^j$	normal and tangential augmented multipliers associated to constraint j
k, p	scaling and penalty factors (augmented Lagrangian method)
$\mathcal{L}$	augmented Lagrangian functional
$\mathbf{F}^{\mathcal{L}}$	vector whose roots correspond to the solution of the augmented Lagrangian formulation
$\mathrm{d}\boldsymbol{v}$	differential measure of the nodal velocities
$\mathrm{d}\mathbf{i}, \mathrm{d}\mathbf{i}_N, \mathrm{d}\mathbf{i}_T$	total, normal and tangential impulse measures associated to the constraints

$\mathbf{p}_i, \mathbf{p}_{i,N}, \mathbf{p}_{i,T}$	total, normal and tangential impulse producing the velocity jump at time t_i
$\mathrm{d}t$	Lebesgue measure for time

BIBLIOGRAPHY

[1] M. Smith. *ABAQUS/Standard User's Manual, Version 6.9*. Dassault Systèmes Simulia Corp, United States, 2009.

[2] J. O. Hallquist. *LS-DYNA Keyword User's Manual, Version 971 R6.1.0*. Livermore Software Technology Corporation (LSTC), Livermore United States, 2006.

[3] G. J. DeSalvo and J. A. Swanson. *ANSYS Engineering Analysis System User's Manual*. Swanson Analysis Systems, Houston, United States, 1985.

[4] Hewlett Packard. Simulation drives move to virtual prototyping. DYNAlook: 7th European LS-DYNA Conference, 2009.

[5] Fraunhofer ITWM. Identification of model parameters for ips cable simulation with mesomics. `https://www.itwm.fraunhofer.de/en/departments/mf/technikum/mesomics-ips-cable-simulation.html`, 2023.

[6] J. Linn and K. Dreßler. Discrete Cosserat Rod Models Based on the Difference Geometry of Framed Curves for Interactive Simulation of Flexible Cables method. In *Math for the Digital Factory*, chapter 14. Springer, 2017.

[7] J. Linn, T. Hermansson, and F. Schneider. Kinetic aspects of discrete Cosserat rods based on the difference geometry of framed curves. *Proceedings of the ECCOMAS Thematic Conference on Multibody Dynamics*, 2017.

[8] IPS Cable Simulation. Software for the virtual assembly of cable systems. `https://industrialpathsolutions.se/ips-cable-simulation`.

[9] V. Doerlich, J. Linn, and S. Diebels. Flexible Beam-Like structures-Experimental Investigation and Modeling of Cables. In *Advances in Mechanics of Materials and Structural Analysis*, chapter 2. Springer, 2018.

[10] E. Cottanceau, O. Thomas, P. Véron, M. Alochet, and R. Deligny. A finite element/quaternion/asymptotic numerical method for 3D simulation of flexible cables. *Finite Elem. Anal. Des.*, 139:14–38, 2018.

[11] M. A. Saadat and D. Durville. A mixed stress-strain driven computational homogenization of spiral strands. *Comput. Struct.*, 2023.

[12] D. Durville. *Contribution à la modélisation et à la simulation du comportement mécanique de milieux enchevêtrés.* Université Paris-Saclay, 2021.

[13] B. A. Agarwal, L. J. Broutman, and K. Chandrahshekhara. *Analysis and Performance of Fiber Composites.* Wiley, 2006.

[14] O. T. Adesina, T. Jamiru, E. R. Sadiku, and L. W. Beneke. Mechanical evaluation of hybrid natural fibre-reinforced polymeric composites for automotive bumper beam: a review. *J. Adv. Manuf. Technol.*, 103:1781–1797, 2019.

[15] Y. Steinbrecher, M. Mayr, M. J. Grill, J. Kremheller, C. Meier, and A. Popp. A mortar-type finite element approach for embedding 1d beams into 3D solid volumes. *Comp. Mech.*, 66:1377–1398, 2020.

[16] T. Alpiyldiz. 3D geometrical modelling of tubular braids. *Text. Res. J.*, 82:443–453, 2012.

[17] A. Cagri and J. Carey. 2D braided composites: A review for stiffness critical applications. *Compos. Struct.*, 85:43–58, 2008.

[18] D. Branscomb, D. Beale, and R. Broughton. New Directions in Braiding. *J. Eng. Fibers Fabr.*, 8, 2013.

[19] P. Davies, D. Durville, and D. V. Thanh. The influence of torsion on braided rope performance, modelling and tests. *Appl. Ocean Res.*, 59:417–423, 2016.

[20] J. F. A. Kessels and R. Akkerman. Prediction of the yarn trajectories on complex braided preforms. *Compos. Appl. Sci. Manuf.*, 33:1073–1081, 2002.

[21] G. Zhou, X. Sun, and Y. Wang. Multi-chain digital element analysis in textile mechanics. *Compos. Sci. Technol.*, 64:239–244, 2004.

[22] S. Razavi and L. Iannucci. Simulation of the Braiding Process in LS-DYNA. *Proceedings of the 15th International LS-DYNA Users Conference*, 2018.

[23] A. K. Pickett, J. Sirtautas, and A. Erber. Braiding Simulation and Prediction of Mechanical Properties. *Appl. Compos. Mater.*, 16:345–394, 2009.

[24] G. A. Costello. *Theory of Wire Rope.* Springer, 1997.

[25] F. Foti and L. Martinelli. Mechanical modeling of metallic strands subjected to tension, torsion and bending. *Int. J. Solids Struct.*, 91:1–17, 2016.

[26] F. Foti and L. Martinelli. Modeling the axial-torsional response of metallic strands accounting for the deformability of the internal contact surfaces: Derivation of the symmetric stiffness matrix. *Int. J. Solids Struct.*, 171:30–46, 2019.

[27] E. De Menezes and R. Marczak. Comparative analysis of different approaches for computing axial, torsional and bending stiffnesses of cables and wire ropes. *Eng. Struct.*, 241, 2021.

[28] F. Bertails, B. Audoly, M.-P. Cani, F. Leroy, and J.-L. Lévêque. Super-Helices for Predicting the Dynamics of Natural Hair. *ACM Trans. Graph.*, 25:1180–1187, 2006.

[29] E. L. Starostin and G. H. M. Van Der Heijden. Theory of equilibria of elastic 2-braids with interstrand interaction. *J. Mech. Phys. Solids*, 64:83–132, 2014.

[30] M. J. Grill, W. A. Wall, and C. Meier. A computational model for molecular interactions between curved slender fibers undergoing large 3D deformations with a focus on electrostatic, van der Waals, and repulsive steric forces. *Int. J. Numer. Methods Eng.*, pages 1–46, 2020.

[31] D. Hellier, F. Albermani, B. Evans, H. De Visser, C. Adam, and J. Passenger. Flexural and torsional rigidity of colonoscopes at room and body temperatures. *Proc. Inst. Mech. Eng.*, 225:389–399, 2010.

[32] L. Blanc, A. Delchambre, and P. Lambdert. Flexible Medical Devices: Review of Controllable Stiffness Solutions. *Actuators*, 6, 23, 2017.

[33] M. Stavole, Sato Martin De Almagro R. T., M. Lohk, and S. Leyendecker. Homogenization of the Constitutive Properties pf Composite beam Cross-Sections. *Proceedings of the ECCOMAS ECCM Oslo*, 2022.

[34] V. Denoël. Advantages of a semi-analytical approach for the analysis of an evolving structure with contacts. *Commun. Numer. Meth. Eng.*, 00:1–16, 2000.

[35] V. Denoël and E. Detournay. Eulerian formulation of constrained elastica. *Int. J. Solids Struct.*, 48:625–636, 2011.

[36] A. Huynen, E. Detournay, and V. Denoël. Eulerian formulation of elastic rods. *Proc. R. Soc.*, 472, 2016.

[37] H. E. Goicoechea, F. S. Buezas, and M. B. Rosales. A non-linear Cosserat rod model for drill-string dynamics in arbitrary borehole geometries with contact and friction. *Int. J. Mech. Sci.*, 157-158:98–110, 2019.

[38] THREAD. Joint training on numerical modelling of highly flexible structures for industrial applications. https://thread-etn.eu/.

[39] M. Géradin and A. Cardona. *Flexible Multibody Dynamics*. Wiley, 2001.

[40] V. Sonneville. *A geometric local frame approach for flexible multibody systems*. PhD thesis, University of Liege, 2015.

[41] A. Bosten, J. Linn, A. Cosimo, V. Sonneville, and O. Brüls. The SE(3) Lie group framework for flexible multibody systems with contact. *Contribution at the NumDiff Halle*, 2021.

[42] J. M. Selig. *Geometric Fundamentals of Robotics*. Springer, 1996.

[43] J. N. Reddy. *An introduction to continuum mechanics*. Cambridge University Press, 2013.

[44] F. Essenburg. On the significance of the inclusion of the effect of transverse normal strain in problems involving beams with surface constraints. *ASME J. Appl. Mech.*, 42:127–132, 1975.

[45] P.M. Naghdi and M.B. Rubin. On the significance of normal cross-sectional extension in beam theory with application to contact problems. *Int. J. Solids Struct.*, 25:249–265, 1989.

[46] J-S. Chen. On the contact behavior of a buckled Timoshenko beam constrained laterally by a plane wall. *Acta Mech.*, 222:225–232, 2011.

[47] A. Bosten, A. Cosimo, J. Linn, and O. Brüls. Effective inelastic bending behavior of multi-wire cables using finite elements accounting for wire contact. *Proceedings of the ECCOMAS ECCM*, 2022.

[48] D. Doyen, A. Ern, and S. Piperno. Time-integration schemes for the finite element dynamic Signorini problem. *SIAM J. Sci. Comput.*, 33:223–249, 2011.

[49] G. Daviet, F. Bertails-Descoubes, and L. Boissieux. A hybrid iterative solver for robustly capturing Coulomb friction in hair dynamics. *ACM Transactions on Graphics*, 30:1–12, 2011.

[50] P. Flores. Contact mechanics for dynamical systems: a comprehensive review. *Multibody Syst. Dyn.*, 54:127–177, 2022.

[51] A. Bosten, A. Cosimo, J. Linn, and O. Brüls. A mortar formulation for frictionless line-to-line beam contact. *Multibody Syst. Dyn.*, 54:31–52, 2021.

[52] A. Bosten, V. Denoël, A. Cosimo, J. Linn, and O. Brüls. A beam contact benchmark with analytic solution. *Z. Angew. Math. Mech*, 103(11):1–12, 2023.

[53] B. Bauer, A. Bosten, M. Roller, and J. Linn. Physical validation of simulation tools for slender elastic structures. *Proceedings of ECCOMAS Multibody*, 2023.

[54] J. C. Simo. A finite strain beam formulation: The three dimensional dynamic problem. Part I. *Comput. Methods Appl. Mech. Eng.*, 49:55–70, 1985.

[55] J. C. Simo and L. Vu-Quoc. A three dimensional finite strain rod model. Part II: Computational aspects. *Comput. Methods Appl. Mech. Eng.*, 58:79–116, 1986.

[56] A. Genoese, A. Genoese, A. Bilotta, and G. Garcea. A generalized model for heterogeneous and anisotropic beams including section distortions. *Thin Walled Struct.*, 74:85–103, 2014.

[57] A. Cardona and M. Géradin. A beam finite element non-linear theory with finite rotations. *Int. J. Numer. Methods Eng.*, 26:2403–2438, 1988.

[58] A. Ibrahimbegovic. On finite element implementation of geometrically nonlinear Reissner's beam theory: three-dimensional curved beam elements. *Comput. Methods Appl. Mech. Eng.*, 122:11–26, 1995.

[59] G. Jelenic and M. A. Crisfield. Geometrically exact 3D beam theory: implementation of strain-invariant finite element for statics and dynamics. *Comput. Methods Appl. Mech. Eng.*, 171:141–171, 1999.

[60] P. Betsch and P. Steinmann. Frame-indifferent beam finite elements based upon the geometrically exact beam theory. *Int. J. Numer. Methods Eng.*, 54:1775–1788, 2002.

[61] I. Romero. The interpolation of rotations and its application to finite element models of geometrically exact rods. *Comput. Mech.*, 34:121–133, 2004.

[62] J. Harsch, G. Capobianco, and S. R. Eugster. Finite element formulations for constrained spatial nonlinear beam theories. *Math. Mech. Solids*, 26:1838–1863, 2021.

[63] O. A. Bauchau and S. Han. Interpolation of rotation and motion. *Multibody Syst. Dyn.*, 31:339–370, 2014.

[64] S. Han and O. A. Bauchau. On the global interpolation of motion. *Comput. Methods Appl. Mech. Eng.*, 337:352–386, 2018.

[65] C. Meier, A. Popp, and W. A. Wall. Geometrically exact finite element formulations for slender beams: Kirchhoff-Love versus Simo-Reissner theory. *Arch. Comput. Methods Eng.*, 26:163–243, 2017.

[66] M. Borri and C. Bottasso. An intrinsic beam model based on a helicoidal approximation - Part I: formulation. *Int. J. Numer. Methods Eng.*, 37:2267–2289, 1994.

[67] C. L. Bottasso and M. Borri. Integrating finite rotations. *Comput. Methods Appl. Mech. Engrg.*, 164:307–331, 1998.

[68] V. Sonneville, A. Cardona, and O. Brüls. Geometrically exact beam finite element formulated on the special Euclidean group $SE(3)$. *Comput. Methods Appl. Mech. Eng.*, 268:451–474, 2014.

[69] S. Grazioso, G. Di Geronimo, and B. Siciliano. A geometrically exact model for soft continuum robots: The finite element deformation space formulation. *Soft Robot.*, 6:790–811, 2019.

[70] R. Jödicke, U. Jungnickel, and A. Müller. Lie group modeling of nonlinear helical beam elements. *Proceedings of ASME: IDETC/CIE (Buffalo, USA)*, 2014.

[71] D. Zupan and M. Saje. Finite-element formulation of geometrically exact three-dimensional beam theories based on interpolation of strain measures. *Comput. Methods Appl. Mech. Eng.*, 192:5209–5248, 2003.

[72] E. Zupan and D. Zupan. Velocity-based approach in non-linear dynamics of three-dimensional beams with enforced kinematic compatibility. *Comput. Methods Appl. Mech. Eng.*, 310:406–428, 2016.

[73] D. Lolic, D. Zupan, and M. Brojan. A consistent strain-based beam element with quaternion representation of rotations. *Comput. Mech.*, 65:1397–1412, 2020.

[74] H. Lang, J. Linn, and M. Arnold. Multi-body dynamics simulation geometrically exact Cosserat rods. *Multibody Syst. Dyn.*, 25:285–312, 2011.

[75] T. Leitz, R. Sato Martin de Almagro, and S. Leyendecker. Multisymplectic Galerkin Lie group variational integrators for geometrically exact beam dynamics

based on unit dual quaternion interpolation–no shear locking. *Comput. Methods Appl. Mech. Eng.*, 374:113475, 2021.

[76] S. Hante, D. Tumiotto, and M. Arnold. A Lie group variational integration approach to the full discretization of a constrained geometrically exact Cosserat beam model. *Multibody Syst. Dyn.*, 54:97–123, 2021.

[77] E. H. Dill. Kirchhoff's Theory of Rods. *Arch. Hist. Exact Sci.*, 44:1–23, 1992.

[78] H. Lang and M. Arnold. Numerical aspects in the dynamic simulation of geometrically exact rods. *Appl. Numer. Math.*, 62:1411–1427, 2012.

[79] J. Linn, H. Lang, and A. Tuganov. Geometrically exact Cosserat rods with Kelvin-Voigt type viscous damping. *Mech. Sci.*, 4:79–96, 2013.

[80] M. Bergou, M. Wardetzky, S. Robinson, B. Audoly, and E. Grinspun. Discrete Elastic Rods. *In proceedings of ACM: SIGGRAPH (Los Angeles, USA)*, 2008.

[81] C. Meier, A. Popp, and W. A. Wall. An objective 3D large deformation finite element formulation for geometrically exact curved Kirchhoff rods. *Comput. Methods Appl. Mech. Eng.*, 278:445–478, 2014.

[82] C. Meier, A. Popp, and W. A. Wall. A locking-free finite element formulation and reduced models for geometrically exact Kirchhoff rods. *Comput. Methods Appl. Mech. Eng.*, 290:314–341, 2015.

[83] A. A. Shabana. Definition of the Slopes and the Finite Element Absolute Nodal Coordinate Formulation. *Multibody Syst. Dyn.*, 1:339–348, 1997.

[84] R. Y. Yakoub and A. A. Shabana. Three Dimensional Absolute Nodal Coordinate Formulation for Beam Elements: Implementation and Applications. *J. Mech. Des.*, 123:614–621, 2001.

[85] J. Gerstmayr and A. A. Shabana. Analysis of Thin Beams and Cables Using the Absolute Nodal Co-ordinate Formulation. *Nonlinear Dyn.*, 45:109–130, 2006.

[86] I. Sokolov, S. Krylov, and I Harari. Extension of non-linear beam models with deformable cross sections. *Comput. Mech.*, 56:999–1021, 2015.

[87] P. Wriggers and G. Zavarise. On contact between three-dimensional beams undergoing large deflections. *Comput. Methods Appl. Mech. Eng.*, 40:815–826, 2007.

[88] G. Zavarise and P. Wriggers. Contact with friction between beams in 3-D space. *Int. J. Numer. Methods Eng.*, 49:977–1006, 2000.

[89] P. Litewka. Hermite polynomial smoothing in beam-to-beam frictional contact problem. *Int. J. Numer. Methods Eng.*, 49:977–1006, 2000.

[90] P. Litewka. Finite Element Analysis of Beam-to-Beam Contact. In F. Pfeiffer and P. Wriggers, editors, *Lecture Notes in Applied and Computational Mechanics*, volume 53. Springer, 2010.

[91] P. Litewka. Frictional beam-to-beam multiple-point contact finite element. *Comput. Mech.*, 56:243–264, 2015.

[92] A. Konyukhov and K. Schweizerhof. On the solvability of closest point projection procedures in contact analysis: analysis and solution strategy for arbitrary surface approximations. *Comput. Methods Appl. Mech. Eng.*, 197:3045–3056, 2008.

[93] A. Konyukhov and K. Schweizerhof. Geometrically exact covariant approach for contact between curves. *Comput. Methods Appl. Mech. Eng.*, 199:2510–2531, 2010.

[94] A. G. Neto, P. M. Pimenta, and P. Wriggers. A master-surface to master-surface formulation for beam to beam contact. PartII: Frictional interaction. *Comput. Methods Appl. Mech. Eng.*, 319:146–174, 2017.

[95] D. Durville. Modélisation du comportement mécanique de câbles métalliques. *Revue Européenne des Eléments Finis*, 7:9–22, 1998.

[96] D. Durville. Numerical simulation of entangled materials mechanical properties. *J. Mat. Sci.*, 40:5941–5948, 2005.

[97] D. Durville. Contact-friction modeling within elastic beam assemblies: an application to knot tightening. *Comput. Mech.*, 49:687–707, 2012.

[98] O. Weeger, B. Narayanan, L. De Lorenzis, and M. L. Dunn. An isogeometric collocation method for frictionless contact of Cosserat rods. *Comput. Methods Appl. Mech. Eng.*, 321:361–382, 2017.

[99] Q. Wang, Q. Tian, and H. Hu. Dynamic simulation of frictional contacts of thin beams during large overall motions via absolute nodal coordinate formulation. *Nonlinear Dyn.*, 77:1411–1425, 2014.

[100] Q. Wang, Q. Tian, and H. Hu. Dynamic simulation of frictional multi-zone contacts of thin beams. *Nonlinear Dyn.*, 83:1919–1937, 2016.

[101] M. Chamekh, S. Mani-Aouadi, and M. Moakher. Modeling and numerical treatment of elastic rods with frictionless self-contact. *Comput. Methods Appl. Mech. Eng.*, 198:3751–3764, 2009.

[102] C. Meier, A. Popp, and W. A. Wall. A finite element approach for the line-to-line contact interaction of thin beams with arbitrary orientation. *Comput. Methods Appl. Mech. Eng.*, 308:377–413, 2016.

[103] M.-J. Choi, S. Klinkel, and R. A. Sauer. An isogeometric finite element formulation for frictionless contact of Cosserat rods with unconstrained directors. *Comput. Mech.*, 70:1107–1144, 2022.

[104] C. Meier, W. A. Wall, and A. Popp. A unified approach for beam-to-beam contact. *Comput. Methods Appl. Mech. Eng.*, 315:972–1010, 2017.

[105] C. Meier, M. J. Grill, W. A. Wall, and A. Popp. Geometrically exact beam elements and smooth contact schemes for the modeling of fiber-based materials and structures. *Int. J. Solid Struct.*, 154:124–146, 2018.

[106] A. Konyukhov, O. Mrenes, and K. Schweizerhof. Consistent development of a beam-to-beam contact algorithm via the curve-to-solid beam contact: Analysis for the nonfrictional case. *Int. J. Numer. Methods Eng.*, 113:1108–1144, 2018.

[107] F. Bertails-Descoubes, F. Cadoux, G. Daviet, and V. Acary. A nonsmooth Newton solver for capturing exact Coulomb friction in fiber assemblies. *ACM Transactions on Graphics*, 30:1–14, 2011.

[108] G. Daviet. *Modèles et algorithmes pour la simulation du contact frottant dans les matériaux complexes. Application aux milieux fibreux et granulaires*. PhD thesis, Université Grenoble Alpes, 2016.

[109] A. Tasora, S. Benatti, D. Mangoni, and R. Garziera. A geometrically exact isogeometric beam for large displacements and contacts. *Comput. Methods Appl. Mech. Eng.*, 358:112635, 2020.

[110] R. Judge, Z. Yang, S. W. Jones, and G. Beattie. Full 3D finite element modelling of spiral strand cables. *Constr. Build. Mater.*, 35:452–459, 2012.

[111] Y. Yu, X. Wang, and Z. Chen. A simplified finite element model for structural cable bending mechanism. *Int. J. Mech. Sci.*, 113:196–210, 2016.

[112] S. Lalonde, R. Guilbault, and F. Légeron. Modeling multilayered wire strands, a strategy based on 3D finite element beam-to-beam contacts-Part I: Model formulation and validation. *Int. J. Mech. Sci.*, 126:281–296, 2017.

[113] F. Ménard and P. Cartraud. Solid and 3D beam finite element models for the nonlinear elastic analysis of helical strands within a computational homogenization framework. *Comput. Struct.*, 257:106675, 2021.

[114] M. Hawwash, V. Dörlich, J. Linn, R. Müller, and R. Keller. Effective inelastic bending behavior of multi-wire cables using finite elements accounting for wire contact. *Proceedings of the ECCOMAS Thematic Conference on Multibody Dynamics*, 2021.

[115] M. Hawwash, V. Dörlich, J. Linn, R. Keller, and R. Müller. Modeling the effective inelastic behavior of multi-wire cables under mechanical load using finite elements. *Proceedings of the ECCOMAS ECCM*, 2022.

[116] A. Cosimo and O. Brüls. Odin. gitlab repository. https://gitlab.uliege.be/am-dept/odin, 2022. https://doi.org/10.5281/zenodo.7468114.

[117] V. Sonneville and O. Brüls. A few good reasons to consider a beam finite element formulation on the Lie group $SE(3)$. *Proceeding of the ASME: IDETC/CIE (Portland, USA)*, 2013.

[118] V. Sonneville, A. Cardona, and O. Brüls. Geometric interpretation of a non-linear beam finite element on the Lie group $SE(3)$. *Arch. Mech. Eng.*, 61:305–329, 2014.

[119] V. Sonneville, O. Bauchau, and O. Brüls. On the compatibility equations in geometrically exact beam finite element. *Proceeding of the ASME: IDETC/CIE (Charlotte, USA)*, 2016.

[120] V. Sonneville, O. Brüls, and O. Bauchau. Interpolation schemes for geometrically exact beams: A motion approach. *Int. J. Numer. Methods Eng.*, 112:1129–1153, 2017.

[121] V. Sonneville and O. Brüls. Sensitivity analysis for multibody systems formulated on a lie group. *Multibody Syst. Dyn.*, 31:47–67, 2013.

[122] A. Lismonde, V. Sonneville, and O. Brüls. A geometric optimization method for the trajectory planning of flexible manipulators. *Multibody Syst. Dyn.*, 47:347–362, 2019.

[123] V. Sonneville, M. Scapolan, M. Shan, and O. Bauchau. Modal reduction procedures for flexible multibody dynamics. *Multibody Syst. Dyn.*, 51:377–418, 2020.

[124] O. Bauchau and V. Sonneville. Formulation of shell elements based on the motion formalism. *Appl. Mech.*, 2:1009–1036, 2021.

[125] W. M. Boothby. *An Introduction to Differentiable Manifolds and Riemannian Geometry.* Academic Press, 2003.

[126] L. W. Tu. *An Introduction to Manifolds.* Springer, 2011.

[127] O. Brüls. *Lecture notes in Kinematics and Dynamics of Mechanisms*. University of Liège, 2023.

[128] J. Bernoulli. *Ars Conjectandi, opus posthumum. Accedit Tractatus de seriebus infinitis, et epistola gallicé scripta de ludo pilae reticularis*. Thurneysen Brothers, Basel, 1713.

[129] E. Celledoni and B. Owren. Lie group methods for rigid body dynamics and time integration on manifolds. *Comput. Methods Appl. Mech. Engrg.*, 192:421–438, 2003.

[130] C. Moler and C. Van Loan. Nineteen Dubious Ways to Compute the Exponential of a Matrix, Twenty-Five Years Later. *SIAM Review*, 45(1):3–49, 2003.

[131] J. Todesco and O. Brüls. Highly accurate differentiation of the exponential map and its tangent operator. *Mech. Mach. Theory (under review)*, 2023.

[132] B. Audoly and Y. Pomeau. *Elasticity and Geometry: From hair curls to the non-linear response of shells*. Oxford University Press, Oxford, 2010.

[133] C. Gear, B. Leimkuhler, and G. Gupta. Automatic integration of Euler-Lagrange equations with constraints. *J. Comput. Appl. Math.*, 12:77–90, 1985.

[134] O. Brüls, V. Acary, and A. Cardona. Simultaneous enforcement of constraints at position and velocity levels in the nonsmooth generalized-α scheme. *Comput. Methods Appl. Mech. Eng.*, 281:131–161, 2014.

[135] O. Brüls, V. Acary, and A. Cardona. On the Constraint Formulation in the Nonsmooth Generalized-α Method. In R. I. Leine, V. Acary, and O. Brüls, editors, *Advanced Topics in Nonsmooth Mechanics*, pages 335–374. Springer, 2018.

[136] A. Cosimo, J. Galvez, F. J. Cavalieri, A. Cardona, and O. Brüls. A robust nonsmooth generalized-α scheme for flexible systems with impacts. *Multibody Syst. Dyn.*, 48:127–149, 2020.

[137] H. Munthe-Kaas. Runge-Kutta Methods on Lie Groups. *BIT*, 38(1):92–111, 1998.

[138] P. E. Crouch and R. Grossman. Numerical Integration of Ordinary Differential Equations on Manifolds. *J. Nonlinear Sci.*, 3:1–33, 1993.

[139] O. Brüls and A. Cardona. On the use of Lie group integrators in multibody dynamics. *J. Comput. Nonlinear Dyn.*, 5(3), 2010.

[140] O. Brüls, A. Cardona, and M. Arnold. Lie group generalized-α time integration of constrained flexible multibody systems. *Mech. Mach. Theory*, 48:121–137, 2010.

[141] M. Arnold, O. Brüls, and A. Cardona. Error analysis of generalized-α Lie group time integration methods for constrained mechanical systems. *Numer. Math.*, 129:149–179, 2015.

[142] V. Romero, M. Ly, A. H. Rasheed, R. Charrondière, A. Lazarus, S. Neukirch, and F. Bertails-Descoubes. Physical validation of simulators in Computer Graphics: A new framework dedicated to slender elastic structures and frictional contact. *ACM Transactions on Graphics*, 40(4), 2021.

[143] W. Bickley. The heavy elastica. *Lond. Edinb. Dublin philos. mag. j. sci.*, 17(113):603–622, 1934.

[144] M. P. do Carmo. *Differential geometry of curves and surfaces.* Prentica-Hall, Englewood Cliffs, NJ, 1976.

[145] L. R. Wilberforce. On the vibrations of a loaded spiral spring. *Lond. Edinb. Dublin philos. mag. j. sci.*, 38(233):386–392, 1894.

[146] R. E. Berg and T. S. Marshall. Wilberforce pendulum oscillations and normal modes. *Am. J. Phys.*, 59(1):32–38, 1991.

[147] N. Kikuchi and J. T. Oden. *Contact Problems in Elasticity.* SIAM, 1988.

[148] T. A. Laursen. *Computational Contact and Impact Mechanics.* Springer, 2002.

[149] P. Wriggers. *Computational Contact Mechanics.* Springer, 2002.

[150] P. Wriggers et al. Analysis and Simulation of Contact Problems. In P. Wriggers and U. Nackenhorst, editors, *Lecture Notes in Applied and Computational Mechanics*, volume 27. Springer, 2006.

[151] G. Zavarise et al. Trends in Computational Contact Mechanics. In G. Zavarise and P. Wriggers, editors, *Lecture Notes in Applied and Computational Mechanics*, volume 58. Springer, 2011.

[152] A. Konyukhov and K. Schweizerhof. *Computational Contact Mechanics: Geometrically Exact Theory for Abritrary Shaped Bodies.* Springer, 2013.

[153] A. Konyukhov and I. Ridvan. *Introduction to Computational Contact Mechanics: A Geometrical Approach.* Wiley, 2015.

[154] P. A. Raviart and J. M. Thomas. Primal Hybrid Finite Element Methods for 2nd Order Elliptic Equations. *Math. Comput.*, 31:391–413, 1977.

[155] F. Ben Belgacem and Y. Maday. The Mortar finite element method for three dimensional finite elements. *Modélisation Mathématique et Analyse Numérique*, 31:289–302, 1997.

[156] F. Ben Belgacem. The Mortar finite element method with Lagrange multipliers. *Numer. Math.*, 84:173–197, 1999.

[157] H. Ben Dhia, I. Vautier, and M. Zarroug. Problèmes de contact frottant en grandes transformations: du continu au discret. *Revue Européenne des Eléments Finis*, 9:243–261, 2000.

[158] T. W. McDevitt and T. A. Laursen. A mortar-finite element formulation for frictional contact problems. *Int. J. Numer. Methods Eng.*, 48:1525–1547, 2000.

[159] M. A. Puso and T. A. Laursen. A mortar segment-to-segment contact method for large deformation solid mechanics. *Comput. Methods Appl. Mech. Eng.*, 193:601–629, 2004.

[160] M. A. Puso and T. A. Laursen. A mortar segment-to-segment frictional contact method for large deformations. *Comput. Methods Appl. Mech. Eng.*, 193:4891–4913, 2004.

[161] S. Hüeber and B. I. Wohlmuth. A primal-dual active set strategy for non-linear multibody contact problems. *Comput. Methods Appl. Mech. Eng.*, 194:3147–3166, 2005.

[162] K. A. Fischer and P. Wriggers. Frictionless 2D Contact formulations for finite deformations based on the mortar method. *Comput. Mech.*, 36:226–244, 2005.

[163] B. Yang, T. A. Laursen, and X. Meng. Two dimensional mortar contact methods for large deformation frictional sliding. *Int. J. Numer. Meth. Eng.*, 62:1183–1225, 2005.

[164] K. A. Fischer and P. Wriggers. Mortar based frictional contact formulation for higher order interpolations using the moving friction cone. *Comput. Methods Appl. Mech. Eng.*, 195:5020–5036, 2006.

[165] M. Gitterle, A. Popp, M. W. Gee, and W. A. Wall. Finite deformation frictional mortar contact using a semi-smooth newton method with consistent linearization. *Int. J. Numer. Methods Eng.*, 84:543–571, 2010.

[166] T. Cichosz and M. Bischoff. Consistent treatment of boundaries with mortar contact formulations using dual Lagrange multipliers. *Comput. Methods Appl. Mech. Eng.*, 200:1317–1332, 2011.

[167] C. Hesch and P. Betsch. Transient three-dimensional contact problems: mortar method. Mixed methods and conserving integrationn. *Comput. Mech.*, 48:461–475, 2011.

[168] M. Tur, E. Giner, F. J. Fuenmayor, and P. Wriggers. 2D contact smooth formulation based on the mortar method. *Comput. Methods. Appl. Mech. Eng.*, 247-248:1–14, 2012.

[169] T. A. Laursen, M. A. Puso, and J. Sanders. Mortar contact formulations for deformable-deformable contact: Past contributions and new extensions for enriched and embedded interface formulations. *Comput. Methods Appl. Mech. Eng.*, 205-208:3–15, 2012.

[170] A. Popp. *Mortar Methods for Computational Contact Mechanics and General Interface Problems*. PhD thesis, Technical University of Munich, 2012.

[171] F. J. Cavalieri, V. D. Fachinotti, and A. Cardona. A mortar contact algorithm for three-dimensional elasticity problems. *Rev. Int. Metodos Numer. para Calc. Diseno Ing.*, 28:80–92, 2012.

[172] F. J. Cavalieri and A. Cardona. An augmented Lagrangian technique combined with a mortar algorithm for modeling mechanical contact problems. *Int. J. Numer. Methods Eng.*, 93:420–442, 2012.

[173] A. Popp and W. A. Wall. Dual mortar methods for computational contact mechanics - overview and recent developments. *GAMM-Mitt.*, 1:66–84, 2014.

[174] T. Doca, F. M. Andrade Pires, and J. M. A. Cesar de Sa. A frictional mortar contact approach for the analysis of large inelastic deformation problems. *Int. J. Solids Struct.*, 51:1697–1715, 2014.

[175] F. J. Cavalieri and A. Cardona. Numerical solution of frictional contact problems based on a mortar algorithm with an augmented Lagrangian technique. *Multibody Syst. Dyn.*, 35:353–375, 2015.

[176] A. Seitz, P. Farah, J. Kremheller, B. I. Wohlmuth, W. A. Wall, and A. Popp. Isogeometric dual mortar methods for computational contact mechanics. *Comput. Methods Appl. Mech. Eng.*, 301:259–280, 2016.

[177] P. Farah, W. A. Wall, and A. Popp. A mortar finite element approach for point, line and surface contact. *Int. J. Numer. Methods Eng.*, 00:1–44, 2017.

[178] P. Farah. *Mortar Methods for Computational Contact Mechanics Including Wear and General Volume Coupled Problems*. PhD thesis, Technical University of Munich, 2018.

[179] A. Bosten. Towards a contact formulation for efficient numerical simulation of marine ice-sheet instabilities. Master's thesis, University of Liège, 2021.

[180] F. Ben Belgacem and Y. Renard. Hybrid finite element methods for the Signorini problem. *Math. Comput.*, 72:1117–1145, 2003.

[181] J. Solberg, R. Jones, and P. Papadopoulos. A family of simple two-pass dual formulations for the finite element solution of contact problems. *Comput. Methods Appl. Mech. Eng.*, 196:782–802, 2007.

[182] S. Hüeber. *Discretization techniques and efficient algorithms for contact problems*. PhD thesis, University of Stuttgart, 2008.

[183] B. Wohlmuth. Variationally consistent discretization schemes and numerical algorithms for contact problems. *Acta Numer.*, 20:569–734, 2011.

[184] M. A. Puso and J. M. Solberg. A dual pass mortar approach for unbiased constraints and self-contact. *Comput. Methods. Appl. Mech. Eng.*, 367:113092, 2020.

[185] M. Mayr and A. Popp. Scalable computational kernels for mortar finite element methods. *arXiv*, https://arxiv.org/abs/2202.03933, 2022.

[186] J. Tomec and G. Jelenic. Analysis of static frictionless beam-to-beam contact using mortar method. *Multibody Syst. Dyn.*, 55:293–322, 2022.

[187] P. Alart and A. Curnier. A mixed formulation for frictional contact problems prone to Newton like solution methods. *Comput. Methods Appl. Mech. Engrg.*, 92:353–375, 1991.

[188] R. I. Leine and H. Nijmeijer. Dynamics and Bifurcations of Non-Smooth Mechanical Systems. In F. Pfeiffer and P. Wriggers, editors, *Lecture Notes in Applied and Computational Mechanics*, volume 18. Springer, 2004.

[189] V Acary and B. Brogliato. *Numerical Methods for Nonsmooth Dynamical Systems*. Springer, 2008.

[190] C. Studer. Numerics of Unilateral Contacts and Friction. In F. Pfeiffer and P. Wriggers, editors, *Lecture Notes in Applied and Computational Mechanics*, volume 47. Springer, 2006.

[191] B. Brogliato. *Nonsmooth Mechanics: Models, Dynamics and Control.* Springer, 2016.

[192] C. Ericson. *Real Time Collision Detection.* Morgan Kaufmann Publishers, 2005.

[193] M. Teschner, B. Heidelberger, M. Müller, D. Pomeranets, and M. Gross. Optimized Spatial Hashing for Collision Detection of Deformable Objects. *Vision, Modeling, Visualization*, pages 47–54, 2003.

[194] M. Teschner, M. Kimmerle, B. Heidelberger, B. Zachmann, G. Raghupathi, L. Fuhrmann, A. Cani, M.-P. Faure, F. Magnetenat, N. Strasser, and P. Volino. Collision detection for deformable objects. *Comput. Graph. Forum*, 24:61–81, 2005.

[195] F. Facchinei and J.-S. Pang. *Finite Dimensional Variational Inequalities.* Springer, 2003.

[196] J. Tomec and G. Jelenic. Frictionless line-to-line contact: comparision of mortar and unbiased formulation in combination with Lagrange-multipliers and penalty method. *Int. J. Solids Struct.*, 2023 (under review).

[197] V. Acary, M. Brémond, and O. Huber. On solving contact problems with coulomb friction: Formulations and numerical comparisons. In R. I. Leine, V. Acary, and O. Brüls, editors, *Advanced Topics in Nonsmooth Mechanics*, pages 375–457. Springer, 2018.

[198] K. Erleben. Numerical methods for linear complementarity problems in physics-based animation. In *ACM SIGGRAPH 2013 Courses*, SIGGRAPH '13. Association for Computing Machinery, 2013.

[199] M. Ap. Tzaferopoulos. On an efficient new numerical method for the frictional contact problem of structures with convex energy density. *Comput. Struct.*, 48(1):87–106, 1993.

[200] F. Cadoux. *Optimisation et analyse convexe pour la dynamique non-régulière.* PhD thesis, Université Joseph Fourir, 2009.

[201] V. Acary, F. Cadoux, C. Lemaréchal, and J. Malick. A formulation of the linear discrete Coulomb friction problem via convex optimization. *Z. Angew. Math. Mech.*, 91(2):155–175, 2010.

[202] G. De Saxcé and Z.-Q. Feng. New inequality and functional contact with friction: The implicit standart material approach. *Mech. Struct. Mach.*, 19(3):301–325, 1991.

[203] J.C. Simo and T.A. Laursen. An augmented Lagrangian treatment of contact problems involving friction. *Comput. Struct.*, 42(1):97–116, 1992.

[204] M. Macklin, K. Erleben, M. Müller, N. Chentanez, S. Jeschke, and V. Makoviychuk. Non-smooth Newton methods for deformable multi-body dynamics. In *ACM Transactions on Graphics*, volume 38, pages 1–20. Association for Computing Machinery, 2019.

[205] G. Daviet. so-bogus. gitlab repository. https://gitlab.inria.fr/elan-public-code/so-bogus, 2016.

[206] Erwin Coumans. Bullet physics sdk. https://github.com/bulletphysics/bullet3, 2016-2021.

[207] A. Bosten, A. Cosimo, J. Linn, and O. Brüls. Towards a Gauß-Seidel solver for problems involving line-to-line beam contact. *Proceedings of the ECCOMAS ECCM*, 2022.

[208] R.T. Rockafellar. Augmented Lagrangians and applications of the proximal point algorithm in convex programming. *Math. Oper. Res.*, 1:97–116, 1976.

[209] J. Galvez, F. J. Cavalieri, A. Cosimo, O. Brüls, and A. Cardona. A nonsmooth frictional contact formulation for multibody system dynamics. *Int. J. Numer. Methods Eng.*, 121:3584–3609, 2020.

[210] A. Cosimo, F. J. Cavalieri, J. Galvez, A. Cardona, and O. Brüls. A General Purpose Formulation for Nonsmooth Dynamics with Finite Rotations: Application to the Woodpecker Toy. *J. Comput. Nonlinear Dyn.*, 16:031001–1, 2021.

[211] E. Burman, P. Hansbo, and M. G. Larson. The Augmented Lagrangian Method as a Framework for Stabilised Methods in Computational Mechanics. *Arch. Comput. Methods Eng.*, 30:2579–2604, 2023.

[212] R. I. Leine and N. van den Wouw. Stability and Convergence of Mechanical Systems with Unilateral Constraints. In F. Pfeiffer and P. Wriggers, editors, *Lecture Notes in Applied and Computational Mechanics*, volume 36. Springer, 2008.

[213] H. Uzawa. Iterative methods for concave programming. In K. Arrow, J. Hurwicz, and H. Uzawa, editors, *Studies in linear and nonlinear programming*, pages 154–165. Stanford University Press, 1958.

[214] L. Qi and J. Sun. A nonsmooth version of Newton's method. *Math. Program.*, 58:353–367, 1993.

[215] E. J. Hinch. *Perturbation Methods.* Cambridge University Press, 1991.

[216] M. Hawwash, V. Dörlich, and Linn. Bending and torsion of twisted cable strands accounting for the effect of friction. *Proceedings of the ECCOMAS Thematic Conference on Multibody Dynamics*, 2023.

[217] A. F. Mahmoud and M. I. Abdallah. Performance testing of twisted pair cables. *J. Comput. Syst. Netw. Commun.*, 2008:1–8, 2008.

[218] Belden Electronics Division. The impact of installation stresses on cable performance. 2001.

[219] D. Gross, W. Hauger, J. Schröder, and W. A. Wall. *Teschnische Mechanik: Band 2: Elastostatik.* Springer, 2007.

[220] R. Featherstone. *Rigid Body Dynamics Algorithms.* Springer, 2008.

[221] R. I. Leine, V. Acary, and O. Brüls. *Advanced Topics in Nonsmooth Dynamics.* Springer, 2018.

[222] M. Jean and J. J. Moreau. Dynamics in the presence of unilateral contacts and dry friction: a numerical approach. In *Unilateral Problems in Structural Analysis*, volume 2, pages 151–196. Springer, 1987.

[223] J. J. Moreau. Unilateral contact and dry friction in finite freedom dynamics. In *Nonsmooth Mechanics and Applications*, volume 302, pages 1–82. Springer, 1988.

[224] M. Jean. The non-smooth contact dynamics method. *Comput. Methods Appl. Mech. Eng.*, 177:235–257, 1999.

[225] L. Paoli and M. Schatzman. A numerical scheme for impact problems I: the one-dimensional case. *SIAM J. Numer. Anal.*, 40:702–733, 2002.

[226] L. Paoli and M. Schatzman. A numerical scheme for impact problems II: the multidimensional case. *SIAM J. Numer. Anal.*, 40:734–768, 2002.

[227] J. Chung and G. M. Hulbert. A time integration algorithm with improved numerical dissipation: The generalized-α method. *J. Appl. Mech.*, 60:371–375, 1993.

[228] M. Arnold and O. Brüls. Convergence of the generalized-α scheme for constrained mechanical systems. *Multibody Syst. Dyn.*, 85:187–202, 2007.

[229] Q-Z. Chen, V. Acary, G. Virlez, and O. Brüls. A nonsmooth generalized-α scheme for flexible multibody systems with unilateral constraints. *Int. J. Numer. Methods Eng.*, 96:487–511, 2013.

[230] A. Cosimo, F. J. Cavalieri, A. Cardona, and O. Brüls. On the adaptation of local impact laws for multiple impact problems. *Nonlinear Dyn.*, 102:1997–2016, 2020.

[231] F. J. Cavalieri, A. Cosimo, A. Sanchez, O. Brüls, and A. Cardona. Simulation of Sliding Friction of Spherical Rigid Bodies Subject to Multiple Impact Collisions. In M. Pucheta, A. Cardona, S. Preidikman, and R. Hecker, editors, *Multibody Mechatronic Systems*, volume 94, pages 151–158. Springer, 2021.

[232] G. Capobianco, J. Harsch, S. Eugster, and R. I. Leine. A nonsmooth generalized-α scheme for mechanical systems with contact. *Int. J. Numer. Methods Eng.*, 122(3):1–31, 2021.

[233] K. Wang and Q. Tian. A nonsmooth method for spatial frictional contact dynamics of flexible multible multibody systems with large deformation. *Int. J. Numer. Methods Eng.*, 124(3):1–28, 2022.

[234] A. Cardona and M. Géradin. Numerical integration of second order differential-algebraic systems in flexible mechanism dynamics. *Comput. Aided Anal. Rigid Flex. Mech. Syst.*, pages 501–529, 1994.

[235] B. Bozorgmehri, X. Yu, Matikainen M. K., A. B. Harish, and A. Mikkola. A study of contact methods in the application of large deformation dynamics in self-contact beam. *Multibody Syst. Dyn*, 103:581–616, 2021.

[236] L. Seidel. Über ein verfahren, die gleichungen, auf welche die methode der kleinsten quadrate führt, sowie lineare gleichungen überhaupt, durch successive annäherungen aufzulösen. *Abh. Math.-Phys. Cl. Königl. Bayer. Akad. Wiss.*, 11:81–108, 1874.